

Modular Construction of Ultra-stable, Porous, Crystalline Covalent Organic Frameworks: Membrane based Water Purification and Energy Storage

Thesis Submitted to AcSIR

For the Award of the Degree of

DOCTOR OF PHILOSOPHY

In

CHEMICAL SCIENCES



(Academy of Scientific and Innovative Research)

By

Arjun Halder

(Registration Number: 10CC14A26018)

Under the guidance of

Dr. Rahul Banerjee

Physical & Materials Chemistry Division
CSIR-National Chemical Laboratory
Pune - 411008, Maharashtra, India

July 2018



सीएसआईआर - राष्ट्रीय रासायनिक प्रयोगशाला

(वैज्ञानिक तथा औद्योगिक अनुसंधान परिषद)

डॉ. होमी भाभा मार्ग, पुणे - 411 008, भारत

CSIR - NATIONAL CHEMICAL LABORATORY

(Council of Scientific & Industrial Research)

Dr. Homi Bhabha Road, Pune - 411 008, India



Certificate

This is to certify that the work incorporated in this Ph.D. thesis entitled “Modular Construction of Ultra-stable, Porous, Crystalline Covalent Organic Frameworks: Membrane based Water Purification and Energy Storage” submitted by Mr. Arjun Halder to Academy of Scientific and Innovative Research (AcSIR) in fulfillment of the requirements for the award of the Degree of Doctor of Philosophy, embodies original research work under my supervision. I further certify that this work has not been submitted to any other University or Institution in part or full for the award of any degree or diploma. Research material obtained from other sources has been duly acknowledged in the thesis. Any text, illustration, table etc., used in the thesis from other sources, have been duly cited and acknowledged.

Arjun Halder

Mr. Arjun Halder

(Student)

Rahul Banerjee

Dr. Rahul Banerjee

(Supervisor)

Communication Channels

NCL Level DID : 2590
NCL Board No. : +91-20-25902000
EPABX : +91-20-25893300
: +91-20-25893400



FAX

Director's Office : +91-20-25902601
COA's Office : +91-20-25902660
SPO's Office : +91-20-25902664

WEBSITE

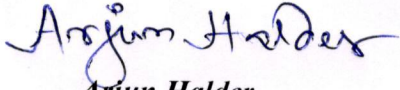
www.ncl-india.org

STATEMENT

*I hereby declare that the matter embodied in this thesis entitled “**Modular Construction of Ultra-stable, Porous, Crystalline Covalent Organic Frameworks: Membrane based Water Purification and Energy Storage**” is the result of investigations carried out by me in the Physical & Materials Chemistry Division, CSIR-National Chemical Laboratory, Pune, India under the supervision of Dr. Rahul Banerjee.*

In keeping with the general practice of reporting scientific observations due acknowledgements have been made wherever the work described is based on the findings of other investigators.

Pune, July 2018


Arjun Halder

**Dedicated to
My Parents and Sister**

ACKNOWLEDGEMENT

*I would take this opportunity to express my sincere gratitude to my supervisor **Dr. Rahul Banerjee**. My heartfelt thanks go to him for introducing me to the wonders of scientific research, for his persistent guidance, encouragement, inspiration and support during every stage of my doctoral research work. Again I warmly thank him for his precious advice, analysis, criticism and discussions on my research work. I am very much thankful to him for his pursuance for improving me as a person as well as my scientific skills. I would also like to sincerely thank my research co-supervisor **Dr. Shatabdi Porel Mukherjee** and my DAC committee members **Dr. Sreekumar Kurungot**, **Dr. S.K. Asha** and **Dr. Narendra Y. kadoo** for their constructive, innovative suggestion and comments throughout my Ph.D. work period at CSIR-NCL, Pune.*

*I extend my sincere thanks to the Director of CSIR-NCL **Prof. Ashwani Kumar Nangia**, former Directors **Dr. Vijayamohanan K. Pillai** and **Dr. Sourav Pal**, Head of Physical and Materials Chemistry Division **Dr. P. A. Joy** and **Dr. Anil Kumar (Ex-HoD)** for their kind help and encouragement during the course of this work. I must earnestly acknowledge the collaborative assistance, valuable scientific discussions and suggestions that I received from **Dr. Ulhas K. Kharul**, **Dr. Sreekumar Kurungot** and **Dr. Kumar Vanka** from CSIR NCL. My sincere thanks and kind acknowledgement to **Dr. Matthew Addicoat** from School of Science and Technology, Nottingham Trent University, Clifton Lane, NG11 8NS Nottingham, United Kingdom and **Dr. Thomas Hein**, from School of Engineering and Science, Jacobs University, Germany, for their help in theoretical calculations in my projects.*

*I am very much grateful to CSIR, New Delhi for fellowship support to carry out my research work. I thank all the non-teaching staff of CSIR-NCL for their assistance on various occasions. I wish to thank all my friendly and cooperative labmates **Tamas Da**, **Pradip Bhaya**, **Arijit Da**, **Chandan Da**, **Subhadeep Da**, **Tanay Da**, **Govinda da**, **Sujit Da**, **Digamber Ji**, **Jayashri Mam**, **Suman da**, **Bishnu da**, **Sharath da**, **Harshitha Di**, **Bikash Da**, **Manas da**, **Amit da**, **Tapan da**, **Arghya Da**, **Sushil Bhaya**, **Shouvik Da**, **Srinu Anna**, **Gargi Di**, **Mohitosh**, **Saibal**, **Suwendu**, **Kaushik**, **Himadri**, **Abdul**, **Shebeeb** and **Kanhu da** for creating a cheerful and enjoyable working atmosphere in the lab. They were extremely*

supportive as well as helpful during my tenure. I also thank project student Priyankar, Pankaj and Ashwathi who helped me in various projects.

*My stay on this campus has been pleasant with the association of all the research scholars at CSIR-NCL. I am thankful to **Anup da, Santi Da, Pravat da, Jayasis da, Kanak da, Achintya da, Susanta da, Arpan da, Arya da, Saikat da, Shyam da, Chandan da, Krishanu da, Tanaya di, Munmun di, Soumen da, Bhawna Di, Vinita, Shrikanth, Suresh Da, Farsa Ram, Subhra, Monika** for their support, guidance, and advice.*

*I would also like to thank to **Siba Da, Subhrasis da, Tapas da, Tamal da, Pronob da, Manzoor, Indradweep, Subrata, Avijit, Pranoy, Sandipan, Sutanu, Anirban, Anagh, Meena, Moumita, Milan, Sanjukta, Gargi, Moumita di, Atanu da, Manik da, Santanu Da, Sudip Da, Chayanika Di, Monalisa Di, Bittu, Atryee Di, Manoj Da, Gablu Da** as my pune stay would have been boring without you people. I am thankful to for their support, guidance, and advice.*

*I would also like to thanks my previous mentor **Dr. Ashis K. Patra** and all my seniors and friends from IIT, Kanpur, specially **Bappa da, Jaydeb Da, Anirban Da, Shrikant Da, Khusbhu Di, Priyaranjan Vaiya, Krithika di, Payel Di, Sourav, Banshi, Somesh, Anupam.***

*I am grateful to all my teachers and I expressed my gratitude for their encouragement in different part of my life. I thank the entire members of my family for their constant care and wishes. Last but not least, I would like to pay high regards to my father **Sahadeb Halder**, mother **Chanchala Halder** and my elder sister **Ganga Halder** for their constant encouragement and inspiration throughout my research work and lifting me uphill this phase of life. Dedicating this thesis to them is a minor recognition for their valuable support and encouragement.*

Arjun Halder

PREFACE

Fundamental research associated with the porous materials has convened inordinate scientific attention in the field of materials science owing to their various potential applications such as in gas storage, catalysis, separation, chemical sensing, conductivity and electrochemistry related works such as for energy storage etc. Among all other porous materials, Metal Organic Frameworks (MOFs) are porous open framework structures, which are constructed from the metal ions clusters and organic linkers. Although MOFs are potential enough for adsorption, separation, and catalysis but the poor chemical and thermal stability of the MOF materials limits their practical applicability. Replacing the weak coordinate bonds with strong covalent bonds is one of the options to improve the chemical and thermal stability of the porous framework materials. In this context, Covalent Organic Frameworks (COFs) represents emerging class of organic porous crystalline material with higher chemical and thermal stability compared to MOFs. Since the sole compositions of COFs are lighter elements they have very low density and could be utilized as an effective gas storage media (For H₂, CO₂ and NH₃).

Although COFs are highly potential for various promising applications, the utilization of this COF material towards real life application is limited due to its unprocessable powder form along with chemical instability in strong acids or bases. Therefore, the development and rapid construction of porous crystalline COFs with ultrahigh chemical stability along with high processability into pellets, beads and membranes for real life applications is highly essential and challenging. Again, fabrication of novel porous COFs as an energy storage material such as for supercapacitor application is also of keen interest. Moreover, apart from chemical constituents, the overall properties and real time applicability of any material largely relies on its nano-scale morphology. Hence, morphological control and growth at nano-scale of these novel COFs could be another promising study for its intended development.

Chapter 2 introduces the rapid and scalable synthesis of a series of porous crystalline imine (-C=N-) based Covalent Organic Frameworks (COFs) [TpOMe-**Tab**,-**Pa1**,-**PaNO₂**,-**BD(NO₂)₂**,-**BPy** & -**Azo**] via PTSA (*p*-toluenesulfonic acid) mediated solid-state mixing approach which showcased extraordinary high chemical stability in abrasive environment including conc. H₂SO₄ (36 N, seven days), conc. HCl (12 N, seven days) and NaOH (9 N, 24 h) and in various protic/aprotic solvents. Introduction of 2,4,6-trimethoxy-1,3,5-benzenetricarbaldehyde (TpOMe) as a prime aldehyde with three bulky methoxy (-OCH₃)

groups adjacent to the aldehyde ($-\text{CHO}$) functionalities assist impregnable COF crystallization with BET surface area as high as $2000 \text{ m}^2/\text{g}$. The DFT calculations revealed the presence of significant numbers of interlayer $\text{C}-\text{H}\cdots\text{N}$ H-bonding between the methoxy ($-\text{OCH}_3$) $\text{C}-\text{H}$ of a particular layer with the imine ($-\text{C}=\text{N}$) nitrogen atoms present in the adjacent layers induces this exceptional chemical stability within these frameworks. This interlayer $\text{C}-\text{H}\cdots\text{N}$ H-bonding improves interlayer stacking interaction and provides enough steric hindrance and hydrophobic crowding around the imine bonds and protects it from being hydrolyzed in such abrasive environment (*Angew. Chem., Int. Ed.*, **2018**, 57, 5797).

Chapter 3 will present the facile construction of porous, crystalline, self-standing covalent organic framework membranes (COFM) with extraordinary chemical stability [in water, acetone, acetonitrile, methanol, ethanol and 18 N sulphuric acid solutions for several days] for real life applications such as water purification and acid recovery. The **TpOMe-Azo** COFM (BET surface area $2100 \text{ m}^2/\text{g}$) showed considerably high solvent (water, acetone, acetonitrile, methanol and ethanol) flux reflecting its potentiality towards waste solvent treatment. Considering the high chemical stability of as-synthesized **TpOMe-Azo** membrane, we have tested the COFM for standard sulphuric acid solution permeance where we have observed as high as $> 99\%$ permeance reflecting its potentiality for sulfuric acid purification. Furthermore, the COFMs were further utilized for challenging separations of expensive ingredients like methylene blue, dye molecules such as rhodamin b, rose Bengal and congo red, from the drinking water with high recyclability (*Angew. Chem., Int. Ed.*, **2018**, 57, 5797).

Chapter 4 discusses strategic design and facile fabrication of a chemically stable, redox active and self-standing **TpOMe-DAQ** COF thin sheet containing several anthraquinone moieties, in its backbone, which upon $2\text{H}^+/2\text{e}^-$ reduction converts to anthracene functionality or vice versa during electrode process and behaves as a supercapacitor electrode material for energy storage. The pristine as synthesized TpOMe-DAQ when employed as free-standing supercapacitor electrode showcased outstanding areal capacitance of 1600 mFcm^{-2} (169 Fg^{-1}) which is the highest value ever achieved in pure COF based SCs and also comparable to other promising electrode materials. The material also exhibits outstanding GCD (galvano-static charge-discharge) cyclic stability even operating over 1,00,000 cycles without losing its capacitive performance or coulombic efficiency even using mordant electrolyte concentration (3 M aq. H_2SO_4) (Manuscript under revision).

Chapter 5 describes the nano-scale morphological evaluation in porous crystalline two-dimensional (2D) Covalent Organic Frameworks with remarkable chemical stability in

3(N) HCl owing to the presence of intramolecular O—H•••N hydrogen bonding. These COFs are found to adopt diverge morphologies including ribbons (**2,3-DhaTta**) and hollow spheres (**2,3-DhaTab**) exhibiting BET surface area as high as 1700 m²/g. The mechanism of formation of ribbons or hollow spheres have been thoroughly and systematically investigated where the morphology of COFs was believed to be tuned based on dihedral angles of linkers and core planarity as evidenced from Density Functional Theory (DFT) calculations. Interestingly we could establish the initial morphology (after 12 h of aging) of a COF crystallite largely depends on its π - π stacking efficiency among adjacent COF layers (*Angew. Chem., Int. Ed.*, **2016**, *27*, 7806).

Finally, Chapter 6 summaries the overall work presented in this thesis. The future direction based on the discussion and understanding of this thesis work also presented in the last section of this chapter.

Arjun Halder

CONTENTS	PAGE
Certificate	iii
Statement	iv
Acknowledgement	v
Preface	vii

CHAPTER 1

Introduction to Covalent Organic Frameworks: Synthesis, Applications, Chemical Stability and Processability issues			1-39
1.1	Background of porous crystalline materials		2
1.2	Classification of the porous materials		3-6
	1.2.1	Inorganic porous framework materials	4
	1.2.2	Inorganic–organic hybrid porous framework materials	5
	1.2.3	Organic porous framework materials	6
1.3	Covalent organic frameworks		6-8
1.4	Types of reversible reaction utilized for the synthesis of COFs		9-10
	1.4.1	Boronic acid trimerisation	9
	1.4.2	Boronate ester formation reaction	9
	1.4.3	Trimerization of nitriles	10
	1.4.4	Schiff base reaction	10
1.5	Basic symmetric rules of combination		10
1.6	Synthetic methods		13-19
	1.6.1	Solvothermal synthesis	15
	1.6.2	Microwave synthesis	16
	1.6.3	Ionothermal synthesis	16
	1.6.4	Synthesis of monolayers on template surface	17
	1.6.5	Room temperature synthesis	18
	1.6.6	Mechanochemical synthesis	19
1.7	Applications of COFs		19-29
	1.7.1	Gas storage application	20
	1.7.2	Hydrogen storage	20
	1.7.3	Methane storage	23
	1.7.4	Carbon dioxide removal	23
	1.7.5	Ammonia storage	23
	1.7.6	Heterogeneous catalysis	24
	1.7.7	Photoelectric and semi conduction applications	26
	1.7.8	Energy storage	27
	1.7.9	Separation	28
	1.7.10	Drug storage and delivery	29
1.8	Chemical stability of COFs		30
1.9	Approaches made to stabilize COFs towards various chemical treatments		32-38

1.10	Morphology of COF crystallites	38-39
-------------	---------------------------------------	--------------

CHAPTER 2

	Ultra-stable Covalent Organic Frameworks: A Role of Interlayer Hydrogen Bonding	40-71
2.1	Introduction	41
2.2	Synthesis of ultra-stable covalent organic frameworks	44
2.2.1	Synthesis and characterization	44
2.2.2	Structural simulation and characterization	47
2.2.3	Chemical characterization	50
2.2.4	Gas adsorption studies	53
2.2.5	Chemical stability investigation	55
2.2.6	Reason behind the exceptional chemical stability	62
2.3	Conclusion	68
2.4	Experimental procedures	68-71
2.4.1	Materials	68
2.4.2	Synthesis of 2,4,6-trimethoxy-1,3,5-benzenetricarbaldehyde (TpOMe)	68
2.4.3	General methods for characterization	70
2.4.4	Structure modeling of COFs	71

CHAPTER 3

	Chemically Stable Covalent Organic Framework Membranes (COFMs) for water purification	72-79
3.1	Introduction	73-76
3.2	Fabrication of ultra-stable covalent organic framework membrane (COFM)	76
3.2.1	Synthesis of TpOMe-Azo COFM	78
3.2.2	Structural simulation and characterization	78
3.2.3	Chemical characterization	81
3.2.4	Gas adsorption studies	82
3.2.5	Morphology investigation	84
3.2.6	Chemical stability investigation	85
3.3	Water purification study using TpOMe-Azo COFM	89
3.4	Sulphuric acid recovery using TpOMe-Azo COFM	91
3.5	Conclusion	94
3.6	Experimental procedures	95

3.6.1	Materials	95
3.6.2	General methods for characterization	95
3.6.3	Solvent flux and sulfuric acid permeance measurement	96
3.6.4	Structure modeling of COFMs	98

CHAPTER 4

Selective Fabrication of Redox Active Covalent Organic Framework as Capacitive Energy Storage Materials 100-133

4.1	Introduction	101-102
4.1.1	Introduction to electrochemical capacitors (Supercapacitors)	101
4.1.2	Advantages of covalent organic frameworks (COFs) as electrode materials	102
4.2	Ultra-stable, self-standing, redox-active COF thin sheet as energy storage material	102
4.2.1	Synthesis of TpOMe-DAQ COF thin sheet	105
4.2.2	Structural simulation and characterization	106
4.2.3	Chemical characterization	108
4.2.4	Gas adsorption studies	110
4.2.5	Chemical stability investigation	112
4.3	Electrochemical study	115-130
4.3.1	Three electrode supercapacitor	116
4.3.2	Two electrode supercapacitor (solid state device)	125
4.4	Conclusions	130
4.5	Experimental procedures	131
4.5.1	Materials	131
4.5.2	General methods for characterization	131
4.5.3	Structure Modeling of COFs	132

CHAPTER 5

Morphological Diversity in 2D Porous Covalent Organic Frameworks: An Effect of Core Planarity modulation 134-164

5.1	Introduction	135
5.2	Detailed investigation of nano-ribbon and hollow spherical morphological evolution in 2D COFs	136
5.2.1	Synthesis of COFs	138
5.2.2	Structural simulation and characterization	138

5.2.3	Chemical characterization	141
5.2.4	Gas adsorption studies	143
5.2.5	Chemical stability investigation	144
5.2.6	Morphological study of COFs and explanation behind their formation	147
5.3	Conclusion	156
5.4	Experimental procedures	157
5.4.1	Materials	157
5.4.2	Synthesis of 4,4',4''-(1,3,5-triazine-2,4,6-triyl)trianiline (Tta)	157
5.4.3	Synthesis of reference compound 2,2',2''-((1E,1'E,1"E)-(((1,3,5-triazine-2,4,6-triyl)tris(benzene-4,1 diyl))tris(azanylylidene))tris(methanylylidene))triphenol (SaTta)	159
5.4.4	X-Ray investigation of single crystals of reference compounds	160
5.4.5	Structure Modelling of COFs	161
 CHAPTER 6		
	Conclusions of All Chapters and Future Directive	165-173
6.1	Conclusions	165-167
6.2	Future directives: Developing self-standing and functionalized covalent organic framework membranes for arsenic-contaminated water purification	168-173
6.2.1.	Introduction	168
6.2.2.	The commercial technique used for arsenic removal	169
6.2.3.	The proposed approach for arsenic removal from drinking water through self-standing COF membrane	170
6.2.4.	COFM based device fabrication for arsenic removal from groundwater	172
 REFERENCES		174-192
About the Author		193
List of Publications and Conferences		194-195

LIST OF FIGURES

Figures	Page	
1.1	<i>Classification of various porous materials based on pore diameter and framework natures.</i>	4
1.2	<i>Schematic representation of a) and c) COF formation by the reversible reaction, b) PAF formation by the irreversible reaction.</i>	7
1.3	<i>Different type of reversible organic reactions used for the COF synthesis.</i>	9
1.4	<i>Schematic representation of various symmetric combinations used during COF framework construction.</i>	11
1.5	<i>Different linker used for COF synthesis. (a) Boronic acid-based building blocks for boron-containing COFs. (b) Different catechol-based linkers for another type of boron-based COFs. (c,d) Aldehyde and amine building units used for imine based COF synthesis.</i>	12
1.6	<i>Different synthetic methods generally used for the construction of COFs.</i>	14
1.7	<i>Schematic representation of different steps involved in the Solvothermal COF synthesis.</i>	15
1.8	Figure 1.8.: <i>(a) Synthesis of COF-5 on a surface of few-layer graphene. (b) & (c) STM images of COF-1 and (d) STM images of COF 10 on HOPG surface. [Reprinted with permission from Ref., Copyright Science, 2010].</i>	17
1.9	<i>Various applications of COFs such as gas storage, photo-conducting materials, heterogeneous catalysis, energy storage, separation and drug/biomolecules storage.</i>	20
1.10	<i>Comparison of excess hydrogen uptake of different COFs (a) at 1 bar and (b) high pressure (open symbols represent experimental results, filled symbols simulated results). (c) Methane adsorption isotherms of COFs at high pressure. (d) Carbon dioxide adsorption isotherms of COFs at high pressure. [Reprinted with permission from Ref. J. Am. Chem. Soc., 2009, 131, 8875[1.37], Copyright American Chemical Society, 2009].</i>	21
1.11	<i>(a) Ammonia adsorption isotherms of COF-10 powder (black) and tablet (blue). (b) Lewis adducts formation between ammonia and boronate ester. [Reprinted with permission from Ref. Nat. Chem., 2010, 2, 235[1.43], Copyright Nature Chemistry, 2010].</i>	24
1.12	<i>(a) Schematic representation of the synthesis of nanoparticle-loaded COFs. (b) and (c) Catalysis performed by nanoparticle immobilized COF-TpPa-1. [Reprinted with permission from Ref. Chem. Commun., 2015, 51, 11717 and Chem. Commun., 2014, 50, 3169 [1.44c-d], Copyright Royal Society of Chemistry, 2014-15].</i>	25
1.13	<i>(a) Schematic representation of the device set up used for the measurement of the photocurrent of TP-COF.(In the device COF powders (blue) were sandwiched between two electrodes). (b) I-V profiles as-synthesized TP-COF (blue) and iodine doped TP-COF (red). (c) Hole (μ_h) and electron (μ_e) carrier motilities of H₂P-COF (blue), ZnP-COF (green) and CuP-COF (red).</i>	26
1.14	<i>Schematic representation of (a) as-synthesized COF (b) partial hydrolysis and release of monomers into solution upon submersion in water (c) Completely</i>	31

	<i>hydrolyzed COF.</i>	
1.15	<i>Attempts made to improve the chemical stability in COFs (a) alkylation (b) doping of pyridine.</i>	32
1.16	<i>(a) Synthesis scheme for chemically stable COFs (TpPa-1 and 2) using Schiff base condensation reaction via a reversible-irreversible reaction route. (b) Construction of an intralayer hydrogen bonded COF DhaTph.</i>	34
1.17	<i>(a) Tautomerism in simple N-salicylideneanilines where enol-form is more stable than its keto form. (b) Tautomerism form is stable when basicity of nitrogen atoms collectively dominates over the aromaticity.</i>	35
1.18	<i>(a) Synthesis of TPB-DMTP-COF from DMTA and TAPB through Schiff base reaction. Inset: The structure of the edge units of TPB-DMTP-COF and the resonance effect of the oxygen lone pairs that weaken the polarization of the C=N bonds and soften the interlayer repulsion in the COF. (b) Synthetic scheme for benzoxazole linked COF LZU-191.</i>	37
1.19	<i>Various Morphologies of COF crystallites reported in the literature.</i>	39
2.1	<i>(a) Schematic representation of the synthesis of highly stable TpOMe-X COFs by using Schiff base condensation between TpOMe aldehyde with six different amines. (b-f) chem. draw and space filling (eclipsed) structures of all COFs. Pore diameter has shown with a double-headed arrow.</i>	42
2.2	<i>(a-e) Schematic representation of COF TpOMe-PaI synthesis. (f) Comparison of PXRD patterns of TpOMe-PaI COF with starting materials at a different stage of the reaction.</i>	44
2.3	<i>General scheme for the construction of Tf-PaI from Tf (1,3,5-triformylbenzene) aldehyde and PaI amine.</i>	45
2.4	<i>(a) PXRD and (b) N₂ adsorption isotherms for Tf-PaI at two different reaction conditions.</i>	46
2.5	<i>Experimental Pore size distribution of Tf-PaI [N₂ at 77 K on carbon (cylindr./sphere pores, QSDFT adsorption branch)] at two different reaction condition.</i>	46
2.6	<i>(a) PXRD patterns of as-synthesized (black) compared with the slip-AA(red) and Staggered (green) of all TpOMe-X (X= Tab, PaI, PaNO₂, BD(NO₂)₂, BPY and Azo) COFs.</i>	48
2.7	<i>The experimental PXRD patterns (red) compared with the simulated (slip AA; blue) and Pawley refined difference (black) [Rp, Rwp and Rwp (w/o bck) have shown in the inset for all COFs]</i>	49
2.8	<i>(left) FT-IR and (right) ¹³C NMR spectra of as-synthesized TpOMe-Ani monomer.</i>	49
2.9	<i>Comparison of FT-IR spectra of synthesized TpOMe-COFs with its starting materials</i>	50
2.10	<i>Solid state ¹³C CP-MASS spectra of synthesized TpOMe-COFs (carbon atoms with probable chemical shift mentioned with numerical in Chem. Draw).</i>	51
2.11	<i>Thermogravimetric analyses (TGA) of TpOMe-COFs.</i>	52
2.12	<i>Nitrogen adsorption analysis isotherms of TpOMe-COFs.</i>	53
2.13	<i>Experimental Pore size distribution of respected TpOMe COFs [N₂ at 77 K on</i>	54

	<i>carbon (cylindr./sphere pores, QSDFT adsorption branch)].</i>	
2.14	<i>PXRD and BET surface area comparison of TpOMe-PaI after treatment in different common solvents (protic and aprotic) as mentioned.</i>	55
2.15	<i>PXRD comparison of COF samples after treatment in a different solvent as mentioned. (a) TpOMe-PaI (b) TpOMe-PaNO₂ (c) TpOMe-BPy and (d) TpOMe-Azo.</i>	56
2.16	<i>FT-IR comparison of COF samples after treatment in a different solvent as mentioned. (a)TpOMe-PaI (b) TpOMe-PaNO₂ (c) TpOMe-BPy and (d) TpOMe-Azo.</i>	57
2.17	<i>N₂ adsorption comparison of COF samples after treatment in a different solvent as mentioned. (a) TpOMe-PaI (b) TpOMe-PaNO₂ (c) TpOMe-BPy and (d) TpOMe-Azo.</i>	58
2.18	<i>PXRD (a) and FT-IR (b) comparison of TpOMe-Tab COF samples after treatment in a different solvent as mentioned.</i>	58
2.19	<i>N₂ adsorption isotherm comparison of TpOMe-Tab (a) and TpOMe-BD(NO₂)₂ COF samples after treatment in a different solvent as mentioned.</i>	59
2.20	<i>(a) PXRD and (b) FTIR comparison of TpOMe-BD(NO₂)₂ COF samples after treatment in a different solvent as mentioned.</i>	60
2.21	<i>SEM images of TpOMe-BD(NO₂)₂: as synthesized and in H₂SO₄ (36 N) 1 day.</i>	60
2.22	<i>SEM images of TpOMe COFs (scale bar 10 μm): as synthesized, in H₂SO₄ (36 N) 7 days and in NaOH (9N) 24 h.</i>	61
2.23	<i>Interlayer C–H•••N H-bonding- (i) distances (H to N atom in dotted line; Å) and angles (C–H•••N) in degree (shown in green) (ii) C to N atom distance in dotted line; Å for (a) TpOMe-Tab, (b) TpOMe-PaNO₂, (c) TpOMe-PaI, (d) TpOMe-BPy, (e) TpOMe-Azo and (f) TpOMe-BD(NO₂)₂.</i>	63
2.24	<i>Crystallographic evidence of C–H•••N and C–H•••O hydrogen bonding (C-grey, H-cyan, N-blue, O-red) in small molecules. (a-c) Intermolecular C–H•••N hydrogen bonding between methoxy (–OCH₃) C–H and imine ‘N’ atom (CCDC No: a-951727, b-722946, c-645628)^[2,9]. (d) Intermolecular C–H•••O hydrogen bonding between methoxy (–OCH₃) C–H of one molecule with methoxy (–OCH₃) ‘O’ atom of another molecule or vice versa (CCDC No.-795700).^[2,10] Hydrogen bond distances (D and d) in Å and bond angles (θ) in degree have shown.</i>	64
2.25	<i>Schematic representation of interlayer C–H•••N hydrogen bonding in TpOMe-BPy, its effect on preventing imine (C=N) bond hydrolysis in the acidic medium through the steric and hydrophobic environment.</i>	66
2.26	<i>Hydrolysis mechanism of imine (C=N) bond in acid (H⁺) medium.</i>	66
2.27	<i>Hydrolysis mechanism of imine (C=N) bond in base (OH⁻) medium.</i>	67
2.28	<i>¹H NMR spectrum (in CDCl₃) of TpOMe aldehyde (4).</i>	69
3.1	<i>(a-c) General synthesis scheme for TpOMe-Azo COFM via Schiff base condensation reaction between TpOMe and Azo starting materials. d) Digital image of a membrane. (e-f) Eclipsed space-filling model and chem. draw structure of TpOMe-Azo COFM respectively.</i>	77
3.2	<i>Digital images of as-synthesized TpOMe-Azo COFM (a) Membranes stored in</i>	78

	<i>distilled water, (b) Membrane kept on a glass petri dish and (c) Membrane shown with a certain flexibility in dry condition.</i>	
3.3	<i>(a) Comparison PXRD of as-synthesized (red) compared with the eclipsed (blue) and staggered (green). (b) Experimental (red) PXRD profiles of TpOMe-Azo COFM compared with an eclipsed arrangement (blue); difference plot is given in (black).</i>	79
3.4	<i>FT-IR data of TpOMe-Azo COFM compared to starting materials.</i>	81
3.5	<i>(a) Solid state ¹³C spectra of TpOMe-Azo COFM (partial chem. draw assigning possible signaling carbons have been shown in inset). (d) TGA data of activated COFM under N₂ atmosphere.</i>	82
3.6	<i>(a) N₂ adsorption and (b) Experimental pore size distribution (cylindr./sphere pores, QSDFT adsorption branch) of as-synthesized TpOMe-Azo COFM.</i>	83
3.7	<i>(a) Top view and (b) cross-section view from SEM of as-synthesized TpOMe-Azo COFM. Scale bars have been shown on inset.</i>	84
3.8	<i>Physical appearance of the TpOMe-Azo COFM after treatment in (a) HCl (12 M) for 7 days, (b) H₂SO₄ (9 M) for 7 days, (c) H₂SO₄ (18 M) for 3 days and (d) NaOH (9 M) for 1 day.</i>	85
3.9	<i>Comparison of (a) PXRD and (b) FTIR of TpOMe-Azo COFMs after treatment in a different solvent as mentioned.</i>	85
3.10	<i>Comparison of (a) N₂ adsorption and (b) Experimental pore size distribution (cylindr./sphere pores, QSDFT adsorption branch) of TpOMe-Azo COFMs after treatment in a different solvent as mentioned.</i>	86
3.11	<i>Interlayer C–H•••N H-bonding: (a) distances (H to N atom in dotted line; Å) and angles (C–H•••N) in degree (b) C to N atom distance in dotted line; Å for TpOMe-Azo COFM.</i>	87
3.12	<i>SEM images of the TpOMe-Azo COFM after treatment in (b) HCl (12 M) for 7 days, (c) H₂SO₄ (9 M) for 7 days, (d) H₂SO₄ (18 M) for 3 days and (e) NaOH (9 M) for 1 day compared to its (a) as-synthesized material.</i>	88
3.13	<i>(a) Solvent permeance study using TpOMe-Azo COFM. (b,c) Schematic illustration of the nano-filtration assembly showing the water purification process from organic dyes (MB- Methylene Blue) through TpOMe-Azo COFM. (d) UV-Vis spectrum comparison for Methylene Blue feed vs permeate. (e) Recyclability test of the TpOMe-Azo COFM for Methylene Blue (MB) for consecutive five cycles. (f) % of other dye rejection from water through TpOMe-Azo COFM.</i>	89
3.14	<i>As-synthesized TpOMe-Azo COF with other different shapes. (a) sphere (b) solid cylinder and (c) beads.</i>	90
3.15	<i>UV-vis spectra comparison of dye molecules. (a) Rose Bengal (RB), (b) Rhodamine B (RH), (c) Congo Red (CR) before (feed) and after (permeate) passing through the TpOMe-Azo COFM.</i>	90
3.16	<i>(a) The physical appearance of the membrane before and after 6 (M) sulfuric acid permeation. (b) Tabular representation for a quantitative test for a proton in permeate through the titration test with standard aq. NaOH base.</i>	91
3.17	<i>UV-Vis absorption spectra comparison of 100 μM ethanol solution of TNT, 1 M aq. H₂SO₄ solution, (1:1; v/v) stock solution (feed) prepared from TNT (200 μM;</i>	93

	<i>ethanol) and H_2SO_4 (2 M; water) and solution permeated through the membrane.</i>	
3.18	<i>(a) Digital image of the complete water purification (from toxic dye molecules) set up. (b) General configuration of a membrane holder. The COFM is used after sandwich between metal support and the o-ring during analysis.</i>	97
4.1	<i>(a) General synthetic scheme of the TpOMe-DAQ thin sheet from aldehyde (TpOMe) and amine DAQ by PTSA (p-toluenesulfonic acid) mediated mechanochemical grinding approach. (b and d) Digital images show the self-standing and flexible nature of the thin sheet. (c) Tilted_AA model of TpOMe-DAQ. (e) Comparison among the experimental (red) with simulated eclipsed tilted-AA (green), refined simulated (blue) PXRD patterns and Pawley refinement difference (black) for TpOMe-DAQ COF.</i>	103
4.2	<i>Schematic representations of TpOMe-DAQ COF thin sheet synthesis and its flexible behavior.</i>	105
4.3	<i>(a) PXRD pattern of as-synthesized (black) compared with the tilted_AA (red) and Staggered (AB) (green) TpOMe-DAQ COF thin sheet. (b) The experimental PXRD patterns (red) compared with the simulated (Tilted_AA; blue) and Pawley refined difference (black) of TpOMe-DAQ [R_p, R_{wp} and R_{wp} (w/o bck) have shown in inset].</i>	106
4.4	<i>Comparison of FT-IR spectra of as-synthesized TpOMe-DAQ with its starting materials.</i>	108
4.5	<i>(left) Solid state ^{13}C CP-MAS spectra and (Right) TGA (Thermo Gravimetric Analysis) of as-synthesized TpOMe-DAQ COF.</i>	109
4.6	<i>(left) N_2 adsorption isotherm plot (highest achieved surface area) and (right) pore size distribution (cylindr./sphere pores, QSDFT adsorption branch model) for TpOMe-DAQ COF.</i>	110
4.7	<i>SEM images (a) Top view and (b) cross-section view of TpOMe-DAQ COF.</i>	111
4.8	<i>PXRD and BET surface area comparison of TpOMe-DAQ after treatment in different common solvents for 3 days (protic and aprotic) as mentioned (surface area $1531\text{ m}^2/\text{g}$ of as-synthesized material).</i>	112
4.9	<i>(a) PXRD and (b) FT-IR comparison of TpOMe-DAQ COF samples after treatment in a different solvent as mentioned.</i>	113
4.10	<i>(left) N_2 adsorption isotherm and (right) pore size distribution cylindr./sphere pores, QSDFT adsorption branch model) comparison of TpOMe-DAQ COF samples after treatment in a different solvent as mentioned.</i>	113
4.11	<i>Interlayer C-H...N H-bonding: (a) distances (H to N atom in dotted line; Å) and angles (C-H...N) in degree (b) C to N atom distance in dotted line; Å for TpOMe-DAQ COF.</i>	114
4.12	<i>Mechanical strength performance of the TpOMe-DAQ thin sheet. (a) Stress (MPa) vs strain (mm/mm) measurement and (b) Digital photograph of the sheet before after the experiment.</i>	115
4.13	<i>(a, b) Working electrode fabrication for three electrode system using 1 cm^2 or 7.5 mm^2 active area COF thin sheets. (c) Complete set up of a three-electrode cell.</i>	116
4.14	<i>(a, b) Cyclic voltammetry (CV); (c) Galvanostatic charge-discharge (GCD) and (d) Current density vs areal capacitance plot of TpOMe-DAQ COF thin sheet (active</i>	117

	<i>area 2.5×3.0 mm²) using 3 M H₂SO₄ as an electrolyte in three electrode assemblies.</i>	
4.15	<i>(a) Basic structure of TpOMe-DAQ COF. (b) Redox behavior of COF sheet via 2H⁺/2e⁻ reversible quinone to hydroquinone transformation. (c) Cyclic voltammetry (CV) plot of TpOMe-DAQ COF thin sheet (active area 2.5×3.0 mm²) during 1 mVs⁻¹ scanning using 3 M H₂SO₄ as an electrolyte in three electrode system.</i>	118
4.16	<i>(a, b) Cyclic voltammetry (CV); (c) Galvanostatic charge-discharge (GCD) of 7.5 mm² (2.5×3.0 mm²) active area of the thin sheet using 2 M aq. H₂SO₄ as an electrolyte. (d) Cyclic stability of TpOMe-DAQ COF thin sheet exposing 1cm² active area in 2 M aq. H₂SO₄ as an electrolyte in three electrode assemblies.</i>	119
4.17	<i>(a) Cyclic voltammetry (CV); (b) Galvanostatic charge-discharge (GCD) of 1 cm² active area of the thin sheet using 2 M aq. H₂SO₄ as an electrolyte.</i>	120
4.18	<i>(a) Cyclic voltammetry (CV); (b) Galvanostatic charge-discharge (GCD) comparison before and after the cyclic stability of 1 cm² active area of the thin sheet using 2 M aq. H₂SO₄ as an electrolyte.</i>	120
4.19	<i>Comparison of (a) PXRD, (b) FTIR, (c) N₂ adsorption and (d) Pore size distribution (cylindr./sphere pores, QSDFT adsorption branch model) of as-synthesized and after 1,00,000 cyclic stability study of TpOMe-DAQ COF electrode.</i>	121
4.20	<i>(a) Top and (b) cross-section view of the TpOMe-DAQ thin sheet after 1,00,000 cyclic performance.</i>	122
4.21	<i>Galvanostatic charge-discharge (GCD) plots for TpOMe-DAQ thin sheet (2.5×3.0 mm² active area) using 3 M (left) and 2 M (right) aq. H₂SO₄ as an electrolyte in a three-electrode cell.</i>	123
4.22	<i>(a) CV, (b) GCD, (c) Impedance plot and (d) cyclic stability (from GCD using 5 mA cm⁻²) of TpOMe-DAQ COF thin sheet (active area 1 cm²) in two electrode solid-state device using 2 M H₂SO₄/PVA as an electrolyte.</i>	125
4.23	<i>Stepwise fabrication of two electrode device using pristine COF thin sheet. Three solid state device connected in a series to enkindle a 1.8 V LED.</i>	129
4.24	<i>(a) CV and (b) GCD plot of three solid state devices connected in series operating in a 3 V potential window.</i>	130
5.1	<i>Schematic representation of the synthesis of (a) 2,3-DhaTta COF and (b) 2,3-DhaTab COF separately reacting 2,3-Dha aldehyde with Tta and Tab amines respectively. The existence of O—H•••N intralayer H-bonding has been shown in the inset.</i>	137
5.2	<i>Crystal structures of the reference compounds (a) SaTta, (b) 2,3-Dha-ani and (c) SaTab. The torsion angles have been shown with double-headed arrows.</i>	139
5.3	<i>(a, c) PXRD comparison of as-synthesized COFs with its simulated eclipsed (AA) and staggered (AB) stacking models. (b,d) Eclipsed model structures of respective COFs.</i>	139
5.4	<i>Crystal structures of the reference compounds (a) SaTta, (b) 2,3-Dha-ani and (c) SaTab. The torsion angles have been shown with double-headed arrows.</i>	140
5.5	<i>FT-IR spectra comparison among 2,3-DhaTta, 4,4',4''-(1,3,5-triazine-2,4,6-triyl)trianiline (Tta) and 2,3-dihydroxyterethaldehyde (2,3-Dha</i>	141
5.6	<i>FT-IR spectra comparison among 2,3-DhaTab, 4,4',4''-(1,3,5-triazine-2,4,6-</i>	142

	<i>triyl)trianiline (Tab) and 2,3-dihydroxyterethaldehyde (2,3-Dha).</i>	
5.7	<i>(a, b) Solid state ¹³C spectra of COFs 2,3-DhaTa and 2,3-DhaTab respectively with partial chem. draw structure on inset. (c) TGA profile of the respective COFs.</i>	142
5.8	<i>Comparison of (a) N₂ adsorption (at 77 K), (b) H₂ adsorption (at 77 K), (c) CO₂ adsorption (at 273 K), (d) water vapor adsorption (at 298 K) isotherms of 2,3-DhaTta and 2,3-DhaTab COFs.</i>	143
5.9	<i>Experimental pore size distribution of 2,3-DhaTta (left) and 2,3-DhaTab (right) COFs.</i>	144
5.10	<i>Comparison of PXRD patterns of 2,3-DhaTta (a & b) and 2,3-DhaTab (c & d) of as-synthesized with after 3 days treatment in water and 3 (M) HCl respectively.</i>	145
5.11	<i>Comparison of IR spectrums of 2,3-DhaTta (a & b) and 2,3-DhaTab (c & d) of as-synthesized with after 3 days treatment in water and 3 (M) HCl respectively.</i>	145
5.12	<i>Comparison of N₂ adsorption isotherms of 2,3-DhaTta (a & b) and 2,3-DhaTab (c & d) of as-synthesized with after 3 days treatment in water and 3 (M) HCl respectively.</i>	146
5.13	<i>From SEM (c, f) & TEM imaging (rest), from 12 to 72 h (a-b) The way of formation of ribbon-shaped morphology in case of 2,3-DhaTta COF and (d-e) Hollow spherical morphology formation in case of 2,3-DhaTab.</i>	147
5.14	<i>AFM image of the 2,3-DhaTab hollow sphere. Height profile reflects spherical nature.</i>	148
5.15	<i>PXRD of 2,3-DhaTta and 2,3-DhaTab at different time intervals (12 h, 24 h, 36 h, 48 h and 72 h).</i>	149
5.16	<i>FT-IR spectra of 2,3-DhaTta and 2,3-DhaTab at different time intervals (12 h, 24 h, 36 h, 48 h and 72 h).</i>	149
5.17	<i>N₂ adsorption isotherm of 2,3-DhaTta and 2,3-DhaTab at different time intervals (12 h, 24 h, 36 h, 48 h and 72 h).</i>	150
5.18	<i>(a) Defragmented of 2,3-DhaTta COF into reference compounds SaTta (planar core) and 2,3-Dha-ani. (b) TEM imaging (12-72 h) and cartoon representation for ribbon-shaped crystallite formation in 2,3-DhaTta COF. (c) The expected growth mechanism of the COF crystallites at 12h, stacking model along with stacking energy value (from DFT) mentioned for the adjacent hexagonal COF layers. (d) PXRD pattern (of 12 h sample) along with intensity ratio of 100 to 001 planes for 2,3-DhaTta COF.</i>	151
5.19	<i>SEM images of 2,3-DhaTta at different time intervals.</i>	152
5.20	<i>TEM images of 2,3-DhaTta at different time intervals.</i>	152
5.21	<i>(a) General definition of '100' and '001' planes in a cubic system. (b) Expansion of the defined planes in a hexagonal system and (c) Finally expanded the concept of planes in stacked hexagonal 2D COF layers.</i>	153
5.22	<i>(a) Defragmented of 2,3-DhaTab COF into reference compounds SaTab (non-planar core) and 2,3-Dha-ani. (b) TEM imaging (12-72 h) and cartoon representation for hollow sphere crystallite formation in 2,3-DhaTab COF. (c) The expected growth mechanism of the COF crystallites at 12h, stacking model along with stacking energy value (from DFT) mentioned for the adjacent hexagonal COF layers. (d) PXRD pattern (of 12 h sample) along with intensity ratio of 100 to 001</i>	154

	<i>planes for 2,3-DhaTab COF.</i>	
5.23	<i>SEM images of 2,3-DhaTta at different time intervals.</i>	155
5.24	<i>TEM images of 2,3-DhaTta at different time intervals.</i>	155
5.25	<i>Understanding of Ostwald ripening process in 2,3-DhaTab.</i>	156
5.26	<i>¹H NMR spectrum (in DMSO-d₆) of 4,4',4''-(1,3,5-triazine-2,4,6-triyl)trianiline (Tta).</i>	158
5.27	<i>¹H NMR spectrum (in CDCl₃) of the reference compound SaTta.</i>	159
5.28	<i>Single Crystal X-ray diffraction structure of the reference compound SaTta. In the ORTEP (with 40% probability level); Carbon (black), Nitrogen (blue), Oxygen (red) and Hydrogen (pink) have been shown [CCDC No: 1451702].</i>	160
6.1	<i>Various symptoms of arsenic poisoning to human health and its different affected stages.</i>	168
6.2	<i>Commercial technique used for arsenic removal from drinking water and their drawbacks.</i>	169
6.3	<i>Proposed synthetic scheme for TpOMe-EtBr Covalent Organic Framework Membrane (COFM) synthesis.</i>	170
6.4	<i>Trapping of arsenite/arsenate in COFM TpOMe-EtBr through irreversible ligand exchange (step 1). Dilute hydrochloric acid treatment for recycling use of the membrane (step 2).</i>	171
6.5	<i>Proposed design of arsenic contaminated water purification instrument using COFM.</i>	172

LIST OF TABLES

Tables		Page
1.1	<i>Hydrogen, carbon-dioxide and methane storage properties of COFs of different surface areas reported in the literature.</i>	22
2.1	<i>Comparison of interlayer C–H•••N hydrogen bonding among TpOMe-X COF and reference crystal structures of Figure 2.24; a, b and c.</i>	65
2.2	<i>Comparison of intralayer C–H•••O hydrogen bonding between TpOMe-BD(NO₂)₂ COF and reference crystal structure of Figure 2.24; d.</i>	65
3.1	<i>Fractional atomic coordinates for the unit cell of TpOMe-Azo</i>	79
3.2	<i>Nano-filtration performance of COFM TpOMe-Azo (350 μm thickness) towards water purification from carcinogenic dyes.</i>	91
3.3	<i>Preparation of various solutions.</i>	92
3.4	<i>Estimation of final strength of a sulfuric acid in permeate.</i>	93
3.5	<i>Preparation of standard sulfuric acid solution.</i>	97
3.6	<i>Preparation of standard sodium hydroxide solution.</i>	97

4.1	<i>Fractional atomic coordinates for the unit cell of TpOMe-DAQ (Tilted_AA).</i>	107
4.2	<i>Inter-layer C–H•••N hydrogen bonding in TpOMe-DAQ COF.</i>	114
4.3	<i>Comparison of areal (mFcm^{-2}) and gravimetric (Fg^{-1}) capacitances with state-of-art promising electrode materials made up off COF and MOF.</i>	128
4.4	<i>Comparison of areal capacitance (mF cm^{-2}) with state-of-art electrode materials.</i>	128
5.1	<i>Structural information of the reference monomer SaTta.</i>	160
5.2	<i>Fractional atomic coordinates for the unit cell of 2,3-DhaTta.</i>	162
5.3	<i>Fractional atomic coordinates for the unit cell of 2,3-DhaTab.</i>	163

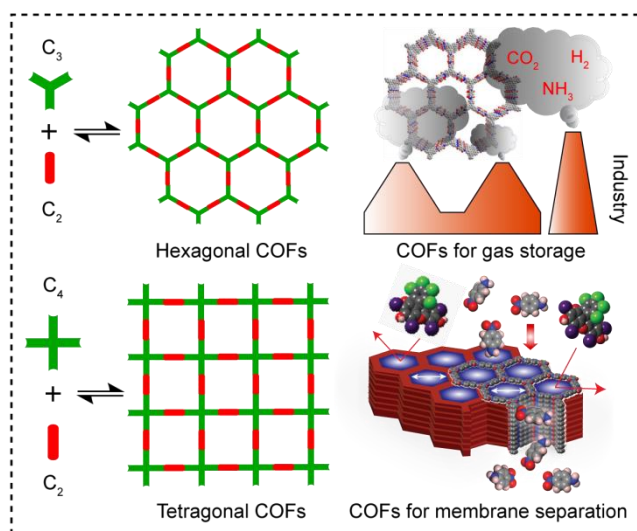
LIST OF SCHEMES

Scheme		Page
2.1	<i>General synthetic scheme for 2,4,6-Trimethoxy-benzene-1,3,5-tricarbaldehyde (TpOMe) starting from 1,3,5-trimethoxybenzene.</i>	68
2.2	<i>General synthetic scheme for reference compound TpOMe-Ani.</i>	70
5.1	<i>General synthetic scheme for the preparation of 4,4',4''-(1,3,5-triazine-2,4,6-triyl)trianiline (Tta).</i>	157
5.2	<i>General synthetic scheme for the preparation of SaTta.</i>	159

CHAPTER 1

Introduction to Covalent Organic Frameworks: Synthesis, Applications, Chemical Stability and Processability issues

Abstract: Fundamental research associated with the porous materials has convened inordinate scientific attention in the field of materials science owing to their various potential applications such as in gas storage, catalysis, separation, chemical sensing, conductivity, and electrochemistry related works such as for energy storage etc. In this context, Covalent Organic Frameworks (COFs)



represents emerging class of organic porous crystalline material with higher chemical and thermal stability compared to other potential porous crystalline materials such as Metal Organic Frameworks (MOFs). Since the sole compositions of COFs are lighter elements they have very low density and could be utilized as an effective gas storage media (For H₂, CO₂, and NH₃). Although COFs are highly promising for various potential applications, the utilization of this material towards real-life application is limited due to its unprocessable powder form along with chemical instability in strong acids or bases. Therefore, the development and rapid construction of porous crystalline COFs with ultrahigh chemical stability along with high processability into pellets, beads, and membranes for real-life applications are highly essential and challenging. Again, fabrication of novel porous COFs as an energy storage material such as for supercapacitor application is also keen of interest. Moreover, apart from chemical constituents, the overall properties and real-time applicability of any material largely relies on its nano-scale morphology. Hence, morphological control and growth at nano-scale of these novel COFs could be another promising study for its intended development.

1.1 Background of porous crystalline materials

Any solids can be defined as a porous material if it contains micro/macro openings on its surface, by which microscopic particles, gases or liquids can pass through. Over last few decades micro/mesoporous materials have plucked a progressively much important and have been considered as one of the most exciting research areas to the chemists. From then, scientists have designed various potential porous materials adopting the ideas from the mother nature such as, for example, various porous structures which exclusively exist in nature such as honeycombs (with hexagonal pores), hollow bamboos, sponges etc [1.1]. Currently, there are plenty of academic or industrial research institutions/groups throughout the world now on the way to explore these novel porous materials for widespread applications. This is only possible owing to their extraordinary surface area, an adjustable framework cavity along with tunable pore size and outstanding surface related properties. Moreover, their unique behavior or potential applications start originating when the pore size of such materials goes down to the micro/nanometer scale [1.2]. Among all other, the most well-known nano-materials which are fundamentally important are porous carbon, zeolites, mesoporous silicas, metal organic frameworks (MOFs) and covalent organic frameworks (COFs) [1.3]. Porous materials could play a very fundamental role in sustainable energy as they have already been tested in various potential applications including photocatalysis, purification of natural gases, optoelectronics, chemical sensing, water purification etc [1.4]. For example, porous carbon-based materials are highly promising in designing water purification systems, gas masks, batteries, catalyst supports, metallurgy, etc [1.5, 1.6]. On the other hand, porous silica and zeolite-based materials are potential for use in various applications such as for industrial catalyst design, as molecular sieves or drug delivery materials, gas storage, etc [1.7].

The first fundamentally important porous materials were the activated charcoal (carbons), which have been exclusively utilized by ancient Indians and Egyptians for applications such as in water purification or in medicinal applications [1.8]. Early to 1970, researchers have mostly used porous carbon towards gas storage, water purification, separation, solvent removal, etc. However, limitations such as non-uniform pore size, low surface area, and crystallinity, have restricted their widespread application. As the time progress, researchers discovered another very interesting inorganic porous material known as zeolites, which do have crystallinity and uniform porosity, was first made in 1862 [1.7]. In principle, zeolites are the part of aluminosilicate family made up of silicate $[\text{SiO}_4]^{4-}$ and

aluminate $[\text{AlO}_4]^{5-}$ whereas tetrahedrons are connected by oxygen atoms. The resulting three-dimensional network consists of nanochannels of having dimensions 0.1–2.0 nm. The surface area of the zeolite materials ranging from 500–900 m^2g^{-1} offering various potential applications. However, the major limitations such as difficulty in pre-designing of structures along with less opportunity for pore surface engineering or tunability limits zeolites for acting as a leading porous material [1.7]. To overcome all these drawbacks of porous carbons and zeolites, in the year of 1995 Yaghi and co-workers have come up with a highly crystalline hybrid (inorganic–organic) porous material known as metal-organic frameworks (MOFs) [1.9]. MOFs are basically composed of metal ions which act as a node and organic linkers as spacers. The opportunity of pore surface engineering along with extremely high crystalline and porous nature made them suitable towards various potential applications in the area of gas storage and separation, catalysis etc [1.10]. However, the major drawback of these materials is the high gravimetric density along with low chemical stability because of labile metal-ligand coordination kind of bonds [1.10]. Hence, replacement of weak coordinate bond with strong covalent linkers maintaining materials properties such as crystallinity and porosity was the major challenge in that time. However, the design and construction of ordered framework materials using pure covalent linkers was not straightforward and was profoundly challenging. Although scientist had come up with in synthesizing 1D crystalline polymers, the construction of 2D or 3D ordered network was not straightforward as during synthesis it most often forms amorphous and cross-linked polymers [1.11]. From the same group in the year 2005, Yaghi and co-workers could solve this long-standing issue and developed another class of purely organic, porous and crystalline materials, known as covalent organic frameworks (COFs) which have showcased great potentiality towards many important applications [1.12].

1.2 Classification of the porous materials

Porous materials are mostly solid-state materials which have pores or voids inside or in the surface of the framework [1.2]. Generally, based on the pore diameters these materials are categorized as follows- a) Microporous materials [pore diameter 0.2–2 nm e.g., metal organic frameworks (MOFs) and zeolites]. b) Mesoporous materials [pore diameter of 2–50 nm e.g., alumina and mesoporous silica]. c) Macroporous materials [pore diameter 50–1000 nm e.g., metal foams] [1.4c]. However, depending on their compositions, the materials can be further defined in three major categories such as-a) Organic porous frameworks b) Organic–

inorganic hybrid porous frameworks, c) Inorganic porous Frameworks. The entire thesis is mainly focused on covalent organic frameworks (COFs) which is the part of organic porous frameworks (**Figure 1.1**).

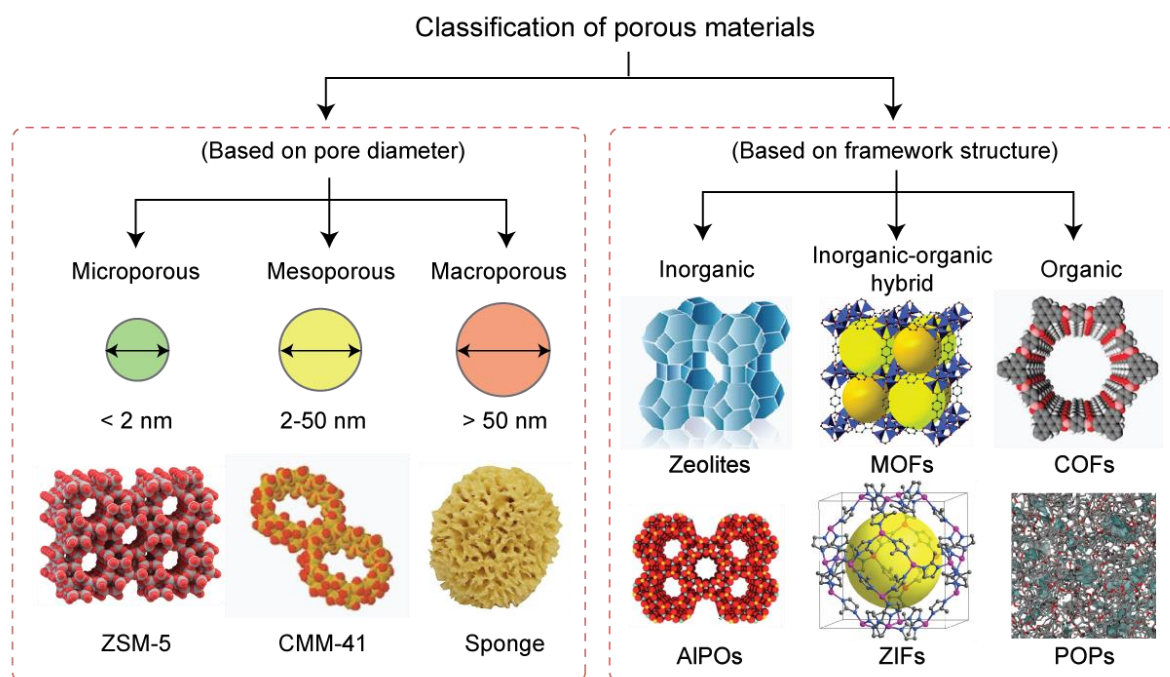


Figure 1.1. Classification of various porous materials based on pore diameter and framework natures.^[1.13]

1.2.1 Inorganic porous framework materials

Zeolites, aluminophosphates, titanosilicates, germanosilicates, metal phosphates (copper, zinc, gallium, iron phosphates, etc.) germanosilicates, are the most common examples of inorganic porous framework materials. Zeolites are the major class of aluminosilicates, with formula $M_{n+x/n} [(AlO_2)_x(SiO_2)_y]_x \cdot wH_2O$ (M = metal), which are mostly constructed when the tetrahedral corners are shared by XO_4 (X = Si, Al) species [1.7a]. The open pore channel in Zeolites varies in the range 3 to 15 Å where the ratio of silicon to aluminium varies in the range of 0 to 1 [1.7b]. Zeolites made up of pure SiO_4 is electrically neutral which when replacement of some of the SiO_4 units with aluminium, results in anionic frameworks. The anionic charge in the frameworks are mostly balanced with cations such as Na^+ , K^+ , Ca^+ and thus zeolites are the promising platforms for cation exchange. Moreover, the presence of bridging hydroxyl functionalities made the zeolites strong bronsted acid. When, in zeolites, the silicon atoms are replaced by aluminium or phosphorous the new material termed as aluminophosphates (AIPOs) are formed which are neutral in nature [1.14]. Whereas,

replacement of aluminium with bivalent metal cations such as copper, zinc or gallium will result in the formation of anionic metal phosphates frameworks [1.15]. Moreover, low production costs, high thermal and chemical stability of zeolites made them industrially relevant promising materials for various potential applications such as adsorbents, catalyst, water purifiers, dehumidification and dehydrating agent etc [1.16].

1.2.2 Inorganic–organic hybrid porous framework materials

The major drawback of inorganic porous framework materials is the less opportunity of pore functionalization and thus these are limited to structural diversity. On this line, the discovery of inorganic–organic hybrid materials could lead various unprecedented structures (**Figure 1.1**). The most important class of materials in this category is the 2D or 3D metal organic frameworks (MOFs) which are mostly constructed from metal ions acting as a node separated with organic linkers as spacers [1.9]. The common metal ions which are exclusively used to synthesize these novel set of materials are transition metals (Fe, Cu, Zn etc.), p-block elements (In, Ga etc.), alkaline earth elements (Sr, Ba etc.) and actinides (U, Th etc.) whereas carboxylate (di, tri, tetra or poly), or phosphate anions, imidazolate and bipyridine ligands etc. act as spacers [1.17]. MOFs follow the basic reticular chemistry of bond formation and thus by interchanging metal ions or organic linkers, huge libraries of structures of diverse functionality with different pore apertures can be synthesized. The three major class of MOFs can be defined as: a) 1st generation– where the MOFs are stable only in presence of mother liquor or solvent which upon removal framework gets collapsed, b) 2nd generation– herein the MOFs could maintain their framework structure even upon removal of solvents and thus are stable and robust and c) 3rd generation– these are flexible in nature and their surface area or porosity gets tuned upon in contact with external stimuli [1.18]. Generally, MOFs are synthesized using the traditional solvothermal method and thus their structures most of the time contains solvent or guest molecules which after removal can produce open framework structures with ultrahigh porosity. From last two decades, MOFs have been exclusively used in storage of various gas molecules (H₂, CO₂, CH₄ etc), their selective adsorption and separations using ordered nano-channels etc. Apart from that, MOFs are highly promising to act as a porous support for catalysis, proton conductivity and drug delivery [1.19]. Despite their various potential applications, MOFs suffer from some limitations like they are mostly microporous in nature which limits their applicability to store bigger sized guest molecules. Again, the weak coordinate bonds are highly labile towards thermal or chemical treatment which restricts their wide potential usage [1.10].

1.2.3 Organic porous framework materials

To overcome the disadvantages of MOFs more recently scientists have developed another set of new materials which are exclusively composed of organic building blocks connected with strong covalent bonds are expected to exhibit high thermal or chemical stability [1.20]. As they are composed of mostly light atoms such as H, C, N, O etc, these materials showcased low gravimetric density and are highly useful in the vehicular gas storage application (**Figure 1.1**). Moreover, based on framework crystallinity they can be defined in two major categories: a) Porous polymeric frameworks (POPs) [1.20a-b] which are amorphous in nature and b) crystalline covalent organic frameworks (COFs) [1.20e-f] with ordered pore channels and decent porosities.

Porous Polymeric Frameworks: POPs are constructed using irreversible chemical reactions and hence they mostly form a disordered network structure with limited porosity (**Figure 1.2**). POPs are basically synthesized using C-C coupling reaction such as Suzuki coupling [1.21a-b], Yamamoto coupling [1.21d-e], Sonogashira-Hagihara [1.21c], Friedel–Crafts reaction [1.21i], oxidative coupling reaction [1.21g-h], phenazine ring fusion [1.21j] reaction etc. Andrew I. Cooper and co-workers first made POP (CMP-0 & CMP-5) with a surface area ranging from $1018 \text{ m}^2 \text{ g}^{-1}$ (CMP-0) to $512 \text{ m}^2 \text{ g}^{-1}$ (CMP-5) which is much lower compared to COFs [1.21]. Despite their amorphous nature, POPs are highly chemically or thermally stable as they are formed through irreversible bond formation reactions and thus could be promising in real life applications such as in separation or storage purpose.

1.3 Covalent organic frameworks

Covalent organic frameworks are pristine sets of crystalline porous organic materials made up of light elements such as B, C, N, O, Si etc. which follows the same avenue of the reticular chemistry of bond formation like MOFs (**Figure 1.1**). Owing to their very interesting properties such as these are pre-designable, the opportunity for smooth tuning and easily functionalizable framework pores, have made them potential towards gas storage, separation, catalysis, and sensors. The high crystalline and porous nature of these completely organic frameworks made them completely different from MOF and Zeolites in terms of properties and applications. COFs are constructed *via* strong covalent linkage formation among various organic building units bearing precise symmetry to their structures [1.22]. The strong covalent bonds prefer them to be stable at elevated temperatures whereas lightweight (C, N, O, H) element compositions could make them suitable for application such as in gas

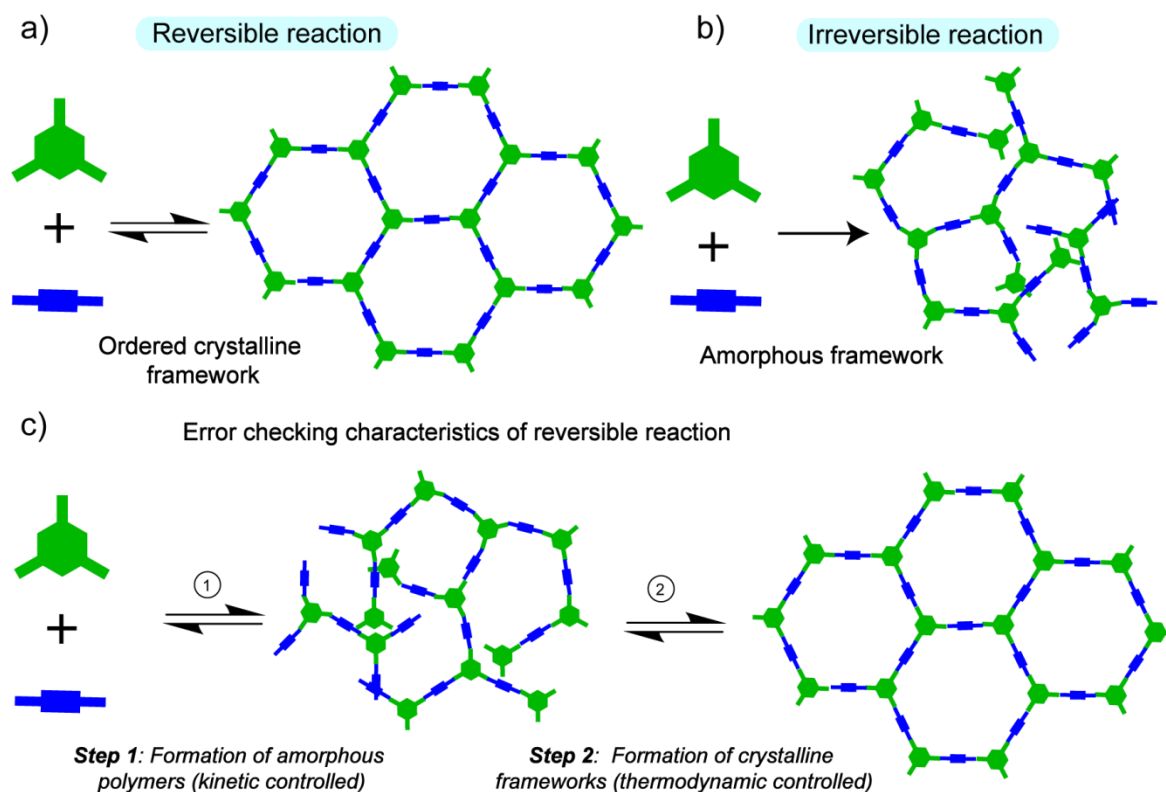


Figure 1.2. Schematic representation of a) and c) COF formation by the reversible reaction, b) PAF formation by the irreversible reaction.

storage and transportation owing to their low gravimetric density [1.23]. Additionally, the COF framework structures can be tuned between two or three dimensions depending on the symmetric combination of used ligands during its formation [1.22]. Most of the COFs (almost 80%) reported adopting 2D structures. However, the number of 3D COFs is limited owing to the non-availability of higher symmetric building units [1.23]. Interestingly, similar to graphite, 2D-COFs have uniformly stacked layer structures where the layers undergo π - π stacking among each other and bring various interesting electronic properties in the frameworks [1.22a]. The pore diameter of 2D COFs can be tuned by properly choosing the length of the building units [1.22]. The most of the 2D COFs are synthesized as microporous materials with pore diameter < 2 nm. However, by following basic rules for reticular structural construction, by simply enhancing the linker size the pore diameter can be tuned up to 4.7 nm which is the highest reported till date in the 2D COF literature [1.24].

The COFs are mostly synthesized following dynamic covalent chemistry i.e. using reversible chemical reactions [1.22a]. The advantages of reversible chemical reaction are the opportunity for self-checking and error correction i.e. self-repairing, as reversibility bears proof-reading characteristic. So if during framework formation if there exist any disorder in

the bond connectivity, the system will repair those defects *via* several reversible bond formation cycles and finally it will proceed to form thermodynamically most stable product i.e. covalent organic frameworks (COFs) (**Figure 1.2**). Thus, the reversibility in bond formation is the salient tool for the formation of crystalline material such as COFs. The reversible chemical reactions which have been mostly implemented during COF formation are: a) boronic acid trimerization reaction [1.23], b) boronate ester formation reaction [1.25], c) nitrile group trimerization [1.26] and d) Schiff base reaction [1.27]. However, the irreversible C–C bond forming reactions (e.g. Suzuki coupling) could exclusively form amorphous porous polymeric frameworks (POPs) or porous aromatic frameworks (PAFs) [1.21].

COFs are very potential porous materials, their ordered pore-channels with the high surface area has been utilized to store natural gases (H_2 , CO_2 , NH_3 , CH_4 etc.) and for bio-molecule storage and its release (enzyme and drugs). In addition, ordered nano-pores have also been used for gas separation, sensing, energy storage and catalysis applications. Again, the applications such as in charge carrier mobility or photo-conducting application conjugated 2D COFs have shown their applicability. Despite all such promising properties, the real-life application of this novel material is limited owing to its chemical instability, processability, and scalability. The straightforward reason that this material is highly unstable to moisture, as discussed earlier, they mostly prepared using reversible condensation reaction which involves the formation of water as a by-product. Since there still exists the possibility of a reversible back reaction, even after the COF crystallization, upon in contact with water, COFs mostly get completely hydrolyzed to form the starting materials [1.28]. Various attempts such as pyridine doping and alkyl chain incorporation have been made in last few decades to stabilize COFs however over doping of such materials could affect the active surface of the COFs due to extensive pore blockage [1.28a-b]. Kandambeth et al. could solve this stability issue by utilizing enol-keto tautomerization phenomenon during framework crystallization or by incorporation of intralayer hydrogen bonding within porous COF backbone [1.28c]. Very recently, Jiang et al. could introduce a new methodology to stabilize imine-based COFs using methoxy functionalities throughout the framework and the material showcased high chemical stability in acid (12 M HCl), base (14 M NaOH) and in common solvents [1.28d].

1.4. Types of reversible reaction utilized for the synthesis of COFs

1.4.1 Boronic acid trimerization: The Boronic acid trimerization reaction involves reversible condensation of three boronic acids units to form a planar six-membered boroxines ring (B_3O_3 ring) and water as a byproduct (**Figure 1.3**). The reaction when carried out using 1,4-benzene diboronic acid, two ends of the molecule undergoes reaction to grow in two dimensions and finally after infinite growth to form a 2D COF-1 framework [1.12]. The other examples of boronic acids based COFs reported in the literature are COF-102, COF-103 and PPy-COF [1.23]. As the boroxines rings are completely planar and the reaction has proceeded with good reversibility the synthesized COF material using this strategy generally exhibit high crystallinity and decent porosity [1.23].

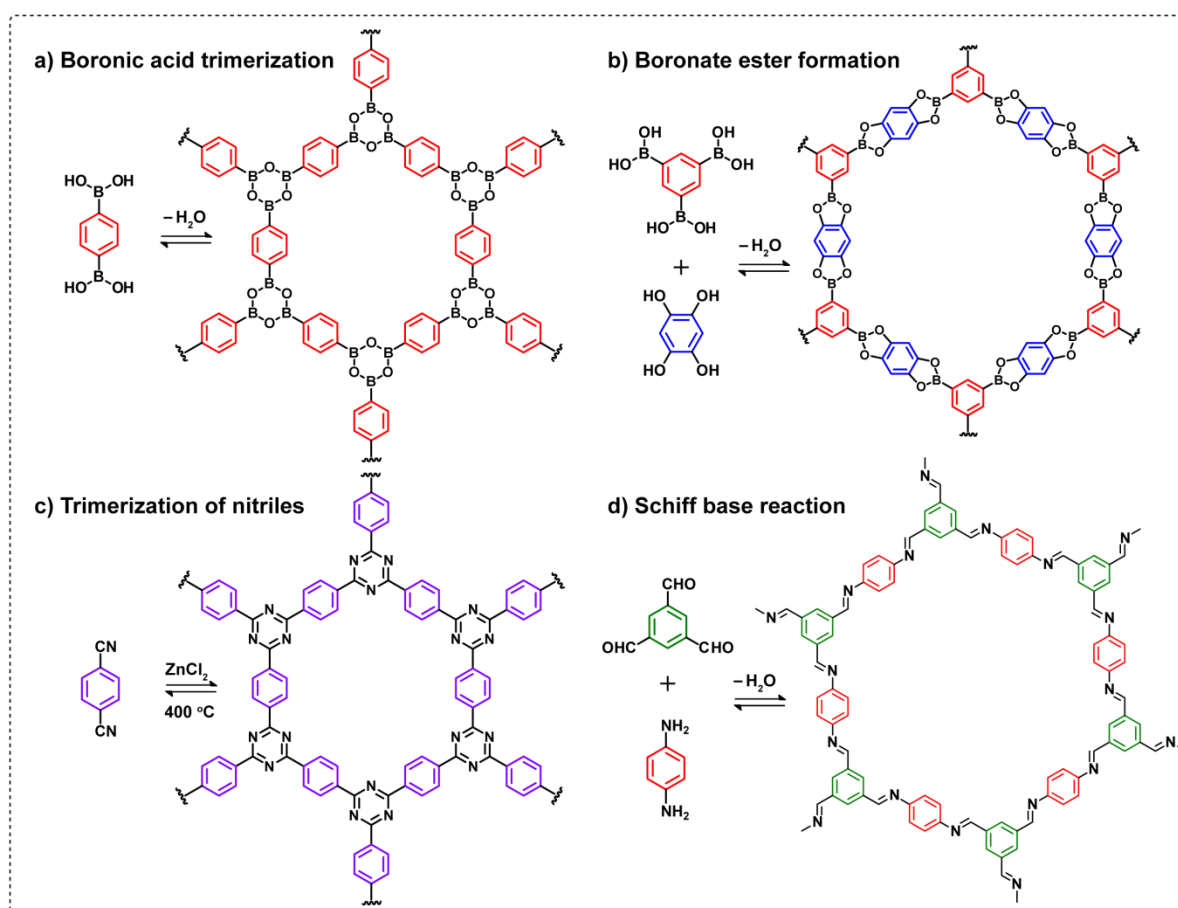


Figure 1.3. Different type of reversible organic reactions used for the COF synthesis.

1.4.2 Boronate ester formation reaction: The reaction involves the reversible condensation reaction between boronic acid with any of aromatic diols to result in a five-membered boronate ester (C_2O_2B) rings (**Figure 1.3**). The condition of COF formation required the co-condensation of two or even more building units. Among two building units, one is the

boronic acid (usually di or tri) whereas the other one is poly-hydroxy aromatic compounds such as 2,3,6,7,10,11-hexahydroxytriphenylene (HHTP) (**Figure 1.3**). The common examples of COFs, in this case, are COF-5, COF-8, COF-10, ZnPc-Py COF, HHTP-DPB COF, etc [1.12, 1.25]. Although due to the formation of planar boronate ester ring with high bond reversibility lead the material with high crystallinity and porosity, COFs belong to this series suffer from chemical stability issue [1.28].

1.4.3 Trimerization of nitriles: The reversible trimerization of nitrile groups ($-CN$) groups generally carried out using the ionothermal method at a higher temperature ($400\text{ }^{\circ}\text{C}$) in presence of a Lewis acid catalyst ($ZnCl_2$) (**Figure 1.3**). The synthesized material generally termed as covalent triazine frameworks (CTFs). In 2008, this methodology was first implemented by Arne Thomas and co-workers to synthesize first CTF-1 [1.26a]. The material synthesized in this method is less crystalline compared to COFs due to less bond reversibility. Again the method is limited to explore in other systems as at high temperatures most of the precursors to prepare CTFs undergoes decomposition. As an alternative, although low-temperature synthesis of triazine core using trifluoromethanesulphonic acid has been attempted it often lead amorphous polymeric material [1.26].

1.4.4 Schiff base reaction: The reaction between an aldehyde and an amine generally known as Schiff base condensation where imine linkage is formed and water produces as a byproduct. O. M. Yaghi and coworkers for the first time could prepare COF-300 using Schiff base reaction [1.27]. The tetra-(4-anilyl) methane (T_d symmetry) and terephthaldehyde (C_2 symmetry) were strategically used to grow COF in three dimensions for the first time. After this report, using similar dynamic covalent chemistry a library of 2D Schiff base COFs were prepared using various symmetry combinations such as $C_3 + C_3$, $C_3 + C_2$, $C_4 + C_2$ etc. The common examples of 2D COFs in these categories are COF-LZU-1, COF-42, COF-43, COF-366 etc [1.27]. Notably, the imine bond reversibility is largely dependent on the pH of the solution and it is completely reversible under acidic condition ($\text{pH} = 4-5$). Hence, during imine COF formation a catalytic amount of aq. acetic acid is always used to maintain the reversibility which helps impregnable COF crystallization [1.27]. Due to its pH-dependent reversibility the imine COFs exhibit hydrolytically more stable compared to boronic acid or boronate ester based COFs however they undergo decomposition at lower pH [1.27].

1.5 Basic symmetric rules of combination

As discussed earlier the reversibility in bond formation is a major criterion in successful COF crystallization. However, apart from reversibility, the used building units should fulfill some

other requirement such as symmetry in their structures to result in a COF with decent crystallinity and porosity after their combination. A slight alteration in basic symmetry combination rules will often result in amorphous material although the reaction is completely reversible [1.22]. Hence, rigid linkers could be one of the best choices to properly maintain the basic symmetry selection rules. Building blocks with one or more flexible cores (e.g. alkyl chains) will have a higher tendency to form bond in multiple directions which often result in a disordered network. In this regard, rigid aromatic building blocks have been widely used in recent years owing to their unique directional properties of bond formation along with π - π stacking tendency between aromatic cores to result ordered stacked 2D COFs [1.22]. Again, the aromatic building blocks should follow some basic symmetric combination such as C_3+C_2 , C_3+C_3 , C_4+C_2 , C_4+C_4 , C_6+C_2 (**Figure 1.4**) [1.20d-f, 1.22] to form 2D COFs.

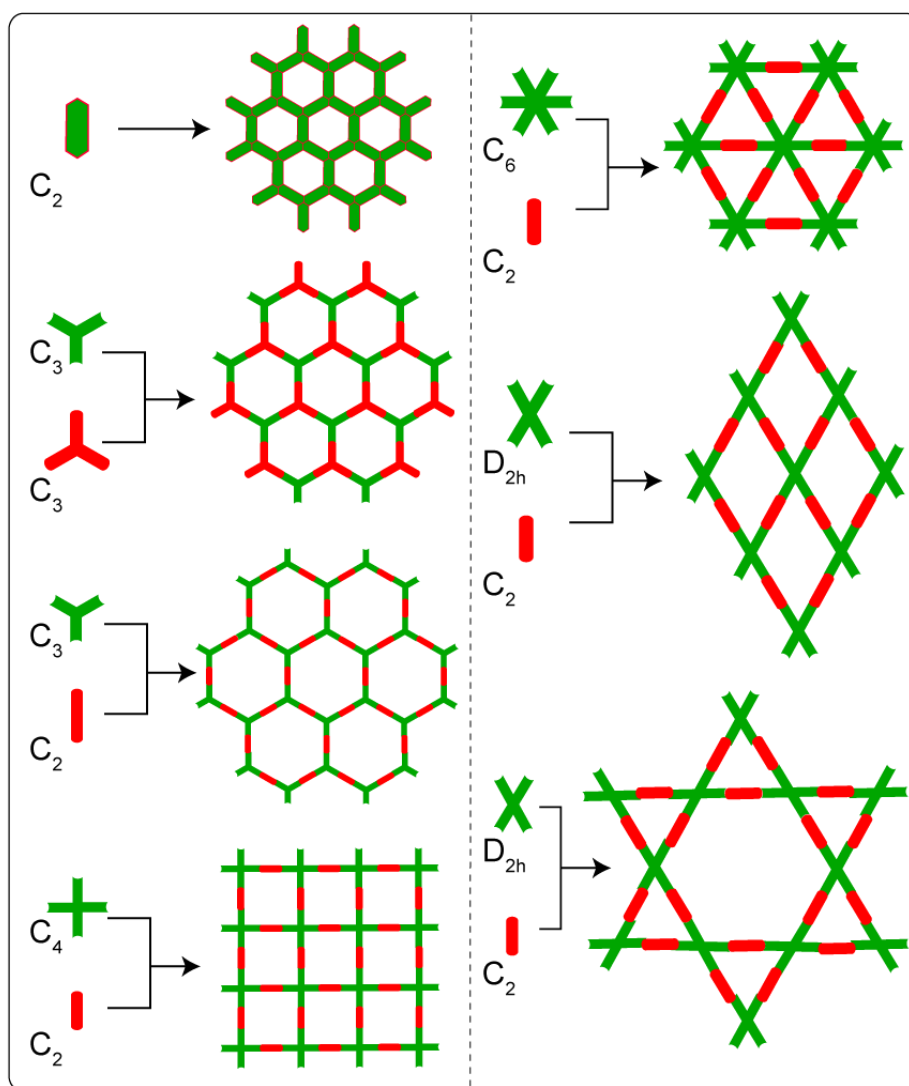


Figure 1.4. Schematic representation of various symmetric combinations used during COF framework construction.

system having space groups $P6/m$ (for eclipsed structure) and $P6_3/m$ (for staggered structure) [1.12]. The symmetric combination using C_4+C_2 and C_4+C_4 usually lead to the formation of tetragonal 2D COFs. COFs containing porphyrin building block in its core belong to this category. The common examples for such symmetric combination are COF-366, NiPc COF, ZnPc-Py COF etc [1.27d, 1.28, 1.29]. Such 2D COFs (made up from C_4+C_2 and C_4+C_4 symmetric combinations) generally modeled using tetragonal crystal system bearing space group $P4/m$. However, C_6+C_2 symmetric combinations are barely used in COF synthesis (**Figure 1.4** & **Figure 1.5**) [1.30]. Only examples reported in this category are $[H_2N]_6HPB$ and $[H_2N]_6HBC$ [1.30]. The imine COFs belong to category possess triangular topologies, with pore size mostly in micro-porous (1.2 and 1.8 nm) region. Notably, using a $D_{2h}+C_2$ symmetric combination, Xin Zhao and coworkers could synthesize novel 2D-COF. Surprisingly, the authors could observe that the 2D-COF adopted a new type of AA-H structure although it was expected to form a regular tetragonal framework (**Figure 1.4**) [1.31]. Interestingly, this special type AA-H structure associated with two different type of pores, one of them in micropore (7.1 Å) range whereas the other one falls in mesoporous (26.9 Å) region [1.31]. Again, the molecular mechanics calculations revealed among other four possible structures the hexagonal AA-H was found to have the lowest energy. Unlike 2D COF, the no. of 3D-COFs are very limited in the COF literature due to less availability of organic building units having higher symmetry (e.g. T_d , O_h etc.). Moreover, tetrahedral (T_d) symmetry was mostly used in making 3D-COFs reported in the literature following symmetric combinations T_d+C_2 , T_d+T_d , T_d+C_3 and T_d+C_4 [1.27a, 1.23].

1.6 Synthetic methods

Construction of general organic polymers is more often performed by irreversible organic reactions which are kinetically controlled. However, on the other hand, unlike polymers, COFs are thermodynamically controlled product where the covalent bonds are formed in a reversible route. The reversibility in a bond formation is highly important to construct a thermodynamically stable product as it allows the system to create or break the bonds and hence, error checking or proof checking characteristics of such systems helps to construct the most ordered and desired crystalline structure in the end with negligible structural defects [1.22]. As most of the building units are generally organic in nature the COFs are usually constructed solvothermally in organic solvents (**Figure 1.6**). Apart from reversibility of bonds, the crystalline product formation depends on some other important parameters such as temperature, solvent ratios, reaction time, pressure and presence/absence

of templates [1.22]. The COF synthesis generally performed solvothermally in a sealed pyrex tube maintaining a reaction temperature of 80 °C to 120 °C under high vacuum (**Figure 1.6**). Notably, most numbers of reversible COF reactions are associated with the formation of water molecules as a byproduct (**Figure 1.3**). During the solvothermal reaction, the advantage of using sealed tubes with high vacuum is that, as the reaction proceeds, the water molecule formed as a byproduct during the reaction, could get diffuse and gather in the empty space of the sealed tube owing to the high vacuum. From Le Chatelier's principle, it is well documented that in a reversible reaction removal of one of the products will always lead to increase the forward reaction rate. Hence, removal of water from the reaction system will help in the formation of the COF crystallites with a faster rate. However, as it is in a sealed condition, the water diffused out will not be allowed to come completely out of the system (**Figure 1.6**). Hence, this closed condition will in turn help to maintain the reversibility, since the system is allowed to utilize those water molecules during the self-healing process. Although the solvothermal method was the benchmark for versatile COF synthesis, some other method such as ionothermal, microwave, mechanochemical and synthesis using a template is some other alternatives for crystalline COF synthesis.

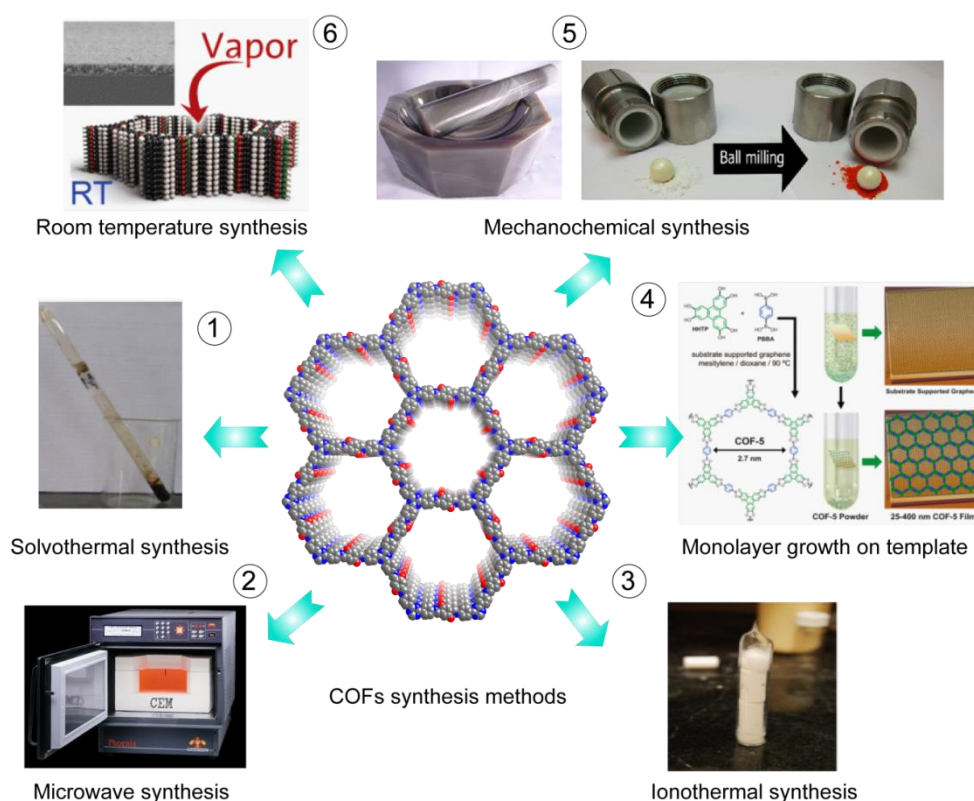


Figure 1.6. Different synthetic methods generally used for the construction of COFs.

1.6.1 Solvothermal synthesis

As mentioned a majority of COFs have been constructed till date utilizing solvothermal COF synthetic condition which is one of the most widely used techniques. MOFs and zeolites are two other categories of porous materials which are also prepared in autoclaves using the solvothermal method. Whereas in case of COF generally sealed pyrex tubes are used during solvothermal preparation of crystalline COFs.

The sealed tube techniques are associated with the following steps (**Figure 1.7**).

- 1) Step 1: The reactants were transferred within an empty pyrex/glance tube.
- 2) Step 2: The solvents were added and the tube was then sonicated for about 5 to 20 minutes (for imine based COF synthesis a catalytic amount of acetic acid is also added during solvent addition).

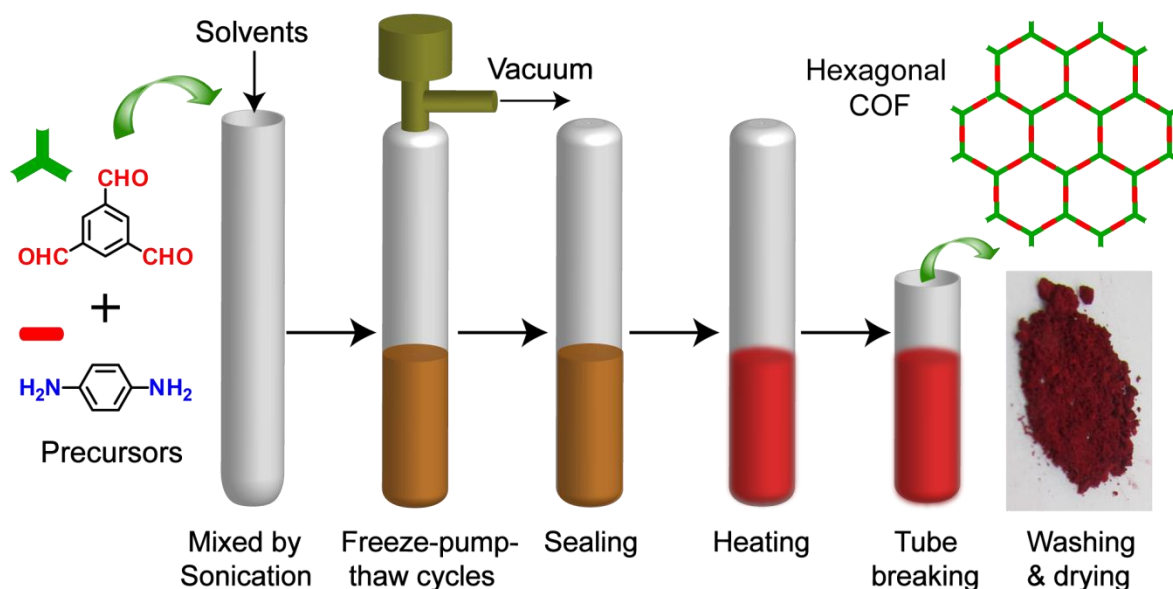


Figure 1.7: Schematic representation of different steps involved in the Solvothermal COF synthesis.

- 3) Step 3: After completion of sonication, the tube containing reactants/solvents was flash frozen (77 K) in a liquid nitrogen bath.
- 4) Step 4: Freeze–pump–thaw cycles were performed 3–4 times to frozen the tube and to create a vacuum inside the tube. And thus, the final pressure was maintained is usually in the range of 50 to 150 mbar inside the tube.
- 6) Step 5: The tube was then sealed off in a flame and was allowed to be warmed up to room temperature. Once it is at room temperature it was transferred to a hot (temp. 90–120 °C) air oven and was kept for 2 to 7 days in an undisturbed condition.

The maintenance of final pressure in the range of 50 to 150 bar, as well as the sealed condition, is highly important because of two reasons. Firstly, the water molecules, which are generated as a byproduct, could easily come out and get diffused inside the empty space thus accelerating forward reaction rate for COF formation. Secondly, the sealed condition will not allow water molecules to come out from the system hence it will maintain the reversibility of the reaction for successful COF crystallization.

The organic solvent combinations which are usually used, such as Mesitylene-dioxane, tetrahydrofurane-methanol-toluene, DMAc-o-dichlorobenzene, DMAc-toluene etc. for COF synthesis [1.22]. The choice of solvents is mainly based on the solubility of the starting materials. The logic behind the use of a mixture of solvents is that the starting materials have to be partially soluble to slow down the reaction which helps to improve the crystallinity and porosity of the COFs [1.12].

1.6.2 Microwave synthesis

The major difference of a microwave-based COF synthesis over solvothermal is that, the microwave technique is faster, generates less number of side product impurities hence it reduces synthetic hurdles or purification difficulties and thus industrially more accepted method. The scientist, Andrew I. Cooper, and co-workers for the first time could introduce a microwave-based technique for COF synthesis by heating a closed tube containing the reactants within a microwave oven [1.32a]. Here, the authors demonstrated two different COF syntheses such as COF-5 and COF-102 only in 20 minutes under microwave reaction conditions [1.32a]. Although it is a faster technique, it could provide the synthesized COFs with comparable crystallinity and surface area compared to solvothermally synthesized COFs [1.32].

1.6.3 Ionothermal synthesis

Ionothermal reactions are mostly used for the construction of covalent-triazine-frameworks (CTFs). Synthesis of CTFs is usually performed at a very high temperature (400 °C) [1.26]. The quartz tubes are usually employed for ionothermal reaction as at high-temperature pyrex or glass tubes cannot be used. Moreover, in a typical ionothermal COF synthesis, the solid reactants and ZnCl₂ (used as a catalyst) were inserted and heated inside a closed quartz tube where such a high temperature (400 °C) ZnCl₂ gradually melts and COF reaction happens within the molten ZnCl₂ [1.26]. The technique is not versatile owing to limited substrate scope as at high temperature most of the precursors undergo decomposition.

1.6.4 Synthesis of monolayers on template surface

COFs are generally composed of various 2D layers which are stacked vertically to generate a one-dimensional nano-pore channel which is important in terms of gas storage or separation applications. However, in electrochemical or photo-conducting application thin layer COF material with limited no. of vertically stacked layers is highly important. In this regard, surface synthesis of 2D COFs are well documented which generally carried on various metal or 2D material surface used as a support. The surface synthesis monolayer COF is supported by scanning tunneling microscope (STM) technique. The scientist, Louis Porte, and coworkers pioneered this research and were able to fabricate the first surface confined covalent organic frameworks (SCOFs) after growing COF-1 and COF-5 on a clean Ag (111) surface [1.33a]. Construction of SCOFs is associated with the steps such as vacuum sublimation of reactants on Ag (111) surface, followed by heating the composite at high temperature. Dichtel and co-workers could develop a new method where the COF thin films can be directly synthesized on a single-layered graphene attached with the SiO₂ surface (**Figure 1.8a**) [1.33b]. The COF thin film fabrication was performed under solvothermal condition whereas the film thickness was controlled *via* adjusting the overall reaction time. The grazing incidence X-ray diffraction technique was used to determine the alignment of COF crystallites on the used SiO₂ surface.

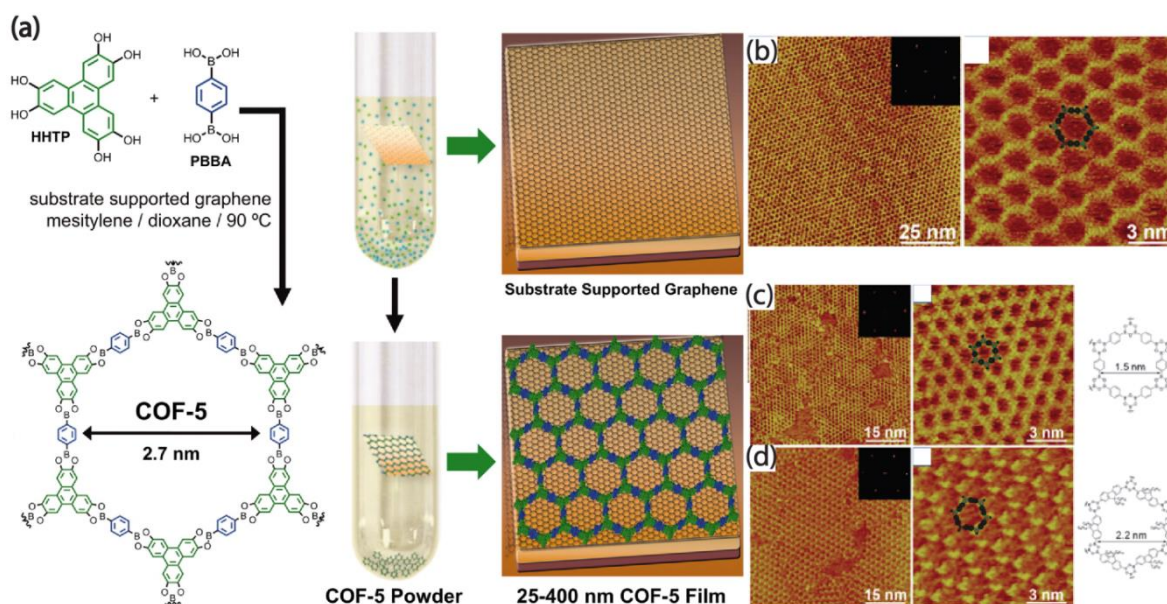


Figure 1.8.: (a) Synthesis of COF-5 on a surface of few-layer graphene. (b) & (c) STM images of COF-1 and (d) STM images of COF 10 on HOPG surface. [Reprinted with permission from Ref., Copyright Science, 2010].

Scientist Li-Jun Wan and co-workers, on the other hand, introduced another novel technique for COF layer fabrication using the surface of a 2D material [1.33c]. The reaction involved by drop-casting of boronic acid reactants on a metal or highly oriented pyrolytic graphite (HOPG) surface, and subsequent heating of the composition on a closed container in presence of $\text{CuSO}_4 \cdot 5\text{H}_2\text{O}$ (**Figure 1.8b**) [1.33c]. They could observe the presence of $\text{CuSO}_4 \cdot 5\text{H}_2\text{O}$ in the reaction chamber is very significant to increase the crystallinity of COFs by adjusting the humidity inside the reaction container. The straightforward reason is that, as the water molecules could reversibly release from $\text{CuSO}_4 \cdot 5\text{H}_2\text{O}$ during the heating-cooling cycles, the reversibility of the reaction gets maintained which helps in improving COF crystallinity [1.33c].

1.6.5 Room temperature synthesis

Although the condensation reactions for COF synthesis generally required some thermal treatment still, sometimes even at room temperature, it is possible to construct this ordered crystalline framework. As for example, Thomas Bein and coworkers were able to grow COF-5 and BTB-COF thin films *via* vapor assisted conversion route [1.34]. The method consisted of the drop casting of boronic acid precursors (one or more starting materials) on top of a glass slide, followed by keeping them inside a closed chamber. The chamber is also contained with Mesitylene: dioxane solvent mixtures (1:1) kept in a separate glass vial. The solvent vapor, with the course of time, diffuses out from the glass vials and starts filling inside of the closed chamber. As soon as, the solvent vapors come in contacts with the glass slide containing precursors the reaction proceeds and the COF thin film grows on the glass slide. It is to be noted that, the solvent diffusion method is very slow and the reaction time is quite higher (> 72 hours) for COF crystallite formation [1.34]. However, COF thin film, in terms of crystallinity and surface area, is comparable to its solvothermal counterpart.

Some other recent reports where the COFs have been synthesized at room temperatures, such as Josep Puigmartí-Luis and coworkers could develop a micro-fluid based method for the construction of imine COFs (MF-COF-1) at room temperature [1.34b]. During synthesis, the reactants and acetic acid were injected into separate nozzles (flow rate 100 $\mu\text{L}/\text{minutes}$) and they were allowed to mix inside the main channel. In the outlet, in a maximum of 11 seconds, the COF product was formed and collected. However, the concentration of the precursors and the acetic acid has to be maintained properly in micro-

fluid based synthesis as the concentration of precursors if is too high then clogs will form in the main channels and it will hamper continuous flow synthesis [1.34b].

1.6.6 Mechanochemical synthesis

Mechanochemical is one of the famous and effective methods of COF synthesis specifically at room temperature. The method involved the grinding of reactants on a mortar pestle or using ball milling for the construction of COFs. Rahul Banerjee and coworkers for the first time could develop this mechanochemical method of COF synthesis [1.35a]. It was associated with initially mechanical grinding of precursors for 15 min on a mortar pestle at room temperature followed by heating at 120 °C for 45 minutes. The method is synthetically easier compared to other methods as it is easy to perform, faster, environmentally friendly, cost-effective etc. However, the major drawback is that the synthesized COFs were found to have significantly low crystallinity or porosity due to delamination of COF layers during the rapid grinding process [1.35a].

However, in the year 2017 from the same group S. Kandambeth *et al.* and S. Karak *et al.* developed a new methodology of mechanochemical COF synthesis where the material could be synthesized with high crystallinity and porosity (BET surface area as high as $>3,000 \text{ m}^2 \text{ g}^{-1}$) [1.35b, 1.35c]. Herein, *p*-toluenesulfonic acid (PTSA) was used as a water reservoir and a molecular organizer entity during COF crystallization and thus a series of β -ketoenamine COFs were synthesized in less than an hour while maintaining its high crystalline and porous nature. Notably, the COFs are always prepared in an insoluble powdered form which restricts this novel material for various potential applications. However, using this unique fabrication technique, not only the COF could be synthesized in industrial scale but also the material with desirable forms. Herein, for the first time, the COF has been fabricated in the form of a membrane and was utilized in water purification. It is to be noted that, this is the first reports in the literature where the rapid scalability and easy processability of the COF material have been discussed [1.35c].

1.7 Applications of COFs

The promising platform for various functionalizations with high crystalline and porous nature of COFs made them suitable for various potential applications such as in storage of gases or bio-molecules, separation, catalysis, sensors, and photo conducting materials. The ordered nano-channel made them suitable for membrane-based separation and water purification application. The conjugated π - π stacked structures of 2D COF is useful for

photo-conducting or as charge carrier mobility. The various potential applications of COFs have been summarized as below (**Figure 1.9**).

1.7.1 Gas storage application

The COFs are mostly nano-porous in nature (< 2 nm) which made them suitable for gas storage application as the pore size are very much comparable to the size of guest gas molecules. Additionally, the pre-designable pores with high porosity and low density are other promising features for using them for storage of different gases such as carbon dioxide (CO₂), hydrogen (H₂), ammonia (NH₃) and methane (CH₄) etc.

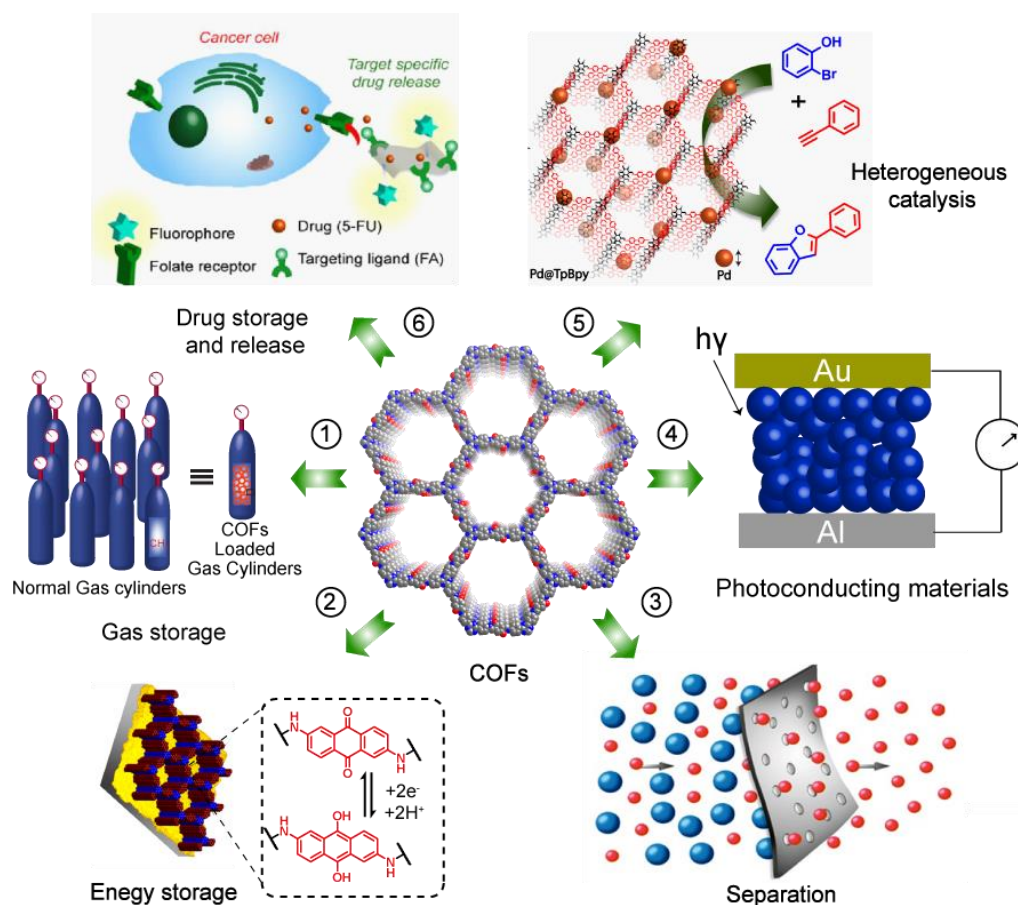


Figure 1.9: Various applications of COFs such as gas storage, photo-conducting materials, heterogeneous catalysis, energy storage, separation and drug/biomolecules storage.

1.7.2 Hydrogen storage

Due to its high energy density, among all other natural gases hydrogen is considered one of the future energy sources. Hence, storage and fruitful use of hydrogen is highly important. However, owing to its very low boiling point ($-252.8\text{ }^{\circ}\text{C}$) and explosive nature, storage of hydrogen under high pressure is to be omitted [1.35]. In this concern, microporous materials

exhibiting very high surface area and pore size less than 1 nm could be promising hydrogen gas storage [1.36].

US Department of Energy (DOE) has set the maximum storage of hydrogen is 5.5 wt% till 2017 at an operating temperature of 40–60 °C and under 100 atm pressure. A series of microporous COFs were used for H₂ storage whereas the highest uptake of hydrogen was achieved by 3D COF-102 (7.24 wt% at 77 K; 1 atm pressure) [1.23]. The H₂ storage value is very much comparable to MOF-5 (7.6 wt% at 77 K; 1 atm pressure) and MOF-177 (7.4 wt% at 77 K; 1 atm pressure). As discussed, low pore diameter with high surface area material are always promising for effective gas storage application. Herein, the ultra-porous ($S_{\text{BET}} = 3620 \text{ m}^2 \text{ g}^{-1}$) 3D COF framework and the small pore size (1.2 nm) enabled COF-102 to showcase a promising hydrogen storage value (**Figure 1.10 and Table 1.1**).

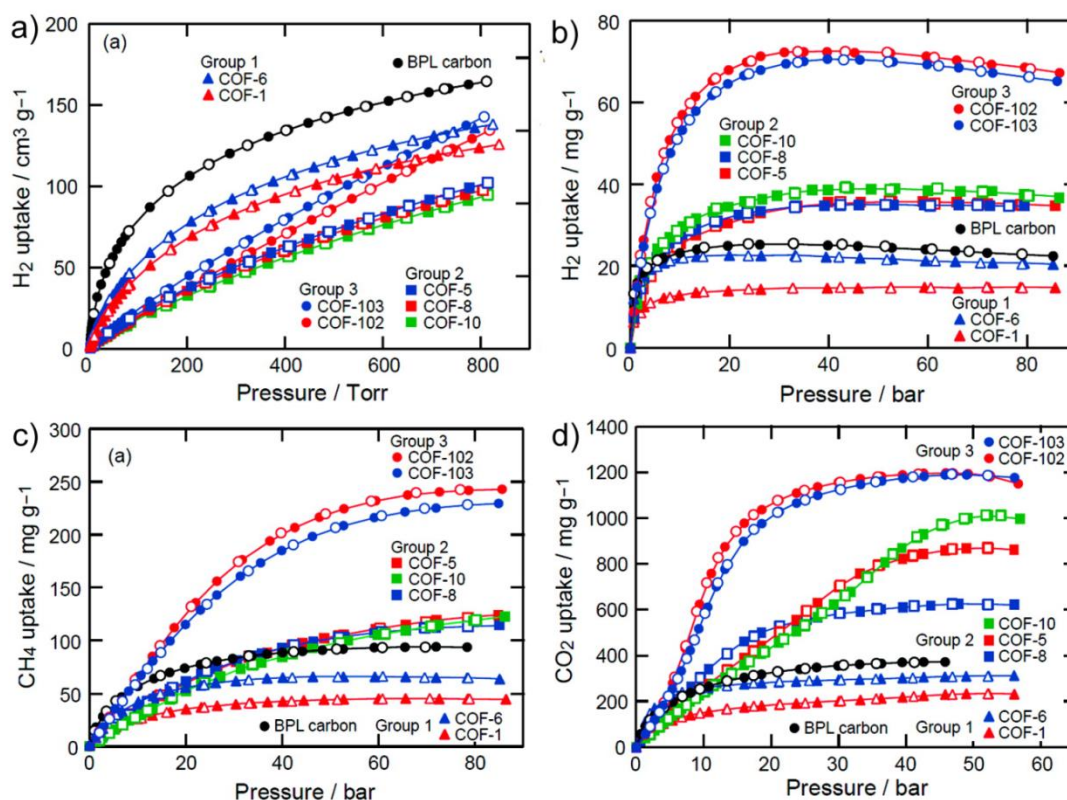


Figure 1.10. Comparison of excess hydrogen uptake of different COFs (a) at 1 bar and (b) high pressure (open symbols represent experimental results, filled symbols simulated results). (c) Methane adsorption isotherms of COFs at high pressure. (d) Carbon dioxide adsorption isotherms of COFs at high pressure. [Reprinted with permission from Ref. *J. Am. Chem. Soc.*, **2009**, 131, 8875[1.37], Copyright American Chemical Society, 2009].

The second highest value is reported for COF-103 ($S_{\text{BET}} = 3530 \text{ m}^2 \text{ g}^{-1}$) is another 3D COF, whereas among 2D COFs the highest H₂ storage value was achieved by COF-10 ($S_{\text{BET}} = 1760$

m^2g^{-1}) [1.23, 1.37]. Although hydrogen storage, at low temperature (77K), using COFs are excellent, the demand for room temperature storage is still on because at room temperature H_2 storage values using COFs is very less compared to DOE targets. Apart from the high surface area and smaller pore diameter, another important factor which could dramatically enhance hydrogen storage is the post-functionalization by which the interaction of hydrogen molecules with porous COF structures can be improved. Theoretician has predicted, one possible for achieving higher hydrogen storage is the lithium ion doping inside COF pores. From DFT binding energy calculation using Møller–Plesset (MP) and Couple Cluster (CC) methods, theoreticians predicted that lithium-ion doped COFs can be a potential candidate for hydrogen storage material [1.39].

Table 1.1: Hydrogen, carbon-dioxide and methane storage properties of COFs of different surface areas reported in the literature.

COF Name	BET Surface area (m^2g^{-1})	H_2 uptake (wt%)	CO_2 uptake (mg g^{-1})	CH_4 uptake (mg g^{-1})	References
COF-102	3620	7.24	1200	187	1.23
COF-103	3530	7.05	1190	175	1.23
COF-10	1760	3.92b	1010	80	1.37
CTC-COF	1710	1.12	—	—	1.38
COF-5	1670	3.58b	870	89	1.37
COF-8	1350	3.50b	630	87	1.37
COF-18A	1263	1.55 (1 bar)	—	—	1.28e
COF-14A	805	1.23 (1 bar)	—	—	1.28e
COF-16A	753	1.40 (1 bar)	—	—	1.28e
COF-6	750	2.26	310	65	1.37
COF-1	628	1.28 (1 bar)	—	—	1.37
COF-11A	105	1.22 (1 bar)	—	—	1.28e

1.7.3 Methane storage

Like hydrogen, methane is another promising material as an energy source towards the vehicular application. Methane storage under ambient temperature required very high pressure (200 bar). Hence, it is quite difficult to store methane in an empty cylinder however such difficulty can be surpassed using porous materials. It is well established that the use of porous material can bring down the methane storage pressure below 50 bar while keeping energy density intact [1.40]. The DOE target value for methane storage fixed by US Department of Energy is 365 (v/v) at 35 bar or 65 bar pressure and at room temperature. The easy functionalizable nature along with high surface area value, are the most attractive features of COFs, for making them suitable for methane storage. The COF-102 (187 mg g^{-1} ; 35 bar and 298 K) showed the highest methane storage value whereas second highest value was reported for the 3D COF-103 (175 mg g^{-1} 35 bar and 298 K) (**Figure 1.10 and Table 1.1**) [1.37].

1.7.4 Carbon dioxide removal

Carbon dioxide (CO_2) is considered as one of the harmful greenhouse gases as it contributes maximum to the overall global warming effect. CO_2 is produced in larger quantity *via* combustion of the fossil fuels. Whereas, removal of CO_2 from flue gas, emitted from various industries, is highly important as it contained 10–15% of CO_2 . [1.41]. Various porous materials e.g. porous carbons, zeolites, MOFs and finally COF were successively tested for CO_2 storage. Yaghi and coworkers revealed for COF-102 the max. CO_2 uptake of 27 mmol g^{-1} at 298 K and 35 bar, which is higher in performance than of zeolites (8 mmol g^{-1}) and of MOF-5 (22 mmol g^{-1}) [1.37]. Various computational studies revealed the lithium doping could further enhance the CO_2 uptake in COF-102 and COF-105. The study predicted, Lithium doped COF-102 have the potential to store CO_2 409 mg g^{-1} at 298 K and 1 bar (**Figure 1.10 and Table 1**) [1.42].

1.7.5 Ammonia storage

Ammonia gas is one of the most important raw materials used in industries for various purposes such as in fertilizers, wood or paper industries. Ammonia gas generally transported in liquid form and it has a very high health risk. Hence, safe handling and extra care have to be devoted always during its transportation. One way to solve this issue is by using porous micro-materials to store ammonia and its subsequent transport. Boronic acid-based COFs have already been tested for this purpose whereas it showcased outstandingly high ammonia

uptake. The boron center is Lewis acidic in nature hence Lewis base ammonia can interact with boron and can be stored easily *via* acid-base adduct formation which is reversible as well. Yaghi and coworkers reported NH_3 storage in a boronic based COF (COF-10) [1.43].

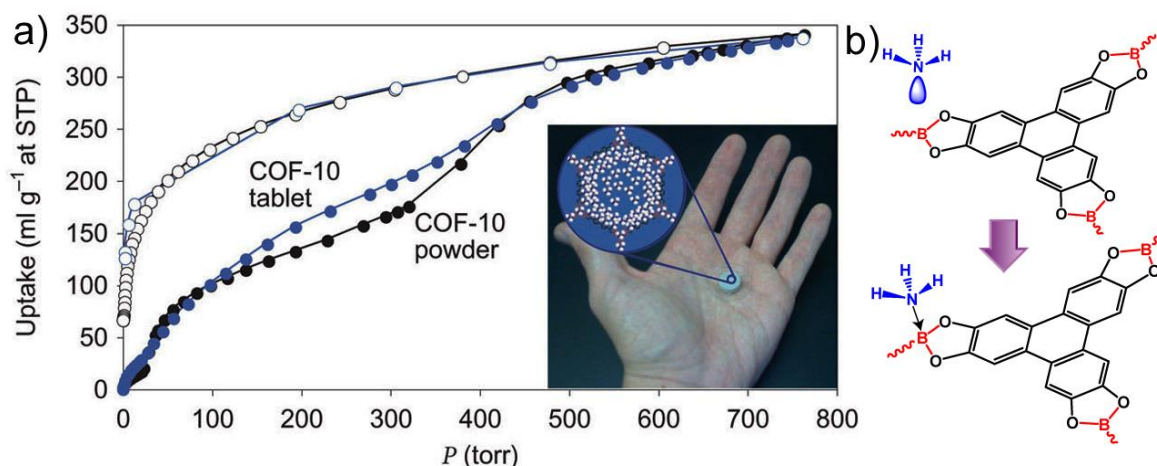


Figure 1.11: (a) Ammonia adsorption isotherms of COF-10 powder (black) and tablet (blue). (b) Lewis adducts formation between ammonia and boronate ester. [Reprinted with permission from Ref. *Nat. Chem.*, **2010**, 2, 235[1.43], Copyright Nature Chemistry, 2010].

They could achieve an ammonia storage of 15 mol kg⁻¹ (1 bar and 298 K). This is the highest ammonia uptake value achieved using any porous materials. In terms of NH_3 uptake, the COF material (COF-10) also surpasses the commercially used other porous materials i.e. zeolites-13X (9 mol kg⁻¹) and Amberlyst-15 (11 mol kg⁻¹). Interestingly, the NH_3 uptake in COF-10 is found to be completely reversible and ammonia in COF-10 can be easily released by heating (**Figure 1.11**) [1.43].

1.7.6 Heterogeneous catalysis

The long-range ordered structure with easily functionalizable pore walls has made COF frameworks promising specifically in heterogeneous catalysis. As the frameworks are completely insoluble in almost all mediums, it can be recovered easily from the reaction mixture without losing any significant weight [1.44]. During framework construction, it is very easy to architect pore walls with desirable functional groups by proper choice of building units. Notably, high porosity of COFs allows facile diffusion of the reactant molecules into proper catalytic sites. Whereas, the tunable and ordered pore channels of COF help in size-selective catalysis reaction. COFs pore walls can be designed for heterogeneous catalysis in two different ways. 1) Prior incorporation of desirable catalytic sites in the used

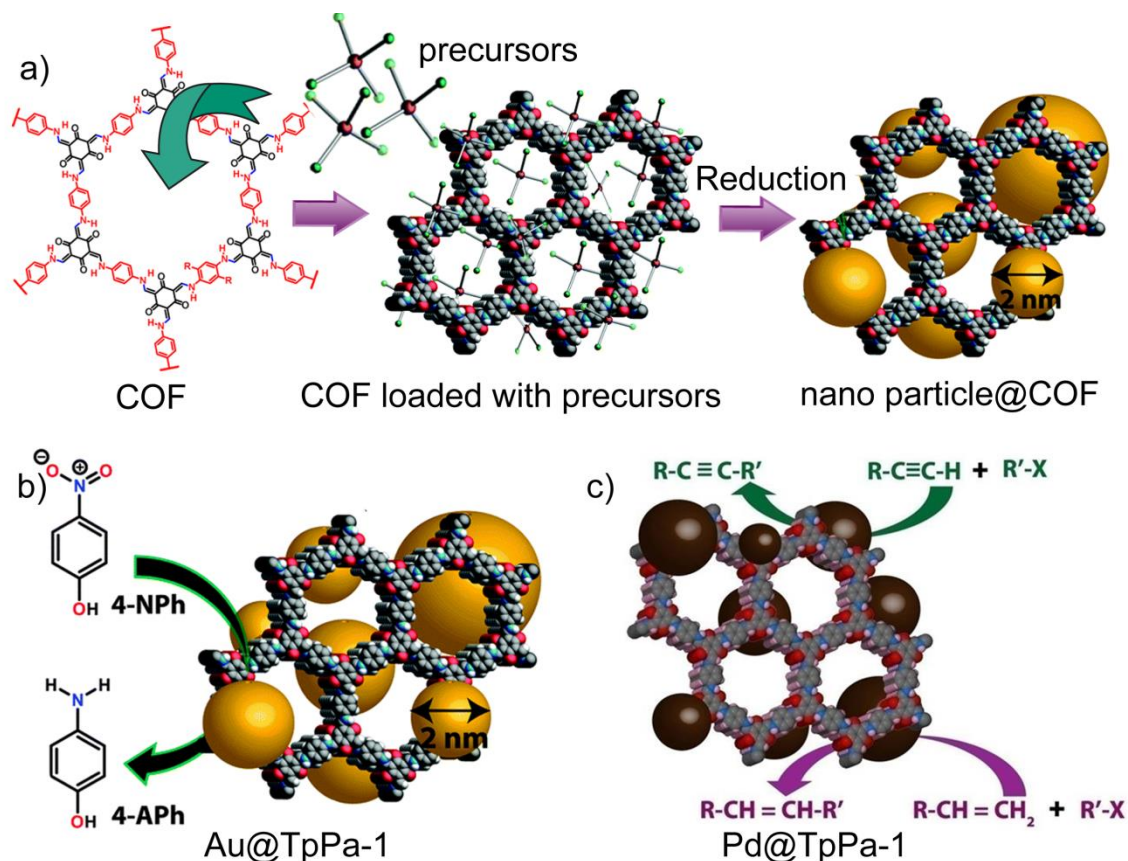


Figure 1.12. (a) Schematic representation of the synthesis of nanoparticle-loaded COFs. (b) and (c) Catalysis performed by nanoparticle immobilized COF-TpPa-1. [Reprinted with permission from Ref. *Chem. Commun.*, **2015**, 51, 11717 and *Chem. Commun.*, **2014**, 50, 3169 [1.44c-d], Copyright Royal Society of Chemistry, 2014-15].

building units [1.44a-b], 2) Post-synthetic doping of catalytically active nano-particles within COF pores [1.44c-d]. Wei Wang and coworkers could perform Suzuki–Miyaura coupling reaction *via* incorporation of Pd²⁺ ions in the pore walls of an imine based COF (COF-LZU1) [1.44a]. They established that the COF pore walls were properly functionalized with the Pd²⁺ ions after complexing with the imine nitrogens (**Figure 1.12**). Rahul Banerjee and co-workers were specifically chosen stable β-keto-enamine based COF framework (**TpPa-1**) to immobilize Palladium (Pd) & Gold (Au) nano-particles [1.44c-d]. In the two-step immobilize process, first nano-particle precursors such as AuCl₄. 3H₂O and Pd(OAc)₂ were successfully loaded within COF pores by stirring or incubation process. In the next step, the loaded precursors were allowed to reduction using sodium borohydride (NaBH₄). The palladium (Pd) nanoparticle loaded **TpPa-1** COF catalyst showed excellent catalytic activity towards C-H bond activation and C–C coupling reaction whereas the gold (Au) nanoparticle loaded **TpPa-1** COF catalyst was successful to reduce of nitro to amine compounds. Again, both the catalyst was very stable and active even after consecutive five cycles [1.44c-d].

1.7.7 Photoelectric and semi conduction applications

2D COFs, are very much similar to graphite, as it posses 2D conjugated framework structure where the layers undergo stacked in the vertical direction. Hence, the individual 2D COF layer is very much analogous to graphene. The long ranged ordered and efficient π - π stacking interactions make them suitable for semiconducting applications. During this stacking in the vertical direction, the pi orbital of one layer could overlap with another pi orbital present in another adjacent layer. And thus, multiple overlapping between several pi orbitals along z-axis brings unique optical or electronic properties in 2D COFs [1.22]. First, 2D COF tested as the photoelectric application is PPy-COF which was synthesized by Donglin Jiang and co-workers *via* boronic acid trimerization among electron rich pyrene-2,7-diyldiboronic acids. Ppy-COF, upon irradiation in visible light, generates photocurrent (5 nA) (**Figure 1.13**) [1.45a].

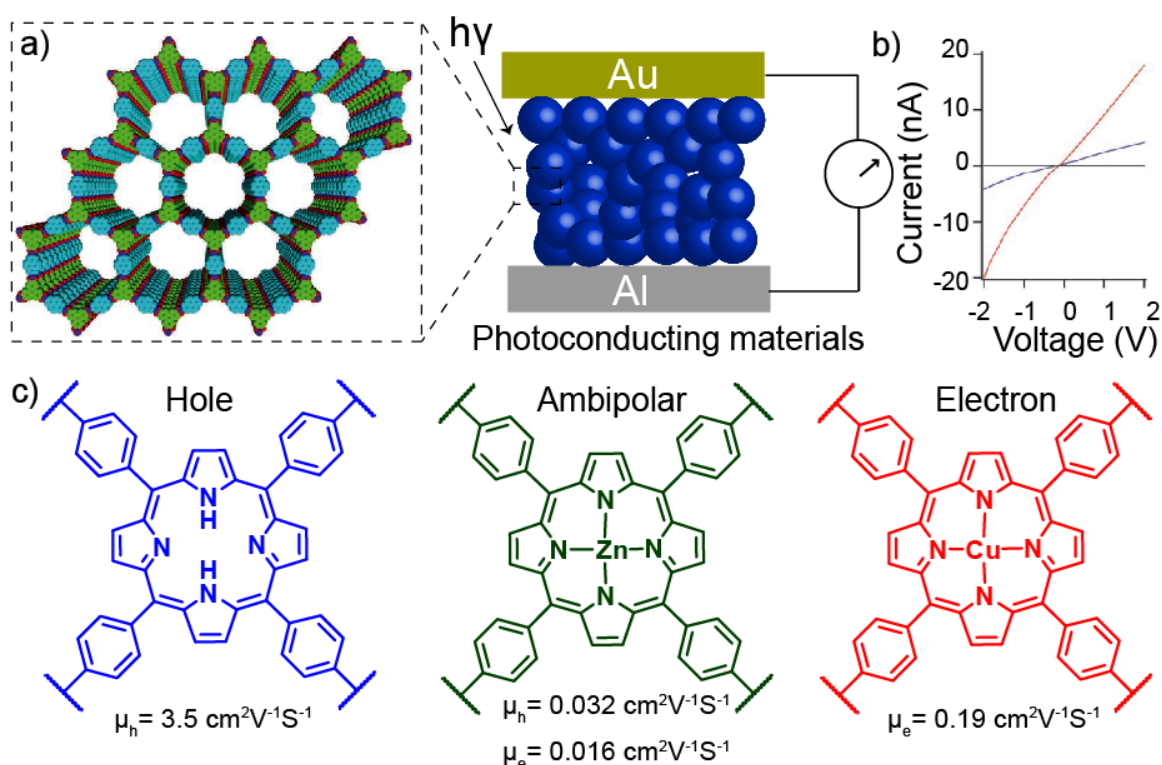


Figure 1.13: (a) Schematic representation of the device set up used for the measurement of the photocurrent of TP-COF. (In the device COF powders (blue) were sandwiched between two electrodes). (b) I-V profiles as-synthesized TP-COF (blue) and iodine doped TP-COF (red). (c) Hole (μ_h) and electron (μ_e) carrier motilities of H₂P-COF (blue), ZnP-COF (green) and CuP-COF (red).

The electron rich pyrene moieties in an ordered stacking arrangement could generate well-defined conduction paths for charge migration (**Figure 1.13a**). Separately, from the same

group, TP-COFs were synthesized *via* boronate ester formation reaction which exhibits *p*-type semiconducting nature and shows a linear I-V curve [1.45b]. Moreover, to extend the overall adsorption capacities in the near-infrared or infrared region, the COFs could be decorated with more conjugated porphyrin and phthalocyanine moieties. Keeping in mind, three separate porphyrin-based COFs with different metal ions (Cu^{2+} & Zn^{2+}) present in porphyrin centers was synthesized by Donglin Jiang and co-workers (**Figure 1.13c**) [1.45c]. Depending on the metal ion present, the COF showcased different charge transport behavior as measured by the flash photolysis time-resolved microwave conductivity study. The nature of metal ions could dramatically affect the charge transfer properties in COFs.

The H_2P -COF i.e. metal-free porphyrin COF displays only hole transport capabilities whereas the CuP-COF (Cu^{2+} doped porphyrin COF) shows good electron transportability (**Figure 1.13c**). However, by surprise, Zn^{2+} doped porphyrin COF (ZnP-COF) shows ambipolar characteristics [1.45c]. Omar M. Yaghi and coworkers using a reversible Schiff base reaction could synthesize two different porphyrin-based imine COFs such as COF-366 and COF-66. Both of them are very promising to showcase considerable hole transport mobility (3.0 and $8.1 \text{ cm}^2\text{V}^{-1}\text{s}^{-1}$), which is also the highest among all π - π stacked layered materials [1.27d]. In another report, where Ni^{2+} is used as metal ion such as Ni^{2+} porphyrin COF (NiPc-COF) showed outstandingly high light-harvesting capabilities specifically in visible and even in near-infrared region and thus could display a significantly high hole transport mobility of $1.3 \text{ cm}^2\text{V}^{-1}\text{s}^{-1}$ [1.45d]. In a recent report, Donglin Jiang and co-workers again attempted to synthesize a donor-acceptor based 2D- COF with ambipolar characteristics where the synthesized 2D D-A COF could display an excellent hole transport mobility of $0.01 \text{ cm}^2\text{V}^{-1}\text{s}^{-1}$ and electron transport mobility of $0.04 \text{ cm}^2\text{V}^{-1}\text{s}^{-1}$ [1.45e].

1.7.8 Energy storage

Energy storage and conversion are one of the most important topics of research in recent years. In this concern, porous material such as COFs can be utilized in terms of supercapacitive energy storage application owing to their long-range porous structure with facile functionalizable pore walls with redox active groups. This pioneering work in COF was reported by William Dichtel and co-workers where they have synthesized an anthraquinone-based β -ketoenamine DAAQ-TFP COF by Schiff base condensation between 1,3,5-triformylphloroglucinol (Tp) and 2,6-diaminoanthraquinone (DAAQ) [1.46]. The presence of redox-active anthraquinone moiety in DAAQ-TFP COF, exhibit reversible redox processes via $2\text{H}^+ / 2\text{e}^-$ quinone-hydroquinone transformations (**Figure 1.10**). Moreover, owing to high

chemical stability (as β -ketoenamine COF), DAAQ-TFP COF was able to retain its capacitance performance even operating over 5000 charge-discharge cycles [1.46a]. In another report from the same group, the DAAQ-TFP COF was fabricated as oriented thin films on a gold (Au) surface. Moreover, they could enhance the capacitance of the thin film i.e. 3 mFcm^{-2} compared to randomly oriented COF powders (0.4 mFcm^{-2}) [1.46b]. Another scientist, Donglin Jiang, and co-workers were also able to introduce redox-active functional groups in a NiP-COF by post-functionalization with TEMPO. This functional group bears a free radical which upon oxidation-reduction can store energy. Moreover, the TEMPO functionalize COF ([TEMPO]_{100%}-NiP-COF) exhibited a very high capacitance value of 167 Fg^{-1} [1.46c]. However, in all cases, the use of COFs in powdered form always leads to the difficulty in electrode fabrication. Again, use of various conducting additives or post-functionalization, for enhancing capacitive performance, affects the active surface area of the material. Therefore, construction of pristine COF based self-standing; high-performance supercapacitive electrode could be the best alternatives to utilize this novel material as a promising energy storage candidate.

1.7.9 Separation

The ordered nano-channels with tailorable pore aperture of COFs could be utilized for gas separation applications. Yanan Gao and coworkers could successfully use COF-320 for N_2/H_2 and H_2/CH_4 separation [1.47a]. The gas separation membranes were fabricated by performing Schiff base reaction of reactants on the surface of porous alumina ceramic support. The presence of various surface amine functionalities, on top of grafted alumina surface, can effectively hold the COF crystallites *via* imine bond formation. Although, on top of porous alumina support, the author could successfully fabricate thin film COF membranes the presence of a large number of crystalline voids reduces the gas selectivity of the membranes [1.47a]. Recently Rahul Banerjee and coworkers could fabricate hybrid membranes made up of COF and PBI polymers composite. These hybrid membranes display moderate selectivity in CO_2/CH_4 and CO_2/N_2 separation. The covering effect of polymer chains on COF pores is a major drawback of such mix-matrix membrane, which prevents those membranes in achieving promising selectivity of separation [1.47b]. Theoreticians recently predicted, the self-standing COF membranes are the best alternatives to achieve high permeability or selectivity during gas separation applications [1.47c]. From the same group in 2017 Rahul Banerjee and co-workers could solve this long-term practical issue after

successful fabrication of self-standing COF membrane for various molecular separation and water purification.

In their study, Kandambeth *et al.* developed a universal strategy for the fabrication of uniform, crack-free, and free-standing COF membranes even in centimeter scale. *p*-toluenesulfonic acid (PTSA) mediated solid-state mixing approach was the basic synthetic tool for the construction of crystalline and porous COF membranes [1.35b]. The aldehyde 1,3,5-triformylphloroglucinol (Tp) was reacted separately with different diamines in presence of PTSA acting as a molecular organizer entity and water reservoir. The free-standing COF membranes also showcased high chemical stability in mineral 3N HCl for several days. The author could achieve high solvent flux (acetonitrile- 278 Lm⁻²h⁻¹bar⁻¹; water-120 Lm⁻²h⁻¹bar⁻¹) under ambient pressure during passing various solvents through the membrane. The as-synthesized COFMs were successfully employed as a self-standing membrane for water purification *via* molecular rejection of toxic dyes (methylene blue, rose Bengal, congo red etc.) from drinking water. The ordered nano-channel with a specific pore diameter of the membrane, allowed them to utilize COFM for selective molecular sieving application. For molecular sieving experiment, they prepared a physical mixture of two different UV active molecules (rose bengal and 4-nitroaniline) having a significant difference in their molecular weight and passes the mixture through the membrane. As they stated, because of low molecular weight, 4-nitroaniline easily pass through the membrane and rose bengal gets rejected (having high molecular weight) which have been determined using UV-Vis spectroscopic analysis [1.35b]. Though the synthesized membranes are promising for molecular sieving or water purification, its usage in drastic environmental conditions (drastic humidity, strongly acidic or basic) were limited owing to their limited chemical stability.

1.7.10 Drug storage and delivery

Since the porosity of COF can be varied from microporous to meso- or even macroporous, the scientist had tried to load larger sized drug or bio-molecules within porous COF pores. Yushan Yan and coworkers could design a 3D polyimide-based PI-COF-4 for successive drug delivery application. The COF PI-COF-4 exhibited an ultrahigh surface area of 2403 m²g⁻¹ which made them applicable in storing ibuprofen (IBU) drug molecule [1.48]. The author calculated the maximum loading of ibuprofen drug in PI-COF-4 as 20 wt%. The overall drug release profile showed a very slow diffusion of ibuprofen (IBU) from the framework pores and takes almost 6 days for complete release.

In 2015, Kandambeth *et al.* could synthesize self-templated hollow spherical COFs with very high porosity ($S_{\text{BET}} = 1500 \text{ m}^2\text{g}^{-1}$). They could utilize the hollow cavity for enzyme loading and release application. The mesoporous walls helped in the successful immobilization of trypsin enzyme inside the hollow cavity via diffusion. The author could successfully load a maximum of $15.5 \mu\text{mol g}^{-1}$ of trypsin inside this hollow spherical COF [1.35d].

1.8. Chemical stability of COFs

Although a variety of 2D or 3D COFs was synthesized in last two decades and have been utilized for various potential applications, this novel material suffers from serious drawbacks such as its chemical instability, processability, and scalability. Since the majority of COFs are synthesized considering reversible organic reaction where water eliminates as a byproduct, there is always a possibility to the reversible back reaction if the synthesized material is again treated with water (**Figure 1.14**) [1.28a]. As a result, the COF readily decomposes to the starting materials. However, for real life applicability of any porous material, the chemical stability should be considered as one of the important aspects which need to be solved. Hence, it was really a challenging task to the chemists to stabilize this novel frameworks from being degraded in humid, mild acidic or basic conditions for its widespread implementation. Apart from chemical stability for industrial application of such materials the other two important criterions such as material's processability and scalability is also a major challenging task. We will first discuss why chemically stable COFs are important and what are the attempts made to date to increase its hydrolytic stability. Finally, we will focus on the attempts made for its bulk scale production and its processability in desirable forms.

As discussed, natural gas storage and its separation are one of the major important tasks for the chemists in recent years. Although in the laboratory, most of the gas storage and their separation study are generally performed in an anhydrous condition. However, for practical use, the adsorbents have to be exposed to an atmosphere containing water and other reactive oxides such as SO_2 , NO_2 , H_2S , etc [1.10d]. Even though the material has good gas storage capability, the framework instability will not allow for its long-term usage and the performance will decrease frequently under given condition due to rapid framework decomposition. Some common examples which demand the chemical stability of porous materials are 1) storage or separation of natural gases, 2) Carbon-di-oxide capture from bio-fuel stream, 3) removal of CO_2 from flue gas, 4) hydrogen storage in fuel cell etc [1.10d].

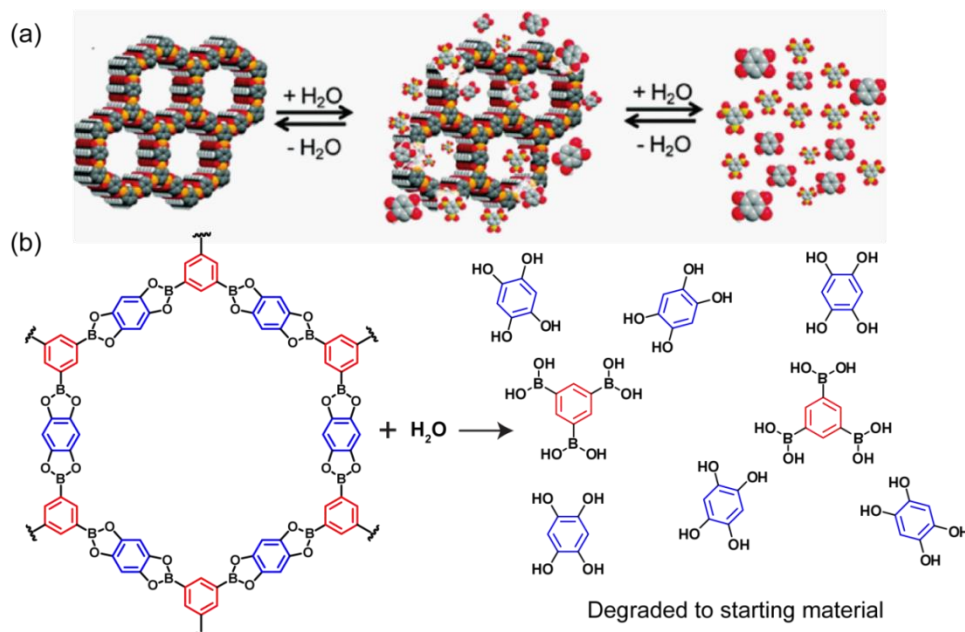


Figure 1.14. Schematic representation of (a) as-synthesized COF (b) partial hydrolysis and release of monomers into solution upon submersion in water (c) Completely hydrolyzed COF.

Natural gas streams regularly contain water vapors which must be completely removed before its transport or storage. The presence of an even tiny amount of water vapor in natural gas can create clogs within natural gas pipelines *via* the formation of clathrates. Again, the presence of humidity can lower down the heat value of natural gases. Hence, the porous materials which are used for natural gas storage or separation should be stable in humid conditions. Chemical stability of porous materials is equally important in CO₂ sequestration process. The industrial flue gases are also contaminated with moisture and various acidic oxides (e.g. SO₂, H₂S, and N₂O) in addition to N₂ and CO₂ [1.10d]. The porous materials exclusively used for the CO₂ capture require decent chemical stability specifically in acidic and humid conditions. Again, hydrolytic stability of such porous materials is highly important in hydrogen storage which is mainly performed for the application in a fuel cell where water molecules are generated as an end product [1.10d]. Hence, although COFs are highly important in natural gas storage and separation and have already covered lots of benchmark in recent years, their most of the applications are limited to laboratory scale only owing to the poor chemical stability of COFs originates mainly from the reversibility during framework formation. Although reversibility helps in improving crystallinity and porosity of COFs, it becomes a disadvantage when we consider the chemical stability of the material. Therefore, for real-life applications, there is an utmost need of improving the chemical stability of the COFs.

1.9. Approaches made to stabilize COFs towards various chemical treatments

Few attempts were executed in the literature for improving the chemical stability of COFs. In 2011, the first attempt, to increase the hydrolytic stability of boronate ester based COFs such as of COF-18Å, was made by John J. Lavigne and coworkers [1.28a]. This material (COF-18Å) is highly unstable towards water treatment (**Figure 1.15**). As soon as, COF-18Å powders were submerged in water, the frameworks undergo rapid decomposition to starting materials and this was supported by using UV absorbance and NMR spectroscopy (**Figure 1.14**). The hydrolytic stability test was performed using COF-18Å powders after covering the COF within a filter paper and the whole composition was then directly submerged in water. After 20 minutes of water treatment, the filter papers were removed and the recovered material was tested using PXRD and N₂ adsorption where COF-18Å loses all its crystallinity and porosity. To enhance the chemical stability, COF-18Å pores were functionalized with hydrophobic alkyl groups (**Figure 1.15a**). The authors have used various functional groups and it was named as COF-16Å (R=Me), COF-14Å (R=Et), COF-11Å (R=Pr). Interestingly, the author could find out an enhancement of hydrolytic stability when a similar experiment was performed using the alkylated COFs such as COF-16Å, COF-14Å,

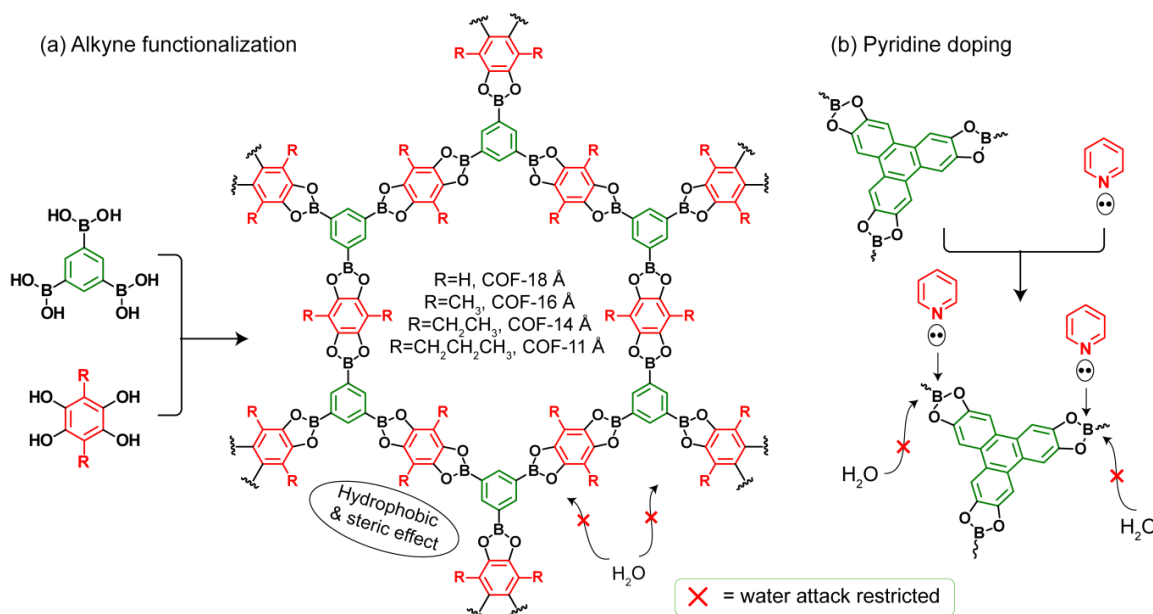


Figure 1.15. Attempts made to improve the chemical stability in COFs (a) alkylation (b) doping of pyridine.

and COF-11Å compared to the pristine COF-18Å. Although this strategy improved the chemical stability of boronic acid-based COFs, the major drawback of this route is that the

active surface area of the material dramatically decreased as the length of the alkyl chain increases. COF-14Å has only a surface area of $496 \text{ m}^2\text{g}^{-1}$ which is 30% of the surface area of COF-18Å. Again upon long term (after 1 day) hydrolytic stability test it was observed, the alkylated COFs (e.g. COF-16Å, COF-14Å. and COF-11Å) also undergo slow decomposition. This result implies that the alkylation strategy is not the permanent solution for solving the chemical stability issue in COFs.

The second approach to enhance the chemical stability of COF-10 by pyridine vapor doping was attempted by David Calabro and coworkers. Boronate esters are susceptible to hydrolysis in contact with water owing to the presence of Lewis acid boron centers. During hydrolytic treatment, the Lewis acid centers (boron) can be readily attacked by water molecules to form acid-base adducts which finally results in framework decomposition. Herein, the authors smartly attempted to block these Lewis acid centers with pyridinic nitrogen to enhance the hydrolytic stability of the COF material (**Figure 1.15b**). The author has performed the doping experiment by submerging powdered COF samples to 1 wt% solution (pyridine to dry acetone) of pyridine for 24 hours. Interestingly, the pyridine modified COF-10 showcased superior hydrolytic stability compared to pristine COF-10. Moreover, the material could retain its crystallinity even after humid air treatment for 7 days, however, direct submerge of pyridine doped COF-10 in water will cause its complete decomposition of the framework. Hence, neither of the two approaches discussed in the earlier sections were up to the mark, thus there was always an utmost demand of developing a new methodology by which chemically stable COFs in extreme conditions (water, acid, base etc) could be fabricated without altering its porosity or crystallinity.

Therefore, stability issues in COFs were running for a quite long time until and unless in 2012, Kandambeth *et al.* and co-workers could come up with a novel versatile methodology of enol-keto tautomerization phenomenon during COF crystallization and subsequent enhancement of chemical stability of COFs in water, acid or base. As mentioned, in 2012, for the first-time in COF literature, Kandambeth *et al.* and co-workers, could develop a versatile methodology to synthesize two new highly crystalline & porous COFs (**TpPa-1** and **TpPa-2**) using a combined reversible/irreversible Schiff base reaction route (**Figure 1.16a**) [1.35e]. Interestingly, these two COFs displayed extraordinary chemical stability towards strong acid (9 N HCl) or base (9 N NaOH) and also in water for 7 days or more. These COFs are prepared solvothermally by the reaction of 1,3,5-triformylphloroglucinol (Tp) separately with *P*-phenylenediamine **Pa-1**) and

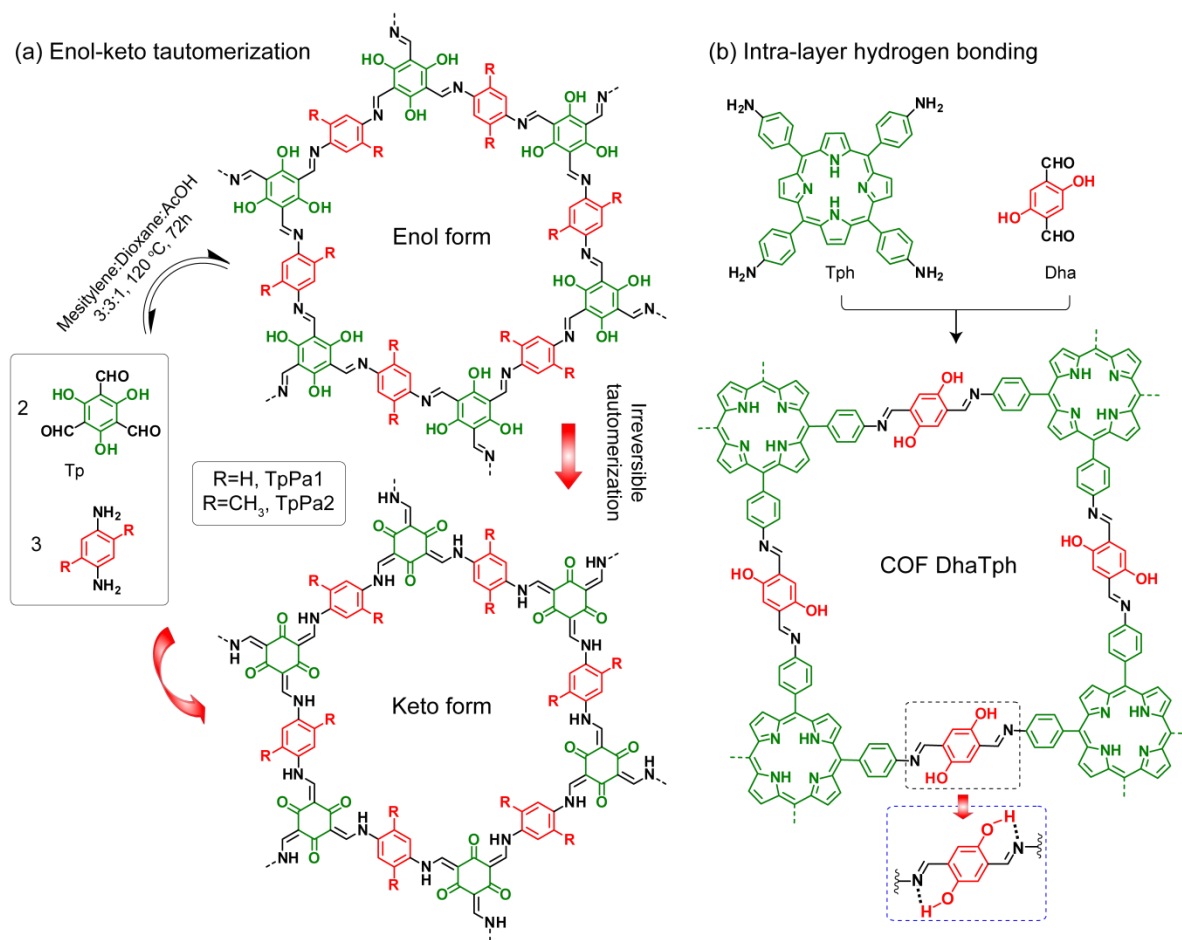


Figure 1.16. (a) Synthesis scheme for chemically stable COFs (TpPa-1 and 2) using Schiff base condensation reaction via a reversible-irreversible reaction route. (b) Construction of an intralayer hydrogen bonded COF DhaTph.

2,5-dimethyl-*p*-phenylenediamine (**Pa-2**) (within a sealed Pyrex tube under vacuum and heated at 120 °C for 3 days. In their report, it was mentioned that the complete reaction can be divided into two successive steps. The first step is the reversible Schiff base reaction which helps for the successful formation of the crystalline framework which in the second step irreversibly converted to keto form *via* enol to keto tautomerization, which in turn helps in bringing chemical stability in the framework. It was believed that the basicity of the imine nitrogen atoms plays a very crucial behind this enol-keto tautomerization. The imine nitrogen atoms when coming in a close proximity of acidic phenolic –OH, it rapidly abstracts the proton and results in this type of tautomerization. However, such tautomerism even exists in simple *N*-salicylideneanilines, however, here enol form is found to be more stable (**Figure 1.17**) [1.35f]. It is to be noted that, two competing effects such as i) aromaticity and ii) basicity of imine nitrogen (–C=N–) atom over phenolic oxygen (O–H) atom decide the final

stable form of the products. As for example in the case of monosubstituted *N*-salicylideneanilines, the aromaticity is more dominating over the imine nitrogen basicity which restricts tautomerization hence the final product exists in enol form.

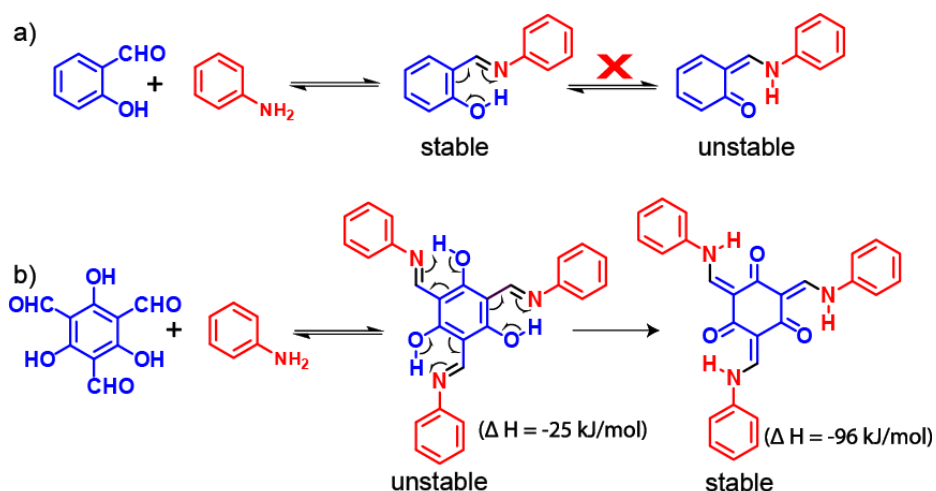


Figure 1.17. (a) Tautomerism in simple *N*-salicylideneanilines where enol-form is more stable than its keto form. (b) Tautomerism form is stable when basicity of nitrogen atoms collectively dominates over the aromaticity.

In contrast, in the case of tris(*N*-salicylideneaniline) derivatives, the basicity of three imine nitrogen atoms which collectively dominates over the aromaticity, as a result, the equilibrium finally shifts completely to right to stabilize the keto-form. Once the keto form dominates, the equilibrium has no choice to revert back to enol form even after heating the sample to any high temperature and hence this transformation can be accepted as a completely irreversible process.

In the year 2014, Kandambeth *et al.* again introduced a new strategy of intramolecular hydrogen bonding in imine based COFs, by which crystallinity, porosity and chemical stability of the frameworks were synergistically improved [1.35g]. In their study, the porphyrin-based ligand (5,10,15,20-Tetrakis(4-aminophenyl)-21H,23H-porphine) [C_4 symmetric] and 2,5-dihydroxyterephthalaldehyde [C_2 symmetric] was strategically used and through C_2+C_4 symmetric combination it produced a tetragonal symmetric 2D COF **DhaTph** structure (**Figure 1.16b**). The synthesized COF gets stabilized in enol-imine structure whereas the presence of hydroxyl ($-OH$) functionality plays a very important role in improving the crystallinity, porosity and chemical stability of the COF through H-bonding interaction. The hydroxyl functionality ($-OH$) close to the imine nitrogen ($-C=N$) atom undergoes an intramolecular H-bonding ($O-H\dots N=C$) interaction. The intra-molecular

hydrogen bonding could lock the phenyl ring rotation and improve the COF layers' planarity, thus could enhance the π - π layer stacking and dramatically improve in the crystallinity and porosity of overall COF frameworks. The surface area compared to a non-substituted porphyrin core based COF (COF-366) is almost doubled in **DhaTph** ($1300 \text{ m}^2\text{g}^{-1}$). In addition, COF-**DhaTph** displayed an increment in chemical stability where it could retain its crystallinity even after treatment in acid (3M HCl) and in water. It was believed that the intramolecular H-bonding reduces the lone pair availability of imine nitrogen ($-\text{C}=\text{N}$) atom towards proton and hence could protect the framework from being degraded in acidic medium.

The latest in 2015, Donglin Jiang's research group came up with some new methodology to stabilize imine linked COFs (**Figure 1.18a**) [1.35h]. They have introduced a new strategy to stabilize imine linked COFs through the introduction of $-\text{OMe}$ (methoxy) functional group within the COF matrix. Herein, they have used 1,3,5-Tris(4-aminophenyl)benzene (**TAPB**) as an amine and 2,5-dimethoxyterephthaldehyde (**DMTA**) as an aldehyde as a source of methoxy functional groups. The as-synthesized material showcased exceptionally high chemical stability towards acid (12M HCl), base (14M NaOH), boiling water and in various protic and aprotic solvents. The surface area of the material varies in the range 2105 (as synthesized), 2074 (base), 2081 (acid) and 2020 (boiling water) before and after chemical treatment for one week. The crystallinity and residual weight percentage ($> 60 \text{ wt}\%$) of the material were found to retain almost in every medium (**Figure 1.18a**). Based on their experimental evidence and theoretical calculations, they have explained the probable reason behind this enormous stability. It was stated that the one hexagon COF pore consists of 12 ' $-\text{C}=\text{N}-$ ' bonds. Based on the electronegative difference the carbon atom bear ' δ^+ ' charge and the N atom affords ' δ^- ' charge (**Figure 1.18a**). As a result, there exist electrostatic repulsion between the successive layers in their eclipsed conformation. Therefore, the π - π stacking interaction among the layers gets hampered due to charge repulsion among the layers. In the COF TPB-DMTP the $-\text{OMe}$ (methoxy) functional group, present in the aldehyde, plays a very crucial role in stabilizing the COF layers through its electron donating property ($+\text{R}$ effect). The lone pair of oxygen atom gets involved in the resonance with adjacent phenyl ring and further proceeds through imine linkages and thus the static electronic charge on imine bond now gets stabilized through resonance effect. Finally, this charge stabilization softens the interlayer repulsion and bound the layers very much tightly. Hence, the resonance effect stabilizes the COF structures from being a rapid attack from acid, base or water molecules.

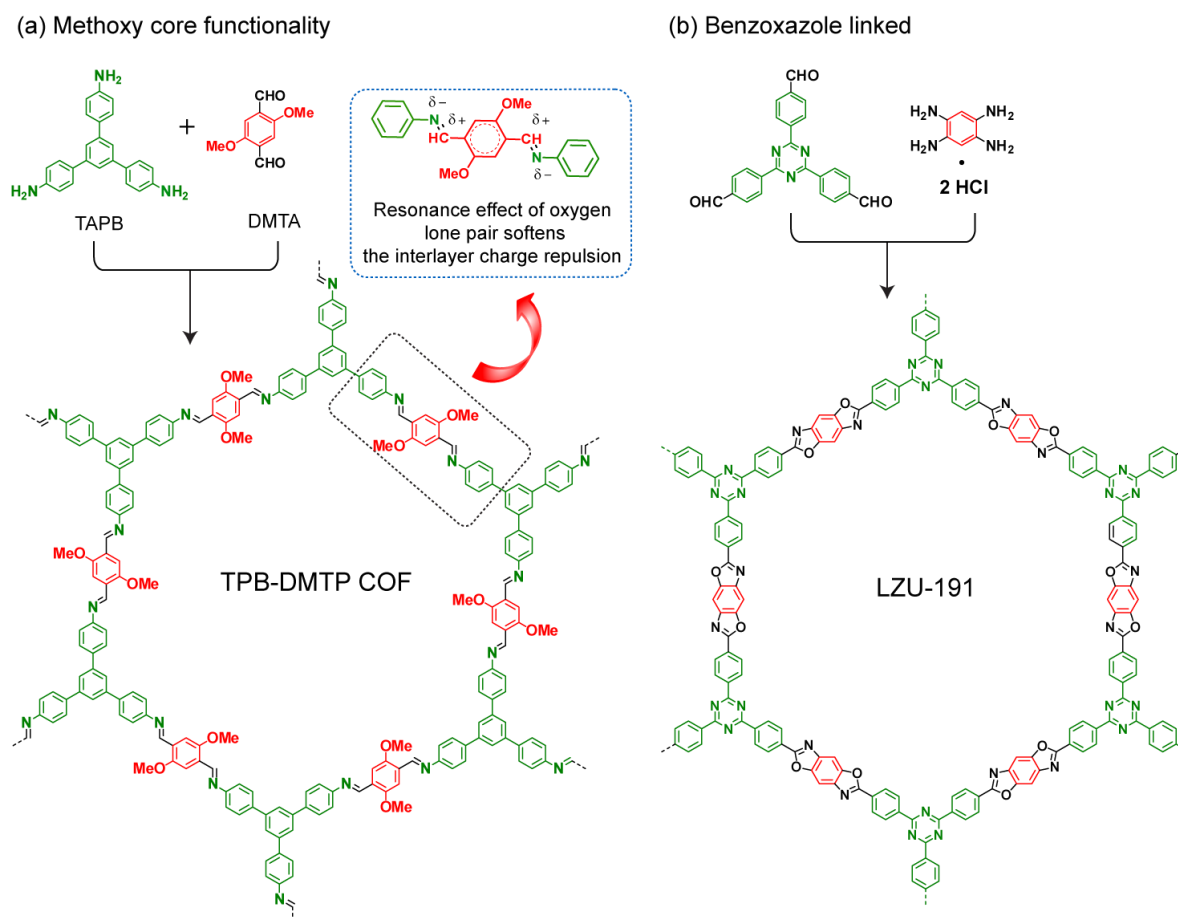


Figure 1.18: (a) Synthesis of TPB-DMTP-COF from DMTA and TAPB through Schiff base reaction. Inset: The structure of the edge units of TPB-DMTP-COF and the resonance effect of the oxygen lone pairs that weaken the polarization of the C=N bonds and soften the interlayer repulsion in the COF. (b) Synthetic scheme for benzoxazole linked COF LZU-191.

Very recently, in 2018, Wei *et al.* developed a chemically stable benzoxazole linker strategy for the construction of chemically stable COFs (**Figure 1.18b**). They have constructed a series of benzoxazole-based COFs LZU-190, LZU-191 and LZU-192 *via* formation of benzoxazole rings through reversible/irreversible cascade reaction whereas the material exhibit exceptionally high chemical stability in strong acid (9M HCl), bases (9M NaOH) and sunlight [1.35i]. The COFs were synthesized solvothermally at 185 °C (1:1; NMP-Mesitylene) in sealed ampules using 2,5-diamino-1,4-benzenediol as a common precursor and was allowed to react with three different aldehydes such as 1,3,5-triformylbenzene (for LZU-190), 2,4,6-tris(4-formylphenyl)-1,3,5-triazine (for LZU-191), and 1,3,6,8-tetrakis(4-formylphenyl)pyrene (for LZU-192). The benzimidazole was used as a common additive in every reaction which acts as a dehydrating and templating agent. The overall product formation was associated with three different steps such as 1) formation of imine (–C=N–)

bond intermediate, b) abstraction of hydroxyl (-OH) proton by benzimidazole and ring closure and c) removal of water and subsequent aromatization to form benzoxazole ring. Moreover, because of aromaticity, benzoxazole ring was highly stable and the overall COF exhibits high structural robustness even in abrasive conditions.

Though all of these attempts have their own fate to develop COFs with enhanced chemical stability, however, all these approaches suffer from few serious drawbacks such as a) tedious synthetic hurdles (solvothermal process), b) material produced only in mg scale, c) powdered form of as-synthesized COFs restricts the processability and limits its further applications.

However, in the year 2017 Kandambeth *et al.* and Karak *et al.* developed a new methodology of mechanochemical COF synthesis using *p*-toluenesulfonic acid (PTSA) a water reservoir and a molecular organizer entity during COF crystallization. Using this strategy, a series of β -ketoenamine COFs were synthesized in less than an hour while maintaining its high crystalline and porous nature. Again, using this unique fabrication technique, not only the COF could be synthesized in industrial scale but also the material with desirable forms. Herein, for the first time, the COF has been fabricated in the form of a membrane and was utilized in water purification. It is to be noted that, this is the first reports in the literature where the rapid scalability and easy processability of the COF material have been discussed [1.35c]. However, the entire methodology was completely restricted for the construction of β -ketoenamine COFs which are chemically stable under certain experimental conditions. Hence, a generalization of a similar strategy for the construction of the other COFs borrowing different linkages such as boronic acid, imine, triazine is yet to be explored.

1.10 Morphology of COF crystallites

COFs are usually precipitated as microcrystalline powders, with particle size mostly in the nanometer to micrometers region. The various internal defects during crystal growth are responsible for limiting COF crystallite size in the nanometer range. Li-Jun Wan and coworkers have done a detailed structural investigation on COF crystallites growth using STM imaging technique at different time span [1.33c]. For this, initially, they have drop cast the starting precursor materials on HOPG surface and the whole setup was heated in a closed chamber. The STM images show although there is a formation of COF on the HOPG surface the COF crystallites formation happened as an island and it was very difficult to have a complete surface coverage (coating) with COFs. The main reason was the presence of several internal defects during the COF film formation which limits its growth in larger domains.

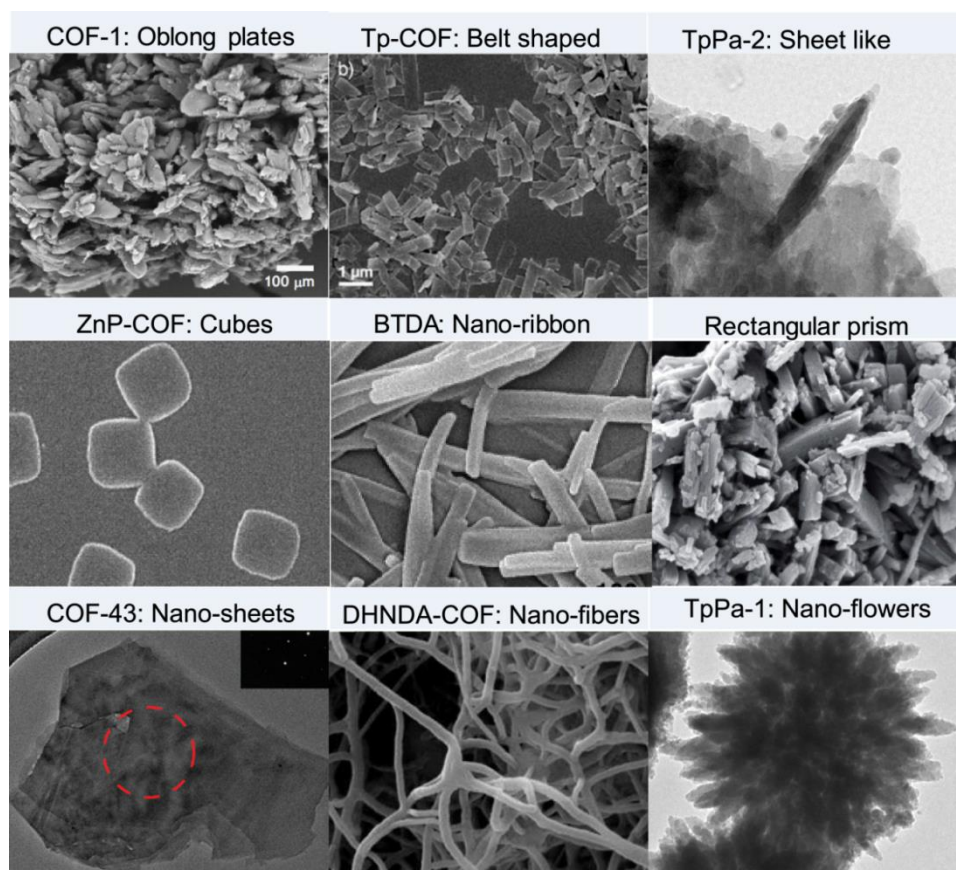


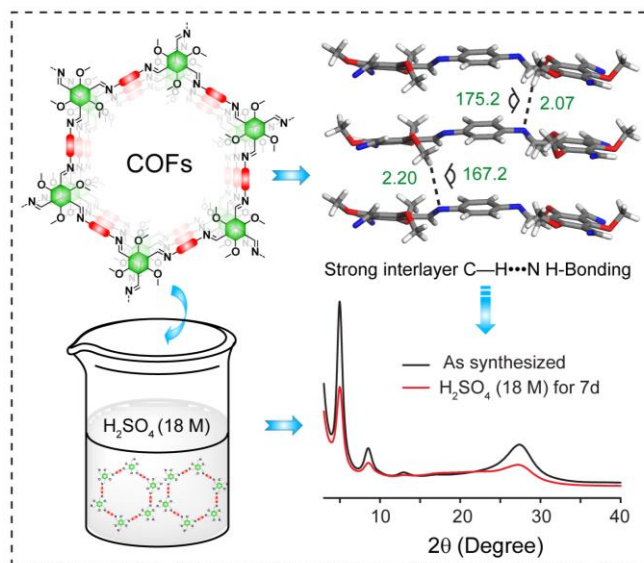
Figure 1.19: Various Morphologies of COF crystallites reported in the literature.

So depending on the reaction conditions and used starting materials COF crystallites are found to adopt various shapes such as fibers [1.36b], sheets [1.35], cubes [1.45a], belts [1.45b], rectangular prism [1.22a] and more recently hollow sphere (**Figure 1.19**) [1.35d]. However, the exact reason behind the evolution of such morphology in nano-domain still remains a mystery. Notably, specific morphological evaluation and development are highly important in the applications such as drug delivery, charge carrier, molecular adsorption, catalysis, and mobility etc. [1.36c]. Although some reports have investigated time-dependent morphological evolution based on crystallites self-assembly, however, morphological control of COF crystallites depending on their molecular level structures of the precursor materials, have been poorly explored.

CHAPTER 2

Ultra-stable Covalent Organic Frameworks: A Role of Interlayer Hydrogen Bonding

Abstract: In this chapter, we presented a novel strategy by which a series of chemically stable imine-based ($-C=N-$) Covalent Organic Frameworks (COFs) can be synthesized. Imine-based COFs, in general, are unstable to water, acids or bases since they are synthesized by the reversible organic reaction. Our strategy involves the synthesis of chemically stable imine-COFs introducing interlayer $C-H\cdots N$ H-



bonding between the methoxy ($-OCH_3$) $C-H$ of a particular layer with the imine ($-C=N-$) nitrogen atoms present in the adjacent layers. Such interlayer $C-H\cdots N$ H-bonding provides enough steric hindrance and the hydrophobic environment around the imine bonds and protects them from being hydrolyzed in abrasive conditions like strong acids (H_2SO_4 , 18 M; HCl , 12 M) or bases ($NaOH$, 9 M). The present synthetic strategy also provides the opportunity for the rapid production of imine-based COFs in industrial scale.

2.1 Introduction

Covalent Organic Frameworks (COFs) are pristine sets of periodically ordered 2D or 3D networks generally contrived through simultaneous polymerization and crystallization of monomeric building blocks made up of light elements such as B, C, N, O, Si etc [2.1]. Since their invention, COFs has drawn significant potential interest to the scientific community in accounts of their widespread applications such as gas storage and separation, energy storage, proton conduction, catalyst support etc [2.2]. These structurally predesigned frameworks ensue similar avenue of reticular chemistry and their crystallization process exhibit dynamic reversible reactions such as boronic acid trimerization, boronate ester formation, Schiff base formation, etc [2.3]. Therefore, the reversible nature of chemical bonds enables them up to limited chemical stability and restricts these novel materials for proper practical implementations. Hence, the design and synthesis of porous crystalline COFs with chemically robust backbone against abrasive environment including drastic humidity, strong acidity or basicity is a key challenge for the modern researcher.

To enhance the air or water stability of the 2D COFs few attempts have been made previously in the literature. The strategies, such as pyridine vapor doping at Lewis acid boron centers [2.4b] and COF pore walls functionalization with alkyl groups [2.4c], were employed to enhance the chemical stability specifically of boronate ester based COFs. Although, these two approaches could enhance slight framework stability; this cannot be considered as ultimate stabilization strategy as the incorporation of such stabilization groups/reagent dramatically decrease active surface area and thus gas storage capacities of COFs. Hence, there is always a high demand for designing and developing new strategies for improving the chemical stability of COFs without affecting its porosity or surface area.

Taking this into consideration, in 2012 Kandambeth *et al.*, to overcome the stability issues in COFs, introduced the enol to keto tautomerization (β -keto-enamine COFs) phenomenon during the framework crystallization. By using this approach, they could synthesize a set of COFs with significantly enhanced chemical (aqueous, acid and base) stability [2.4a]. However, this idea was entirely restricted to β -keto-enamine COFs, which provides minimal substrate scope thus was limited in their widespread exploration. Other approaches such as intralayer H-bonding [2.4d], channel wall functionalization with methoxy ($-\text{OCH}_3$) groups [2.4e], the introduction of benzoxazole linkages [2.4f] were also performed to enhance the

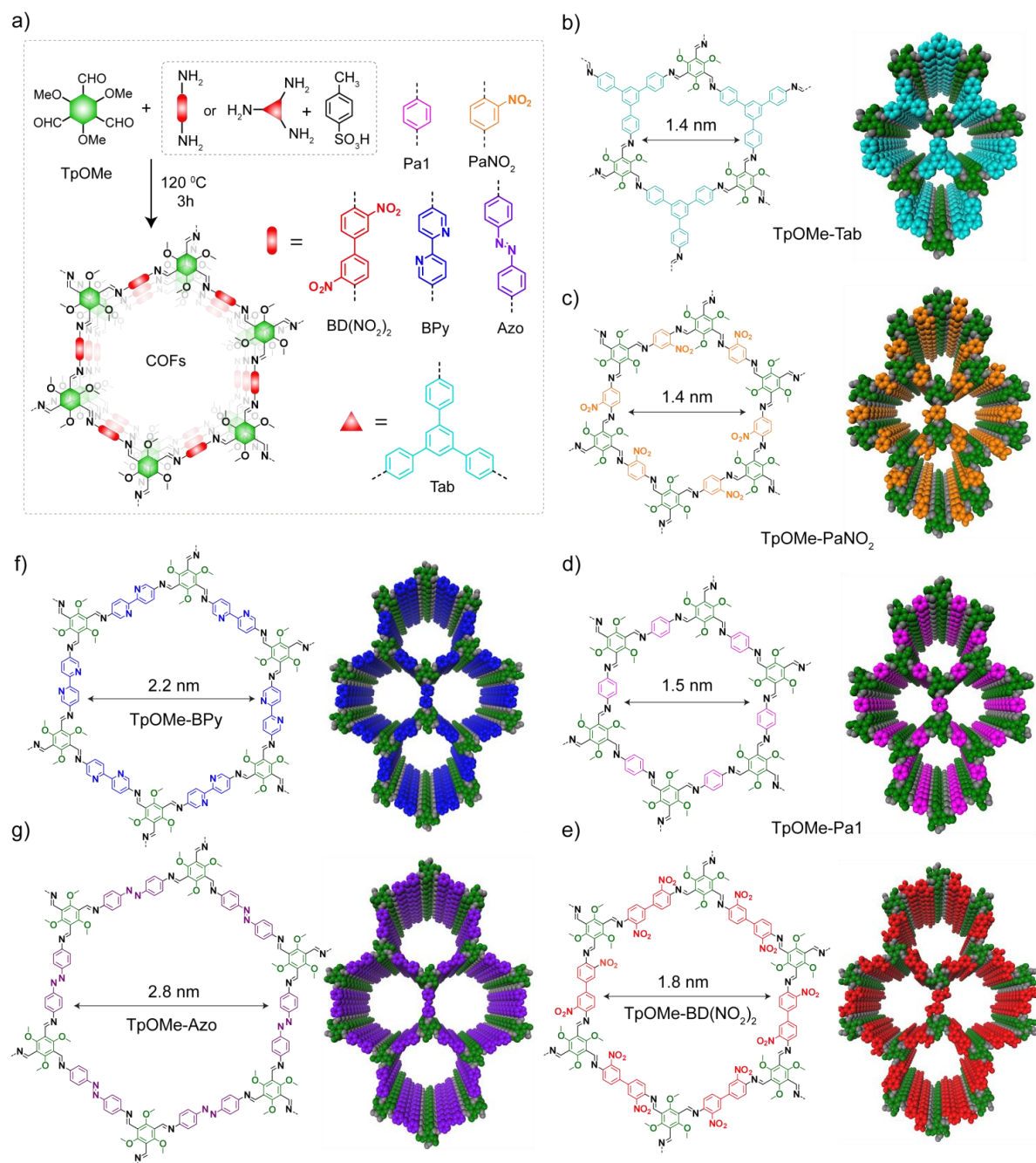


Figure 2.1: (a) Schematic representation of the synthesis of highly stable **TpOMe-X** COFs by using Schiff base condensation between **TpOMe** aldehyde with six different amines. (b-f) chem. draw and space filling (eclipsed) structures of all COFs. Pore diameter has shown with a double-headed arrow.

framework stability. However, although previous attempts could solve the stability issues to some extent it suffers from serious drawbacks such as- 1) as-synthesized COFs are produced only in powdered form hence not processable, 2) involves tedious synthetic hurdles

(solvothermal sealed tube method; required high temperature and longer time), and 3) limited to mg scale production of COFs. Hence, it is very essential to solving those obstacles in COFs for its intended development and potential applications. On the other hand, the development of imine-based COFs has increased dramatically in recent years owing to their superior hydrolytic stability compared to boronic acid COFs along with their extensive substrate-library availability [2.6] hence are more versatile to explore. However, for the widespread implementation of such chemically stable imine based COFs, the synthetic process should: 1) be a greener approach of synthesis i.e. be devoid of toxic solvents or synthetic difficulty [2.5], 2) be rapid and easily scalable (unlike the traditional solvothermal process) to industrial level, [2.7] and 3) provide the opportunity to process the as-synthesized COFs into pellets, beads as well as membranes keeping their properties intact [2.5].

Keeping all these in perspective, herein, we introduce 2,4,6-trimethoxy-1,3,5-benzenetricarbaldehyde (**TpOMe**) as a prime aldehyde building unit for scalable and rapid construction of a series of chemically stable imine-linked COFs via the PTSA (*p*-toluenesulfonic acid) mediated solid-state mixing approach (**Figure 2.1**) [2.5]. The introduction of three bulky methoxy ($-\text{OCH}_3$) groups adjacent to the aldehyde ($-\text{CHO}$) functionalities provide significant steric hindrance and the hydrophobic environment around the imine bonds, promotes impregnable COF crystallization. These as-synthesized materials showcased exceptionally high chemical stability in H_2SO_4 (18 M), HCl (12 M), NaOH (9 M), boiling water and common organic solvents, for several days. To the best of our knowledge, this is the first report illustrating a series of imine based COFs with exceptionally high chemical stability in a drastic medium such as conc. H_2SO_4 (18 M). Calculations with density functional theory reveal the presence of significant numbers of interlayer C–H \cdots N H-bonding [2.8] between the methoxy ($-\text{OCH}_3$) C–H of a particular layer with the imine ($-\text{C}=\text{N}-$) nitrogen atoms present in the adjacent layers. The interlayer C–H \cdots N H-bonding provides enough steric hindrance and hydrophobic crowding around the imine bonds and protects them from being hydrolyzed in such abrasive environment. Additionally, the preferred approach provides the opportunity to process the materials into desirable forms hence reflecting its broad scope applications.

2.2 Synthesis of ultra-stable covalent organic frameworks

2.2.1 Synthesis and characterization

COF- TpOMe-X (X= Pa1, PaNO₂, BD(NO₂)₂, BPy, Azo, and Tab): *P*-toluenesulfonic acid monohydrate (PTSA-H₂O) (1.8 mmol) was mixed separately with 6 different amines in a mortar-pestle. The amount of amines were taken as **Pa1** (0.45 mmol; 48.6 mg), **PaNO₂** (0.45 mmol; 68.8 mg), **BD(NO₂)₂** (0.45 mmol; 123.3 mg), **BPy** (0.45 mmol; 83.7 mg), **Azo** (0.45 mmol; 95.4 mg) and **Tab** (0.3 mmol, 105.3 mg).

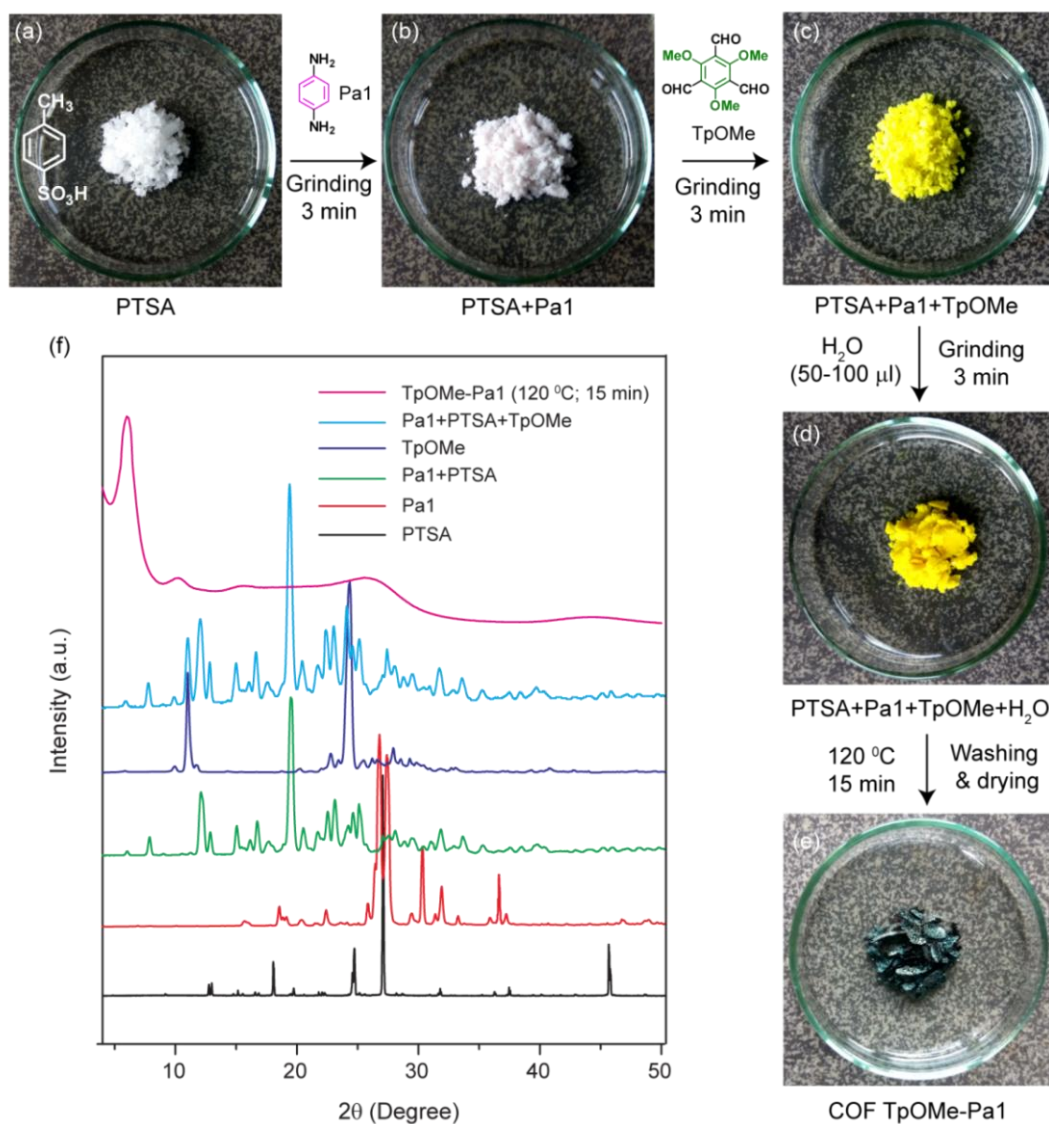


Figure 2.2: (a-e) Schematic representation of COF **TpOMe-Pa1** synthesis. (f) Comparison of PXRD patterns of **TpOMe-Pa1** COF with starting materials at a different stage of the reaction.

The mixture was uniformly grinded for 5 minutes. In that mixture 2,4,6-trimethoxy-1,3,5-benzenetricarbonyl aldehyde (**TpOMe**, 0.3 mmol, 76.2 mg) was added and properly mixed through grinding. To this mixture few drops of water (~100 μL based on requirement) was added. The resulting mixture was then grinded properly until it becomes dough-like material and was additionally allowed to heat at 120 $^{\circ}\text{C}$ for 3 hours or 90 $^{\circ}\text{C}$ for 12 h. After completion, the resulted material was deepened into hot water followed by washing with *N,N*-dimethylacetamide, and acetone to afford resulted in crystalline porous COFs with approx. 85 % (wt%) isolated yield (**Figure 2.2**).

The PTSA mediated solid-state mixing approach has opened up a new route for rapid and bulk scale production of highly crystalline porous COFs, along with a broad opportunity for easy processability of the synthesized material in desirable Forms [2.5]. However, the exploration of the PTSA mediated solid-state mixing approach is not straightforward for the construction of imine linked COFs. The primary concern is the chemical stability of the as-synthesized frameworks under the given reaction conditions. Owing to the intense acidic nature of PTSA ($pK_a = -2.8$; water), the imine-linked COF crystallites, during the framework formation, readily decompose under the experimental conditions leading to high extent of amorphization (**Figure 2.3, 2.4 and 2.5**).

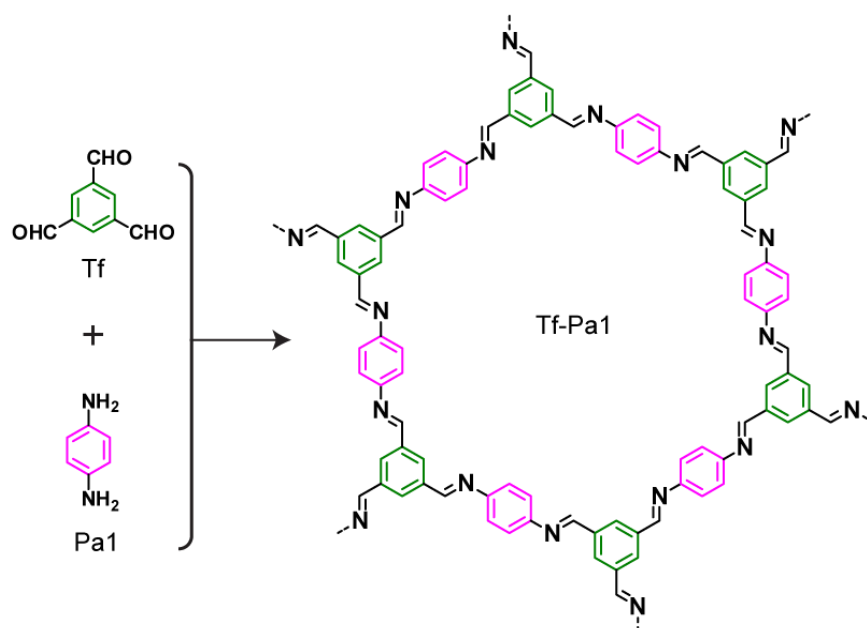


Figure 2.3: General scheme for the construction of **Tf-Pa1** from **Tf** (1,3,5-triformylbenzene) aldehyde and **Pa1** amine.

This makes it profoundly challenging to design suitable linker units to yield the crystalline porous COFs under the aforementioned synthetic conditions. We made a prediction that the synthesis of imine-linked COFs using this approach can only be achieved by providing enough steric hindrance around the imine bonds or by incorporating significant hydrophobic environment to protect it from H^+ and H_2O attack during the COF crystallization.

COF Tf-Pa1: The similar procedure (i.e. TpOMe-X COFs synthesis) was followed for Tf-Pa1 COF synthesis. *P*-toluenesulfonic acid monohydrate (PTSA- H_2O) (1.8 mmol) was mixed with **Pa1** (0.6 mmol; 64.8 mg) and the mixture was uniformly grinded for 5 minutes. In that mixture 1,3,5-benzenetricarbaldehyde (**Tf**, 0.4 mmol, 64.8 mg) was added and properly

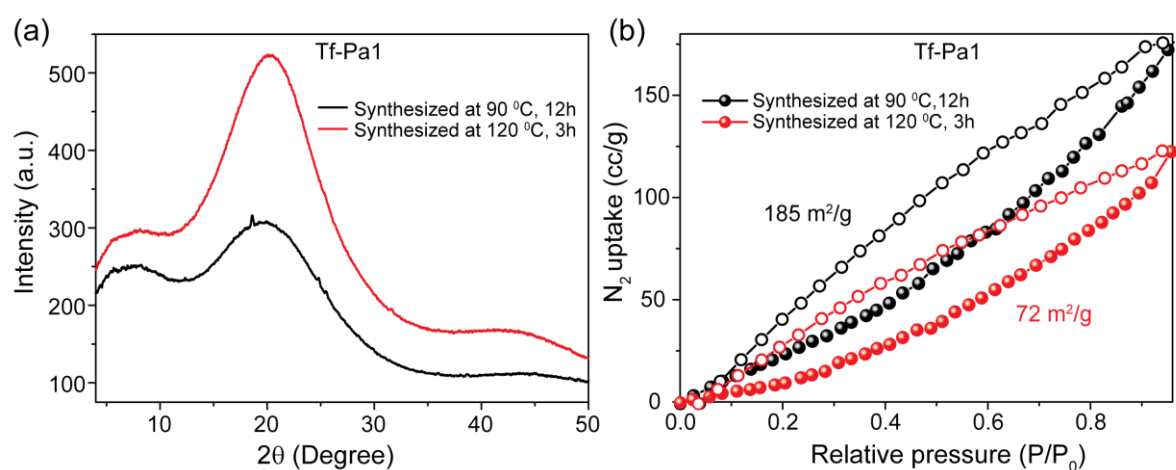


Figure 2.4: (a) PXRD and (b) N_2 adsorption isotherms for **Tf-Pa1** at two different reaction conditions.

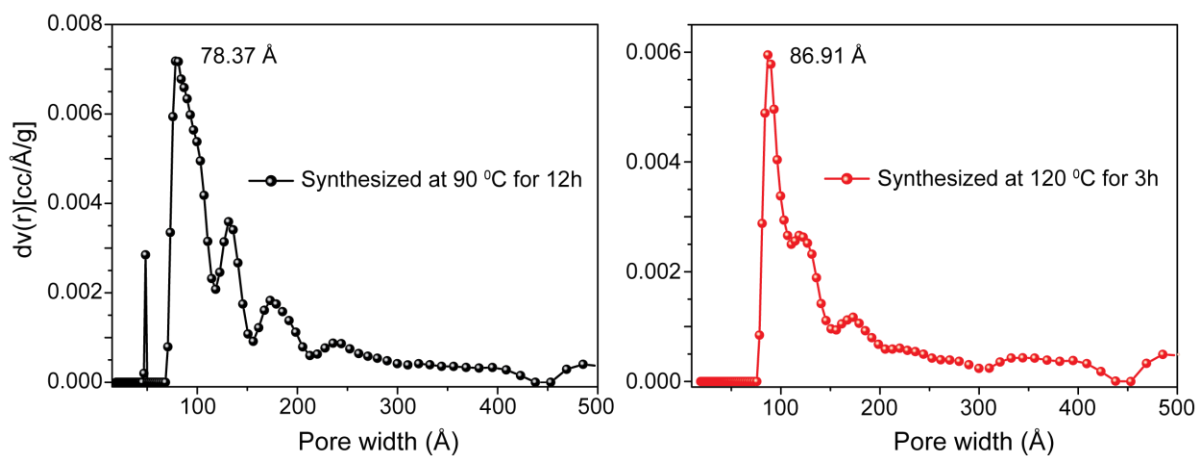


Figure 2.5: Experimental Pore size distribution of **Tf-Pa1** [N_2 at 77 K on carbon (cylinder./sphere pores, QSDFT adsorption branch)] at two different reaction condition.

mixed through grinding. To this mixture few drops of water ($\sim 50\mu\text{L}$) was added. The resulted mixture was then grinded properly and was equally poured in six different vials. Five of them were allowed to heat separately at $120\text{ }^\circ\text{C}$ for 15 min, 30 min, 45 min, 1 h and 3 h. Another one was kept at $90\text{ }^\circ\text{C}$ for 12 h. After completion, the vials were cooled at room temperature followed by washing with water for 2-3 times. It was then washed with tetrahydrofuran (THF) till any unreacted starting material or polymeric impurities washed out completely showing clear solution on top of the residue. Most of the material washed out during THF washing and for 15 min to 1h reaction mixture, no appreciable material was recoverable for further characterization.

The residue was collected for 3h at $120\text{ }^\circ\text{C}$ and 12 h at $90\text{ }^\circ\text{C}$ samples after vacuum dried at $60\text{-}90\text{ }^\circ\text{C}$. Again, the yield of the resulted compound was $< 10\text{ wt}\%$. The PXRD analysis reveals the material is completely amorphous and it shows maximum $185\text{ m}^2/\text{g}$ surface area from N_2 adsorption isotherms (**Figure 2.4**). The experimental pore size distribution also reflects no characteristics of a COF material (**Figure 2.5**). This observation clearly indicates Tf-Pa1 COF has not at all formed in the given experimental condition.

2.2.2 Structural simulation and characterization

Since COFs are synthesized as polycrystalline powder, powder X-ray diffraction (PXRD) is used for determining the crystallinity and investigating the structural details of the material. The formation of **TpOMe-Tab**, **TpOMe-PaNO₂**, **TpOMe-Pa1**, **TpOMe-BD(NO₂)₂**, **TpOMe-BPy** and **TpOMe-Azo** was confirmed by their PXRD patterns (**Figure 2.6**). All the COFs mainly showed distinct peaks corresponding to the 100, 110 and 001 plane in their PXRD patterns. The high-intensity peak at $\sim 4.8^\circ$ (± 0.1 , 2θ), for **TpOMe-Pa1** and **TpOMe-PaNO₂** COFs, could be assigned to the reflections from their 100 planes. In the case of **TpOMe-BD(NO₂)₂** and **TpOMe-BPy** high intense peaks attributed to the 100 planes arise at $\sim 3.6^\circ$ (± 0.1 , 2θ). The **TpOMe-Azo** (with highest pore diameter in the series) and **TpOMe-Tab** (having lowest pore diameter) showed their 100 plane reflections at $\sim 3.3^\circ$ (2θ) and $\sim 6.1^\circ$ (2θ), respectively. The high intensity of 100 planes in all the COFs indicated their highly crystalline nature. All the COFs revealed their 001 plane reflections at $\sim 27.1^\circ$ (± 0.2 , 2θ) in the PXRD patterns.

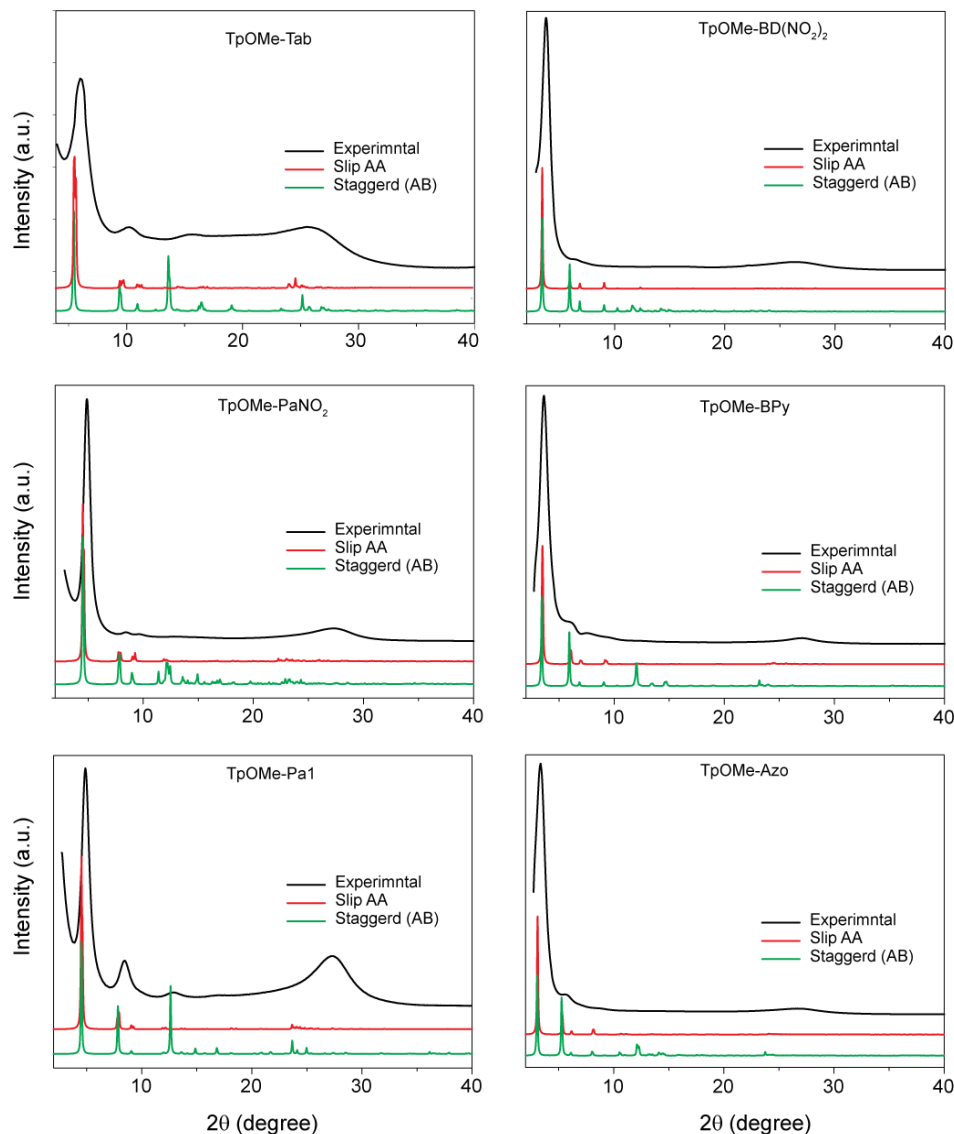


Figure 2.6: (a) PXRD patterns of as-synthesized (black) compared with the slip-AA (red) and Staggered (green) of all TpOMe-X ($X = \text{Tab}, \text{Pa1}, \text{PaNO}_2, \text{BD}(\text{NO}_2)_2, \text{BPy}$ and Azo) COFs.

To find the interlayer stacking constitutions; different model (eclipsed, slipped eclipsed and staggered) structures were simulated by using Materials Studio [2.9]. The experimental PXRD pattern fits well [**TpOMe-Tab** ($R_p = 0.9\%$, $R_{wp} = 1.8\%$); **TpOMe-PaNO₂** ($R_p = 2.7\%$, $R_{wp} = 4.2\%$); **TpOMe-Pa1** ($R_p = 2.3\%$, $R_{wp} = 3.5\%$); **TpOMe-BD(NO₂)₂** ($R_p = 0.7\%$, $R_{wp} = 1.0\%$); **TpOMe-BPy** ($R_p = 1.5\%$, $R_{wp} = 2.4\%$) and **TpOMe-Azo** ($R_p = 2.1\%$, $R_{wp} = 2.9\%$)] with the simulated slipped eclipsed (AA) stacking models (**Figure 2.6 & 2.7**). The unit cell parameters of the synthesized COFs were further evaluated using Pawley refinement of the experimental PXRD patterns.

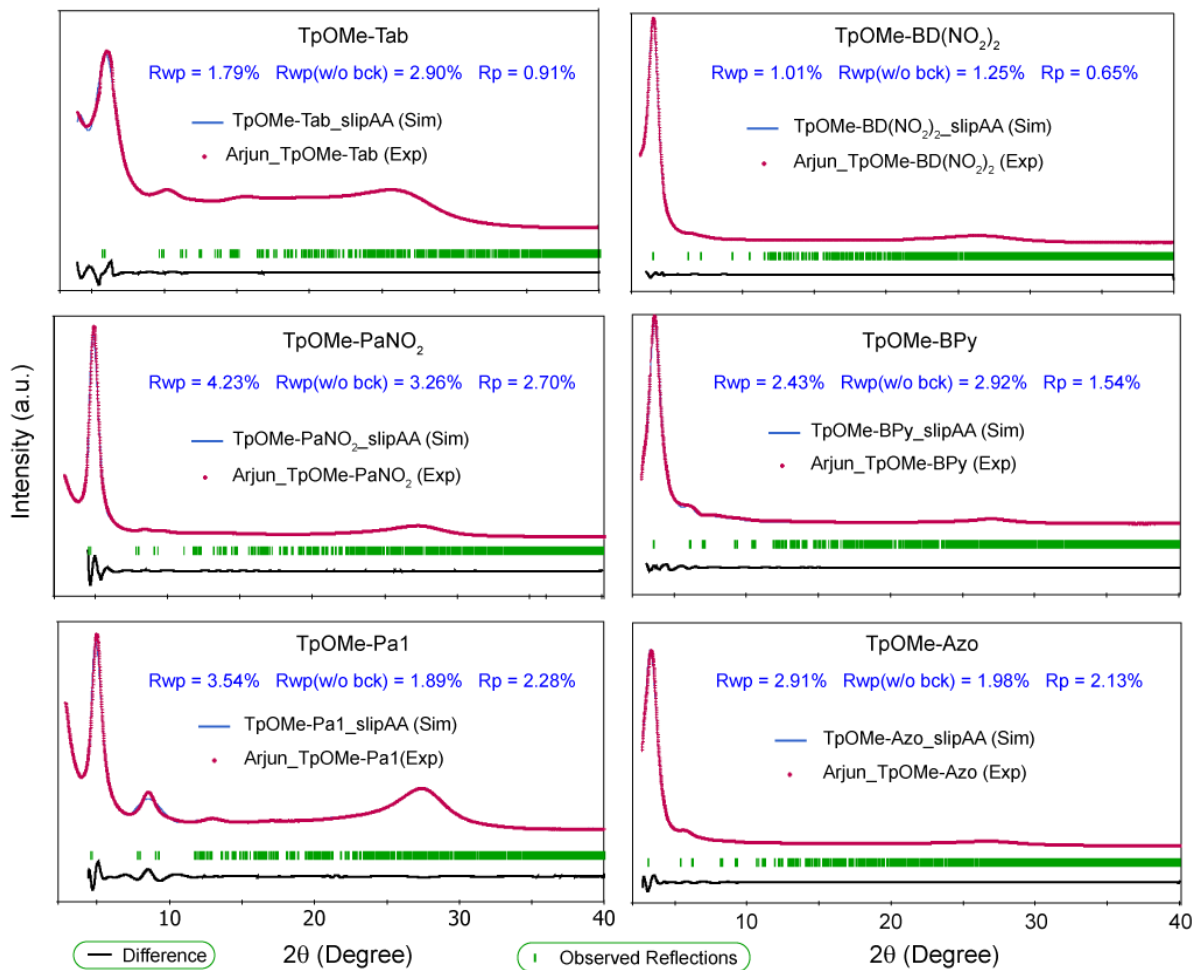


Figure 2.7. The experimental PXRD patterns (red) compared with the simulated (slip AA; blue) and Pawley refined difference (black) [R_p , R_{wp} and R_{wp} (w/o bck) have shown in the inset for all COFs].

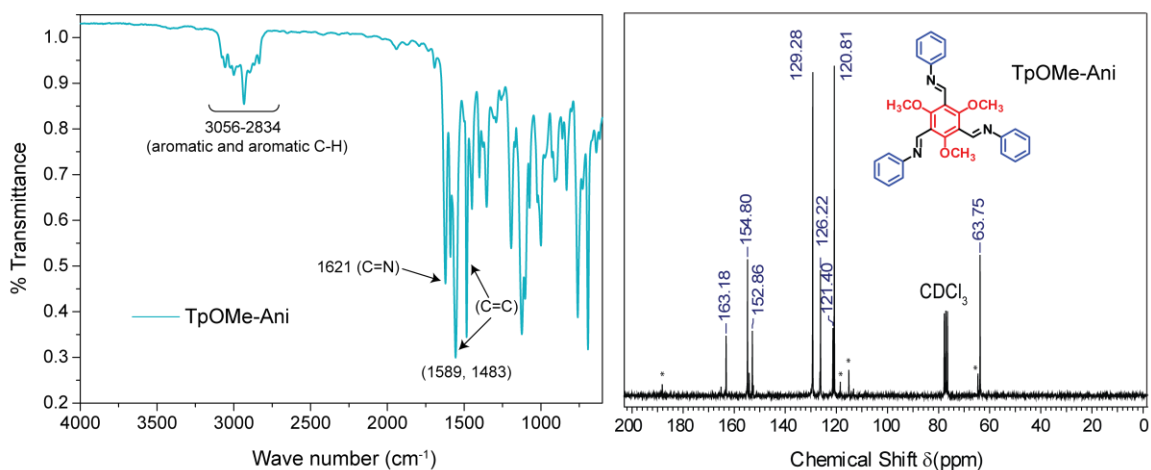


Figure 2.8: (left) FT-IR and (right) ^{13}C NMR spectra of as-synthesized **TpOMe-Ani** monomer.

2.2.3 Chemical characterization

The recorded FTIR spectra showed the complete disappearance of the primary N-H stretching frequency ($3188\text{--}3462\text{ cm}^{-1}$) of the parent amines as well as the C=O stretching frequency at 1682 cm^{-1} for the TpOMe aldehyde used for the synthesis in all COFs reported in this manuscript (**Figure 2.9**). The newly formed C=N bonds (obtained after the aldehyde-amine Schiff base reaction) exhibited stretching frequency in the range of $1574\text{--}1623\text{ cm}^{-1}$,

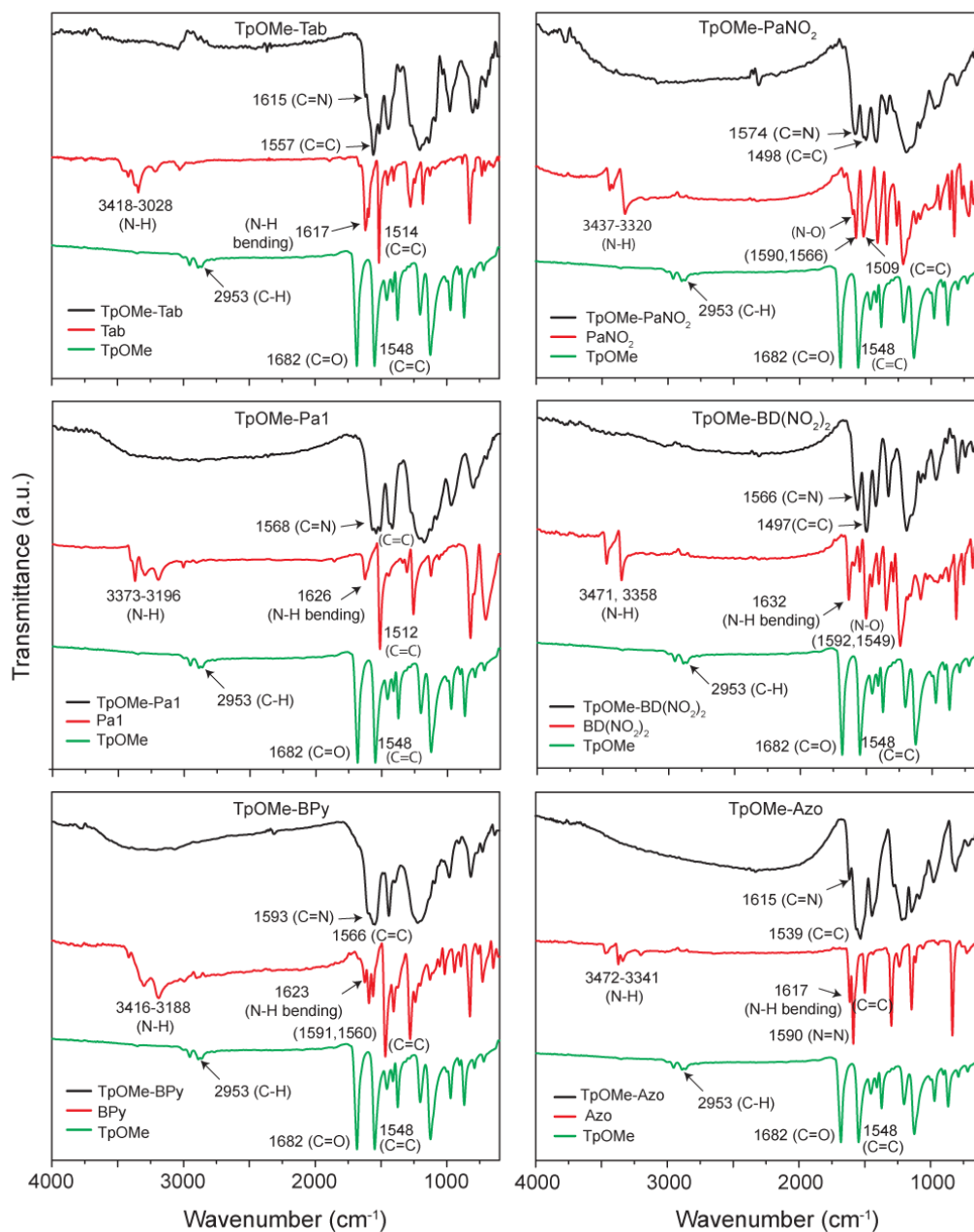


Figure 2.9: Comparison of FT-IR spectra of synthesized *TpOMe-COFs* with its starting materials

confirming the formation of imine bonds in the COFs and the full consumption of the starting materials. The synthesized reference compound **TpOMe-Ani** (prepared from TpOMe aldehyde with aniline) reflected $\text{C}=\text{N}$ stretching at $\sim 1621\text{ cm}^{-1}$ (**Figure 2.8**). The aromatic $\text{C}=\text{C}$ stretching arose around $\sim 1560\text{ cm}^{-1}$ (asymmetric) and $\sim 1498\text{ cm}^{-1}$ (symmetric) in the FTIR spectra in all the COFs. The reference compound showed the similar stretching frequency ~ 1555 and 1483 cm^{-1} , respectively.

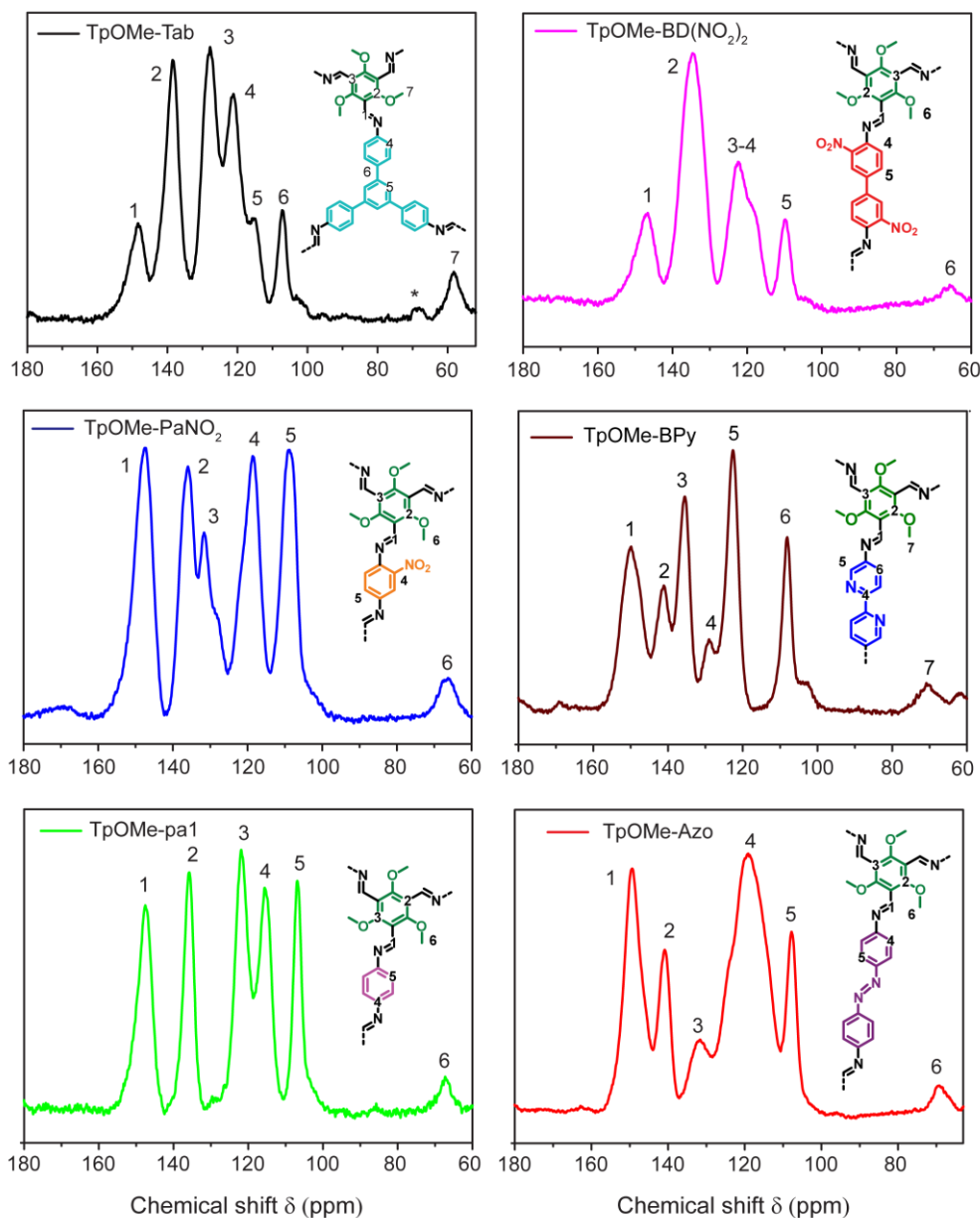


Figure 2.10: Solid state ^{13}C CP-MASS spectra of synthesized **TpOMe-COFs** (carbon atoms with probable chemical shift mentioned with numerical in Chem. Draw).

The overall compositions of the framework materials were further confirmed from solid-state ^{13}C cross-polarization/magic-angle spinning (CP-MAS) spectra, which revealed the main characteristics peak of imine ($-\text{C}=\text{N}-$) bonded carbon atom at ~ 148 ppm whereas the aromatic carbons showed their characteristic signals within the range ~ 53 -70 ppm (**Figure 2.10**). Similarly, the reference compound **TpOMe-Ani** exhibited the characteristics of imine and aromatic carbon signals at ~ 163 ppm and ~ 150 -115 ppm, respectively. Again, for **TpOMe-Ani** the signature of the methoxy ($-\text{OCH}_3$) carbon peak was observed at ~ 63 ppm, almost matching with the methoxy ($-\text{OCH}_3$) carbon signals associated with the reported COFs (**Figure 2.8**).

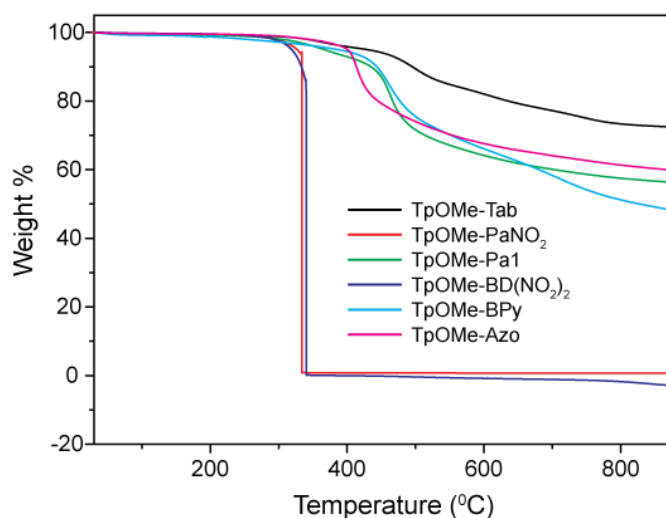


Figure 2.11: Thermogravimetric analyses (TGA) of **TpOMe-COFs**.

Thermogravimetric analyses (TGA) (N_2 atmosphere) of all the COFs showed their thermal stability in the range of 320 - 400 °C (**Figure 2.11**). However, **TpOMe-PaNO₂** and **TpOMe-BD(NO₂)₂** showed rapid weight loss (from 100wt% to almost 0 wt%) within the range of 330 - 340 °C. **TpOMe-Pa1** showcased the highest thermal stability in the series reflecting only 30 % weight loss even after being treated up to 900 °C.

A plausible explanation for rapid weight loss of TpOMe (-NO₂) based COFs during TGA: Both the COFs **TpOMe-PaNO₂** and **TpOMe-BD(NO₂)₂** exhibits rapid weight loss (from 100 wt% to almost 0 wt%) as revealed from their TGA profile within the range 330 - 340 °C. The plausible reason could be due to the presence of both $-\text{NO}_2$ (electron withdrawing) and $-\text{OMe}$ (electron donating) functionality at a time in the framework. These

two COFs are behaving as explosives, like 2,4,6-trinitrotoluene (which contain both electron withdrawing $-\text{NO}_2$ and electron donating methyl functionality), at high temperatures. Best on our understanding, it could be one of the possible reasons for having such unusual TGA profiles for these two COFs.

2.2.5 Gas adsorption studies

The permanent porosity of any porous material imparts crucial information about the internal ordering of pores in that particular material. This information is highly essential in membrane-based separation technologies. Hence, to evaluate the overall porosity of the COF materials reported in this paper, N_2 adsorption isotherms were recorded at 77 K (liq. N_2 temperature) in their completely activated state i.e. after treating the samples under vacuum (<1 torr pressure) and heating at 150°C for 12h. All the COFs showed rapid N_2 uptake at the comparatively lower pressure range $P/P_0 < 0.1$. Beyond this pressure, in the case of **TpOMe-Tab**, **TpOMe-PaNO₂**, **TpOMe-Pa1**, and **TpOMe-BD(NO₂)₂** COFs, the isotherms got almost saturated, reflecting their dominating micro-porous nature (**Figure 2.12**). **TpOMe-BPy** and **TpOMe-Azo**, on the other hand, showed a sharp steep between the pressure $P/P_0 = 0.10$ - 0.20 , exhibiting the ‘type-IV’ adsorption isotherm, which is the characteristic of mesoporous materials (**Figure 2.12**).

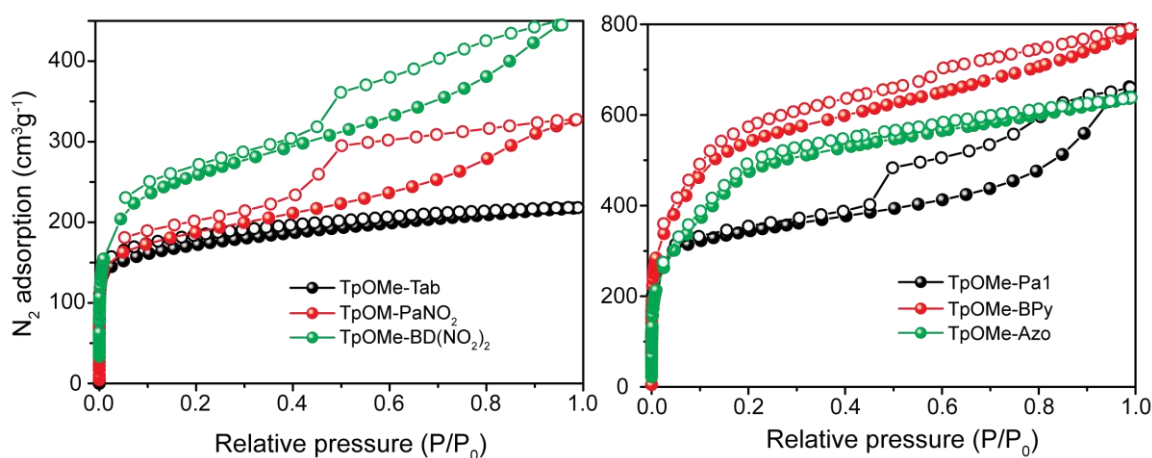


Figure 2.12: Nitrogen adsorption analysis isotherms of **TpOMe-COFs**.

Moreover, based on Brunauer–Emmett–Teller (BET) model **TpOMe-BPy** revealed the highest surface area of $2023\text{ m}^2\text{g}^{-1}$, followed by $1885\text{ m}^2\text{g}^{-1}$ for **TpOMe-Azo**, $1164\text{ m}^2\text{g}^{-1}$ for

TpOMe-Pa1, $913 \text{ m}^2\text{g}^{-1}$ for **TpOMe-BD(NO₂)₂**, $615 \text{ m}^2\text{g}^{-1}$ for **TpOMe-PaNO₂** and $593 \text{ m}^2\text{g}^{-1}$ for **TpOMe-Tab**. The experimental pore size distribution of **TpOMe-Tab**, **TpOMe-PaNO₂**, **TpOMe-Pa1** and **TpOMe-BD(NO₂)₂** COFs (calculated using the QSDFT model: cylindrical pore, adsorption branch), showed the pore width as 1.4, 1.4, 1.5 and 1.8 nm respectively (**Figure 2.13**). The pore diameter for **TpOMe-BPy** and **TpOMe-Azo** was determined as 2.2 and 2.8 nm respectively (**Figure 2.13**). Interestingly, we have tested these COFs for CO₂ uptake both at 0 °C and 25 °C where the **TpOMe-Azo** showed the highest CO₂ uptake of $87 \text{ cm}^3\text{g}^{-1}$ at 0 °C.

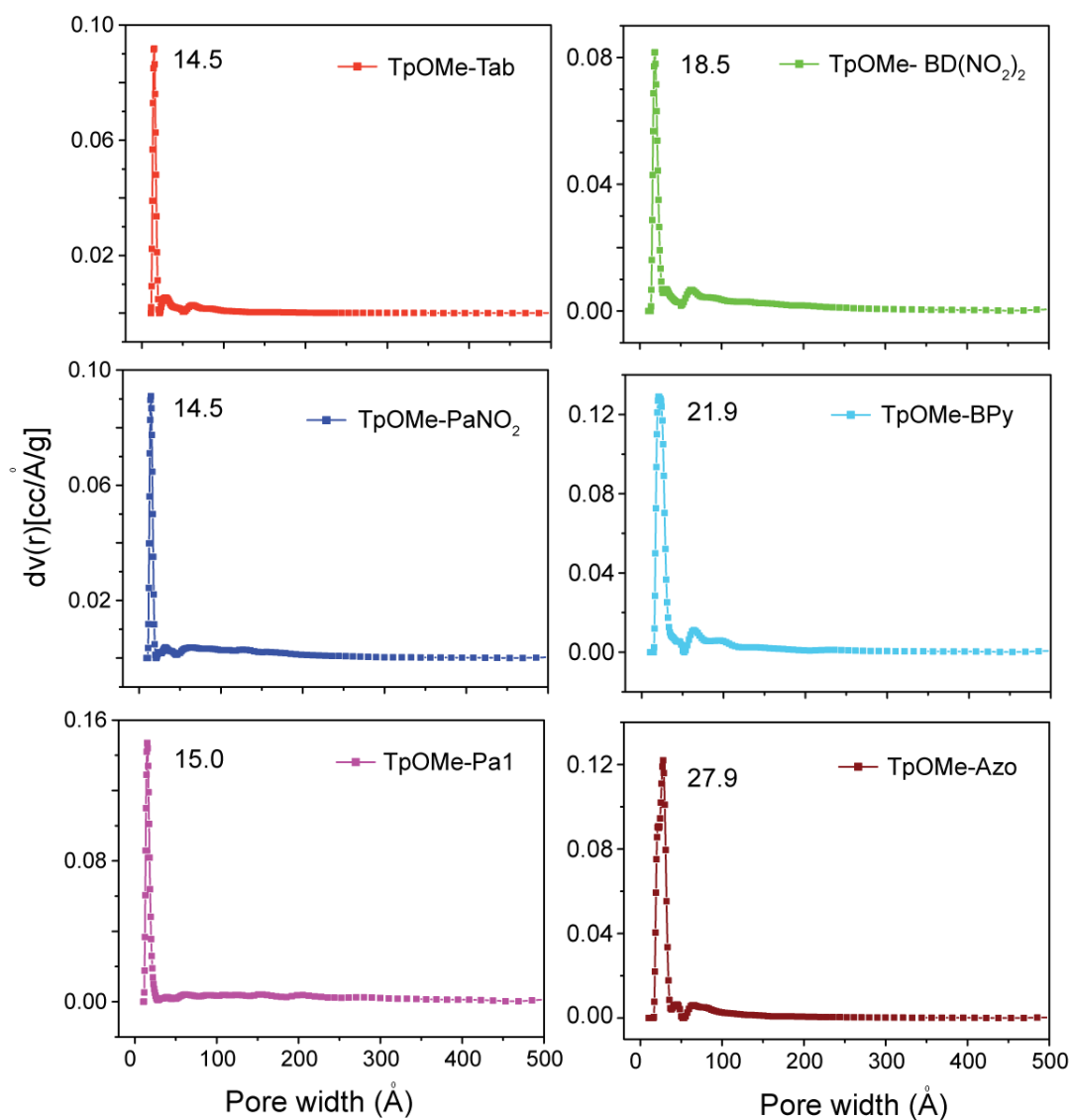


Figure 2.13: Experimental Pore size distribution of respected TpOMe COFs [N_2 at 77 K on carbon (cylindr./sphere pores, QSDFT adsorption branch)].

2.2.5 Chemical stability investigation

The extent of chemical stability of any material dictates its potentiality for extensive usage. Hence, to analyze the chemical stability here, the as-synthesized COF samples (20mg) were submerged in different types of solvents (2 ml) for 7 days. The chemical stability of the COFs was carried out in highly drastic media such as conc. H_2SO_4 (36 N), conc. HCl (12 N), NaOH (9 N, 24 h) and various protic/aprotic solvents including H_2O (boiling), MeOH, EtOH, CH_3CN , *N,N*-Dimethylformamide (DMF), Dimethylsulfoxide (DMSO), and Chloroform (CHCl_3). After the treatment, the material was collected and was washed thoroughly with water and DMAc (*N,N*-dimethylacetamide) followed by acetone, before it was vacuum dried to remove the trapped solvent molecules. The solvent stability, exclusively tested for COF **TpOMe-Pa1**, reported here, although show weight loss ~ 10 -15 wt% in boiling water, however, exhibit tiny weight loss (<0.1 wt%) in other protic or aprotic solvents almost retaining its crystallinity and porosity (**Figure 2.14**).

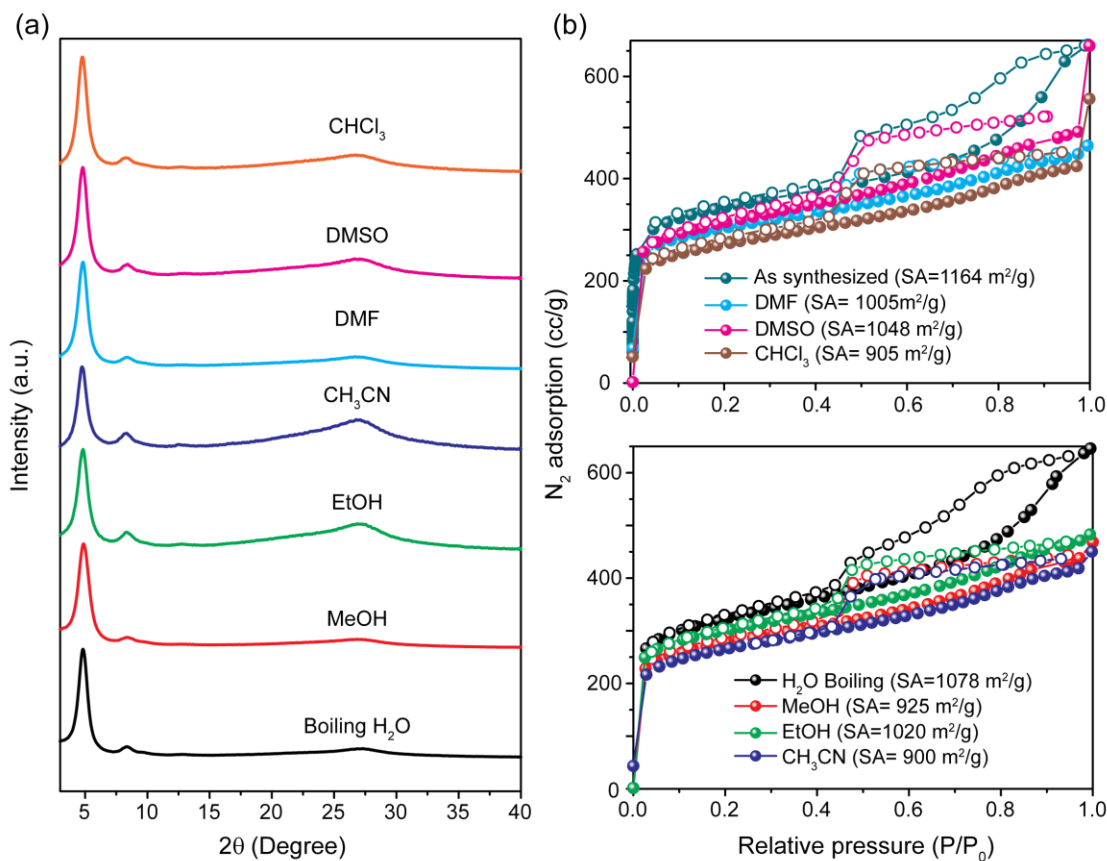


Figure 2.14: PXRD and BET surface area comparison of **TpOMe-Pa1** after treatment in different common solvents (protic and aprotic) as mentioned.

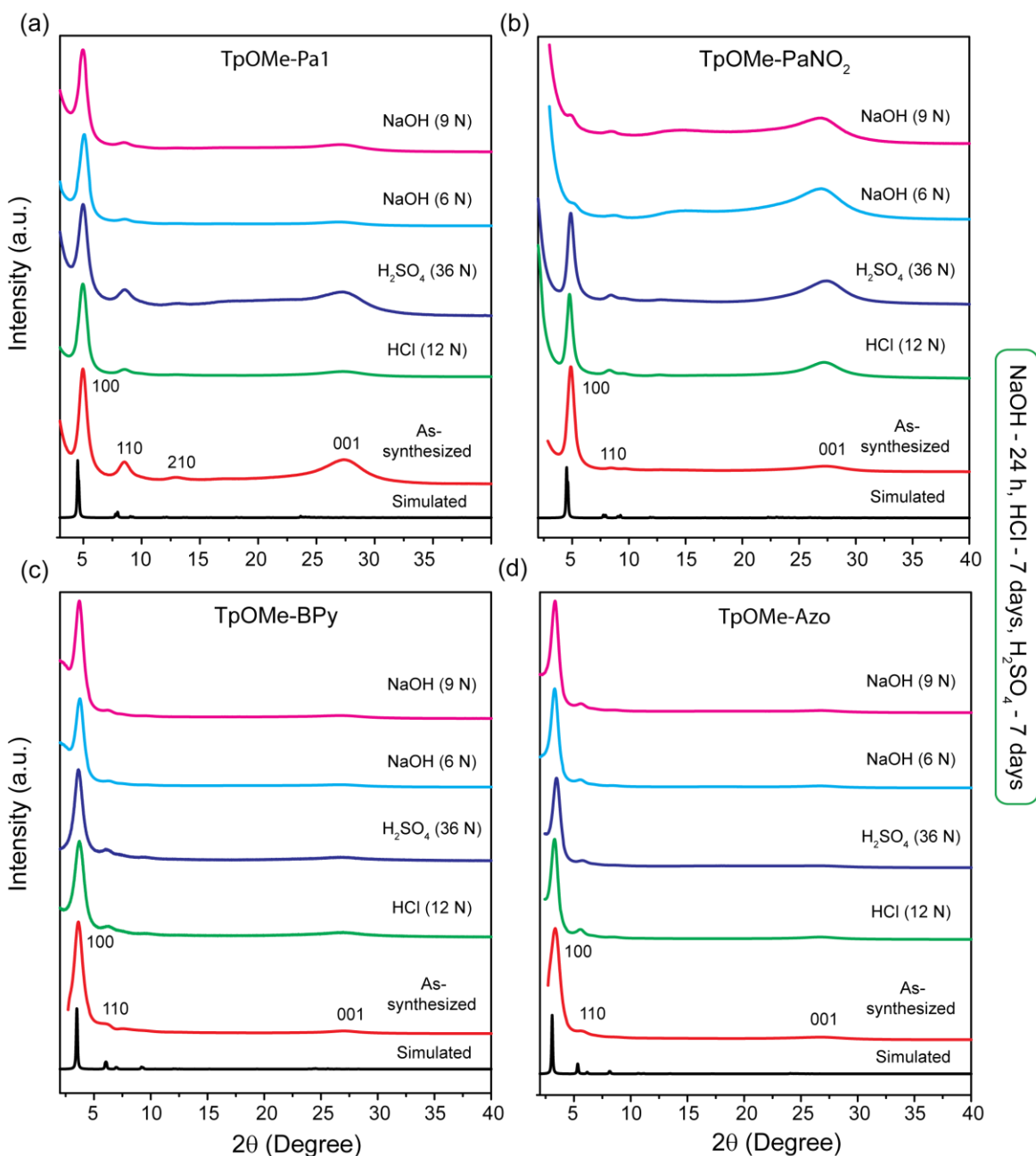


Figure 2.15: PXRD comparison of COF samples after treatment in a different solvent as mentioned. (a) *TpOMe-Pa1* (b) *TpOMe-PaNO₂* (c) *TpOMe-BPy* and (d) *TpOMe-Azo*

Except for **TpOMe-BD(NO₂)₂**, the other COFs maintained the residual weight percentage in the range 70-85 wt% and 80-90 wt% after seven days of treatment in an ultra-abrasive environment such as in conc. H₂SO₄ (36 N) and conc. HCl (12 N) respectively. On the other hand, on an average 50-60 wt% was retained for respective COFs after treatment in NaOH

(9N) for 24 h. **TpOMe-BD(NO₂)₂** was found to be highly sensitive towards conc. H₂SO₄ (36 N) and NaOH (9 N; here it degrades completely) (<24 hours) but found to be stable in HCl (12 N) for 7 days (**Figure 2.20**). For other COFs, the proper matching in the PXRD patterns (**Figure 2.15 & Figure 2.18**), along with their comparatively identical FTIR spectra (**Figure 2.16 & Figure 2.18**), concerning the as-synthesized material, revealed their structural rigidity in such drastic media.

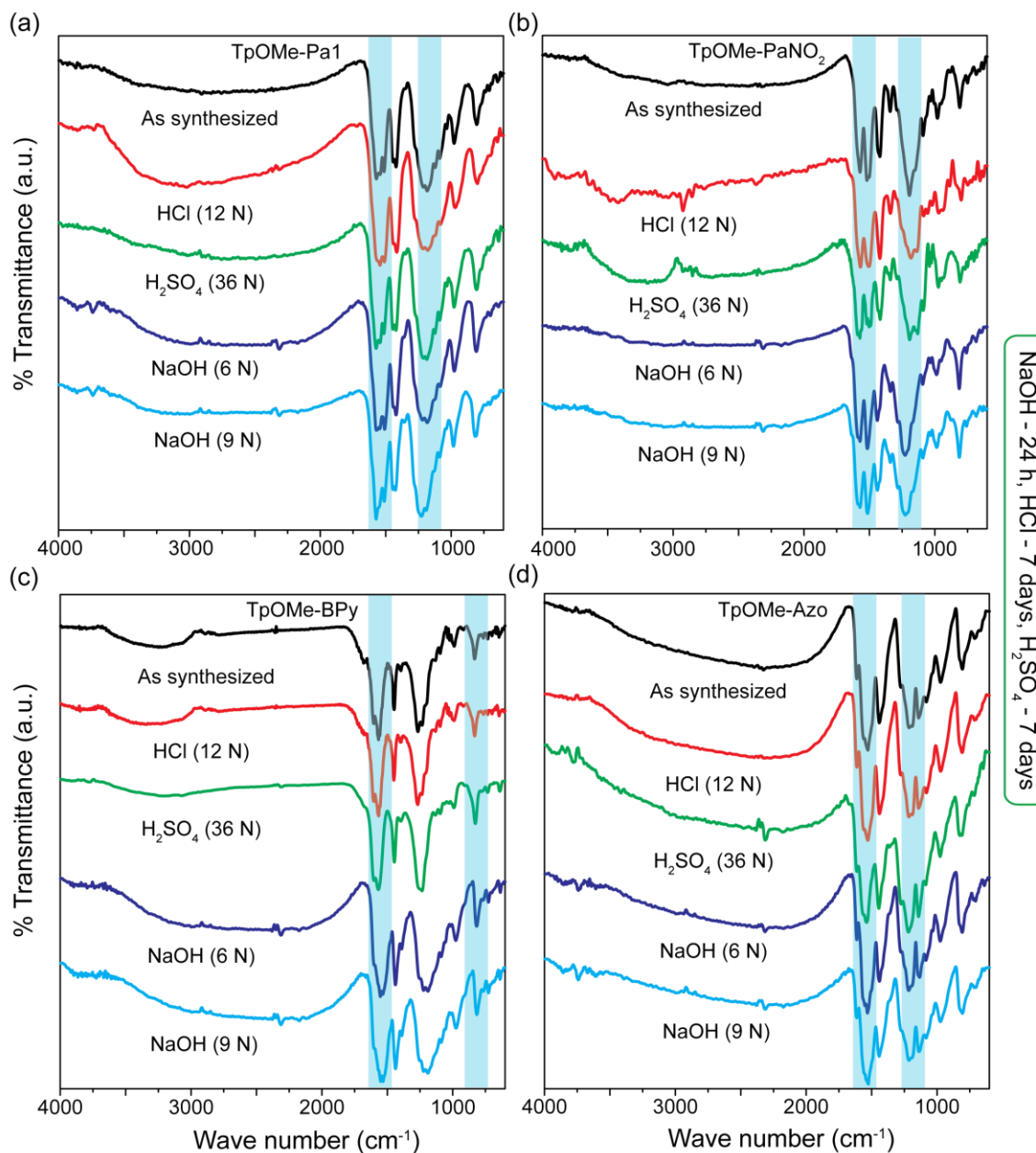


Figure 2.16: FT-IR comparison of COF samples after treatment in a different solvent as mentioned. (a) **TpOMe-Pa1** (b) **TpOMe-PaNO₂** (c) **TpOMe-BPy** and (d) **TpOMe-Azo**

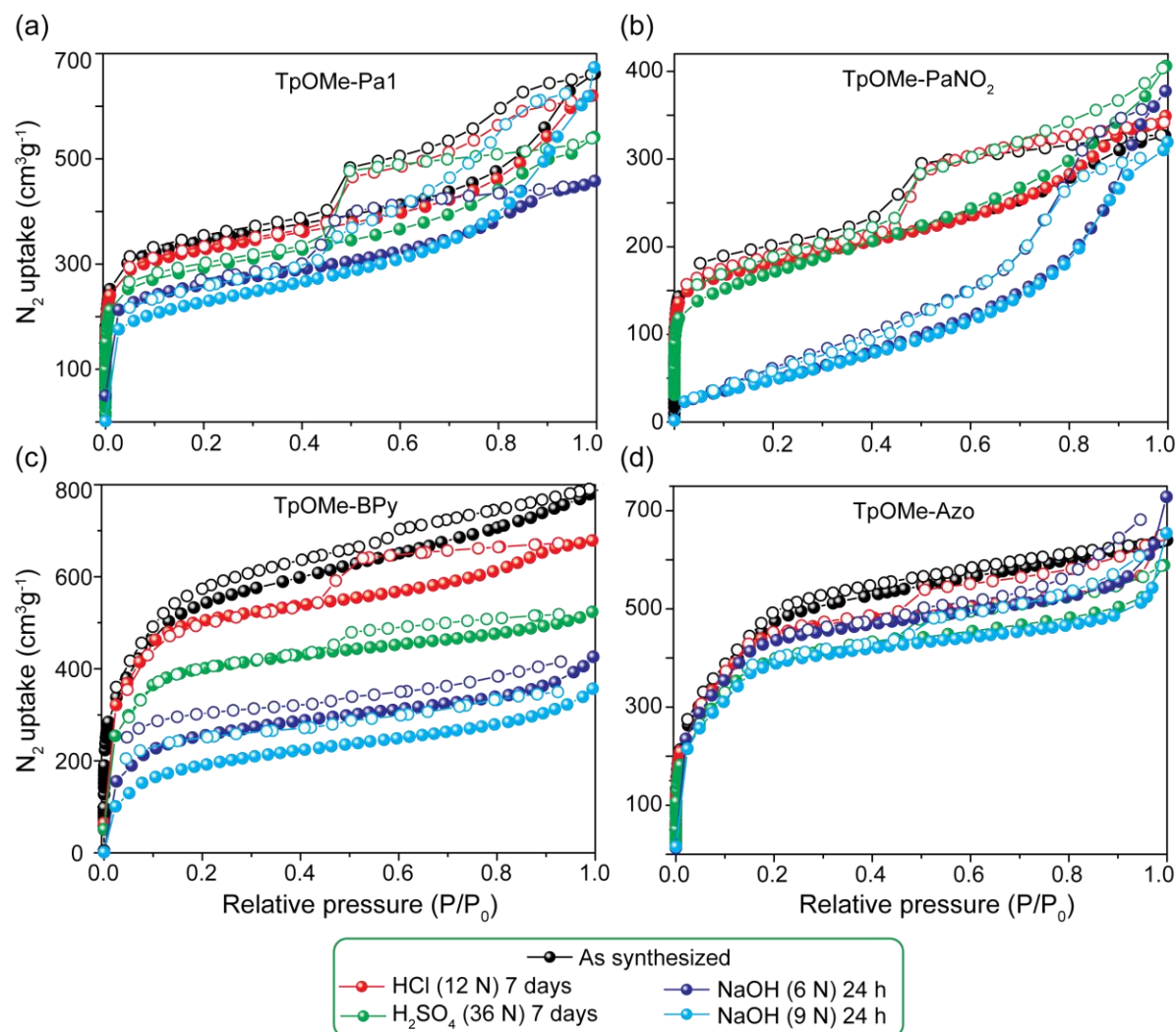


Figure 2.17: N_2 adsorption comparison of COF samples after treatment in a different solvent as mentioned. (a) **TpOMe-Pa1** (b) **TpOMe-PaNO₂** (c) **TpOMe-BPy** and (d) **TpOMe-Azo**

Notably, N_2 adsorption isotherms revealed the acid treated COFs maintained significantly high porosity. BET surface areas were recorded as for **TpOMe-BPy** (1512, 1844 and 689 m^2g^{-1}), **TpOMe-Azo** (1527, 1805 and 1469 m^2g^{-1}), **TpOMe-Pa1** (1014, 1112, 780 m^2g^{-1}), **TpOMe-BD(NO₂)₂** (170, 770 and 0 m^2g^{-1}), **TpOMe-PaNO₂** (603, 612 and 206 m^2g^{-1}) and **TpOMe-Tab** (584, 590 and 104 m^2g^{-1}) after treating the respective COF samples in conc. H_2SO_4 (36 N, seven days), conc. HCl (12 N, seven days) and NaOH (9 N, 24h) respectively (**Figure 2.17** & **Figure 2.19**).

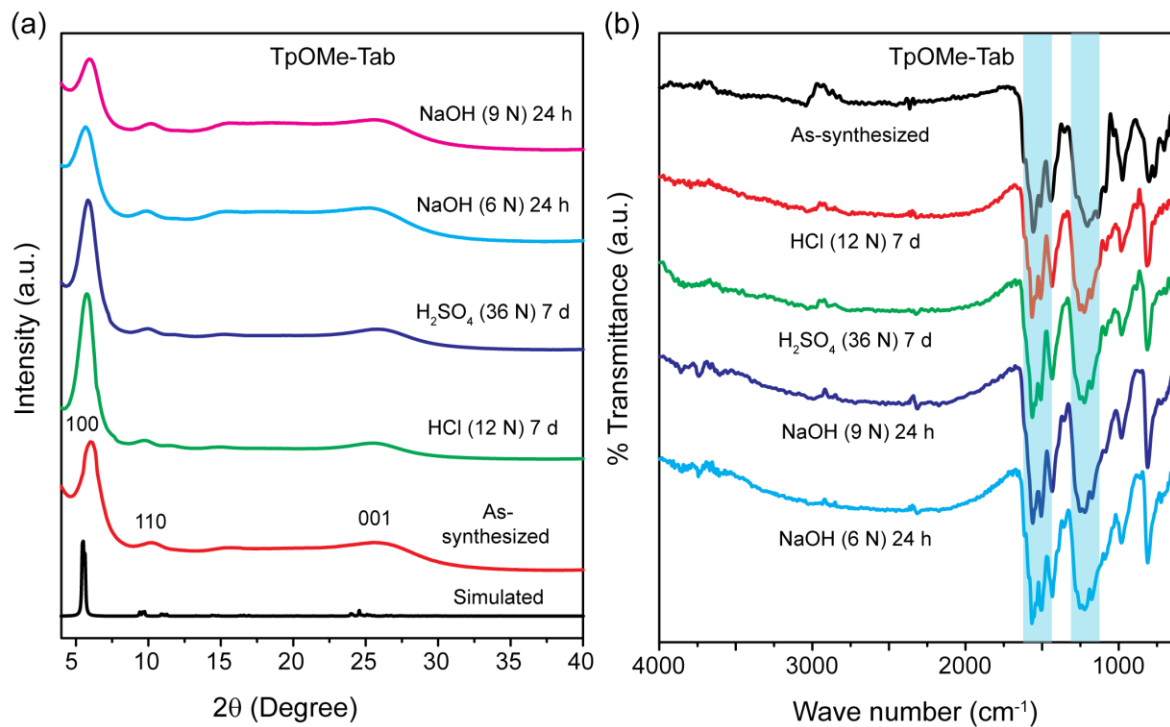


Figure 2.18: PXRD (a) and FT-IR (b) comparison of *TpOMe-Tab* COF samples after treatment in a different solvent as mentioned.

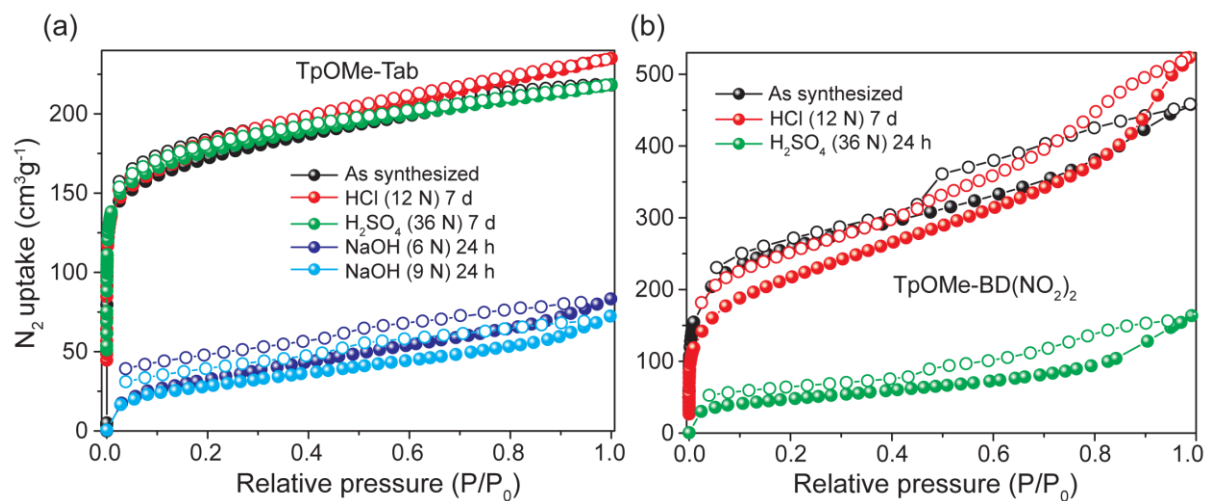


Figure 2.19: N₂ adsorption isotherm comparison of *TpOMe-Tab* (a) and *TpOMe-BD(NO₂)₂* COF samples after treatment in a different solvent as mentioned.

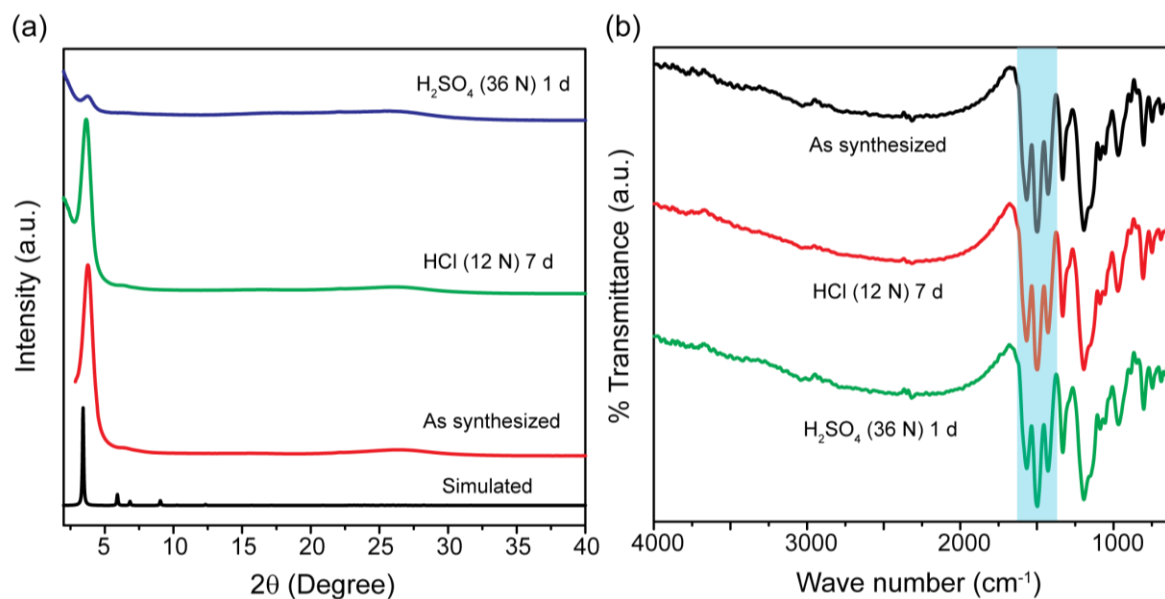


Figure 2.20: (a) PXRD and (b) FTIR comparison of **TpOMe-BD(NO₂)₂** COF samples after treatment in a different solvent as mentioned.

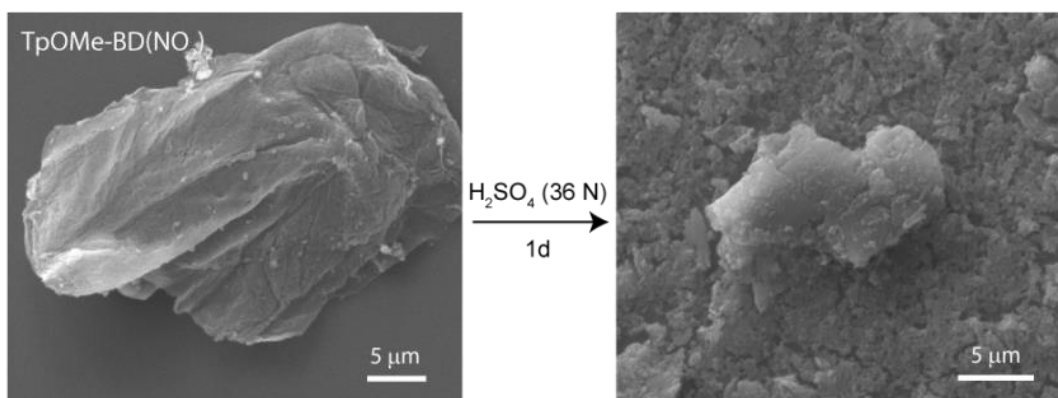


Figure 2.21: SEM images of **TpOMe-BD(NO₂)₂**: as synthesized and in H₂SO₄ (36 N) 1 day.

The morphological change before and after chemical treatment was investigated using scanning electron microscopy (SEM) techniques. From SEM the **TpOMe-X** COFs showcased significantly bigger crystallites composed from nicely packed sheets stacked in the perpendicular direction are formed. However, after chemical treatment **TpOMe-BD(NO₂)₂** undergoes complete decomposition smaller fragments whereas other COFs [**TpOMe-Pa1**, **TpOMe-PaNO₂**, **TpOMe-BPy**, **TpOMe-Azo** and **TpOMe-Tab**] could retain their crystallite packed structure with minimal degradation (**Figure 2.21** & **Figure 2.22**).

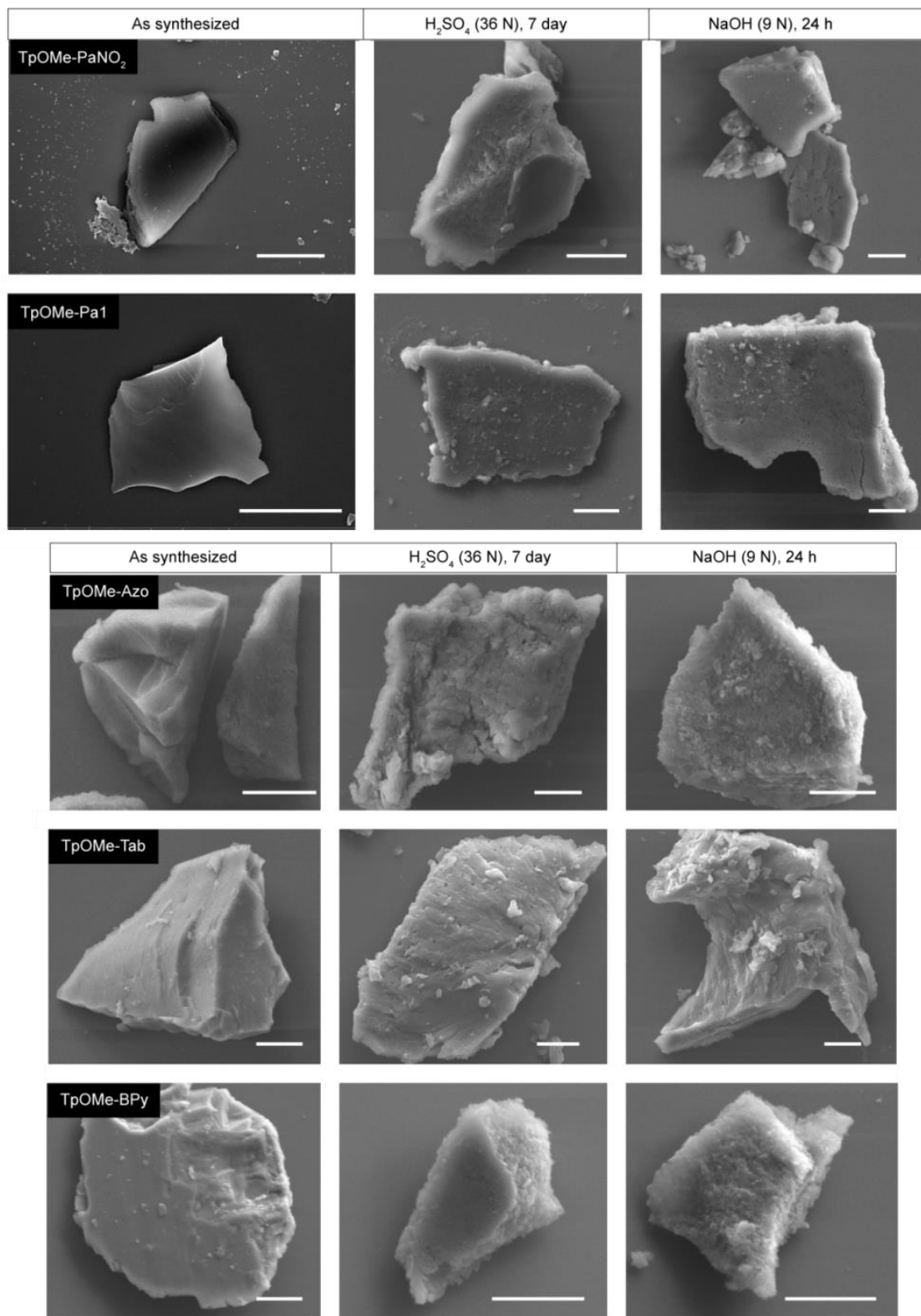


Figure 2.22: SEM images of TpOMe COFs (scale bar 10 μm): as synthesized, in H₂SO₄ (36 N) 7 days and in NaOH (9N) 24 h.

2.2.6 Reason behind the exceptional chemical stability

Density functional tight binding (DFTB) and density functional theory (DFT) calculations were undertaken to gain more insights about the exceptionally high chemical stability of the COFs. Interestingly, it was observed that the methoxy ($-\text{OCH}_3$) groups present in the aldehyde subunits played a very crucial role in stabilizing these materials. However, their mere presence does not impart the stability. The methoxy ($-\text{OCH}_3$) groups present in the COFs, except **TpOMe-BD(NO₂)₂**, were almost perpendicularly directed into the interlayer spacing in all the structures (**Figure 2.23**). As a result, a significant number (6-12 H-bonding per two stacked hexagons) of interlayer C-H...N H-bonding was discerned between the methoxy ($-\text{OCH}_3$) C-H of a particular layer and the imine ($-\text{C}=\text{N}-$) nitrogen atom present in the adjacent layer [2.7]. The calculated H-bonding distances in the slipped-AA structures for **TpOMe-Pa1** [$D=3.17\text{Å}, d=2.07\text{Å}, \theta=175.2^\circ$], **TpOMe-PaNO₂** [$D=3.31\text{Å}, d=2.26\text{Å}, \theta=157.9^\circ$], **TpOMe-Tab** [$D=3.24\text{Å}, d=2.17\text{Å}, \theta=160.4^\circ$], **TpOMe-BPy** [$D=3.24\text{Å}, d=2.16\text{Å}, \theta=163.5^\circ$], **TpOMe-Azo** [$D=3.24\text{Å}, d=2.15\text{Å}, \theta=166.3^\circ$] suggested the existence of C-H...N H-bonding in these COFs (**Figure 2.23a-e** & **Table 1**). However, in the case of **TpOMe-BD(NO₂)₂** (slip-AA), the methoxy ($-\text{OCH}_3$) groups lie mainly in the plane of the aldehyde phenyl ring, due to the presence of intralayer C-H...O [$D=3.27\text{Å}, d=2.18\text{Å}, \theta=167.5^\circ$] H-bonding between the methoxy ($-\text{OCH}_3$) C-H of the aldehyde and the nitro ($-\text{NO}_2$) oxygen atom of the BD(NO₂)₂ amine (**Figure 2.23f** & **Table 2**). The calculated distances in either case are within the range of appreciable C-H...N or C-H...O ($d \leq 2.7\text{Å}, \theta \geq 150^\circ$) H-bondings, as evidenced from similar kind of H-bonding interactions reported in small molecule crystal structures (**Figure 2.24**) [2.10a-c & 2.11]. The presence of such C-H...N H-bondings thereby provide significant steric hindrance and the hydrophobic environment around the imine bonds making it safe from hydrolysis (**Figure 2.25**). In contrast, **TpOMe-BD(NO₂)₂** lacks such interlayer C-H...N H-bonding, instead it maintains only intralayer C-H...O H-bonding. Hence, the imine ($-\text{C}=\text{N}-$) bonds, which are devoid of such stabilizing H-bonding get disrupted *via* the rapid attack from H^+ or OH^- , signifying the lower chemical stability of **TpOMe-BD(NO₂)₂** (**Figure 2.19** & **Figure 2.20**). Hence, the overall findings evidently indicate that the remarkable chemical stability of these materials does not depend upon the mere presence of the methoxy ($-\text{OMe}$) functionality in the frameworks but due to the existence of such stabilizing interlayer H-bonding.

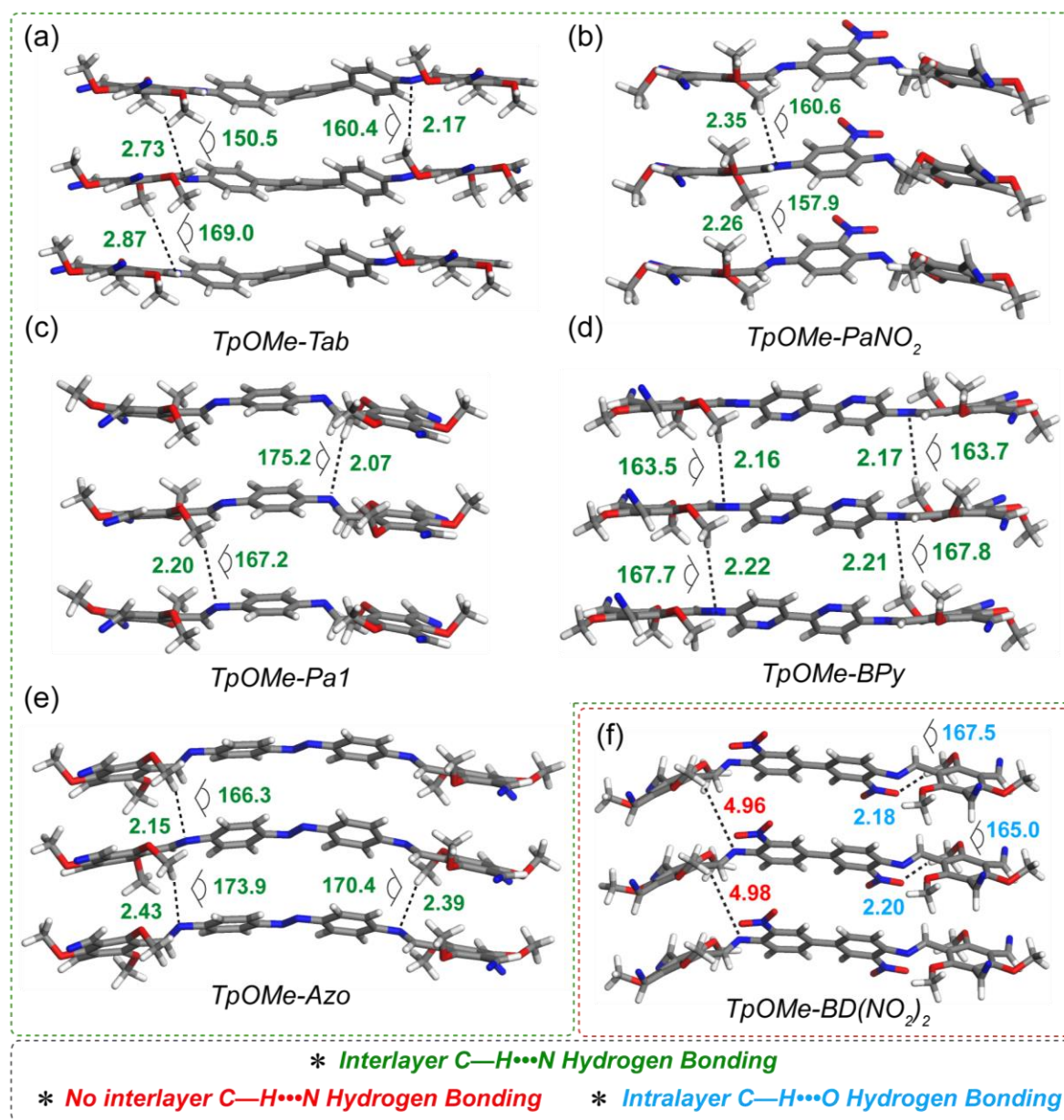


Figure 2.23: Interlayer C—H...N H-bonding- (i) distances (H to N atom in dotted line; Å) and angles (C—H...N) in degree (shown in green) (ii) C to N atom distance in dotted line; Å for (a) **TpOMe-Tab**, (b) **TpOMe-PaNO₂**, (c) **TpOMe-Pa1**, (d) **TpOMe-BPy**, (e) **TpOMe-Azo** and (f) **TpOMe-BD(NO₂)₂**.

In order to validate the theoretically (from DFT and DFTB calculation) predicted C—H...N (interlayer) and C—H...O (intralayer) hydrogen bonding respectively in **TpOMe-X** (X= **Tab**, **PaNO₂**, **Pa1**, **Azo** and **BPy**) and **TpOMe-BD(NO₂)₂** COFs we have considered here the crystal structures of four different reference molecules reported in the literature. These

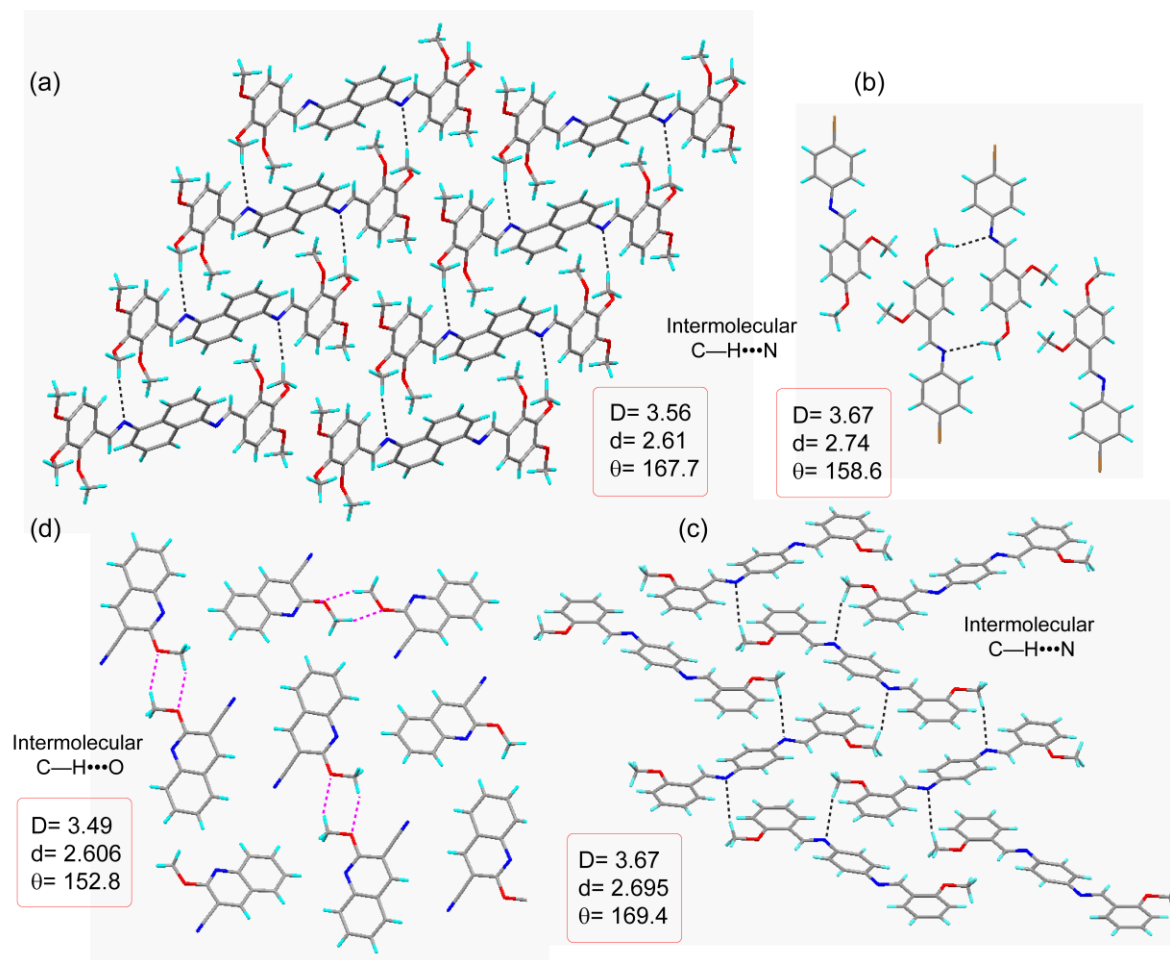


Figure 2.24: Crystallographic evidence of C-H...N and C-H...O hydrogen bonding (C-grey, H-cyan, N-blue, O-red) in small molecules. (a-c) Intermolecular C-H...N hydrogen bonding between methoxy ($-OCH_3$) C-H and imine 'N' atom (CCDC No: **a-951727**, **b-722946**, **c-645628**)^[2.10]. (d) Intermolecular C-H...O hydrogen bonding between methoxy ($-OCH_3$) C-H of one molecule with methoxy ($-OCH_3$) 'O' atom of another molecule or vice versa (CCDC No.-**795700**)^[2.11] Hydrogen bond distances (D and d) in Å and bond angles (θ) in degree have shown.

crystal structures reflect the methoxy ($-OCH_3$) C-H can undergo intermolecular C-H...N hydrogen bonding interaction with imine 'N' atom (**Figure 2.24a-c**). Also methoxy ($-OCH_3$) C-H can form C-H...O hydrogen bonding with more electronegative 'O' atom (**Figure 2.24d**). Hence, the calculated distance (from H to N) and the angles (around C-H...N) in the TpOMe-X (X= **Tab**, **PaNO₂**, **Pa1**, **Azo** and **BPy**) COFs reflects the existence of interlayer C-H...N hydrogen bonding (**Table 1**). On the other hand, after comparing with crystal structure data, the calculated distance (from H to O) and the angles (around C-H...O)

indicate there exist an intralayer C–H•••O hydrogen bonding in **TpOMe-BD(NO₂)₂** COF (**Table 2**).

Table 2.1: Comparison of interlayer C–H•••N hydrogen bonding among **TpOMe-X** COF and reference crystal structures of **Figure 2.24; a, b and c**.

COFs	D (Å)	d (Å)	θ (degree)
TpOMe-Tab	3.74	2.73	150.5
	3.24	2.17	160.4
	3.96	2.87	169.0
TpOMe-PaNO₂	3.41	2.35	160.6
	3.31	2.26	157.9
TpOMe-Pa1	3.17	2.07	175.2
	3.29	2.20	167.2
TpOMe-BPy	3.24	2.16	163.5
	3.25	2.22	167.7
	3.30	2.17	163.7
	3.31	2.21	167.8
TpOMe-Azo	3.24	2.15	166.3
	3.53	2.43	173.9
	3.48	2.39	170.4
Crystal structure- 'a'	3.56	2.61	167.7
Crystal structure- 'b'	3.67	2.74	158.6
Crystal structure- 'c'	3.67	2.69	169.4

Note: **D** (Å) is the distance between methoxy (–OCH₃) ‘C’ atom to imine ‘N’ atom; **d** (Å) is the distance between methoxy (–OCH₃) ‘H’ atom to imine ‘N’ atom; and **θ** (degree) is the angle around C–H•••N hydrogen bond.

Table 2.2: Comparison of intralayer C–H•••O hydrogen bonding between **TpOMe-BD(NO₂)₂** COF and reference crystal structure of **Figure 2.24; d**.

COF	D (Å)	d (Å)	θ (degree)
TpOMe-BD(NO₂)₂	3.27	2.18	167.5
	3.28	2.20	165.0
Crystal structure- 'd'	3.49	2.61	152.9

Note: In **TpOMe-BD(NO₂)₂** COF, **D** (Å) is the distance between methoxy (–OCH₃) ‘C’ atom to (–NO₂) ‘O’ atom; **d** (Å) is the distance between methoxy (–OCH₃) ‘H’ atom to (–NO₂) ‘O’ atom; and **θ** (degree) is the angle around C–H•••O hydrogen bond.

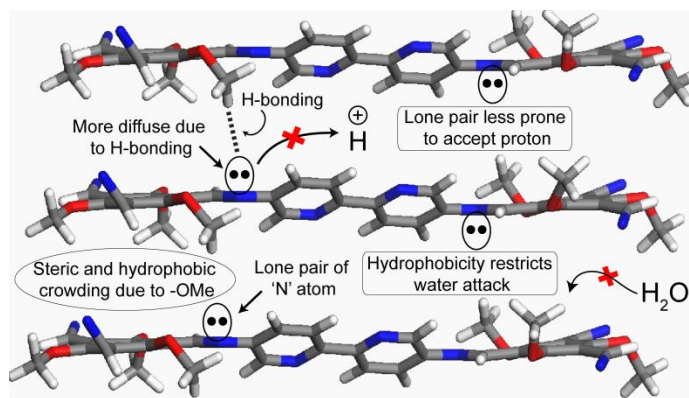


Figure 2.25: Schematic representation of interlayer C–H...N hydrogen bonding in **TpOMe-BPy**, its effect on preventing imine (C=N) bond hydrolysis in the acidic medium through the steric and hydrophobic environment.

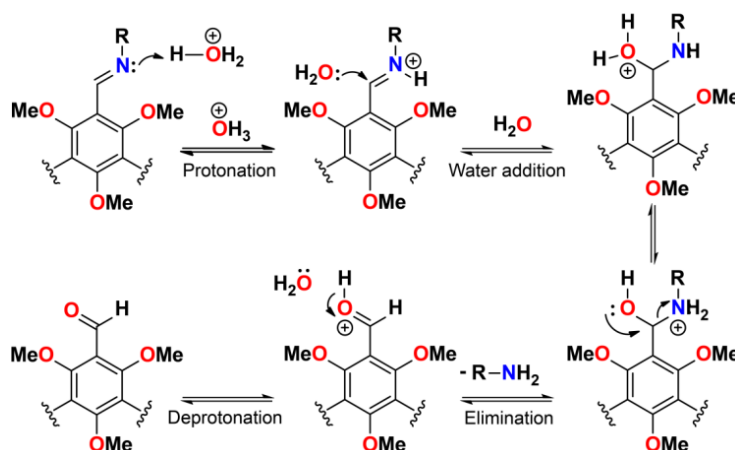


Figure 2.26: Hydrolysis mechanism of imine (C=N) bond in acid (H^+) medium.

The reason behind the high chemical stability of TpOMe-X COFs in strong acid (H^+) medium: In an acid medium, at first the ‘N’ atom of imine (C=N) bond undergoes protonation. In the next step, water molecule attacks at imine ‘C’ atom and the rest of the hydrolysis process proceeds as shown in **Figure 2.26**). Hence, at the beginning of the hydrolysis process in the acid medium, the protonation of imine ‘N’ is highly essential. In other **TpOMe-X** (X= **Tab**, **PaNO₂**, **Pa1**, **BPy** and **Azo**) COFs, except **TpOMe-BD(NO₂)₂**, interlayer C–H...N hydrogen bonding (H-bonding) interactions exist among the individual layers. Thus, the lone pair of imine ‘N’ atom is diffused and is shared in forming interlayer C–H...N H-bonding. Hence, the availability of lone pair present on the imine ‘N’ atom is

drastically reduced for protonation in acid (H^+) medium which affects rest of the hydrolysis steps. Again H-bonding interaction provides a steric and hydrophobic environment to affect H_2O attack at imine 'C' atom (2nd step of the hydrolysis process) (**Figure 2.26**). As a result, respective **TpOMe-X** (X= **Tab**, **PaNO₂**, **Pa1**, **BPy** and **Azo**) COFs shows extremely high chemical stability in strong acidic medium such as in conc. H_2SO_4 (36 N).

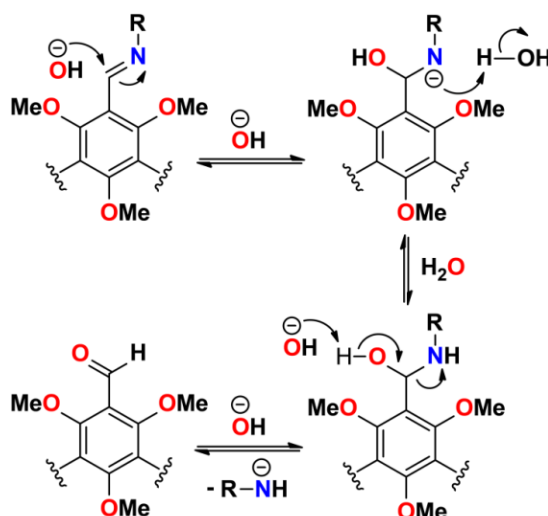


Figure 2.27: Hydrolysis mechanism of imine (C=N) bond in base (OH^-) medium.

The reason behind comparatively less chemical stability in strong base (OH^-) medium: On the other hand, in a basic medium at first the 'C' atom of imine (C=N) bond is attacked by hydroxide (OH^-) ion as shown in **Figure 2.27**. Hence, the hydroxyl group adds to imine 'C' atom and π electron cloud of imine bond moves on 'N' atom and the rest of the hydrolysis steps progress. In all **TpOMe-X** (X= **Tab**, **PaNO₂**, **Pa1**, **BD(NO₂)₂**, **BPy** and **Azo**) COFs, the imine 'C' atom is free to undergo attack from OH^- ion though it is considerably protected (except **TpOMe-BD(NO₂)₂**) through steric and hydrophobic environment due to the interlayer C-H...N H-bonding. As a result, the respective COFs show comparatively less chemical stability in strong base (OH^-) compared to acid (H^+) medium. Again, due to absence of such stabilizing C-H...N H-bonding **TpOMe-BD(NO₂)₂** gets degraded in strong acid (H_2SO_4 , 36 N) and strong base (NaOH, 9 N).

2.3 Conclusion

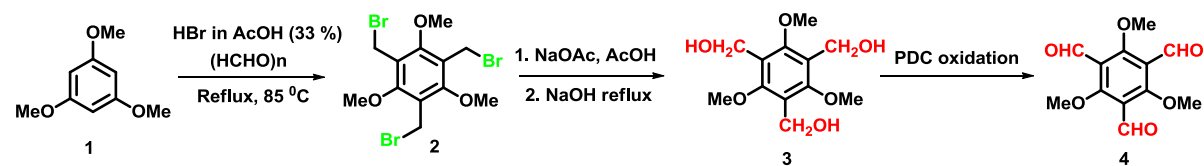
In summary, we have designed and synthesized a series of imine ($-\text{C}=\text{N}-$) linked porous and crystalline COFs *via* the salt (*p*-toluenesulfonic acid- H_2O) mediated crystallization process. This preferred approach is economically beneficial as it provides a very simple route for rapid and bulk scale production of the incredibly versatile imine-based COFs, with high crystallinity and porosity. The as-synthesized materials showcased ultra-high chemical stability in extremely drastic media such as strong acids (conc. H_2SO_4 , 36 N and conc. HCl , 12 N; seven days) and base (NaOH , 9N; 24h). DFT calculations of the structures revealed that the presence of interlayer H-bonding is mainly responsible for the ultrahigh stability of these materials, as it protected the imine bond from hydrolysis by providing enough steric hindrance and hydrophobic environment.

2.4 Experimental Procedures

2.4.1 Materials

2,4,6-Trimethoxy-benzene-1,3,5-tricarbaldehyde (TpOMe) was prepared from 1,3,5-trimethoxybenzene using the reported literature procedure [2.12]. 4,4'-diamino-2,2'-bipyridine (BPy) was prepared following the reported literature procedure [2.13]. All other reagents and solvents were commercially available and used as received.

2.4.2 Synthesis of 2,4,6-Trimethoxy-benzene-1,3,5-tricarbaldehyde (TpOMe).



Scheme 2.1: General synthetic scheme for 2,4,6-Trimethoxy-benzene-1,3,5-tricarbaldehyde (TpOMe) starting from 1,3,5-trimethoxybenzene.

Compound 2 (1,3,5-tris-bromomethyl-2,4,6-trimethoxybenzene): Compound 2 was synthesized according to the reported literature procedure [2.14].

Compound 3 (1,3,5-tris-hydroxymethyl-2,4,6-trimethoxybenzene; triol): Compound 2 (1.00 g, 2.24 mmol) and NaOAc (2.27 g, 27.7 mmol) were added in glacial AcOH (20 mL) in a round bottom flask and the open system was heated to reflux for 4-6 hours. After cooling to room temperature, the resulting suspension was diluted with dichloromethane (40 mL), the

solid precipitate was removed by suction filtration and the filtrate was evaporated to dryness leaving a crude white solid. This was dissolved in ethyl acetate (50 mL) and was washed with saturated aqueous NaHCO₃ (2 x 50 mL), water (30 mL), brine (30 mL) before it dried over MgSO₄. The solvent was evaporated in vacuum and the crude triacetate (0.860 g, quant.) was obtained as a white solid. The as-synthesized material was then dissolved in EtOH (8 mL) and aq. NaOH (1.50 g, 37.5 mmol; 10 mL water) solution was added. The resulting mixture was allowed to reflux for 12-18 hours. The EtOH was then removed in vacuo and the remaining aqueous mixture was neutralized with 1.0 M HCl followed by saturated with NaCl. This was then extracted with ethyl acetate (3 x 40 mL) and the organic layers were combined, dried over Na₂SO₄, and concentrated to dryness to give the triol (0.48 g, 83%) as a white solid: ¹H NMR (DMSO-*d*₆): δ 3.87 (s, 9H), 4.45-4.46 (d, 6H), 4.76-4.78 (t, 3H) ppm (*Scheme 2.1*).

Compound 4 (2,4,6-Trimethoxy-benzene-1,3,5-tricarbaldehyde). To a stirring mixture of the triol (1.50 g, 5.81 mmol) in dry dichloromethane (35 mL) and 3 Å molecular sieves, was added PDC (10.94 g, 29.08 mmol). The resulting suspension was allowed to stir under argon for overnight. It was then diluted with methylene chloride (100 mL) and all solid material was removed *via* suction filtration. The filtrate was concentrated to a crude residue and was purified *via* column chromatography (3:2 hexanes/EtOAc) to afford the trialdehyde (0.98 g, 67%) as a colorless solid. ¹H NMR (CDCl₃): δ 3.96 (s, 9H), 10.28 (s, 3H) ppm (*Figure 2.28*) (*Scheme 2.1*).

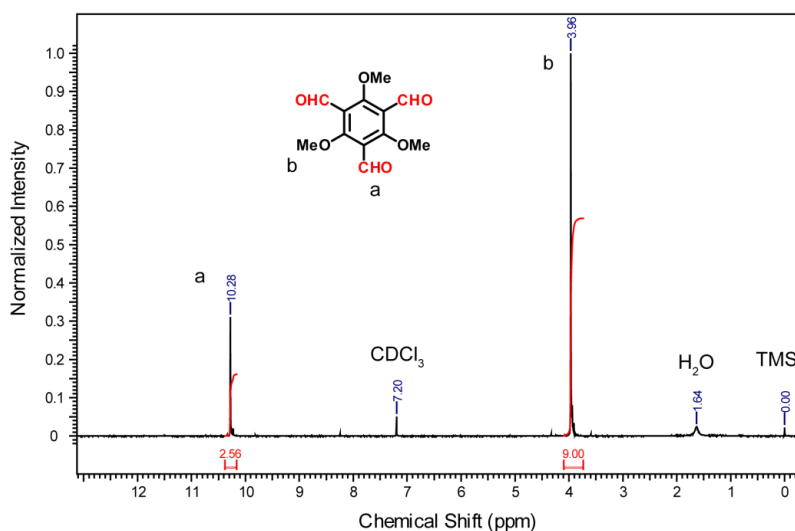
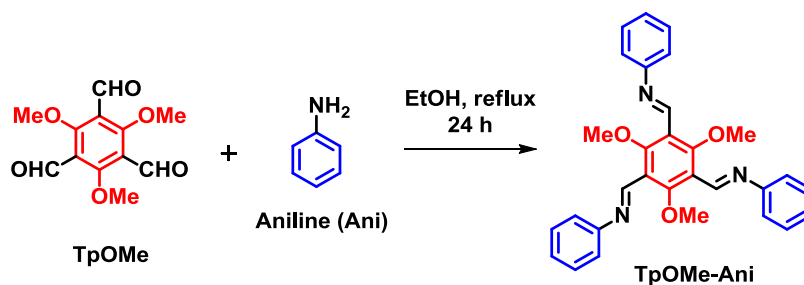


Figure 2.28: ¹H NMR spectrum (in CDCl₃) of *TpOMe* aldehyde (**4**).

2.4.2 Synthesis of reference model compound (TpOMe-Ani).



Scheme 2.2: General synthetic scheme for reference compound TpOMe-Ani.

This reference compound was synthesized by the reaction between 2,4,6-trimethoxybenzene-1,3,5-tricarbaldehyde (**TpOMe**) (254 mg, 1 mmol) and distilled aniline (**Ani**) (280 mg, 3 mmol), in 30 mL ethanol, under refluxing condition for one day (*Scheme 2.2*). Later, the solution was cooled to room temperature and the insoluble precipitate was separated by filtration. The filtrate was vacuum dried and an oily compound was dissolved in ethyl acetate and was kept for slow evaporation of the solvent, which results in the microcrystalline compound. The resulting crystalline material was collected and washed with cold diethyl ether. The final reddish yellow crystalline compound resulted with 80% of isolated yield. ^1H NMR (200 MHz, CDCl_3): δ 8.78 (s, 3H), 7.46-7.22 (m, 15H), 3.96 (s, 9H). ^{13}C NMR (200 MHz, CDCl_3): δ 163, 154, 152, 129, 126, 121, 120, 63. IR (powder, cm^{-1}): 3056-2834 (m, C-H), 1621 (s, C=N), 1589 (s), 1555 (s), 1483 (s), 1413 (m).

2.4.3 General methods for characterization

(a) **Powder X-Ray Diffraction (PXRD)**: The PXRD data were recorded on a Phillips PANalytical diffractometer using a Cu $K\alpha$ radiation ($\lambda = 1.5406 \text{ \AA}$), with a scan rate of 2° min^{-1} . The tube current and voltage were fixed at 30 mA and 40 kV respectively. The sample holder containing the COF powders was scanned between 2 and $50^\circ 2\theta$ (step size of 0.02°).

(b) **Thermogravimetric Analysis (TGA)**: TGA was recorded on an SDT Q 600 TG-DTA analyzer instrument. Approximately 5-7 mg of the COF sample was added to an aluminum crucible and heated from 25 to 900°C under N_2 atmosphere (heating rate of $10^\circ \text{C min}^{-1}$).

(c) **IR Spectroscopy**: The Fourier transform infrared spectra (FTIR) of the COFs were collected on a PERKIN ELMER FT-IR SPECTRUM (Nicolet) spectrometer in ATR mode.

The FTIR data were collected over the range of 4000-600 cm^{-1} .

(d) Gas Adsorption: The gas adsorption experiments were performed specifically for the activated COF powders using an *Autosorb* automatic volumetric instrument (*Quantachrome*).

COF powder activation procedure: Approximately 40 mg of the as-synthesized COF powders were evacuated under vacuum at 120 °C for 12 h. Finally, the activated samples were used for gas adsorption (H_2 , N_2 , and CO_2).

(e) Water adsorption measurements: Low-pressure water adsorption (volumetric) measurements were performed at 298 K, within a pressure range of 0 to 0.9 [relative pressure (P/P_0)] using a *Quantachrome Autosorb-iQ-MP* automatic volumetric instrument.

2.4.4 Structure Modeling of COFs

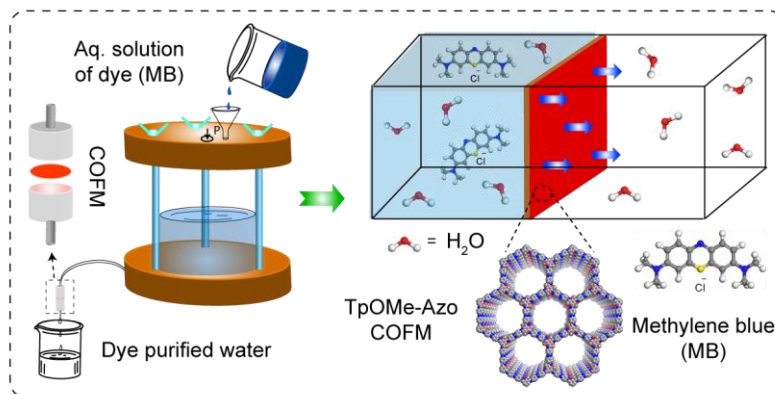
Atomic positions and cell sizes of modeled COF layers were optimized using the Self-Consistent-Charge Density-Functional Tight-Binding (SCC-DFTB) method. The layer stacking is affected by the Coulomb repulsion between the partial atomic charges in adjacent layers [2.15]. Hence, several slipped AA stacking possibilities were considered for each COF by shifting adjacent layers with respect to each other in different directions up to 6Å. In addition, different orientations of the methoxy groups (in plane, above plane, below plane) were considered. The predicted slipped structure has the lowest energy while maintaining an agreement with the experimental PXRD pattern. All the COFs have been modeled in the triclinic space group (*P1*) by comparing the experimental and simulated PXRD patterns. Refinements of PXRD pattern were done using Reflex module of the Material studio.

NOTE: All results of this chapter have already been published in *Angew. Chem., Int. Ed.*, **2018**, 57, 5797; with the title: “*Ultra-stable Imine-based Covalent Organic Frameworks for Sulfuric acid Recovery: An Effect of Interlayer Hydrogen Bonding*”. The stated publication was the results of the collaboration between the group of Dr. Rahul Banerjee and his student Mr. Arjun Halder from National Chemical Laboratory, Pune, India and the group of Dr. Thomas Heine and his student Dr. Matthew Addicoat from Jacobs University, Germany. Apart from computational study major works contributed by Arjun Halder.

CHAPTER 3

Chemically Stable Covalent Organic Framework Membranes (COFMs) for Water Purification

Abstract: Covalent organic frameworks (COFs) have attracted enormous scientific attention over the past few years because of their unique tunable porosity and long-range ordered structures with high atomic precision.



Although the high crystalline nature with considerable porosity fashioned these novel materials as eligible candidates for diverse applications, the ordered nano-channels with controllable pore aperture, especially with regard to membrane separations in extreme conditions, have been poorly explored. Herein, we have demonstrated a rapid and scalable synthesis of an ultra-stable [H_2SO_4 (18 M), conc. HCl (12 M) and $NaOH$ (9 M)] imine-linked highly crystalline and porous covalent organic framework membrane (COFMs) via a salt (*p*-toluenesulfonic acid) mediated solid state crystallization approach. The COFMs were successfully utilized to separate various environmentally toxic materials from drinking water with high water flux. In addition, owing to their highly robust backbone, the COFMs have shown unprecedented sulfuric acid (6 M) permeance thus reflecting their potential applications for sulfuric acid purification. Also, the as-synthesized COFMs exhibit exceptionally high permeance of acetonitrile ($280 \text{ Lm}^{-2}\text{h}^{-1}\text{bar}^{-1}$) and acetone ($260 \text{ Lm}^{-2}\text{h}^{-1}\text{bar}^{-1}$) reflecting its applicability for water solvent treatment.

3.1 Introduction

One of the leading challenges for the sustainability of the present society is the inadequate supply of purified water, as water is the primary source of life and one of the very important resources for human civilizations and their survivals. Though 71% of the overall earth's surface is finely covered with water, the freshwater resources which can be utilized for the humans are limited in numbers. The important resources of clean water such as freshwater lakes, river water, and the shallow groundwater, however, are only 0.03% of the total water resources worldwide. Again, with the rapid progress of wide human activities and industrial developments such as in fertilizers, metal plating, tanneries, batteries, pesticides, papers etc. many harmful organic or inorganic pollutants are rapidly released into the water thereby seriously endangers the freshwater resources [3.1-3.2]. In addition, population growth, rapid urbanization, and climate disruption have now become unprecedented global issues towards clean water shortage. Notably, in the current scenario, nearly one in five people on earth don't have proper access to the safe drinking water, and according to WHO (World Health Organization) around 3900 children die every day due to the disease communicated from unsafe water uptake and poor hygiene. Again, according to the report from U. N. world water development, the current situation is projected to be worsened by 2050 when there would be at least a quarter of people, in the world, will live in such countries which will seriously suffer from recurring drinking water shortages [3.3].

Therefore, water purification extensively for human usage, agriculture, ecosystem management and for industrial use is emerging as a foremost global priority. To that end, a significant number of technologies have been rapidly developed in current decades for sustainable water purification [3.4]. The most commonly used techniques are air flotation, adsorption, distillation, flocculation and advanced oxidization processes (AOPs). Moreover, most of the aforementioned technologies associated with high energy consumption and demands complex equipment set up and huge operation cost. Apart from that, some of these even require the usage of a large amount of chemicals during its operation which could produce various chemical by-products and lead water treatment more complicated. Therefore, the design and development of environmentally friendly, robust, low cost and energy-efficient technologies for clean and sustainable water treatment and its purification are of keen importance.

Owing to its cost-effective, energy saving with minimal environmental impacts membrane-based technology has now become one of the indispensable platforms for sustainable water purification which includes seawater desalination and industrial or municipal wastewater treatment. Moreover, the novel methods associated with the membrane-based purification are micro-filtration (MF), ultra-filtration (UF), nano-filtration (NF), reverse osmosis, forward osmosis, membrane distillation etc. therefore, have been recognized as the foremost water purification technologies [3.5].

Among all other, the nanofiltration (NF) membranes are considered as highly important for wastewater treatment as it covers a wide range of water contaminants removal [3.6]. However, the major drawback of this series of membranes is the lack of ordered nanochannels as most of them are prepared from amorphous polymeric materials ex. polyimide, poly (amide-imide) crosslinked polymers etc [3.7]. Again, comparatively denser internal structure, lacking in ordered pore connectivity and hence inferior porosity of such polymer-based nano-filtration membranes readily hinders proper solvent permeance through their channels. However, the solvent permeance of such NF based membranes is primarily enhanced by increasing active area of the membrane or by reducing the membrane thickness to nano-meter level [3.8]. The construction of such thin membranes is carried out by using various techniques such as spin coating [3.8c], interfacial polymerization [3.8a] or plasma polymerizations [3.8b] etc. Moreover, the membranes composed entirely from a crystalline material with well-defined pore channels (1-3 nm) could provide a significant improvement in NF based membranes in terms of solvent permeability and selectivity. To that end, compared to other traditional polymeric membranes, the potentially important porous and crystalline materials such as zeolites [3.9] and metal organic frameworks (MOFs) [3.10] are promising in terms of molecular separation through adsorption in their ordered pore channels. However, as they are mostly used as fillers or sometimes their growth within polymer matrices, the permeance or separation performance of such hybrid membranes is significantly less [3.10]. Hence, to achieve a complete advantage of ordered nano-channels of such porous crystalline materials a self-standing membrane needs to be fabricated. However, ordering such crystallites to a self-standing membrane form is profoundly challenging and if it is done will be a breakthrough in various quality separations associated with industrial or

environmental significance. Beside wastewater treatment, another significant category of purification is of H_2SO_4 is highly important industrially.

Sulfuric acid is one of the most used and highly important compounds manufactured by the chemical industry. It has been widely used, literally, in hundreds of reactions and chemical treatments including polymerization of alkenes, nitration, and sulfonation of aromatics, esterification etc. because of its distinct properties and relative inexpensiveness compared to other acids [3.11a]. As a result, a plenty amount of waste sulphuric acid is getting generated every year, which create serious environmental complications including soil acidification and ecosystem collapse if it is dispensed without proper treatment. A conventional and direct solution could be to neutralize the sulphuric acid with limestone or ammonical water solution. However, this process could produce plenty of gypsums and ammonical wastewater leading another serious disposal issue. Furthermore, valuable sulphuric acid gets wasted during this operation which could otherwise be retrieved for future reuse. However, some other methods rather than neutralization to recover sulfuric acid include ion exchange, solvent extraction, diffusion dialysis and oxidative degradation. Moreover, these methods are extremely tedious and could generate a sulfuric acid with limited purity only [3.11b-c]. Hence it is highly desirable to fabricate synthetically easy and economically facile route such as membrane separation of sulfuric acid from industrial waste. Therefore, synthetically easy and bulk scale production of crystalline porous membranes with enormous thermochemical stability could serve as an efficient platform for sulfuric acid purification from industrial waste.

Emerging as a pristine category of porous and crystalline material, covalent organic framework (COFs) consist with uniformly ordered and well-defined nano-porous channels [3.12]. Although, COFs have revealed its potentiality towards storage applications of different gases, enzymes, drugs, and nanoparticles; beneficial use of its ordered nanochannels in terms of water purification *via* molecular separation have been poorly explored. The major alarming barriers, which restrict this novel material towards real-time separation applications, comprises its difficult synthetic procedures, substandard scalability, chemical instability and insolubility in common solvents [3.13]. Furthermore, it is quite difficult to fabricate COF crystallites into a self-standing, chemically stable membrane form to employ its ordered pore channels for selective molecular separations. Recent theoretical proceedings esteemed

covalent organic framework membranes (COFMs) as a true potential entrant in terms of molecular separation [3.14]. Hence, self-standing COFMs derived solely from COF crystallites with ordered pore channels could fulfill the concerned task. However, to attain this goal, the foremost complication is in synthesizing COFs as a continuous membrane as it precipitates as a microcrystalline powder. Furthermore, a massive no. of internal defects terminates their growth up to nanodomains only. Therefore, it would be marvelous if self-standing, continuous COFMs are synthesized from mother COF crystallites in the millimeter scale. Our recent report enlightened the development of self-standing COFMs and has showcased its utility towards separation application [3.15]. Although the reported COFMs, was well enough to perform in mild conditions (max. up to as likely as 3 M HCl), they were completely unsafe in functioning at drastic conditions. In a broader sense, till date the COFMs, because of its structural instability in a hazardous environment, have not been well explored in terms of sulphuric acid purification through a separation which is industrially highly relevant and if achieved could be a break-through for this novel membrane to serve as an acid purifier.

3.2 *Fabrication of ultra-stable covalent organic framework membrane (COFM)*

Towards an attempt for solving both the issues of water and sulphuric acid purification discussed in previous sections, herein we have demonstrated the constructed of an imine linked COFMs with high crystallinity and porosity *via* salt mediated crystallization approach (**Figure 3.1**). Herein, *p*-toluene sulfonic acid (PTSA-H₂O) perform as a molecular organizer entity during the crystallization process and 2,4,6-trimethoxy-1,3,5-benzenetricarbaldehyde (TpOMe) has been employed as a prime aldehyde building unit. The as-synthesized COFMs showcased exceptionally high chemical stability in strong acids such as H₂SO₄ (18 M, 3d; 9 M, 7d); HCl (12 M; 7d) and NaOH (9 M; 1d) base. From the best of our knowledge, this is the first report where we have illustrated an imine linked COFMs with exceptionally high chemical stability in a rigorous drastic medium such as in conc. H₂SO₄ (18 M). In order to perceive the reason behind the high chemical stability of the COFMs, we have taken into consideration their molecular level investigation by DFT (Density Functional Theory) optimization of the framework structures. Moreover, it was observed the methoxy (–OCH₃) groups, present in the aldehyde, were directed into the interlayer space. Interestingly, we

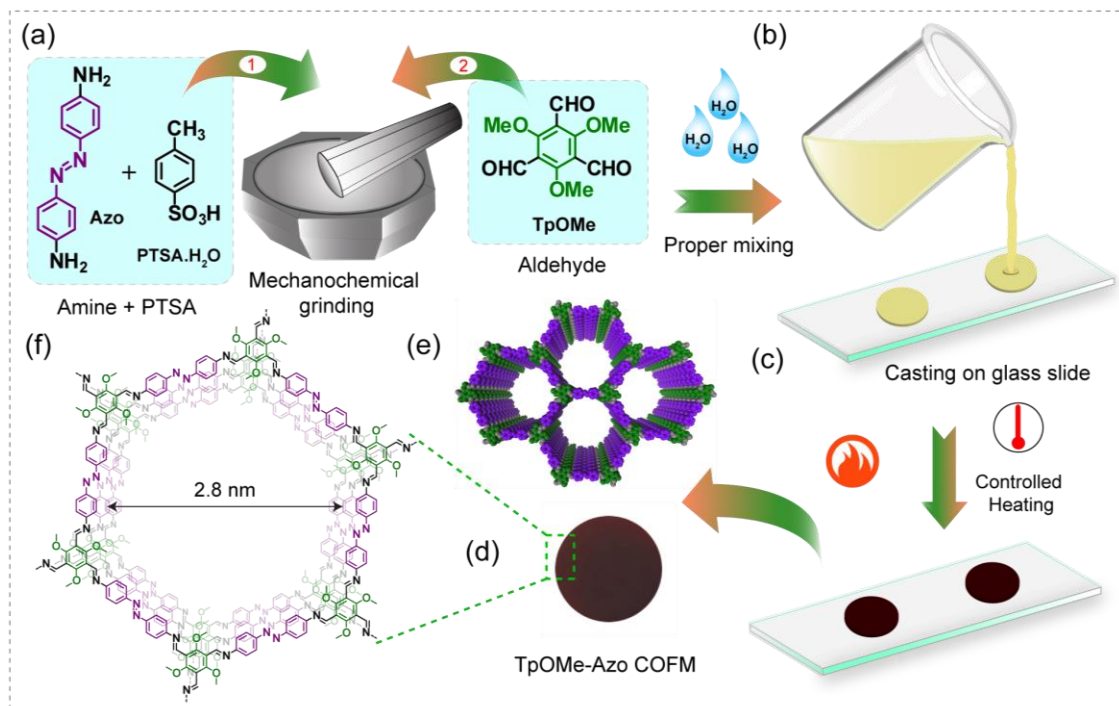


Figure 3.1: (a-c) General synthesis scheme for **TpOMe-Azo** COFM via Schiff base condensation reaction between **TpOMe** and **Azo** starting materials. d) Digital image of a membrane. (e-f) Eclipsed space-filling model and chem. draw structure of **TpOMe-Azo** COFM respectively.

noticed a significant number of interlayer C–H•••N hydrogen bonding present between the ‘C–H’ bond of methoxy (–OCH₃) group of a particular layer with imine (–C=N) nitrogen atom present in the next adjacent layers. It was believed the presence of strong interlayer C–H•••N hydrogen bonding (H-bonding) interactions among the individual layers provides significant steric hindrance and a hydrophobic environment and as a result, the labile imine (–C=N) bond get protected from being hydrolysis in strongly acidic or basic treatment. As an initial attempt, the COFM showed considerably high solvent flux for acetonitrile (280 Lm⁻²h⁻¹bar⁻¹), followed by acetone (260 Lm⁻²h⁻¹bar⁻¹), methanol (200 Lm⁻²h⁻¹bar⁻¹), water (170 Lm⁻²h⁻¹bar⁻¹), ethanol (150 Lm⁻²h⁻¹bar⁻¹) and aq. H₂SO₄ solution reflecting its potentiality towards waste solvent treatment. The as-synthesized COFMs were successfully employed as a nano-filtration membrane to separate various toxic organics from drinking water. In this case, challenging separations of expensive ingredients like methylene blue (MB), toxic dye molecules such as rhodamine b (RH), rose bengal (RB) and congo red (CR) from drinking water with high recyclability have been done. Moreover, the advancement of chemical stability showcased these COFMs to serve as a sulphuric acid purifier as well specifically

from nitroaromatics (herein 2,4,6-trinitrotoluene (TNT)) generated during toluene nitration process.

3.2.1 Synthesis of TpOMe-Azo COFM

TpOMe-Azo COFM: *P*-toluenesulfonic acid monohydrate (PTSA-H₂O) (1.8 mmol) was taken in a mortar-pestle. **Azo** (0.45 mmol; 95.4 mg) amine was added and the mixture was uniformly grinded for 5 minutes. In that mixture 2,4,6-trimethoxy-1,3,5-benzenetricarbaldehyde (**TpOMe**, 0.3 mmol, 76.2 mg) was added and properly mixed through grinding for another 5 minutes. To this mixture few drops of water (~100 μ L based on requirement) was added. The resulted soft dough material was molded into proper geometrical shape (here circular mold have been used with 1 cm diameter) prior to stepwise heating such as at 60 $^{\circ}$ C (2 days) and at 90 $^{\circ}$ C (6 h). The synthesized COFMs were properly washed with water followed by DMAc until all other side products/monomers or unreacted starting materials get removed. The COFMs were then stored in distilled water prior to several analysis (**Figure 3.1** & **Figure 3.2**). It is to be noted that the membranes can be also fabricated by directly heating at 90 $^{\circ}$ C for 1 day but rapid heating at this temperature mostly result in cracked membrane although the material could be constructed with high crystallinity and porosity at this reaction condition.

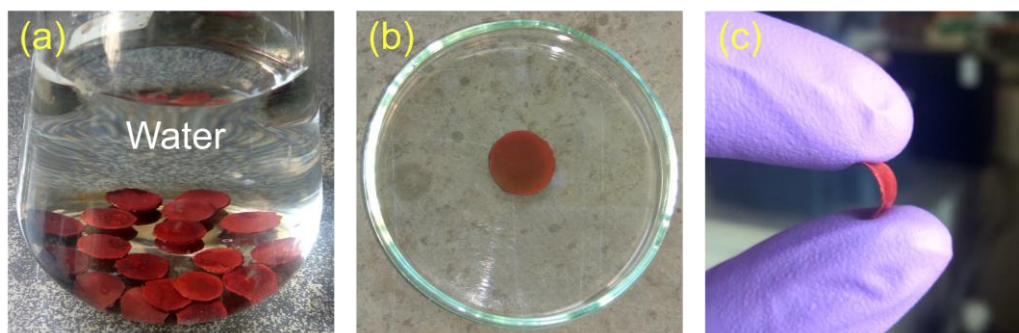


Figure 3.2: Digital images of as-synthesized **TpOMe-Azo** COFM (a) Membranes stored in distilled water, (b) Membrane kept on a glass petri dish and (c) Membrane shown with a certain flexibility in dry condition.

3.2.2 Structural simulation and characterization

The formation of COFM material was firmly confirmed from their powder X-ray diffraction pattern (**Figure 3.3**). The high intense peak at $\sim 3.3^{\circ}$ (± 0.1 , 2θ) for **TpOMe-Azo** COFM could be assigned from the strong reflection from its 100 planes. The excessive

intensity of 100 planes indicates its high crystalline nature of the membrane. The small 2θ value corresponds to 100 planes reflect its larger pore aperture. Additionally, the COFM reveal their 001 plane reflection at $\sim 27.1^\circ$ (± 0.2 , 2θ) in the PXRD pattern. The ‘d’ spacing value in ‘001’ plane is used to calculate the interlayer stacking distance among the hexagonal COF layers which is ~ 3.4 Å. To elucidate exact framework stacking and its internal arrangements different model structures such as AA, slip_AA, and AB were modeled. The experimental PXRD pattern mostly fits [TpOMe-Azo ($R_p = 2.91$ %, $R_{wp} = 2.13$ %, R_{wp} (w/o bck)=1.98 %)] with slip_AA stacking model hence the material crystallizes in slipped eclipsed manner. Pawley refinement was done on the simulated slip_AA model structure of the COFM with respect to its experimental PXRD pattern using Material studio software and was used to calculate the cell parameters. The calculation revealed the material crystallizes in a triclinic system having space group *P1* with unit cell parameters: $a = 33.1$ Å, $b = 33.3$ Å, $c = 3.72$ Å; $\alpha = 87.5^\circ$, $\beta = 89.6^\circ$, $\gamma = 59.2^\circ$ (Table 3.1).

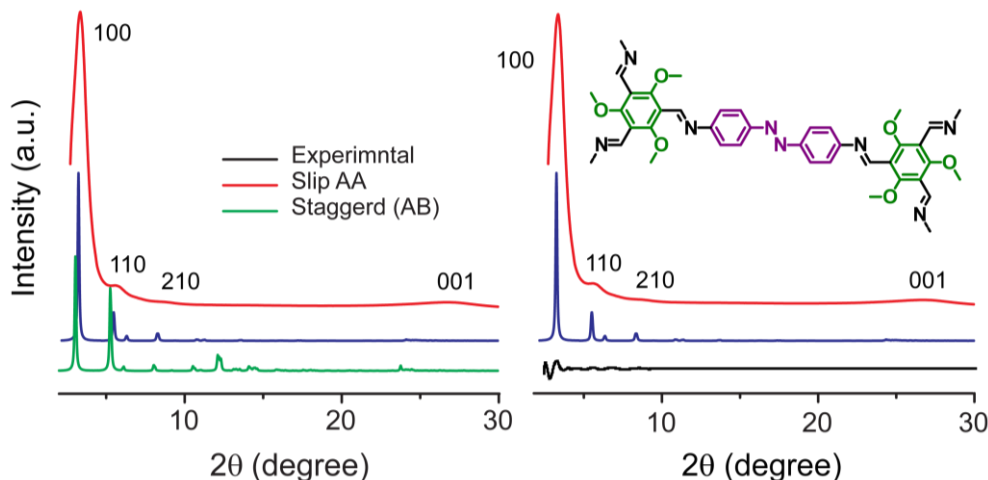


Figure 3.3: (a) Comparison PXRD of as-synthesized (red) compared with the eclipsed (blue) and staggered (green). (b) Experimental (red) PXRD profiles of TpOMe-Azo COFM compared with an eclipsed arrangement (blue); difference plot is given in (black).

Table 3.1. Fractional atomic coordinates for the unit cell of TpOMe-Azo

TpOMe-Azo (Space group- <i>P1</i>)											
$a = 33.1269$ Å, $b = 33.352$ Å, $c = 3.72031$ Å; $\alpha = 87.5191^\circ$, $\beta = 89.5664^\circ$, $\gamma = 59.2975^\circ$											
Atom	x	y	z	Atom	x	y	z	Atom	x	y	z
C1	0.82933	0.33493	0.9095	C34	0.09811	0.81474	0.06	C67	0.84511	0.3033	0.41025
C2	0.85677	0.35592	0.93763	C35	0.11837	0.76391	0.06235	C68	0.86651	0.43893	0.52791

C3	0.835	0.40431	0.97333	C36	0.1662	0.73524	0.01607	C69	0.7057	0.46533	0.39003
C4	0.78539	0.432	0.96314	C37	0.09275	0.74146	0.10502	C70	0.8958	0.22537	0.51686
C5	0.75717	0.41339	0.91301	C38	0.18861	0.68606	0.02389	C71	0.86444	0.20852	0.50487
C6	0.78	0.3646	0.89164	C39	0.11295	0.69225	0.10665	C72	0.94382	0.19342	0.55671
C7	0.84719	0.28423	0.91001	C40	0.16211	0.66469	0.07673	C73	0.8811	0.16088	0.52737
C8	0.86537	0.42359	0.00553	C41	0.23942	0.65511	0.99682	C74	0.96037	0.14591	0.57955
C9	0.70617	0.44498	0.89417	C42	0.0796	0.67562	0.13727	C75	0.92913	0.12895	0.56587
C10	0.89428	0.20752	0.03332	C43	0.31206	0.63397	0.86839	C76	0.88362	0.49655	0.60103
C11	0.86354	0.19057	0.00544	C44	0.34166	0.65226	0.83108	C77	0.92884	0.46839	0.68059
C12	0.94152	0.17568	0.08515	C45	0.33169	0.58495	0.87565	C78	0.86857	0.54335	0.54639
C13	0.88028	0.14282	0.02262	C46	0.3897	0.62271	0.8102	C79	0.95851	0.4862	0.69821
C14	0.95822	0.12806	0.10134	C47	0.32651	0.69035	0.82419	C80	0.8985	0.56082	0.56141
C15	0.92778	0.1109	0.06963	C48	0.37977	0.5554	0.85477	C81	0.94427	0.53229	0.63618
C16	0.87959	0.48215	0.09523	C49	0.53239	0.52636	0.77693	C82	0.00336	0.00678	0.64695
C17	0.92575	0.455	0.16707	C50	0.563	0.54315	0.73494	C83	0.97719	0.98763	0.58011
C18	0.86112	0.53022	0.052	C51	0.55171	0.4783	0.82383	C84	0.04924	0.97637	0.71665
C19	0.95314	0.47522	0.18816	C52	0.6115	0.51329	0.74523	C85	0.99685	0.93954	0.58019
C20	0.8889	0.55007	0.06913	C53	0.60011	0.44827	0.8312	C86	0.0693	0.92812	0.71447
C21	0.93562	0.52263	0.13615	C54	0.63061	0.46562	0.79726	C87	0.0436	0.90915	0.64209
C22	0.00228	0.98825	0.13434	C55	0.75689	0.51365	0.87474	C88	0.99454	0.60424	0.59271
C23	0.97453	0.96961	0.07982	C56	0.93248	0.29018	0.84269	C89	0.97888	0.65056	0.52937
C24	0.04936	0.95744	0.19049	C57	0.72979	0.33379	0.98553	C90	0.04177	0.57563	0.65304
C25	0.99345	0.92156	0.08171	C58	0.21922	0.76272	0.09059	C91	0.00894	0.66824	0.52852
C26	0.06874	0.9093	0.18823	C59	0.00986	0.78946	0.01798	C92	0.07215	0.59289	0.64868
C27	0.04104	0.89086	0.13199	C60	0.17483	0.58754	0.18546	C93	0.05607	0.63964	0.58942
C28	0.98339	0.59665	0.09791	C61	0.82724	0.35374	0.41674	C94	0.10336	0.83255	0.58029
C29	0.96858	0.64327	0.04229	C62	0.85503	0.37339	0.4595	C95	0.12114	0.78231	0.56836
C30	0.03117	0.56591	0.14642	C63	0.83472	0.42175	0.48799	C96	0.16892	0.75222	0.52457
C31	0.00049	0.65881	0.0343	C64	0.78545	0.45093	0.46238	C97	0.09238	0.76256	0.59664
C32	0.06318	0.58108	0.1358	C65	0.75651	0.43309	0.41393	C98	0.18798	0.70349	0.50633
C33	0.04824	0.62777	0.08032	C66	0.77821	0.38442	0.39136	C99	0.11029	0.71386	0.58883
C100	0.15817	0.68524	0.54419	C107	0.38184	0.57059	0.37871	C114	0.63049	0.48313	0.29378
C101	0.23595	0.67032	0.45082	C108	0.4102	0.58811	0.31205	C115	0.76335	0.52916	0.34797
C102	0.07773	0.6965	0.6162	C109	0.53238	0.54159	0.25606	C116	0.93304	0.31862	0.34585
C103	0.31319	0.64904	0.36851	C110	0.56255	0.55821	0.20382	C117	0.72472	0.35627	0.46659
C104	0.34145	0.66631	0.29682	C111	0.55212	0.49458	0.32065	C118	0.23245	0.76529	0.60791
C105	0.33422	0.60037	0.40716	C112	0.61106	0.52948	0.22268	C119	0.01128	0.81719	0.50174
C106	0.38909	0.63655	0.26878	C113	0.60051	0.46559	0.3364	C120	0.19154	0.60602	0.67406
N1	0.87965	0.25519	0.02132	N9	0.26384	0.66545	0.88955	N17	0.98665	0.05495	0.6425
N2	0.85019	0.46392	0.07118	N10	0.08212	0.64099	0.05792	N18	0.9769	0.54728	0.6506
N3	0.6792	0.43424	0.81132	N11	0.45797	0.54124	0.8126	N19	0.96197	0.58911	0.58593
N4	0.94282	0.063	0.07986	N12	0.48384	0.55901	0.77544	N20	0.06166	0.86111	0.63427
N5	0.98595	0.03633	0.13186	N13	0.88107	0.27301	0.50546	N21	0.26658	0.68204	0.40818
N6	0.96682	0.53925	0.14984	N14	0.85213	0.48081	0.57549	N22	0.0884	0.65486	0.57885
N7	0.95024	0.58211	0.09482	N15	0.67888	0.45292	0.31719	N23	0.45861	0.55605	0.30282
N8	0.05877	0.84263	0.13355	N16	0.9442	0.0811	0.58214	N24	0.48371	0.57352	0.24845
O1	0.76222	0.47882	0.01328	O5	0.1908	0.75735	0.95525	O9	0.9037	0.346	0.49163
O2	0.75442	0.34334	0.8426	O6	0.18939	0.61663	0.08908	O10	0.0453	0.79067	0.64705
O3	0.90513	0.33301	0.93709	O7	0.76309	0.49879	0.49504	O11	0.19479	0.77395	0.48263
O4	0.04564	0.76785	0.16015	O8	0.75188	0.36506	0.33145	O12	0.17677	0.63739	0.51455

3.2.3 Chemical characterization

The successful formation of imine bonds in **TpOMe-Azo** COFM was firmly confirmed by FT-IR and ^{13}C CP-MAS solid-state NMR analysis. Prior to the analysis, the as-synthesized COFM were completely activated at elevated temperature ($120\text{ }^\circ\text{C}$) for 12 h at vacuum to remove any trapped solvent molecules and to avoid any spectral contributions from the solvents. Moreover, the FTIR analysis of the **TpOMe-Azo** revealed the complete disappearance of any primary N–H stretching ($3341\text{--}3472\text{ cm}^{-1}$) of the Azo amine and C=O stretching generally appeared at 1682 cm^{-1} in the TpOMe aldehyde (**Figure 3.4**).

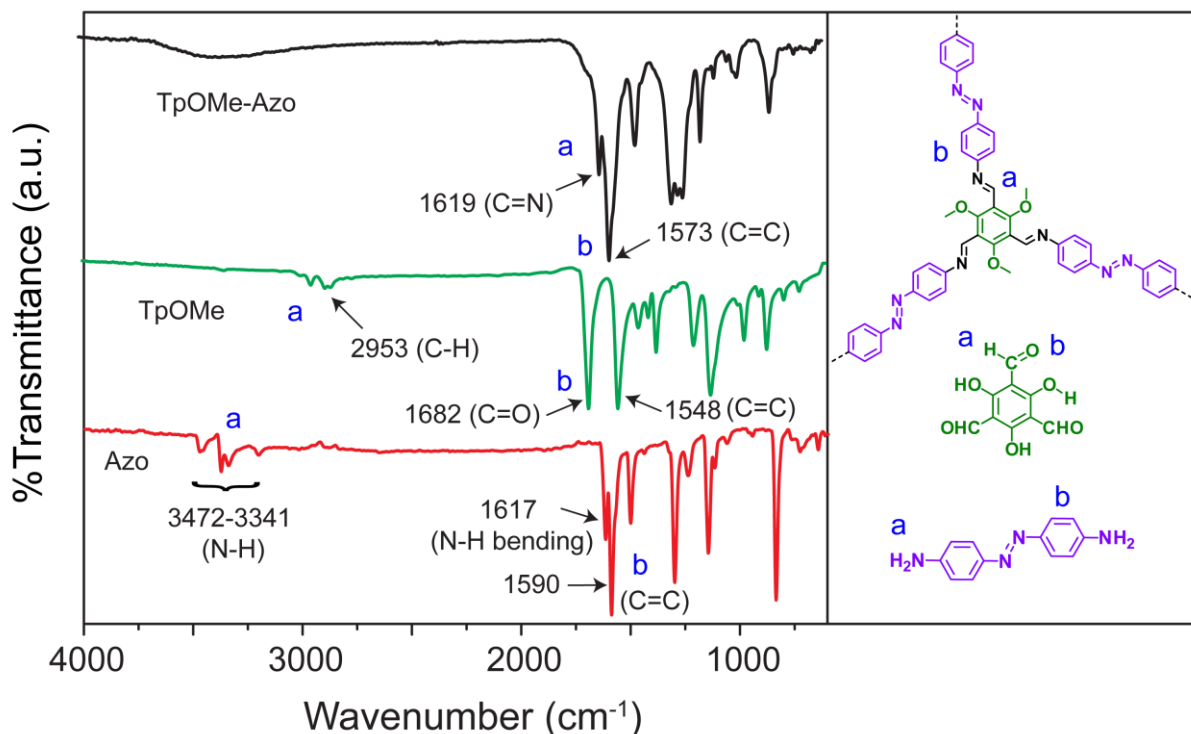


Figure 3.4: FT-IR data of **TpOMe-Azo** COFM compared to starting materials.

The newly formed imine bond ($-\text{C}=\text{N}-$) which is resulted from the Schiff base condensation reaction between amine ($-\text{NH}_2$) and aldehyde ($-\text{CHO}$) functionalities appeared at 1619 cm^{-1} . The successful formation of imine linkage ($-\text{C}=\text{N}-$) in the spectrum with the disappearance of any signature of amine and aldehyde revealed the complete consumption of starting material during the reaction and their successful transformation to 2 D COF structure. The aromatic C=C stretching frequency appeared in as-synthesized COFM as well as in the starting materials appeared at $1548\text{--}1590\text{ cm}^{-1}$. The atomic level construction of various carbon atoms was further evaluated using solid-state ^{13}C CP-MAS spectra (**Figure 3.5a**).

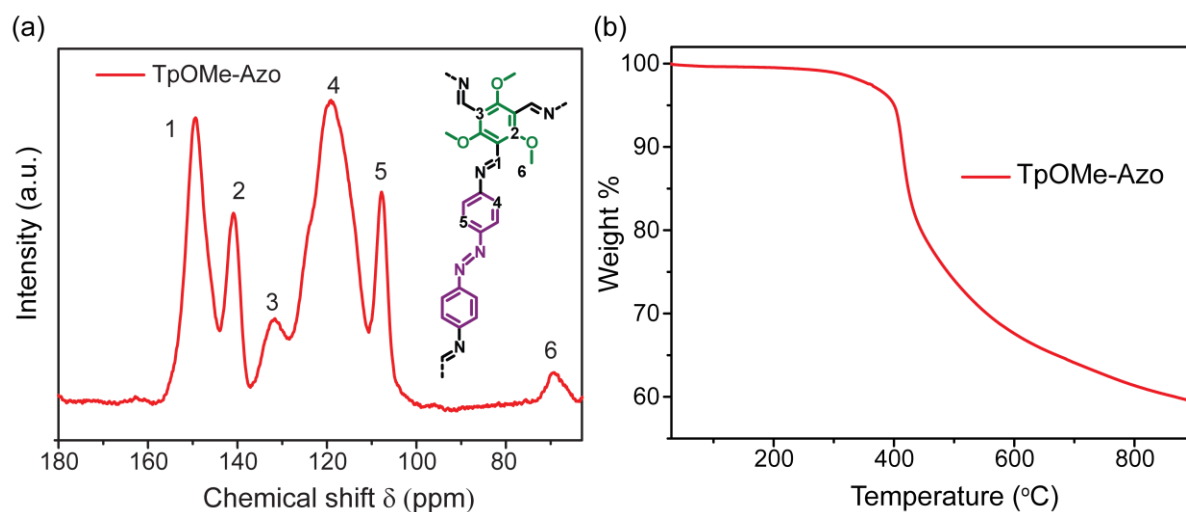


Figure 3.5: (a) Solid state ^{13}C spectra of **TpOMe-Azo COFM** (partial chem. draw assigning possible signaling carbons have been shown in inset). (d) TGA data of activated COFM under N_2 atmosphere.

The imine ($-\text{C}=\text{N}-$) linked carbon atom reflect its characteristics signal at 149.3 ppm whereas the signature of all other aromatic carbons appeared in the range 140-108 ppm in the spectrum. The methoxy carbons showed its characteristics chemical shift at about 69.5 ppm.

Thermogravimetric analysis (TGA) of as-synthesized **TpOMe-Azo COFM** was performed using the temperature, ranging from 25 to 900 °C to analyze the overall thermal stability of the material (**Figure 3.5b**). During the gradual increment of the temperature, no significant weight loss was observed up to 400 °C was observed. Moreover, the framework stability up to this temperature is considered as very promising value reported for framework materials. Once it exceeds 400 °C there happens a gradual weight drop from 100 % to 60 % which revealed rapid gradual framework degradation after that it got saturated. Moreover, the TGA profile showed running up to 900 °C the material could retain up to 60 wt% of its overall weight.

3.2.4 Gas adsorption studies

The porosity or surface area is considered as one of the very important properties of porous materials as it is directly connected to its most accessible void space. Again, the extent of surface area value reflects very crucial information regarding the internal ordering of pores within a material. To that end, such information is highly important when those materials are directly employed for molecular sieving or removal of toxic contaminants from

drinking water. Moreover, the stated experiments are largely dependent on the molecular level pore aperture of such materials. Therefore, herein to evaluate the porosity or surface area N_2 adsorption was recorded for the activated (120 °C, 12 h under vacuum) COFM samples (**Figure 3.6a**). The isotherm mostly follows type IV where an initial steep in nitrogen uptake was observed in the range $P/P_0 = 0.03$ to 0.2 bar. Such steep are the predominant nature of mesoporous materials. The surface area calculation was done using Brunauer-Emmett-Teller (BET) model where the maximum surface area of the COFM was evaluated as 2,154 m^2/g is one of the highest surface areas reported in the literature for a 2 D crystalline COFs. To analyze the specific pore aperture of the COFM is important for its potential usage in separation application, pore size distribution of the as-synthesized COFM was also calculated using cylindr./sphere pores, QSDFT adsorption branch model. Moreover, from that model, the experimental pore diameter was evaluated as 27.9 nm (half pore width 13.95 nm) which also signifies the material is predominantly mesoporous in nature (**Figure 3.6b**).

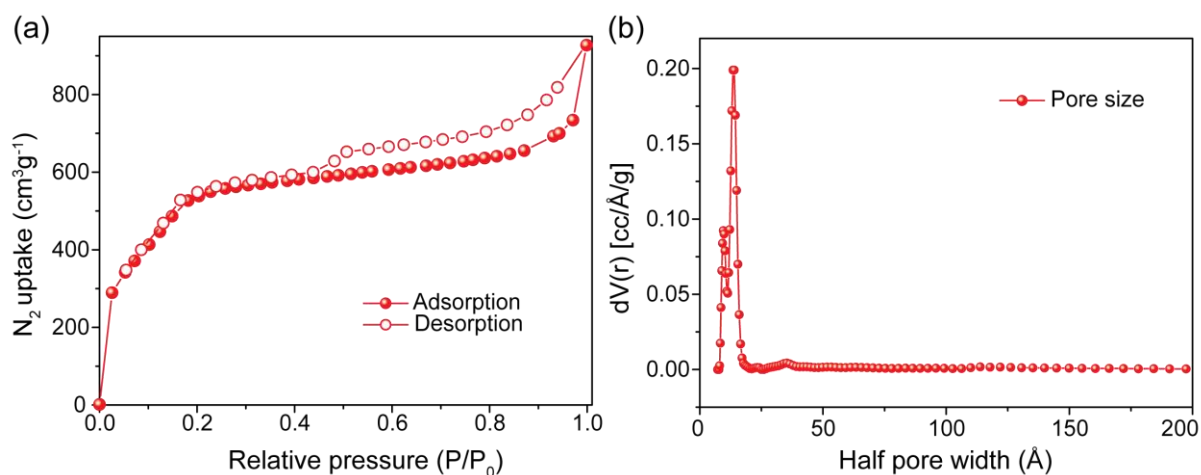


Figure 3.6: (a) N_2 adsorption and (b) Experimental pore size distribution (cylindr./sphere pores, QSDFT adsorption branch) of as-synthesized **TpOMe-Azo** COFM.

The nano-scale crystallite morphology and the thickness of the **TpOMe-Azo** COFM were evaluated using scanning electron microscopy (SEM) studies. Herein, the crystallite morphology was determined from both top and cross-view of the COFM. Moreover, perpendicular view (top view) of SEM analysis revealed the material is mostly composed of

small crystallites (length ca. 1-3 μm) which are perfectly packed with each other to bring a continuous, self-standing and crack-free nature to the membrane (**Figure 3.7a**).

3.2.5 Morphology investigation

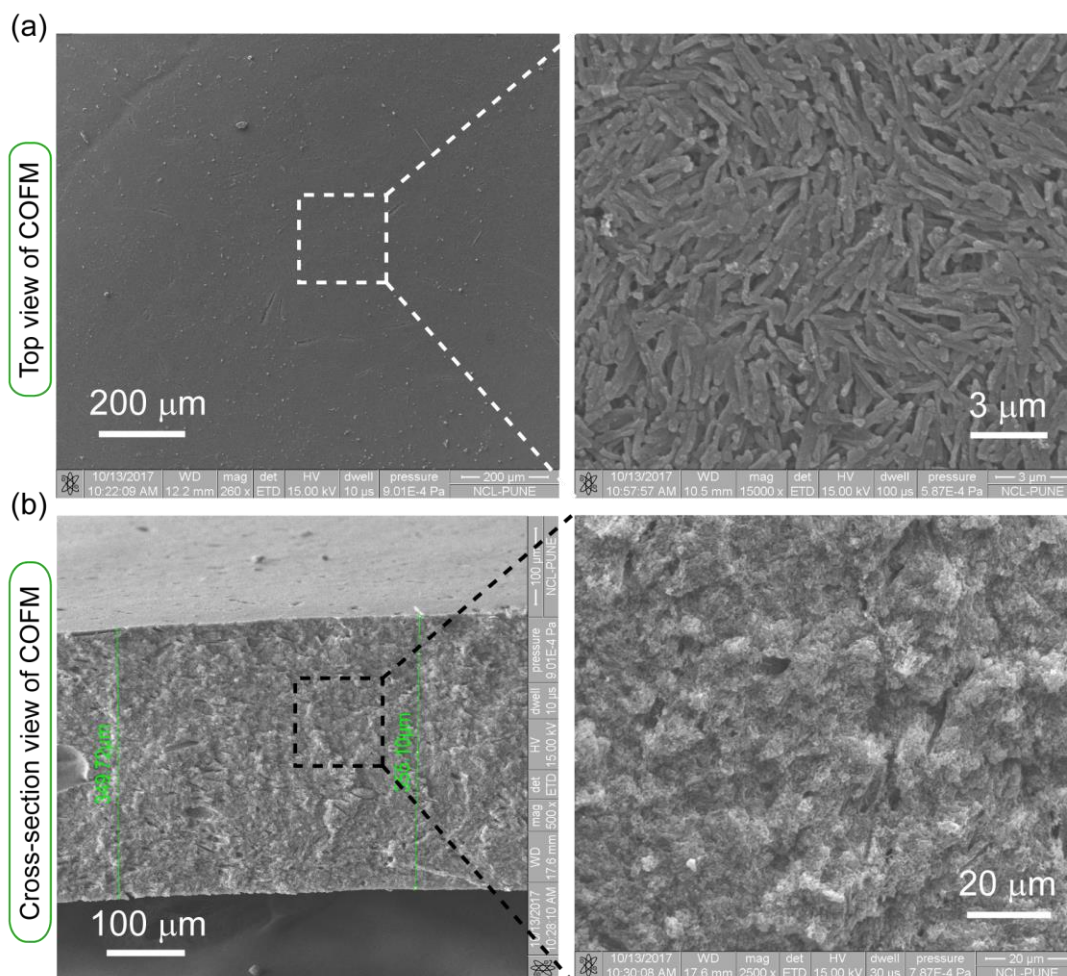


Figure 3.7: (a) Top view and (b) cross-section view from SEM of as-synthesized *TpOMe-Azo* COFM. Scale bars have been shown on inset.

The cross-section SEM analysis was used to calculate the thickness of the sheet, which varies in the range 200-220 μm (**Figure 3.7b**). The efficient crystallite-crystallite packing could significantly reduce the number of grain boundaries hence the internal defects associated with the membrane. These novel characteristics of the membrane would help its proper utilization of pore channels for various potentially important separation applications where specific pore aperture with tiny structural defects usually played a very incredible role.

3.2.6 Chemical stability investigation

The chemical stability measurement of the as-synthesized **TpOMe-Azo** COFM was performed using relatively drastic media. This is important in terms of its applicability to equally perform in such environmental conditions where relatively harsh separation conditions are employed. Therefore, in the present study, to analyze the chemical stability of **TpOMe-Azo** COFM, the as-synthesized membrane (1 cm diameter) was treated in more vigorous conditions like conc. H_2SO_4 (18 M; 3 days), conc. HCl (12 M; 7 days), dil. H_2SO_4 (9 M; 7 days) and in NaOH (1 day; 9M) for stipulated time duration.

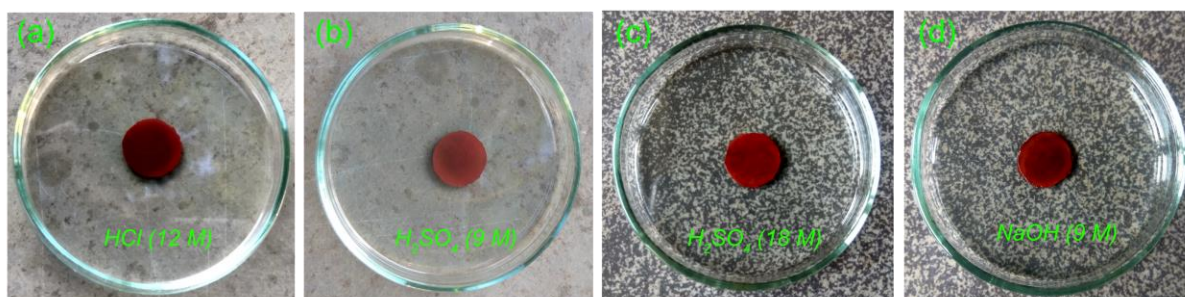


Figure 3.8: Physical appearance of the **TpOMe-Azo** COFM after treatment in (a) HCl (12 M) for 7 days, (b) H_2SO_4 (9 M) for 7 days, (c) H_2SO_4 (18 M) for 3 days and (d) NaOH (9 M) for 1 day.

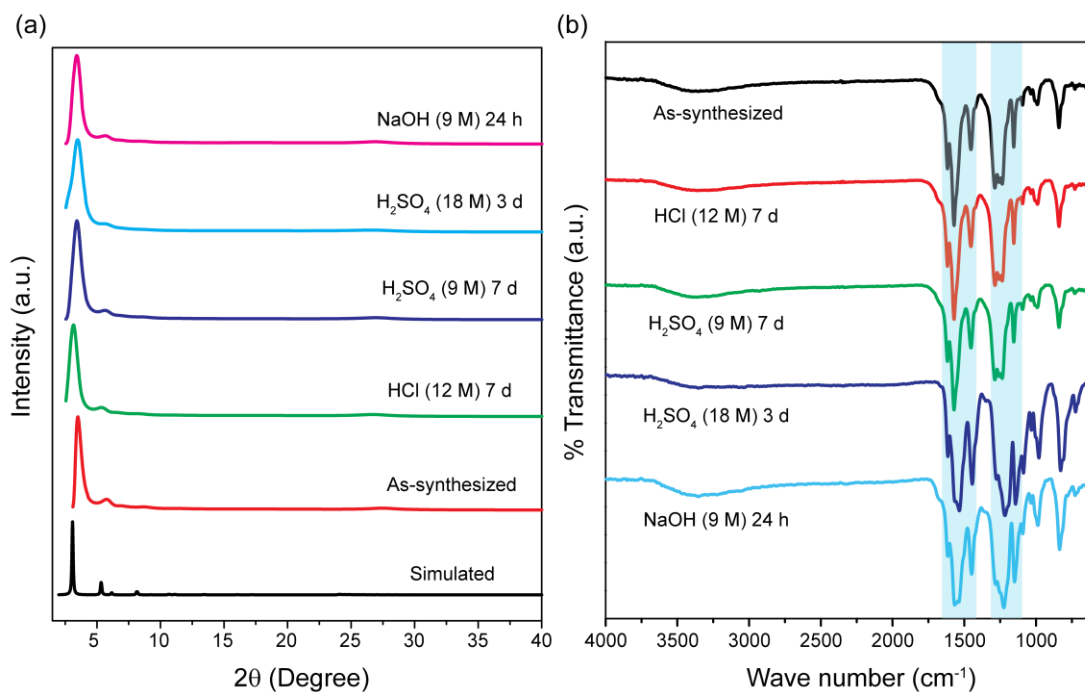


Figure 3.9: Comparison of (a) PXRD and (b) FTIR of **TpOMe-Azo** COFMs after treatment in a different solvent as mentioned.

After completion of its respective time duration, the membranes were isolated and were thoroughly washed with water, N, N-dimethylacetamide, and acetone prior to drying. The dried membrane was then activated at 120 °C for 12 h in vacuum and was used for its further characterizations such as PXRD, FT-IR, and surface area analysis. However, for SEM analysis the activation step was avoided and partially dried membrane was directly coated on Si-wafer for data collection.

Moreover, the physical appearance of the membrane after treatment in such vigorous solvent conditions was similar to its as-synthesized form. The color and shape of the membrane were also more or less intact after such treatment (**Figure 3.8**). The PXRD of the treated membrane also showcased similar crystallinity as its parent material, as most of the peaks in the treated membrane were properly visible in the PXRD pattern though there was a slight decrease in the peak intensities (**Figure 3.9a**). On the other hand, the FTIR spectra revealed the similar stretching frequency of its various characteristic bands present in treated samples compared to the as-synthesized material (**Figure 3.9b**). Hence, the material could retain its internal structural arrangements even after treatment in such drastic solvent media.

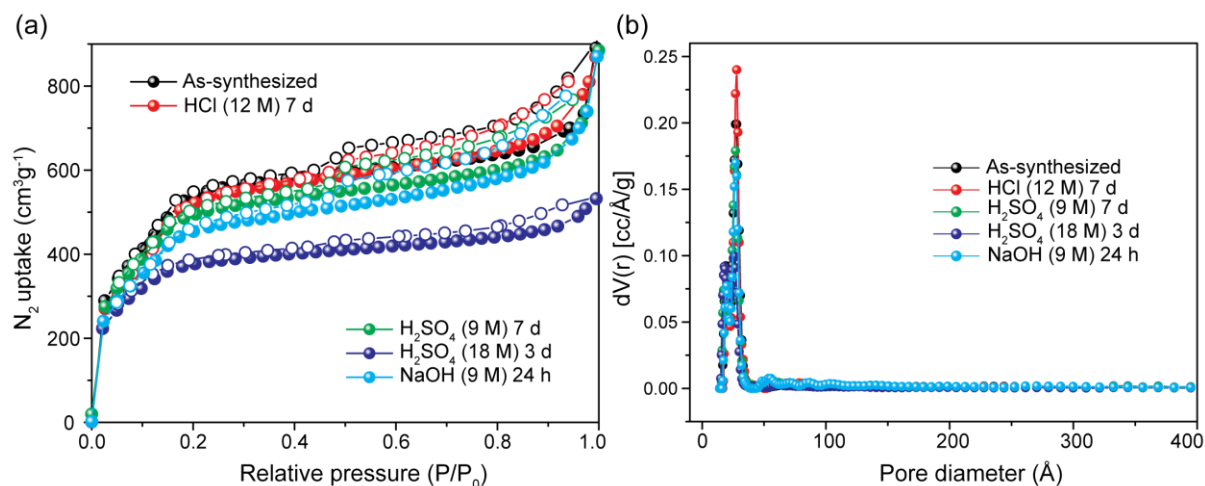


Figure 3.10: Comparison of (a) N_2 adsorption and (b) Experimental pore size distribution (cylindr./sphere pores, QSDFT adsorption branch) of **TpOMe-Azo** COFMs after treatment in a different solvent as mentioned.

Separately, we have also performed the surface area measurement of the treated membranes using N_2 adsorption analysis (77 K; liq. N_2 temperature) (**Figure 3.10a**). The S_{BET} revealed, the acid or base treated samples almost retained their porosity reflecting its structural rigidity

in such abrasive conditions. The BET surface area of the material was evaluated as 2141, 1996, 1416, 1935 m²/g with compared to as synthesized (2154 m²/g) material after treatment in conc. HCl (12 M; 7 days), dil. H₂SO₄ (9 M; 7 days), conc. H₂SO₄ (18 M; 3 days), and in NaOH (1 day; 9M) respectively. Experimental pore size distribution also reflects maintenance of one type of major pore in the treated samples (**Figure 3.10b**).

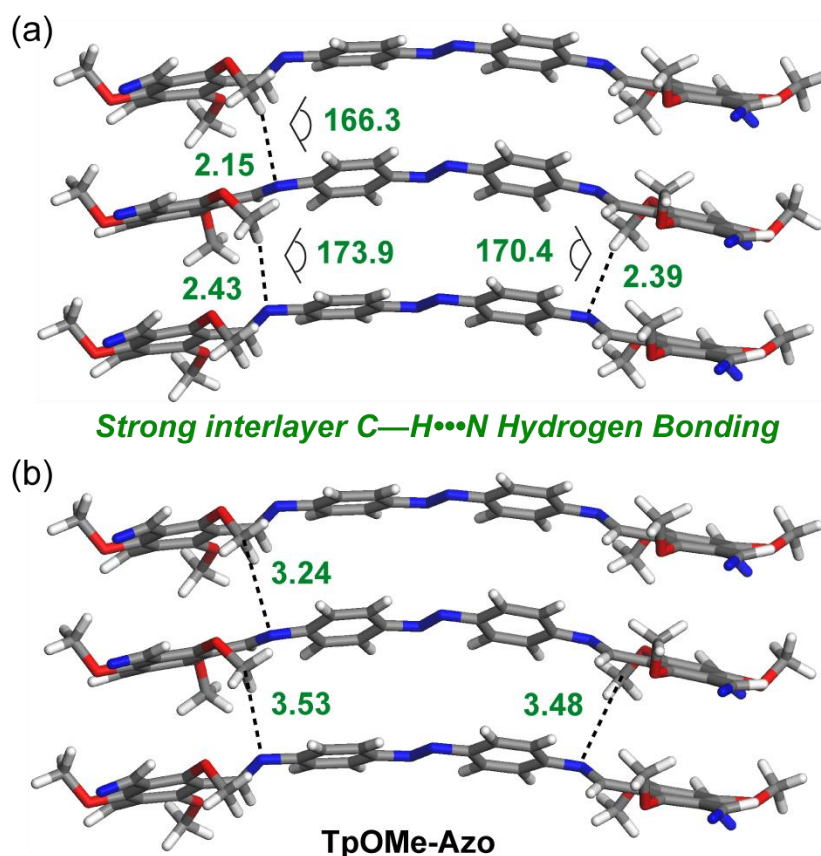


Figure 3.11: Interlayer C—H...N H-bonding: (a) distances (H to N atom in dotted line; Å) and angles (C—H...N) in degree (b) C to N atom distance in dotted line; Å for TpOMe-Azo COFM.

The high chemical stability was attributed due to the presence of strong interlayer C—H...N hydrogen bonding between methoxy C—H of one layer with imine ‘N’ atom present in the adjacent layer (**Figure 3.11**). The interlayer C—H...N H-bonding allows the methoxy groups to occupy interlayer spacing hence create both hydrophobic and steric effect around the adjacent imine bonds and protect them from being hydrolyzed in such abrasive environment (strong acid or base).

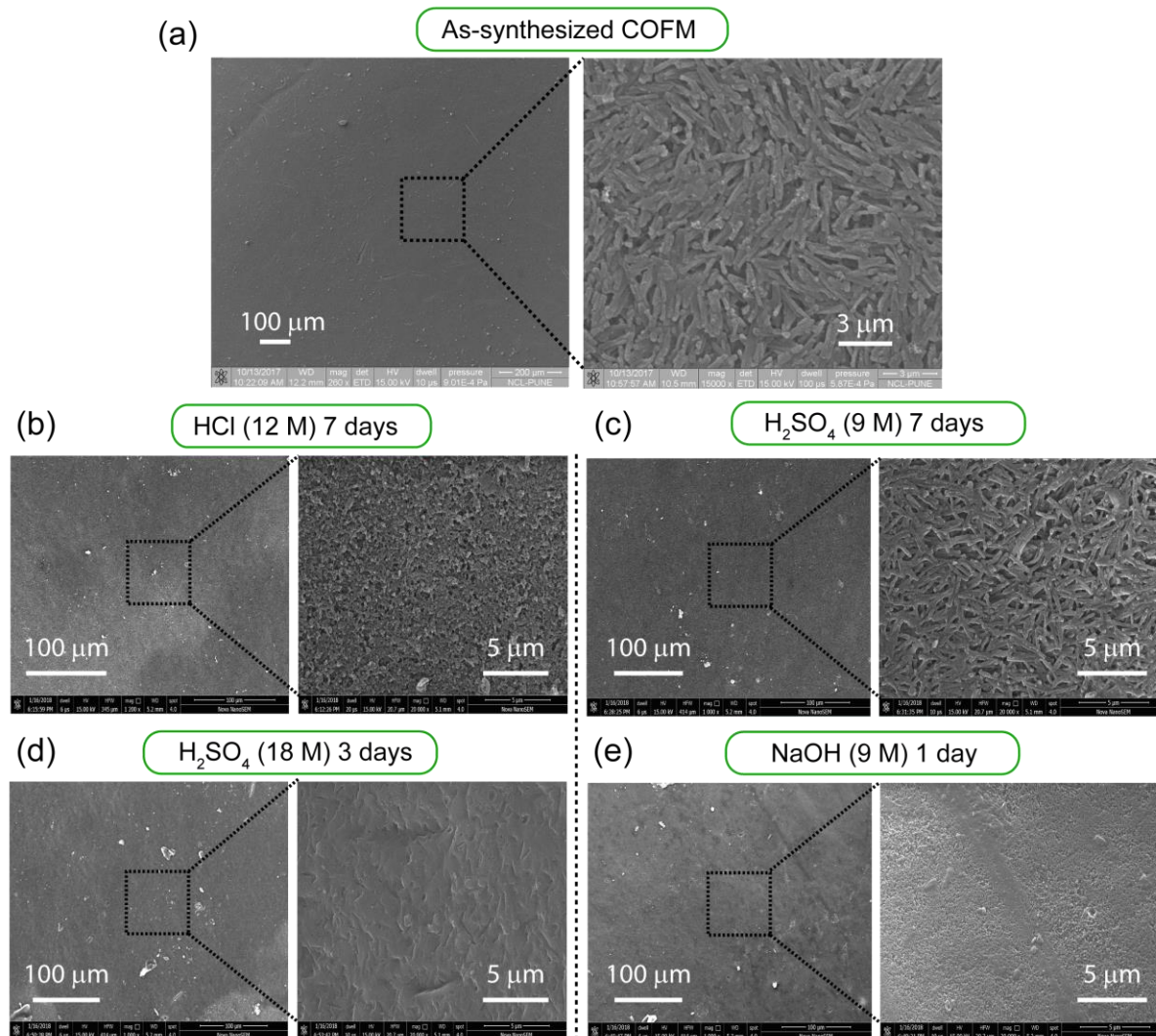


Figure 3.12: SEM images of the TpOMe-Azo COFM after treatment in (b) HCl (12 M) for 7 days, (c) H_2SO_4 (9 M) for 7 days, (d) H_2SO_4 (18 M) for 3 days and (e) NaOH (9 M) for 1 day compared to its (a) as-synthesized material.

Apart from PXRD, FT-IR and N_2 adsorption analysis, the chemical stability investigation was also performed using scanning electron microscopy (SEM) imaging technique. The SEM was recorded for the treated samples and was compared the same with the as-synthesized COFM. Among all other, the COFM treated in 9 (M) H_2SO_4 for 7 days reveal almost identical crystallite nature compared to its parent as-synthesized COFM. However, the other solvent treated membranes showed a significant change in their crystallite morphology compared to as-synthesized COFM (**Figure 3.12**).

3.3 Water purification study using *TpOMe-Azo* COFM

Since the as-synthesized *TpOMe-Azo* COFM were highly stable at drastic solvent conditions we decided to utilize the COFM as the high-performance separation membranes in a drastic environment, where toxic solvents or highly acidic solution are involved. Moreover, Owing to their comparatively easy route of process-ability apart from self-standing ***TpOMe-Azo*** COF membranes (COFMs) fabrication, some other shapes such as spheres, cylinders, and beads were also synthesized reflecting the generality of the process (**Figure 3.14**). However, we mostly concentrated on the membrane for its important use in separation technology. As an initial attempt, the COFM showed considerably high solvent flux for acetonitrile ($280 \text{ Lm}^{-2}\text{h}^{-1}\text{bar}^{-1}$), followed by acetone ($260 \text{ Lm}^{-2}\text{h}^{-1}\text{bar}^{-1}$), methanol ($200 \text{ Lm}^{-2}\text{h}^{-1}\text{bar}^{-1}$), water ($170 \text{ Lm}^{-2}\text{h}^{-1}\text{bar}^{-1}$) and ethanol ($150 \text{ Lm}^{-2}\text{h}^{-1}\text{bar}^{-1}$), reflecting its potentiality towards waste solvent treatment (**Figure 3.13a**).

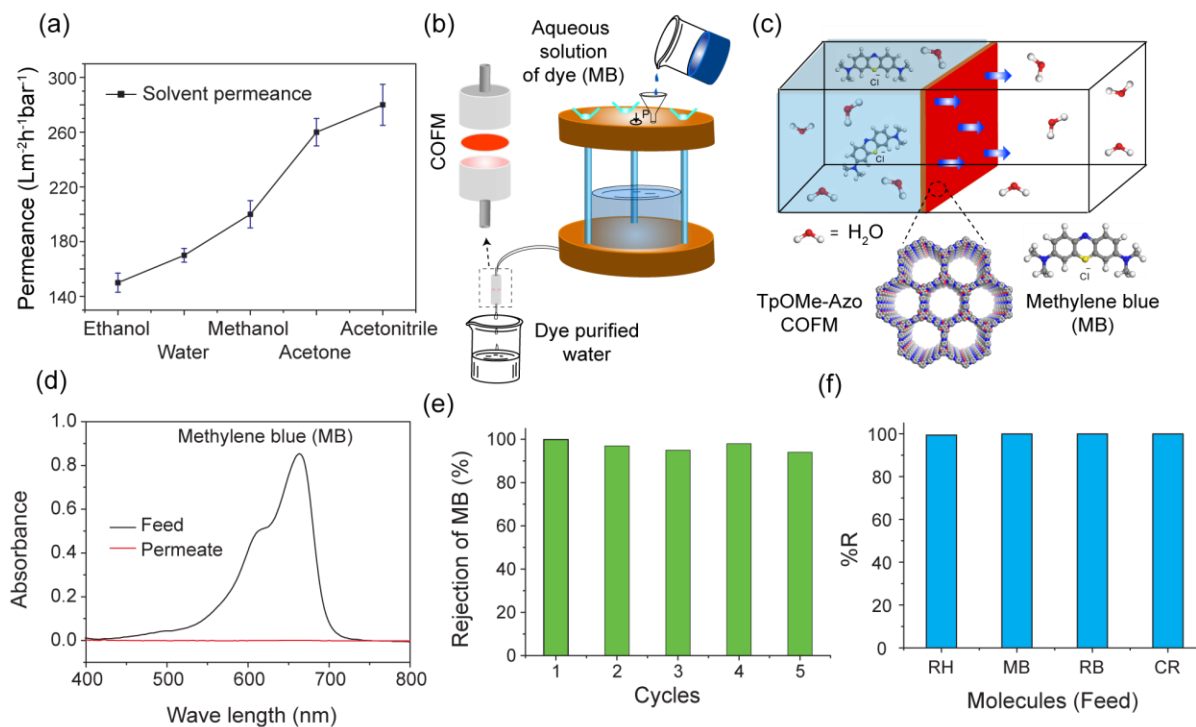


Figure 3.13: (a) Solvent permeance study using *TpOMe-Azo* COFM. (b,c) Schematic illustration of the nano-filtration assembly showing the water purification process from organic dyes (MB-Methylene Blue) through *TpOMe-Azo* COFM. (d) UV-Vis spectrum comparison for Methylene Blue feed vs permeate. (e) Recyclability test of the *TpOMe-Azo* COFM for Methylene Blue (MB) for consecutive five cycles. (f) % of other dye rejection from water through *TpOMe-Azo* COFM.

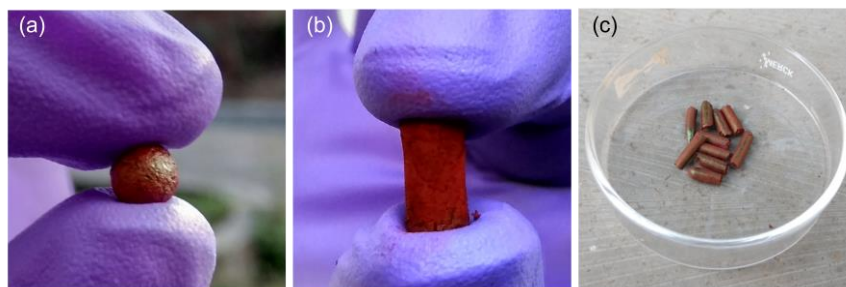


Figure 3.14: As-synthesized TpOMe-Azo COF with other different shapes. (a) sphere (b) solid cylinder and (c) beads.

Apart from that, owing to its high porosity associated with ordered pore channels (as revealed from its uniform pore size distribution), the as-synthesized COFMs were utilized for the challenging separations of expensive ingredients like methylene blue (MB), toxic dye molecules such as rhodamine b (RH), rose bengal (RB) and congo red (CR) from drinking water with high recyclability (**Figure 3.13b-f** & **Table 3.2**). The rejection performance of the COFMs was realized from the UV-Vis spectra of permeate by comparing with its mother feed solution. From these UV-Vis analyses, complete disappearance of the main characteristics absorption peaks in the range 450-700 nm has been observed for the permeate, signifying with >99% rejection (**Figure 3.13d** & **3.15a-c**) for all the dyes. The high rejection capability for a broad range of water contaminants further suggests the applications of COFMs for the water purification technologies. Again, the high acid stability of the membrane empowered us to utilize the same for acid purification which is considered as one of the most important applications associated with the industries.

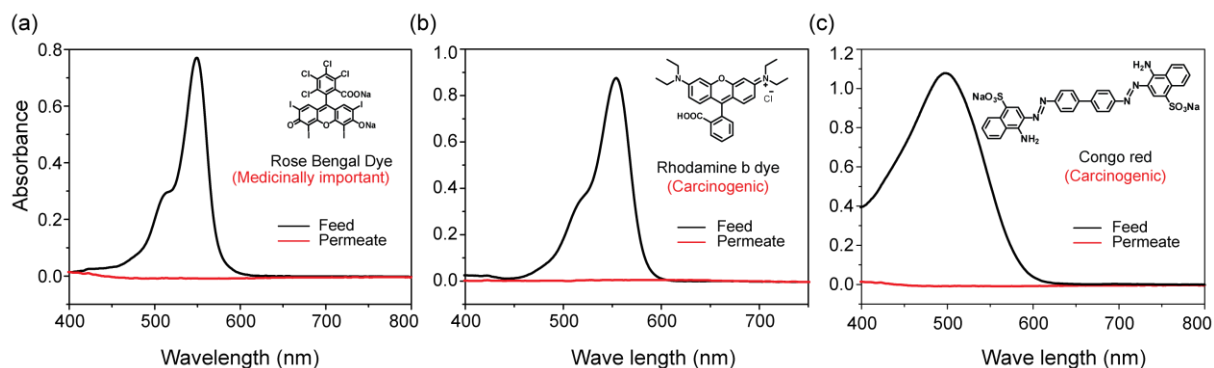


Figure 3.15. UV-vis spectra comparison of dye molecules. (a) Rose Bengal (RB), (b) Rhodamine B (RH), (c) Congo Red (CR) before (feed) and after (permeate) passing through the TpOMe-Azo COFM.

Table 3.2: Nano-filtration performance of COFM **TpOMe-Azo** (350 μm thickness) towards water purification from carcinogenic dyes.

Dye molecules	Molar mass (g/mol)	Solvent	Rejection (%)
Methylene blue (MB)	319.85	H ₂ O	99.9%
Rose Bengal Na salt (RB)	1,017.65	H ₂ O	99.9%
Rhodamine b (RH)	479.02	H ₂ O	99.4%
Congo Red Na Salt (CR)	696.66	H ₂ O	99.9%

3.4 Sulphuric acid recovery using **TpOMe-Azo** COFM

Among all other acids, sulphuric acid is an industrially used and highly important manufactured chemical by many industries, not only due to its usability in various reactions but also due to its high reactivity. Although many methods have been demonstrated for its decomposition after the reaction, very few attempts have been done for its recovery from the reaction mixture [3.11]. In these circumstances, we believe that sulfuric acid purification *via* membrane permeance could be another route for its recovery process.

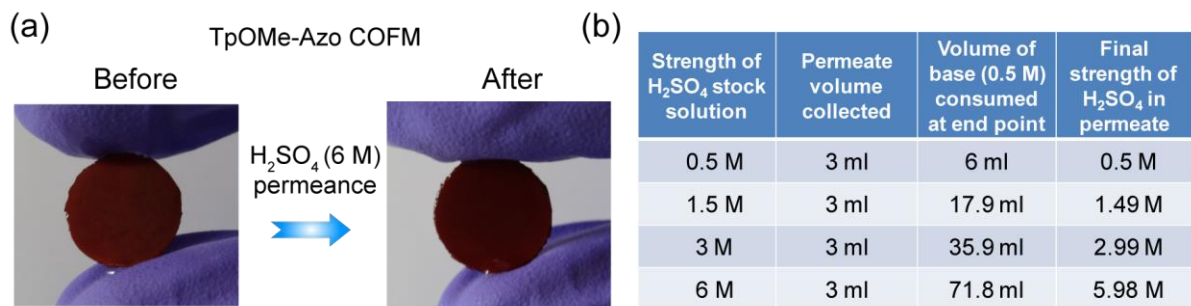


Figure 3.16. (a) The physical appearance of the membrane before and after 6 (M) sulfuric acid permeation. (b) Tabular representation for a quantitative test for a proton in permeate through the titration test with standard aq. NaOH base.

Considering the high chemical stability of the as-synthesized **TpOMe-Azo** membrane, we tested the same for standard sulphuric acid solution permeance. Initially, we passed a different aqueous solution of H₂SO₄ with a concentration of 0.5 M, 1.5 M, 3 M and 6 M through the membrane to analyze its permeance performance, where we observed the permeance as high as >99% (**Figure 3.16b**). The physical appearance of the membrane was significantly intact reflecting its robustness during the process (**Figure 3.16a**). On every occasion, the strength of the eluted sulphuric acid solution was estimated *via* titration with

the standard aqueous sodium hydroxide (0.5 M) using phenolphthalein as an acid-base titration indicator (**Table 3.6**). By measuring the volume of the base consumed at the endpoint, the final strength of sulphuric acid was calculated, which reflects the comparable concentration in elute with respect to the stock solution (**Figure 3.16b**). Based on the result obtained, we could conclude that the membranes are very much promising towards good aq. H₂SO₄ permeance. Keeping this in perspective we have tried to recover aq. H₂SO₄ similar to its recovery during toluene nitration process which is industrially very important as that H₂SO₄ can be reused or recycled.

Herein, we have prepared a stock solution of 2,4,6-trinitrotoluene (TNT) [**Caution:** TNT is firmly used in the making of explosive materials also toxic, hence should be handled very carefully] in ethanol with sulfuric acid in water. We made a separate solution of 2 M H₂SO₄ in water and 200 μM TNT solutions in ethanol. After that to make a stock solution, we mixed the same volume of TNT (in ethanol) and aq. acid solution where the final strength of TNT and H₂SO₄ was maintained as 100 μM and 1 M respectively. The complete preparation procedure is provided in **Table 3.3**. We also separately prepared 100 μM TNT (in ethanol) and 1 M aq. H₂SO₄ solution. The as-prepared stock solution (feed; a mixture of TNT and acid) was passed through the **TpOMe-Azo** membrane and permeate was collected for further analysis. We collected UV-Vis absorption spectra of the following solutions: 1) 100 μM ethanol solution of TNT, b) 1 M aq. H₂SO₄ solution, c) (1:1; v/v) stock solution (feed) prepared from TNT (200 μM; ethanol) and H₂SO₄ (2 M; water) solution and d) solution permeated through the membrane.

Table 3.3: Preparation of various solutions

Components	Amount taken	Solvent added	Final strength
TNT	4.54 mg	100 ml ethanol	200 μM
H ₂ SO ₄	8 ml (18 M)	64 ml water	2 M
Stock solution preparation			
TNT (200 μM)	50 ml ethanol solution	Final volume 100 ml	100 μM
H ₂ SO ₄ (2 M)	50 ml aq. solution		1 M

Note 1: In toluene nitration process there is a possibility for the formation of TNT which is a highly explosive material. Hence we have specifically chosen TNT separation from sulfuric acid to showcase possible application of COFM as an explosive material separation as well.

Note 2: Stock solution: 1:1 v/v mixture of TNT (in ethanol) and H₂SO₄ (in water) where the final strength of TNT and H₂SO₄ was maintained as 100 μM and 1 M respectively.

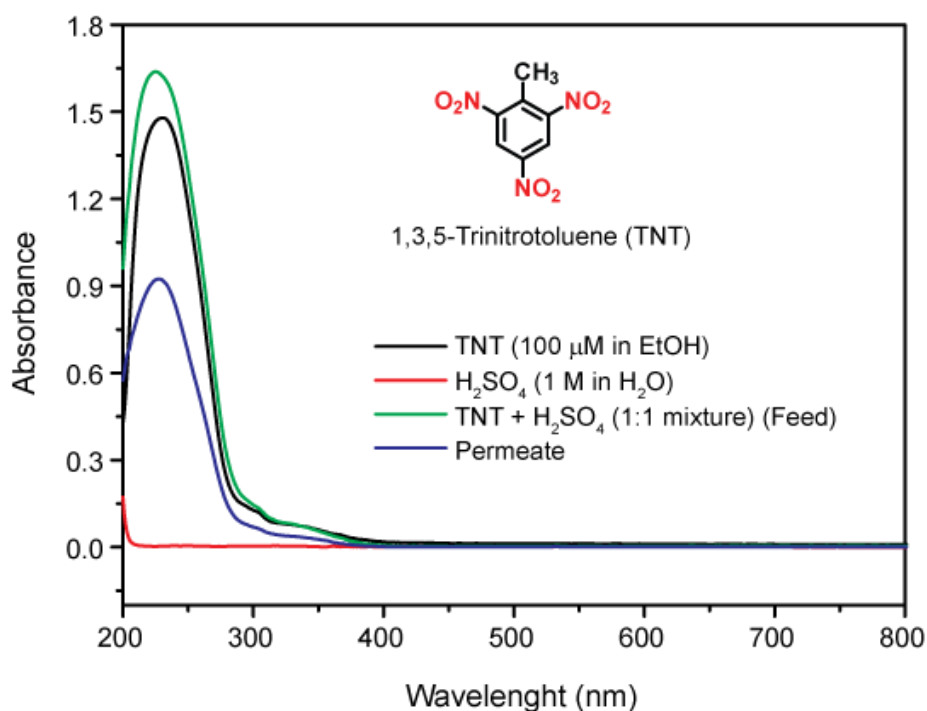


Figure 3.17: UV-Vis absorption spectra comparison of 100 μM ethanol solution of TNT, 1 M aq. H₂SO₄ solution, (1:1; v/v) stock solution (feed) prepared from TNT (200 μM; ethanol) and H₂SO₄ (2 M; water) and solution permeated through the membrane.

Table 3.4: Estimation of final strength of a sulfuric acid in permeate

The strength of H ₂ SO ₄ in the stock solution	Permeate volume collected	The volume of the base (0.5 N) consumed at end point	Final strength of H ₂ SO ₄ in permeate
1 M	3 ml	11.5 ml	0.96 M

UV-Vis spectra analysis: UV-Vis spectra (**Figure 3.17**) revealed that TNT (100 μM , ethanol) solution showed an absorption peak at wavelength ~ 230 nm and aq. H_2SO_4 solution (1 M) didn't show any absorption peak in the entire spectrum range. The stock solution showed an absorption peak at ~ 227 nm with slightly higher absorbance which we believed, was mostly due to the TNT. After that, we passed the stock solution (feed; 10 ml) solution through **TpOMe-Azo COFM** and permeate was collected (6 ml). Then, we have tested the sulfuric acid strength, through neutralization of protons by standard aq. NaOH (0.5 M) solution and using phenolphthalein as an indicator, at the permeate solution which reflected $>95\%$ permeance of the acid (**Table 3.4**). Again, UV-Vis spectra of the permeate, showed significantly lower absorbance value (compared to feed) at wavelength ~ 227 nm, revealed that there is a 27-30 % rejection of the TNT in the permeate solution hence signifying the opportunity for purification of H_2SO_4 from the nitro-aromatics generated during toluene nitration process. It is to be noted that the kinetic diameter of the TNT molecule (< 1 nm; calculated using material studio software) is very smaller than COFM pore diameter (2.8 nm) hence we believe the rejection happened mostly due to the absorption of TNT in COFM frameworks. Again, if the kinetic diameter of the nitro-aromatics is comparable or more than the pore diameter of COFM we expect there would be a complete rejection of the nitro-aromatics.

3.5 Conclusion

In summary, herein we have successfully synthesized an imine ($-\text{C}=\text{N}-$) linked porous and crystalline covalent organic framework membranes (COFMs) *via* the salt (*p*-toluenesulfonic acid- H_2O) mediated crystallization process. This preferred approach is simple, scalable and economically beneficial and provides the opportunity to construct other desirable shapes such as sphere, cylinders, beads etc. with high crystallinity and porosity. The as-synthesized COFM showcased ultra-high chemical stability in extremely drastic conditions such as strong acids (conc. H_2SO_4 , 18 M and conc. HCl, 12 M; seven days) and base (NaOH, 9 M; 24h). DFT calculations of the structures revealed that the presence of interlayer H-bonding is mainly responsible for the ultrahigh stability of these materials, as it protected the imine bond from hydrolysis by providing enough steric hindrance and the hydrophobic environment through methoxy functionality. The as-synthesized COFMs also associated with other novel properties such as these are self-standing, continuous and defect-free with significantly high

crystallinity and porosity, along with considerable chemical stability. These COFMs were found to be highly useful for the purification of sulphuric acid, and the removal of toxic substances and organic carcinogenic dyes from water. In these circumstances, we believe the easy and large-scale production of COFMs using this approach may pave its future applications in water purification technologies.

3.6 Experimental Procedures

3.6.1 Materials

2,4,6-Trimethoxy-benzene-1,3,5-tricarbaldehyde (TpOMe) was prepared from 1,3,5-trimethoxybenzene using the reported literature procedure [3.16]. The preparation procedure of this aldehyde has also discussed in the previous chapter of this thesis. The amine 4,4'-azodianiline (Azo) was purchased from across organics and used as received. All other reagents and solvents were commercially available and used as received.

3.6.2 General methods for characterization

(a) Powder X-Ray Diffraction (PXRD): The PXRD data were recorded on a Phillips PANalytical diffractometer using a Cu K α radiation ($\lambda = 1.5406 \text{ \AA}$), with a scan rate of 2° min^{-1} . The tube current and voltage were fixed at 30 mA and 40 kV respectively. The sample holder containing the COF powders was scanned between 2 and $50^\circ 2\theta$ (step size of 0.02°).

(b) Thermogravimetric Analysis (TGA): TGA was recorded on an SDT Q 600 TG-DTA analyzer instrument. Approximately 5-7 mg of the COF sample was added to an aluminum crucible and heated from 25 to 900°C under N_2 atmosphere (heating rate of $10^\circ \text{C min}^{-1}$).

(c) IR Spectroscopy: The Fourier transform infrared spectra (FTIR) of the COFs were collected on a PERKIN ELMER FT-IR SPECTRUM (Nicolet) spectrometer in ATR mode.

The FTIR data were collected over the range of $4000\text{-}600 \text{ cm}^{-1}$.

(d) Gas Adsorption: The gas adsorption experiments were performed specifically for the activated COF powders using an Autosorb automatic volumetric instrument (*Quantachrome*).

COF powder activation procedure: Approximately 40 mg of the as-synthesized COF powders were evacuated under vacuum at 120°C for 12 h. Finally, the activated samples were used for gas adsorption (H_2 , N_2 , and CO_2).

3.6.3 Solvent flux and sulfuric acid permeance measurement

Measurement of solvent flux of TpOMe-Azo COFM: Solvent permeation analysis was carried out using TpOMe-Azo membrane by passing 40 mL of different protic and aprotic solvents like water, ethanol, methanol, acetone, and acetonitrile. The membranes were properly fitted on a dead-end-mode stirred cell (active area cal. 2.5 cm²) pressurized under 1 atm upstream pressure. The diameter of the membrane was fixed to 1 cm. Five consecutive readings were collected and respective fluxes were calculated using the equation (1). In each case the overall solvent flux was measured using three separate COFM coupons and their average data was reported.

Based on equation (1) the solvent flux (J) can be calculated as:

$$J = V/(A.t)\{\text{unit: liters per square meter hour (Lm}^{-2}\text{h}^{-1})\} \dots\dots\dots(1)$$

Where (V) is the volume of the permeate, (A) is unit area and (t) is unit time

And the overall permeance (P) was determined using the following equation (2):

$$P = V/(A.t.\Delta p)\{\text{unit: liters per square meter hour bar (Lm}^{-2}\text{h}^{-1}\text{bar}^{-1})\} \dots\dots\dots(2)$$

Rejection analysis of various dyes using TpOMe-Azo COFM: Rejection analyses of TpOMe-Azo COFM were performed using various dyes such as rose bengal, congo red, rhodamine b and methylene blue. During the rejection analysis concentration of the dyes, feed was maintained as 50 μ M in water. A 50 mL of dye solution in water was passed using a dead end stirred cell assembly and was passed through the membrane, the permeate was collected at 1 bar upstream pressure. Initial 1 mL of the filtrate was thrown and 5 mL was collected for the rejection analysis. The dye concentration in the feed and permeate was analyzed using a double beam UV-Vis spectrophotometer (Chemito, Spectrascan UV 2700). The percent rejection (% R) was calculated using the following equation 3,

$$\% R = [1 - (C_p/C_f)] \times 100 \dots\dots\dots (3)$$

where, C_p is the concentration of permeate, while C_f is the feed concentration. The complete water purification set up has been shown below.

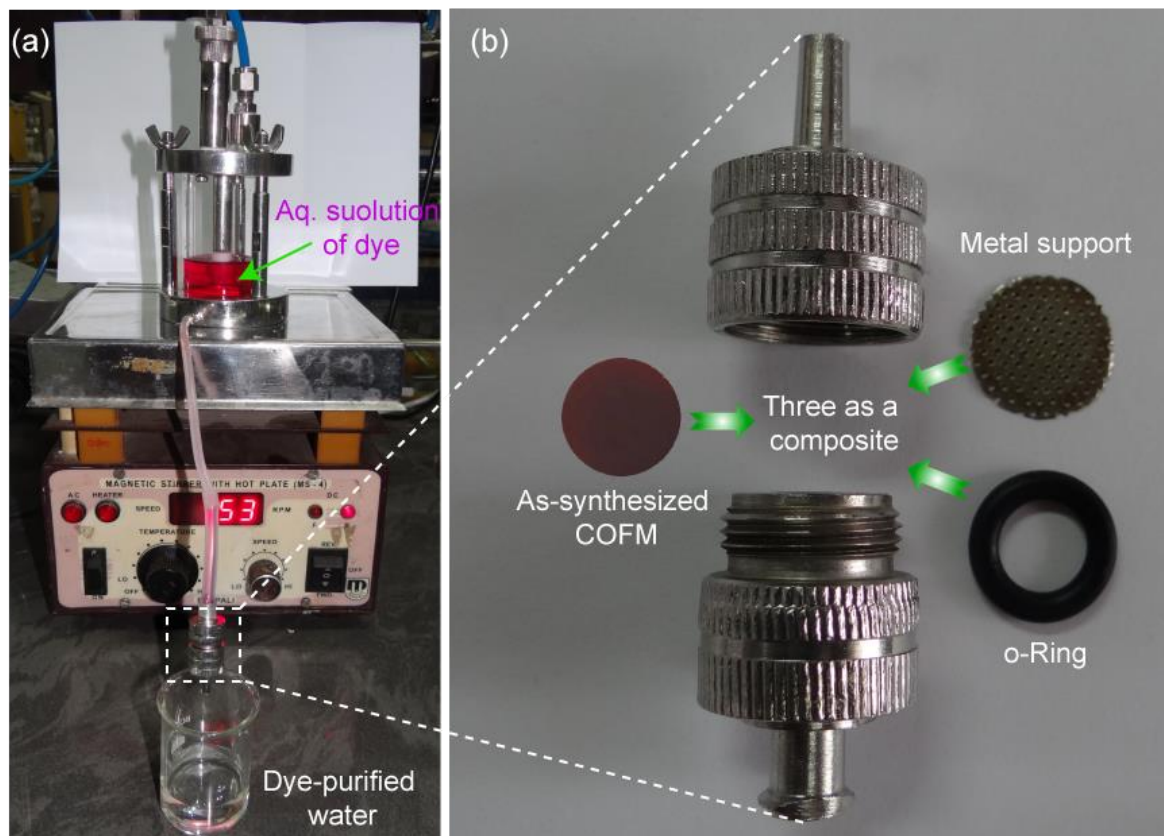


Figure 3.18: (a) Digital image of the complete water purification (from toxic dye molecules) set up. (b) General configuration of a membrane holder. The COFM is used after sandwich between metal support and the o-ring during analysis.

Table 3.5: Preparation of standard sulfuric acid solution

Volume of water taken	Volume of conc. H_2SO_4 (36 N) mixed	Final volume of diluted acid maintained	Final strength of acid in stock solution
35 ml	1 ml	36 ml	0.5 M
33 ml	3 ml	36 ml	1.5 M
30 ml	6 ml	36 ml	3 M
24 ml	12 ml	36 ml	6 M
18 ml	18 ml	36 ml	12 M

Table 3.6: Preparation of standard sodium hydroxide solution

Molar Mass (mol/g) of NaOH	Weight taken	Final volume maintained with water	Strength of base in stock solution
40	10 g	500 ml	0.5 M
	12 g	100 ml	3 M
	24 g	100 ml	6 M
	36 g	100 ml	9 M

Procedure for analysing final strength of H_2SO_4 permeated through TpOMe-Azo COFM:

The standard sulfuric acid solutions (1 N, 3 N, 6 N and 12 N) were prepared according to way mentioned in **Table 3.5** and passed through the **TpOMe-Azo** COFM while the permeate (3 ml) sulfuric acid solution from each batch was collected separately in a conical flask. One drop of phenolphthalein indicator solution was added in this. The standard sodium hydroxide solution (0.5 M), following **Table 3.6** was taken in a burette and was dropwise added to the acid (H^+) solution until the whole H^+ gets neutralized by OH^- and phenolphthalein shows a distinct pink color solution. The volume of base consumed at the endpoint was noted and was back calculated to estimate the H^+ concentration (acid strength) in the permeate solutions.

3.6.4 Structure modeling of COFMs

Atomic positions and cell sizes of modeled COF layers were optimized using the Self-Consistent-Charge Density-Functional Tight-Binding (SCC-DFTB) method. The layer stacking is affected by the Coulomb repulsion between the partial atomic charges in adjacent layers [3.17]. Hence, several slipped AA stacking possibilities were considered for each COF by shifting adjacent layers with respect to each other in different directions up to 6Å. In addition, different orientations of the methoxy groups (in plane, above plane, below plane) were considered. The predicted slipped structure has the lowest energy while maintaining an agreement with the experimental PXRD pattern. The fractional coordinates of the material have been provided in **Table 3.1**.

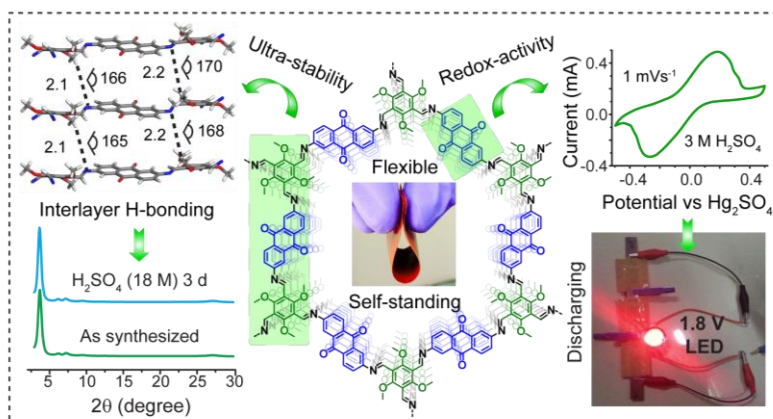
All the COFs have been modeled in the triclinic space group ($P1$) by comparing the experimental and simulated PXRD patterns. Refinements of PXRD pattern were done using Reflex module of the Material studio.

NOTE: All results of this chapter have already been published in *Angew. Chem., Int. Ed.*, **2018**, *57*, 5797; with the title: “*Ultra-stable Imine-based Covalent Organic Frameworks for Sulfuric acid Recovery: An Effect of Interlayer Hydrogen Bonding*”. The stated publication was the results of the collaboration between the group of Dr. Rahul Banerjee and his student Mr. Arjun Halder from CSIR National Chemical Laboratory, Pune, with Dr. Ulhas K. Kharul and his student Mr. Shebeeb H. Kunjattu from CSIR National Chemical Laboratory, Pune for water purification experiment. The computational study was performed *via* collaboration with Dr. Thomas Heine from Jacobs University, Germany and his student Dr. Matthew Addicoat from School of Science and Technology, Nottingham Trent University, Nottingham, United Kingdom. Apart from computational study major works contributed by Mr. Arjun Halder. The manuscript was written by Mr. Arjun Halder under the guidance of Dr. Rahul Banerjee.

CHAPTER 4

Selective Fabrication of Redox-Active Covalent Organic Framework as Capacitive Energy Storage Materials

Abstract: Two-dimensional (2D) crystalline covalent organic frameworks (COFs), bearing ordered nanochannels with intrinsic-mesoporosity, are eligible candidates towards channel-wall decoration with desirable functional groups. To



that end, pore-wall functionalization using redox-active functional groups could dramatically influence the frameworks to behave as promising supercapacitive energy storage material. However, their insoluble powder like nature, poor capacitive performance in pristine form, integrated with inferior electrochemical stability is a primary concern for their long-term use in electrochemical-devices. Keeping this in perspective, herein, we report a redox active and hydrogen bonded COF TpOMe-DAQ with ultrahigh chemical stability in conc. H₂SO₄ (18 M), conc. HCl (12 M) and NaOH (9 M). The as-synthesized COF fabricated as thin sheets were efficiently employed as a free-standing supercapacitor electrode material using 3 M aq. H₂SO₄ as an electrolyte. Moreover, the pristine COF showcased outstanding areal capacitance 1600 mFcm⁻² (gravimetric 169 Fg⁻¹) and excellent cyclic stability (> 1,00,000) without compromising its capacitive performance or coulombic efficiency. Superior capacitive performance was due to the emergence of excellent pseudo-capacitance by virtue of precise molecular level control over redox functionalities present in the COF backbone. Moreover, as a proof-of-concept, a solid-state supercapacitor device was also assembled and subsequently tested.

4.1 Introduction

Global energy production and consumption has now been increasing extensively day by day with over expanding human population and to fulfill their day in and day out needs. The primary example could be the rapid development of fast-growing market of portable electronic devices and as consumption fuels for hybrid electric vehicles [4.1-4.3]. It has already been examined that the global energy demands will become roughly doubled in mid-century and finally will become triple by 2100 [4.4]. Hence, the global energy consumption, if happens in current consumption rate, will soon become inevitable in near future signifying its alarming sign to the society. Therefore, there has been always an urgent need to develop new synthetic methodologies to manufacture advanced, cheap and eco-friendly energy storage and conversion devices in parallel to the development of clean, sustainable and renewable energies such as solar, wind, tides, to fulfill the ever growing demands of modern society [4.2, 4.5]. Among all other energy storage and conversion devices, lithium-ion batteries (LIBs) [4.6] and supercapacitors [4.7, 4.8] are the two promising candidates in this category. Though, LIBs exhibited significantly high energy density, its low power density restricts its fruitful usage in various energy storage devices where a high power delivery is required in faster rate [4.5, 4.9]. However, supercapacitors in contrast, at a time exhibit promising energy and power density thus is more promising materials to be developed [4.10].

4.1.1 Introduction to electrochemical capacitors (Supercapacitors)

Electrochemical capacitors (ECs), also known as supercapacitors, have drawn significant scientific attention in recent years as a true energy storage and conversion media. This is possible because of its high energy and power density, rapid charging/discharging capability, long cycle life (>100000), and comparatively low maintenance cost [4.7, 4.8]. Moreover, supercapacitor bridges electrolytic capacitors with batteries in terms of power delivery. Based on its charge storage mechanism, the supercapacitors can be classified into two major categories such as; a) electrical double layer capacitors (EDLCs) and b) pseudocapacitor. In EDLCs, electronic charges are stored *via* adsorption of ions on the surface of the electrode, whereas in pseudocapacitor, faradic reactions are occurred on or near to the electrode surface. Moreover, to utilize both the edges such as of high energy density associated with batteries and high power density from supercapacitors, scientists are more interested to develop the asymmetric supercapacitor where one electrode acts as batteries leading another

one to be acted as supercapacitors. The EDLCs are mostly activated carbons and other related similar materials such as carbide-derived carbons, carbon nanotubes, nanotubes, and nanohorns etc. [4.9]. The activated carbons are exclusively used in electrodes of EDLCs because of its low cost, high surface area, and excellent electrochemical stability. In contrast, most of the conducting polymers such as PEDOT, polyaniline, polypyrrole, and metal oxides ex. RuO_2 , Co_3O_4 , MnO_2 etc. are the leading candidates for pseudo-capacitors. Although it possesses high capacitance value, these materials suffer from low cycling stability [4.10-4.11]. Moreover, to improve the energy density of supercapacitor, researchers mostly focused on the development of new stable materials bearing the aids of the highly accessible electro-active surface area, high electrical conductivity, and optimized pore aperture with a high density of redox-active units [4.12-4.17].

4.1.2 Advantages of covalent organic frameworks (COFs) as electrode materials

There are significant advantages of COFs if used as an active electrode material, such as-

- (a) **Porous structure:** Porous structure of the material will improve the electrode/electrolyte interaction via effective immobilization of ions inside the pore.
- (b) **Structural rigidity:** Significantly robust framework structure will favor high electrochemical stability during the electrochemical reaction on the electrode surface.
- (c) **The Precise introduction of redox active groups:** The reticular structural construction will enable to precisely decorate the pore walls with desirable redox-active groups.
- (e) **High crystallinity and porosity:** High crystallinity will help to characterize and to understand the mechanism during the electrochemical process whereas high porosity will induce maximum electrodes/electrolytes interaction and will improve in EDLCs.
- (f) **Insolubility:** COFs are 2D/3D organic crystalline polymers and are mostly insoluble in any solvents. So the capacitance loss due to its leaching during electrode process can be avoided.

4.2 Ultra-stable, self-standing, redox-active COF thin sheet as energy storage material

Covalent organic frameworks (COFs) have attracted enormous scientific attention because of their tunable porosity and periodically ordered structures with high atomic precision [4.18]. As discussed, recently, COFs have been identified as promising materials

for supercapacitors (SCs), owing to their long-range ordered arrangement with the high accessible surface area which is ideal for efficient ion transport within the electrode-electrolyte interface [4.18, 4.19]. Also, advantages of reticular structural construction led to the explicit incorporation of redox-active functionalities within the porous COF backbone thereby resulting in them becoming suitable for pseudo-capacitive energy storage [4.20]. However, their insoluble granular nature (hence the difficulty in the electrode fabrication), inferior capacitive performance in pristine form due to their non-conductive nature and poor electrochemical stability restrict their potential usage in SCs. Therefore, the fabrication of a COF based high-performance electrode material, with sizeable electrolyte-accessible surface areas integrated with excellent cyclic stability in mordant electrolyte condition is still challenging and highly desirable.

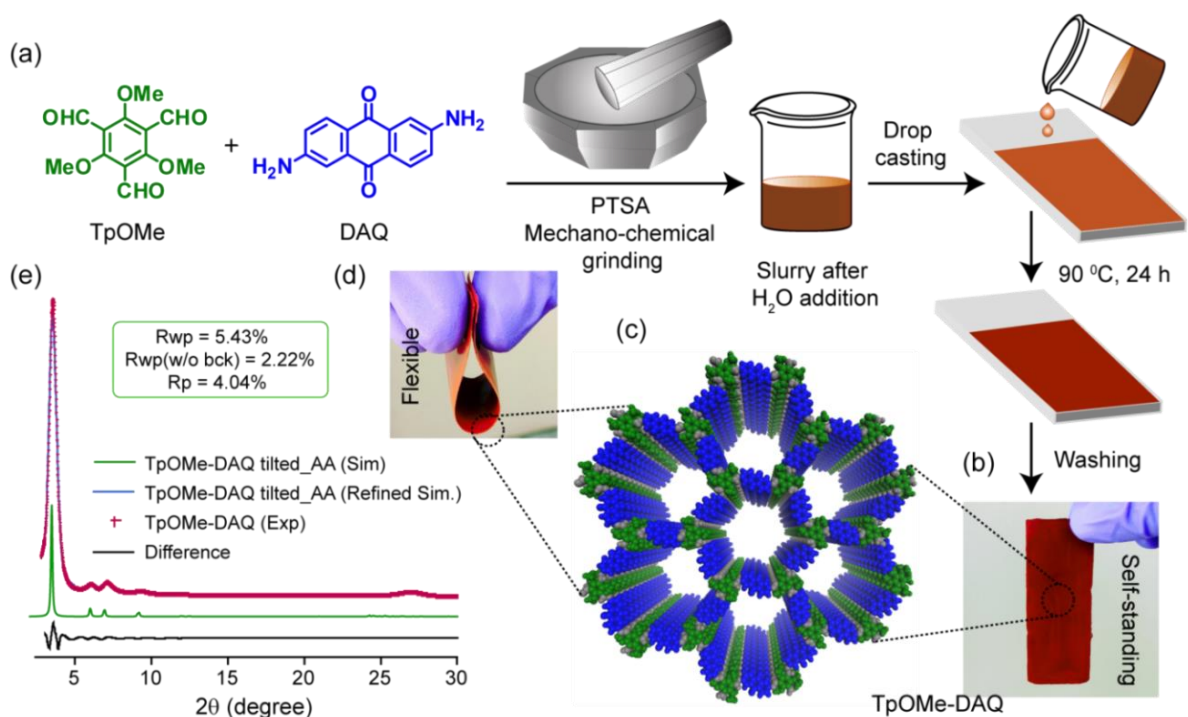


Figure 4.1. (a) General synthetic scheme of the **TpOMe-DAQ** thin sheet from aldehyde (**TpOMe**) and amine **DAQ** by PTSA (*p*-toluenesulfonic acid) mediated mechano-chemical grinding approach. (b and d) Digital images show the self-standing and flexible nature of the thin sheet. (c) Tilted_AA model of **TpOMe-DAQ**. (e) Comparison among the experimental (red) with simulated eclipsed tilted-AA (green), refined simulated (blue) PXRD patterns and Pawley refinement difference (black) for **TpOMe-DAQ** COF.

The β -keto-enamine-based COFs, since their discovery, have enriched the COF literature as promising pseudo-capacitors [4.21]. However, their usage mostly in powdered form (or in few cases on the support), low capacitive performance in the pure state as well as limited cyclic stability compared to EDLCs (electrical double layer capacitors) [4.22] during the electrochemical process have conveyed a restriction towards their extensive usage. Additionally, the non-conjugative nature of β -keto-enamine COFs could make them sluggish towards good electrochemical response compared to more conjugated imine (C=N) based COFs. Although additional conductive additives or post-functionalization could enhance the capacitive performance, they would lead to further synthetic hurdles, and their presence could dramatically affect the active surface area due to the extensive pore blockage [4.23].

Keeping this in perspective, herein we report an imine-based, redox active COF **TpOMe-DAQ** that has been constructed from 2,4,6-trimethoxy-1,3,5-benzenetricarbaldehyde (TpOMe) and 2,6-diaminoanthraquinone (DAQ) as building units. The judicious choice of such linker units could combine both electrochemical stability (due to the explicit incorporation of the methoxy functionality) and reversible redox response due to the quinone/hydroquinone transformation (DAQ amine) for energy storage [4.21, 4.23]. **TpOMe-DAQ** exhibits ultrahigh chemical stability in drastic conditions [strong acids (18 M H₂SO₄; 12 M HCl) or bases (9 M NaOH)] due to the presence of strong interlayer C–H...N H-bonding [$D=3.26$ Å, $d=2.17$ Å, $\theta=168.2^\circ$; $D=3.16$, $d=2.07$, $\theta=165.8^\circ$] between methoxy C–H and the imine ‘N’ atom of adjacent layers [4.24a,b]. Furthermore, this COF could be fabricated as uniform and continuous thin sheets even in centimeter scale while maintaining the thickness of ~ 200 μm (**Figure 4.1a-d**). These findings encouraged us to utilize these COF thin sheets as free-standing supercapacitor electrodes using concentrated aq. H₂SO₄ (2 and 3 M) as an electrolyte. Moreover, in three electrode assemblies using 3 M aq. H₂SO₄, the COF thin sheets showcased exceptionally high areal capacitance of 1600 mFcm⁻² (gravimetric 169 Fg⁻¹) which is the highest value ever achieved in pure COF based SCs and also comparable to other promising electrode materials (**Table 4.3 & Table 4.4**). **TpOMe-DAQ**, in 2 M aq. H₂SO₄ showcased outstanding capacitive performance (1280 mFcm⁻² and 135 Fg⁻¹) and galvanostatic charge-discharge (GCD) cyclic stability exceeding 1,00,000 cycles without compromising the capacitance. Additionally, in a solid-state device, the COF thin sheet could retain $\sim 65\%$ of its initial capacitance even after 50,000 continuous charge-discharge cycles,

keeping the coulombic efficiency intact. Therefore, employing this unique design strategy, for the first time not only we could achieve such exceptionally high areal capacitance but also excellent cyclic stability in a free-standing (without additive or binder) COF based supercapacitor electrode even using harsh electrolyte conditions.

4.2.1 Synthesis of TpOMe-DAQ COF thin sheet

P-toluenesulfonic acid monohydrate (PTSA-H₂O) (1.8 mmol) was mixed with DAQ amine (0.45 mmol; 108 mg) in a mortar-pestle. The mixture was uniformly grinded for 3 minutes. In that mixture 2,4,6-trimethoxy-1,3,5-benzenetricarbaldehyde (**TpOMe**, 0.3 mmol, 76.2 mg) was added and properly mixed through grinding. To this mixture few drops of water (~100-200 μ L based on requirement) was added. The resulting mixture was then grinded properly until it becomes dough-like material. It was then drop cast on a glass slide (length 5 cm and

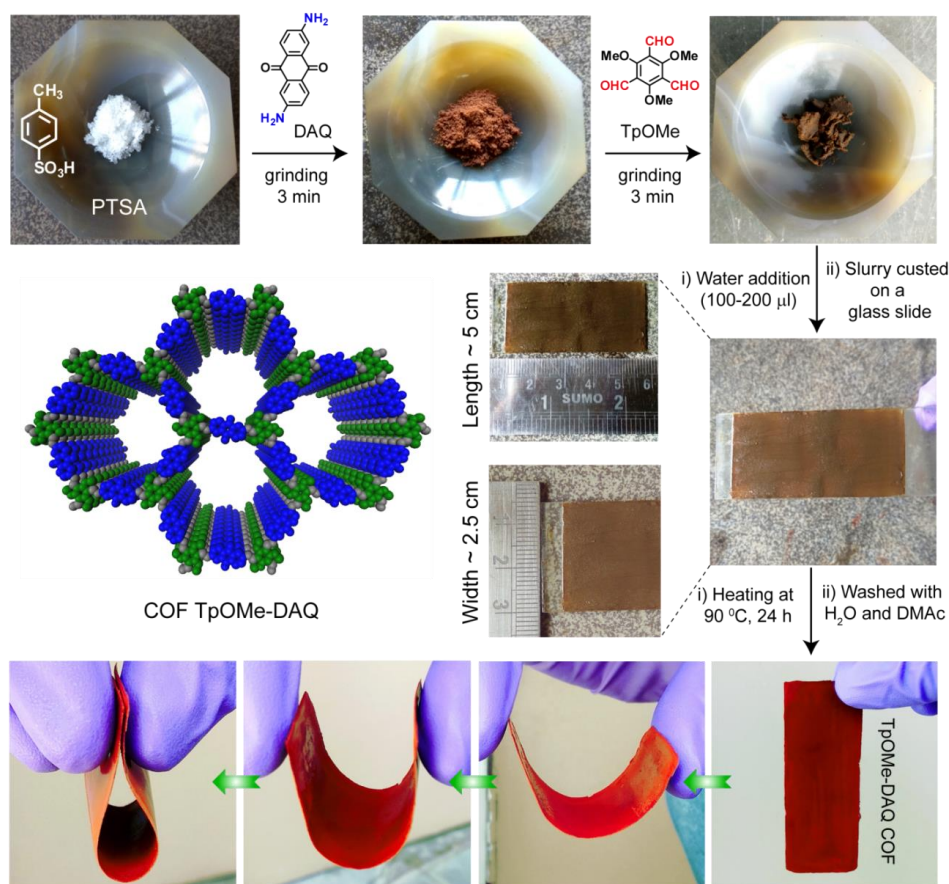


Figure 4.2: Schematic representations of **TpOMe-DAQ** COF thin sheet synthesis and its flexible behavior.

diameter 2.5 cm) with uniform thickness and was additionally allowed to heat at 90 °C for 24 h in a closed container under humid condition. After completion, the glass slide coated with COF deepened into hot water to isolate COF sheet and to remove PTSA. It was then washed with *N,N*-dimethylacetamide to remove unreacted starting materials or oligomeric impurities. The crystalline and porous COF thin sheets (80-85 % isolated yield; wt. %) were then stored finally in distilled water before it is used for further studies (**Figure 4.2**).

4.2.2 Structural simulation and characterization

The formation of **TpOMe-DAQ** was confirmed by its PXRD analysis (**Figure 4.3a**). The PXRD pattern shows five distinct characteristic peaks at 3.5, 6.0, 7.1, 9.3 and 27.1 (± 0.1 , 2θ) which belongs to the reflections from the planes 100, 110, 200, 210 and 001 respectively. The high intense peak was attributed from 100 planes indicates its high crystalline nature. The interlayer stacking distances were measured using the d-spacing among the 001 planes which showed about 3.4 Å inter-planar separation among the layers. Moreover, different model structures such as AA, slip-AA, AA-3, AB were simulated using Material Studio software. The experimental PXRD patterns fit with the simulated tilted-AA structure [Rwp-5.4%, Rwp (w/o bck)- 2.2% and Rp-4.1%] (**Figure 4.1e** & **Figure 4.3b**).

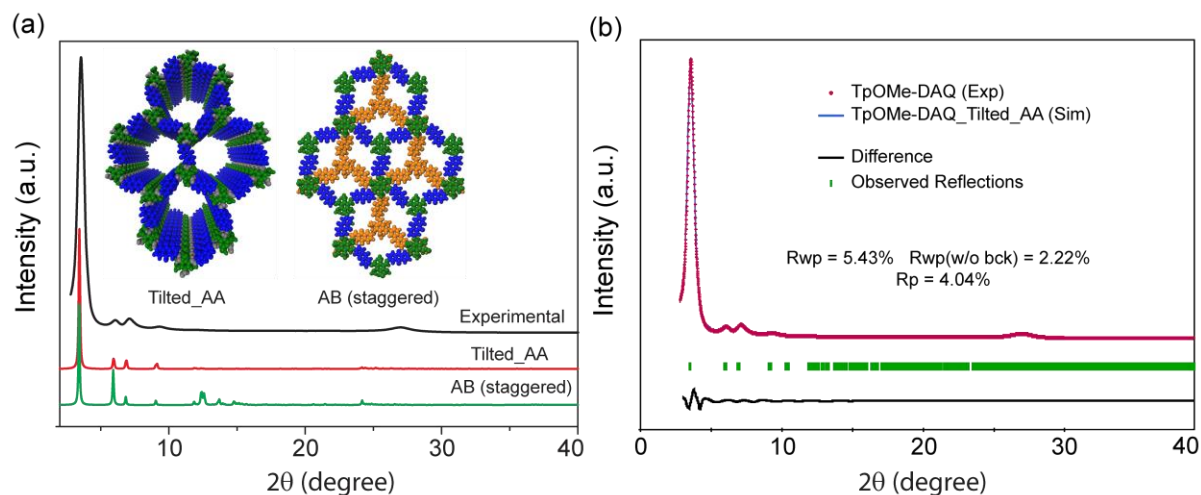


Figure 4.3: (a) PXRD pattern of as-synthesized (black) compared with the tilted_AA (red) and Staggered (AB) (green) **TpOMe-DAQ** COF thin sheet. (b) The experimental PXRD patterns (red) compared with the simulated (Tilted_AA; blue) and Pawley refined difference (black) of **TpOMe-DAQ** [Rp, Rwp and Rwp (w/o bck) have shown in inset].

Moreover, Pawley refinement was taken into consideration to analyze the unit cell parameters (Space group *P1*; $a=29.9$, $b=29.9$, $c=3.7$ & $\alpha=87.0$, $\beta=83.0$, $\gamma=59.0^\circ$ for tilted-AA) (Table 4.1).

Table 4.1. Fractional atomic coordinates for the unit cell of *TpOMe-DAQ* (Tilted_AA)

TpOMe-DAQ (Space group- <i>P1</i>)											
$a = 29.8974 \text{ \AA}$, $b = 29.9057 \text{ \AA}$, $c = 3.70642 \text{ \AA}$; $\alpha = 87.0124^\circ$, $\beta = 83.2858^\circ$, $\gamma = 59.1346^\circ$											
atoms	x	y	Z	atoms	x	y	Z	atoms	x	y	Z
C1	0.23737	0.74898	0.07289	C14	0.2664	0.63972	0.18923	C27	0.84617	0.39073	0.69435
C2	0.26687	0.64113	0.6897	C15	0.20885	0.66797	0.19814	C28	0.88008	0.3355	0.69813
C3	0.20929	0.66826	0.70099	C16	0.1852	0.63719	0.19554	C29	0.79127	0.41123	0.71067
C4	0.18707	0.6357	0.70853	C17	0.17529	0.72305	0.21446	C30	0.86002	0.30144	0.7156
C5	0.17465	0.72302	0.71328	C18	0.13001	0.65928	0.21841	C31	0.76966	0.37812	0.73796
C6	0.13209	0.65689	0.73371	C19	0.11984	0.74645	0.24766	C32	0.80454	0.32356	0.74346
C7	0.11929	0.74548	0.75164	C20	0.09812	0.71384	0.2562	C33	0.89125	0.24408	0.71194
C8	0.09898	0.71155	0.77054	C21	0.10267	0.63078	0.20748	C34	0.71189	0.40494	0.74961
C9	0.10567	0.62675	0.73381	C22	0.08891	0.80393	0.25368	C35	0.96923	0.27303	0.77994
C10	0.0885	0.80309	0.75739	C23	0.22218	0.54807	0.30664	C36	0.76379	0.49988	0.59502
C11	0.21549	0.54491	0.79853	C24	0.01138	0.76905	0.42618	C37	0.74274	0.29616	0.87578
C12	0.23651	0.74936	0.57208	C25	0.76375	0.49988	0.09544	C38	0.87256	0.42098	0.17797
C13	0.00945	0.7739	0.91282	C26	0.87256	0.42132	0.67884	C39	0.84599	0.39056	0.19425
C40	0.87983	0.33532	0.19847	C58	0.95835	0.08078	0.13112	C79	0.85635	0.54063	0.33186
C41	0.79108	0.41119	0.21075	C59	0.03732	0.08113	0.0066	C104	0.09414	0.56115	0.62773
C42	0.85966	0.30138	0.21648	C60	0.93103	0.13531	0.1417	C105	0.3458	0.62766	0.27129
C43	0.76937	0.37816	0.23812	C61	0.01033	0.13529	0.02021	C106	0.37759	0.57421	0.22589
C44	0.80418	0.3236	0.24394	C62	0.95693	0.16308	0.0901	C107	0.36981	0.6549	0.32019
C45	0.8907	0.244	0.21358	C63	0.01877	0.88488	0.68429	C108	0.43225	0.54907	0.22152
C46	0.71164	0.40496	0.24904	C64	0.04397	0.91226	0.61696	C109	0.424	0.62985	0.31865
C47	0.96916	0.27264	0.27873	C65	0.96479	0.91278	0.74606	C110	0.45599	0.57694	0.26787
C48	0.74238	0.29621	0.37656	C66	0.01611	0.96696	0.61687	C111	0.46467	0.49305	0.16337
C49	0.0169	0.88498	0.19008	C67	0.93734	0.967	0.74888	C112	0.51395	0.55105	0.26666
C50	0.04182	0.91243	0.12027	C68	0.96242	0.99474	0.68572	C113	0.52259	0.46694	0.16465
C51	0.96298	0.9128	0.25265	C69	0.0438	0.99517	0.54494	C114	0.54628	0.49492	0.21041
C52	0.01388	0.96709	0.11947	C70	0.93204	0.05273	0.69518	C115	0.55468	0.41378	0.11716
C53	0.93538	0.96705	0.25404	C71	0.01395	0.05321	0.56086	C116	0.60087	0.46977	0.20789
C54	0.96026	0.99488	0.18915	C72	0.96021	0.08076	0.62913	C117	0.60882	0.38862	0.11862
C55	0.04163	0.99509	0.04619	C86	0.01753	0.55217	0.19858	C118	0.6327	0.4161	0.16632
C56	0.92997	0.05292	0.19739	C87	0.12387	0.5069	0.06776	C119	0.34611	0.6289	0.773
C57	0.01206	0.05306	0.06248	C88	0.09641	0.55841	0.13802	C120	0.37774	0.57537	0.72862
C73	0.03891	0.08159	0.50536	C89	0.88371	0.48911	0.76996	C121	0.3703	0.65614	0.82011
C74	0.93259	0.13528	0.63995	C90	0.93768	0.46602	0.71143	C122	0.43243	0.55013	0.72319
C75	0.01163	0.13577	0.51921	C91	0.85543	0.54149	0.83131	C123	0.42453	0.63093	0.81811
C76	0.95819	0.16334	0.58895	C92	0.96249	0.49517	0.70732	C124	0.45637	0.57793	0.76825
C77	0.88425	0.48845	0.26856	C93	0.88021	0.57024	0.83037	C125	0.46465	0.49411	0.66493
C78	0.9381	0.46529	0.20786	C94	0.93374	0.5478	0.7676	C126	0.51435	0.55185	0.76674
C80	0.85635	0.54063	0.33186	C95	0.01913	0.47004	0.63495	C127	0.5226	0.46782	0.66584
C81	0.96326	0.4941	0.2045	C96	0.95938	0.57937	0.76876	C128	0.5465	0.49565	0.71099
C82	0.88144	0.56904	0.33177	C97	0.04454	0.50188	0.63348	C129	0.5545	0.41463	0.61851
C83	0.93492	0.54644	0.26783	C98	0.12387	0.5069	0.06776	C130	0.60113	0.47031	0.70806

C84	0.01972	0.46898	0.12949	C99	0.09641	0.55841	0.13802	C131	0.60866	0.38929	0.61953
C85	0.96105	0.5774	0.27209	C101	0.09781	0.47992	0.5673	C132	0.63276	0.41661	0.66667
C100	0.01577	0.55447	0.69424	C102	0.04035	0.58386	0.68864	C103	0.12233	0.50896	0.56439
N1	0.12495	0.58376	0.14344	O1	0.18933	0.75992	0.68745	O13	0.08672	0.97112	0.97397
N2	0.04402	0.83022	0.1913	O2	0.22424	0.58324	0.69704	O14	0.88404	0.07703	0.26122
N3	0.29113	0.65677	0.77865	O3	0.04728	0.72595	0.81565	O15	0.089	0.97137	0.47377
N4	0.12129	0.58824	0.62336	O4	0.19149	0.75881	0.19543	O16	0.88616	0.07667	0.75977
N5	0.04561	0.83005	0.68307	O5	0.21962	0.58404	0.16128	O17	0.04319	0.42474	0.0664
N6	0.29086	0.65576	0.2752	O6	0.04481	0.7323	0.28045	O18	0.93766	0.62145	0.33697
N7	0.931	0.21779	0.09708	O7	0.75324	0.46308	0.69819	O19	0.0431	0.42545	0.57483
N8	0.68765	0.38853	0.16276	O8	0.93235	0.32038	0.69222	O20	0.93567	0.62358	0.83227
N9	0.85651	0.46202	0.77836	O9	0.7902	0.28625	0.76354	O21	0.44427	0.47007	0.11265
N10	0.93196	0.21807	0.59663	O10	0.75312	0.46307	0.19818	O22	0.53439	0.57429	0.31465
N11	0.68773	0.3889	0.66246	O11	0.9321	0.32019	0.19245	O23	0.4441	0.4713	0.61408
N12	0.85679	0.46162	0.27741	O12	0.78978	0.28632	0.26395	O24	0.53499	0.57497	0.81415

4.2.3 Chemical characterization.

The FTIR analysis was performed to understand the type of bonds is associated with the as-synthesized COF. The spectra were recorded in its fully activated condition of the COFs just to avoid any spectral contributions from the solvents if trapped within the pore. Moreover, the FTIR analysis of the **TpOMe-DAQ** revealed the complete disappearance of the primary N-H stretching ($3420\text{-}3199\text{ cm}^{-1}$) of the DAQ amine and C=O stretching at 1682

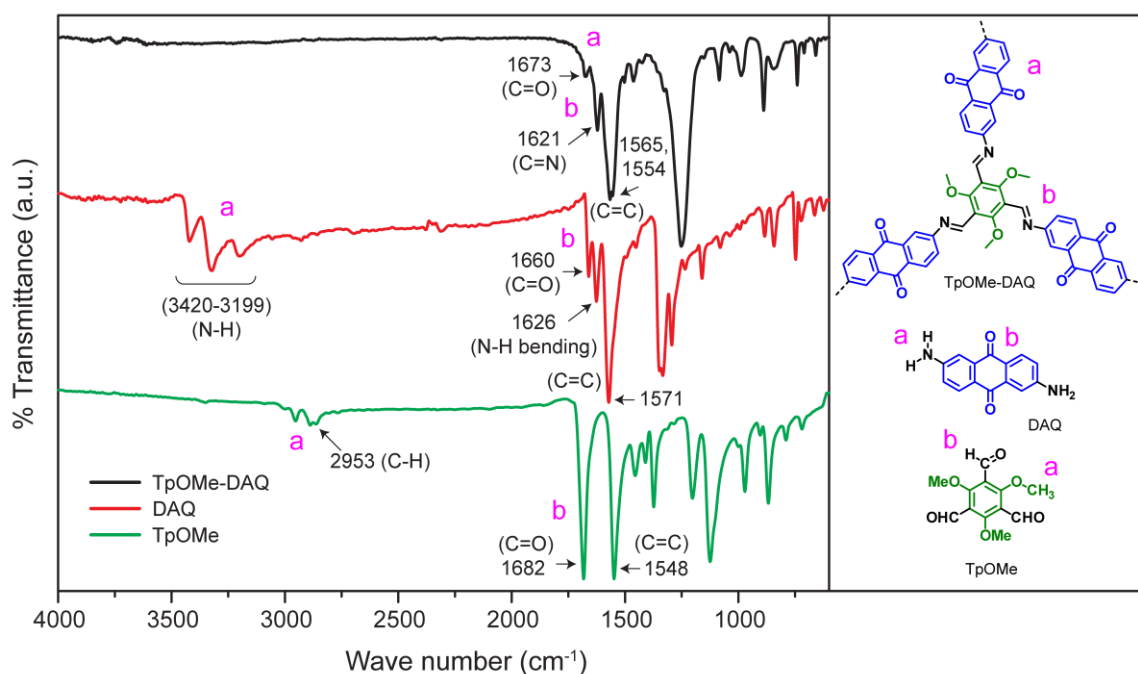


Figure 4.4: Comparison of FT-IR spectra of as-synthesized **TpOMe-DAQ** with its starting materials.

cm^{-1} from TpOMe aldehyde (**Figure 4.4**) hence signifying the complete consumption of starting materials. The newly formed C=N stretching (originated from aldehyde-amine Schiff base reaction) appeared at 1621 cm^{-1} whereas the C=O stretching (observed at 1660 cm^{-1} in DAQ amine) was observed at 1673 cm^{-1} . The C=O stretching (1660 cm^{-1} in DAQ amine) appeared at 1673 cm^{-1} in the COF strongly suggest the existence of amine counterpart throughout the framework. The COF as well as in the starting materials attributed their C=C stretching frequency at $1565\text{-}1548 \text{ cm}^{-1}$ in the spectrum. The overall structural compositions of **TpOMe-DAQ** COF were further confirmed using solid-state magic angle spinning ^{13}C CP-MAS spectra analysis. The C=O stretching at 180.8 ppm belongs to the DAQ (quinone C=O) amine reflecting its firm existence in the COF structure. The imine C=N reflect its characteristics signal at 147.7 ppm whereas the signature of all the aromatic carbons appeared in the range 153-108 ppm in the spectrum. The methoxy carbons showed its characteristics chemical shift at about 64 ppm (**Figure 4.5**).

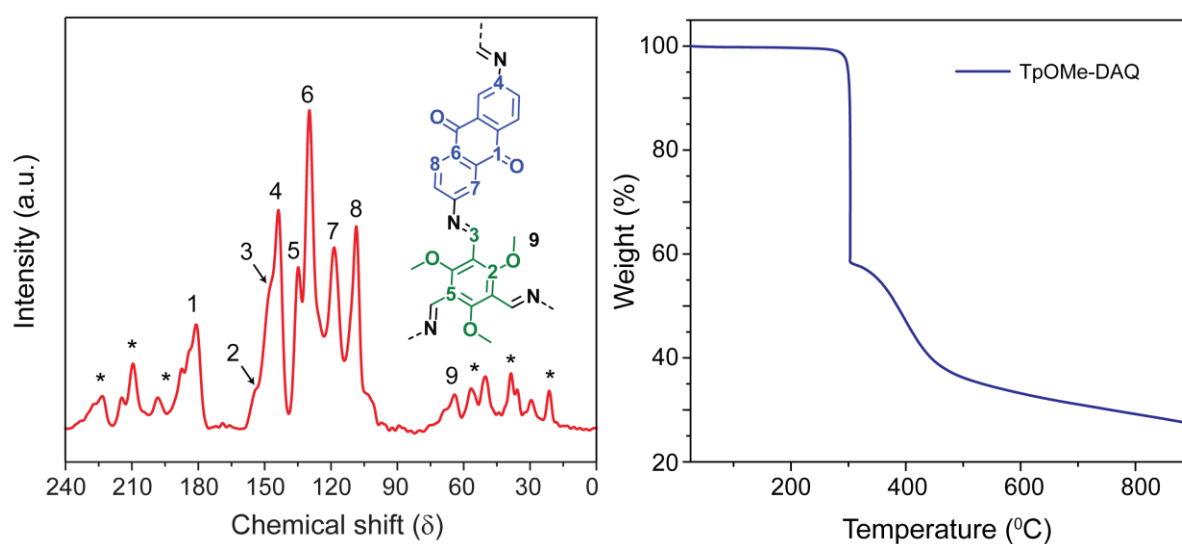


Figure 4.5: (left) Solid state ^{13}C CP-MAS spectra and (Right) TGA (Thermo Gravimetric Analysis) of as-synthesized **TpOMe-DAQ** COF.

Thermogravimetric analysis (TGA) was performed in the temperature range 25 to 900 °C to analyze the thermal stability of the COF. During the gradual increment of the temperature, no significant weight loss was observed up to 300 °C which reveals the framework stability up to that particular temperature. Once it exceeds 300 °C there happens a rapid drop in weight from 100 % to 60 % which revealed rapid framework degradation. However, TGA showed

only gradual weight loss after that and running up to 900 °C the material could retain up to 30 wt% of its overall weight.

4.2.4 Gas adsorption studies

The effective surface area of an electrode material reveals its ability to hold electrolytes/ions during various electrode process associated with this. Hence, the overall porosity or surface area plays a very crucial role in designing such electrodes to be utilized for EDLC (electrical double layer capacitance) [4.22] or pseudo-capacitive energy storage materials. In the present study, the porosity of the as-synthesized **TpOMe-DAQ** COF was analyzed using N₂ adsorption studies at 77 K (liq. N₂ temperature) *via* stepwise activating the

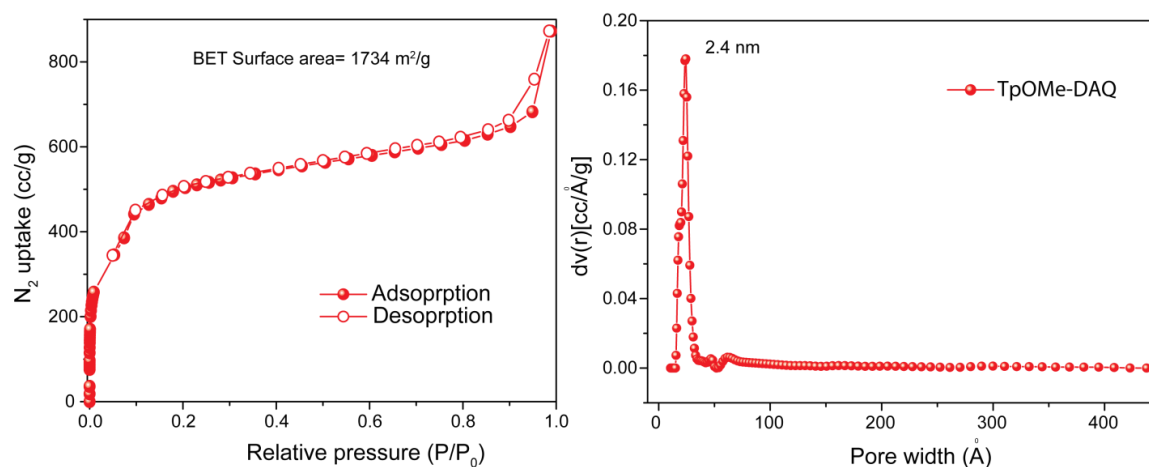


Figure 4.6: (left) N₂ adsorption isotherm plot (highest achieved surface area) and (right) pore size distribution (cylindr./sphere pores, QSDFT adsorption branch model) for **TpOMe-DAQ** COF.

samples at 120 °C (for 12 h) in vacuum. The isotherm of the as-synthesized COF reflects a step increment in the pressure range 0.05-0.15 which further increment of pressure gets almost saturated reflecting its type-IV nature. The average BET surface area of the as-synthesized COF thin sheet was found as high as 1531 m²/g (highest achieved 1731 m²/g) (**Figure 4.6**). The experimental pore size distribution (calculated using cylindr./sphere pores, QSDFT adsorption branch) showed the pore diameter of 2.27 nm which is the predominant nature of mesoporous materials (**Figure 4.6**). This predominant mesoporosity (suitable for efficient electrolyte movement) in combination with the high surface area could lead **TpOMe-DAQ** to serve as an ideal porous support towards EDLCs.

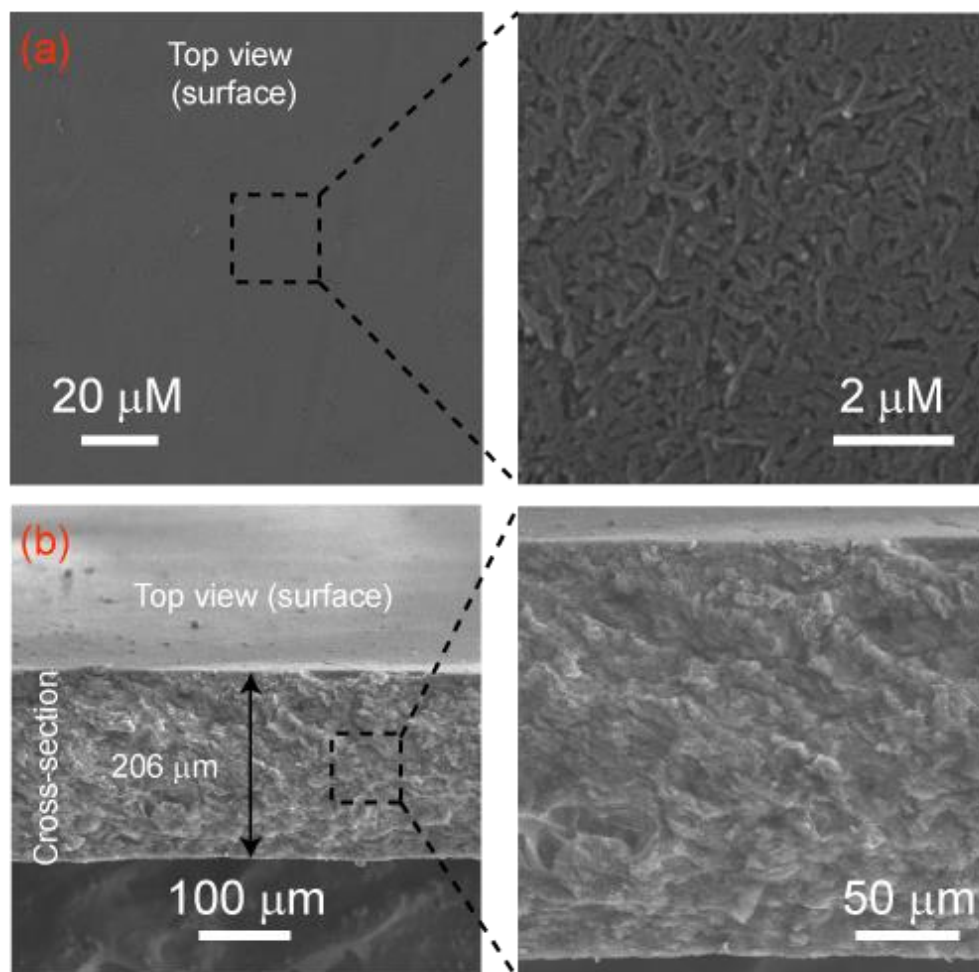


Figure 4.7: SEM images (a) Top view and (b) cross-section view of *TpOMe-DAQ* COF.

The nano-scale morphology and the thickness of the thin sheet were evaluated using scanning electron microscopy (SEM) studies [4.25-4.26]. Perpendicular view of SEM analysis revealed the material is basically composed of small crystallites (length ca. 3 μm) which are perfectly packed with each other to bring self-standing and crack-free nature to the sheet (**Figure 4.7a**). The cross-section SEM analysis provided the thickness of the sheet which varies in the range 200-220 μm (**Figure 4.7b**). The efficient crystallite-crystallite packing could significantly reduce the number of grain boundaries hence the internal defects and could enhance the electrical conductivity during electrochemical studies. The enhanced electrical conductivity hence will help to increase the capacitive performance of the COF thin sheet.

4.2.5 Chemical stability investigation

The extent of chemical stability of an electrode material is the first-hand quantification of its ability to perform under vigorous electro-chemical condition. Therefore, in the present study, to analyze the chemical stability of **TpOMe-DAQ**, the as-synthesized sheet was treated primarily in different solvents (protic or aprotic) such as water (boiling), methanol, ethanol, acetonitrile, tetrahydrofuran, chloroform, N,N'-dimethylformamine, and dimethyl sulfoxide for 7 days. Separately the as-synthesized COF was also treated in more vigorous conditions like conc. H₂SO₄ (18 M; 3 days), conc. HCl (12 M; 7 days), dil. H₂SO₄ (9 M; 7 days) and in NaOH (1 day; 9M) for stipulated time duration.

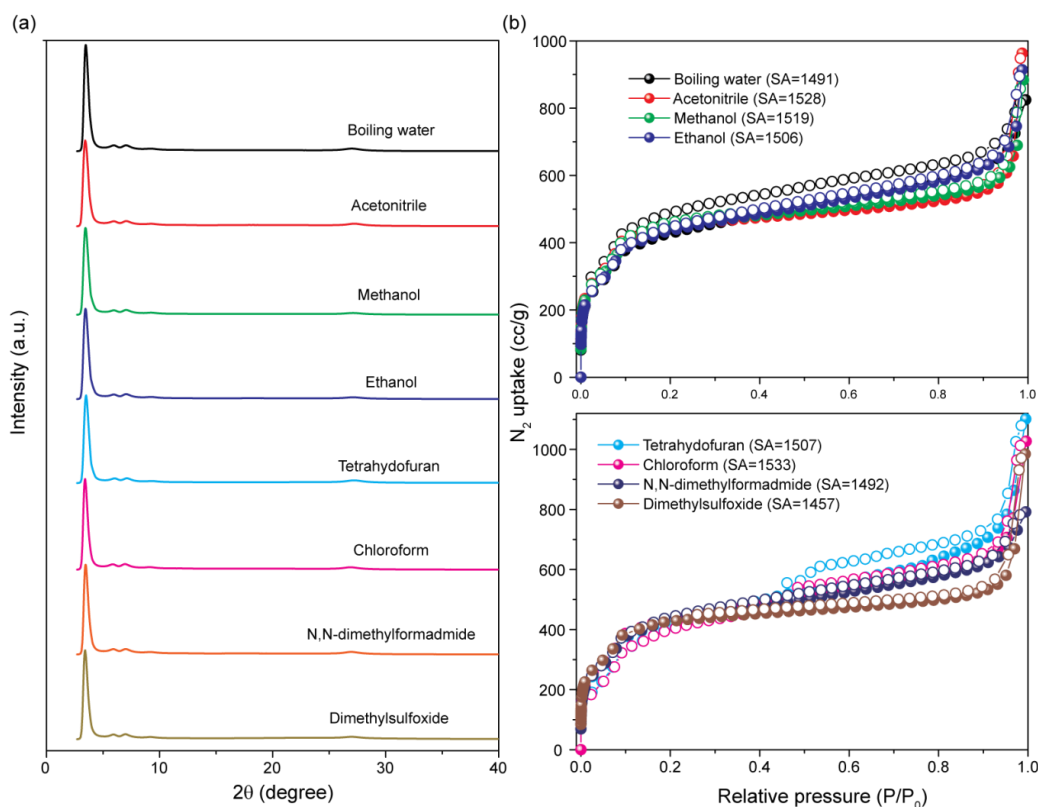


Figure 4.8: PXRD and BET surface area comparison of **TpOMe-DAQ** after treatment in different common solvents for 3 days (protic and aprotic) as mentioned (surface area 1531 m²/g of as-synthesized material).

The proper matching in the PXRD pattern (**Figure 4.8a** & **Figure 4.9a**) with almost identical FTIR spectra (**Figure 4.9b**) of the treated samples with respect to the mother COF revealed the structural rigidity of the materials almost in every medium.

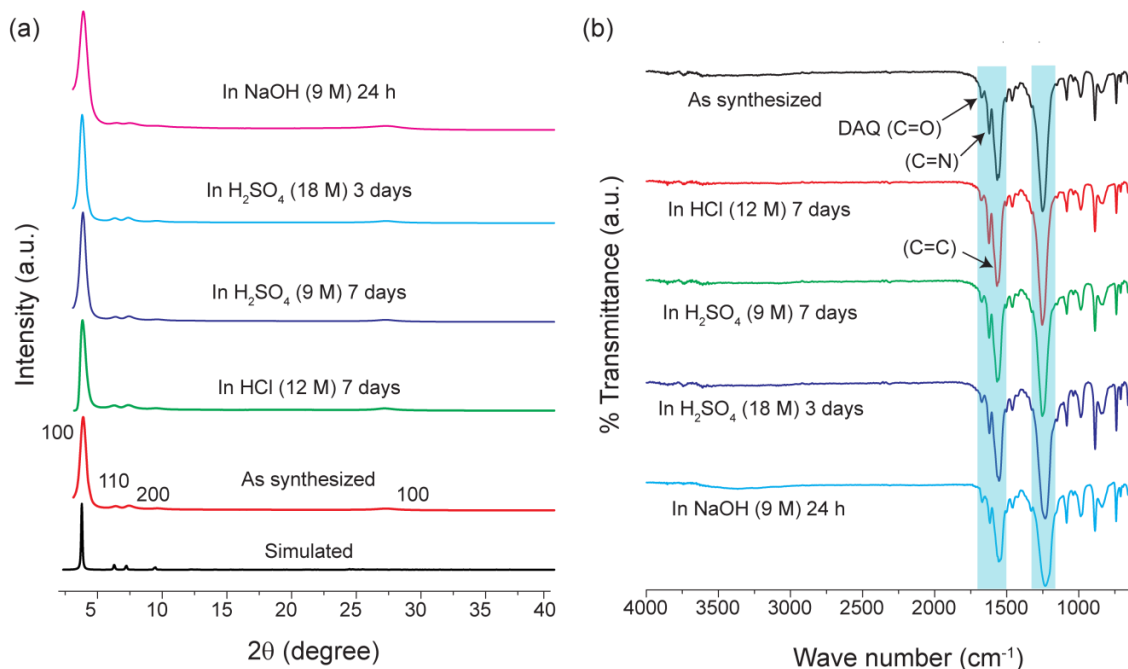


Figure 4.9: (a) PXRD and (b) FT-IR comparison of TpOMe-DAQ COF samples after treatment in a different solvent as mentioned.

The solvent or acid treated samples almost retained their porosity reflecting their structural rigidity in such abrasive conditions whereas in base the material also retained descent porosity (**Figure 4.8b** & **4.10**). The BET surface area of the material was evaluated as 1520, 1486, 1479, 1107 m^2/g with compared to as synthesized (1531 m^2/g) material after treatment

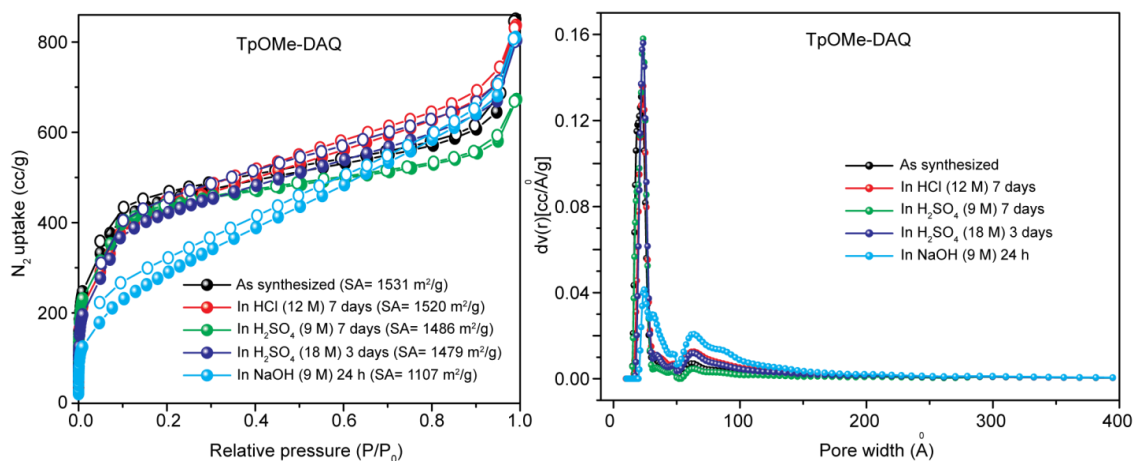


Figure 4.10: (left) N_2 adsorption isotherm and (right) pore size distribution cylindr./sphere pores, QSDFT adsorption branch model) comparison of TpOMe-DAQ COF samples after treatment in a different solvent as mentioned.

in conc. HCl (12 M; 7 days), dil. H₂SO₄ (9 M; 7 days), conc. H₂SO₄ (18 M; 3 days), and in NaOH (1 day; 9M) respectively (**Figure 4.10**). It is to be noted that, the exceptionally high chemical stability was attributed due to the presence of strong interlayer C–H···N H-bonding interaction between methoxy C–H of one layer with imine ‘N’ atom present in the adjacent layer (**Figure 4.11 & Table 4.2**). The hydrogen bonding interaction not only reduces the protonation property of imine nitrogen (key step for acidic hydrolysis) but also provides

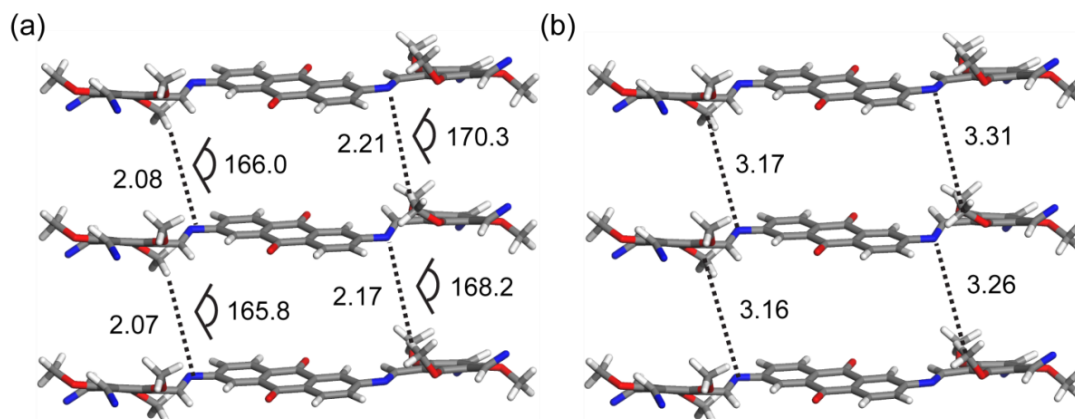


Figure 4.11: Interlayer C–H···N H-bonding: (a) distances (H to N atom in dotted line; Å) and angles (C–H···N) in degree (b) C to N atom distance in dotted line; Å for **TpOMe-DAQ** COF.^[1]

Table 4.2: Inter-layer C–H···N hydrogen bonding in **TpOMe-DAQ** COF

COFs	D (Å)	d (Å)	θ (degree)
TpOMe-DAQ	3.16	2.07	165.8
	3.17	2.08	166.0
	3.26	2.17	168.2
	3.31	2.21	170.3

Note: **D** (Å) is the distance between methoxy (–OCH₃) ‘C’ atom to imine ‘N’ atom; **d** (Å) is the distance between methoxy (–OCH₃) ‘H’ atom to imine ‘N’ atom; and **θ** (degree) is the angle around C–H···N hydrogen bond.

significant steric and hydrophobic environment around the imine bond to prevent water attack (second step of the hydrolysis in acid medium) and thus protect it from being hydrolyzed in strongly acidic conditions as reported in our previous chapters. Separately we have performed the mechanical strength of the as-synthesized sheet using stress-strain experiment. Moreover, the mechanical strength measurement of **TpOMe-DAQ** thin sheets

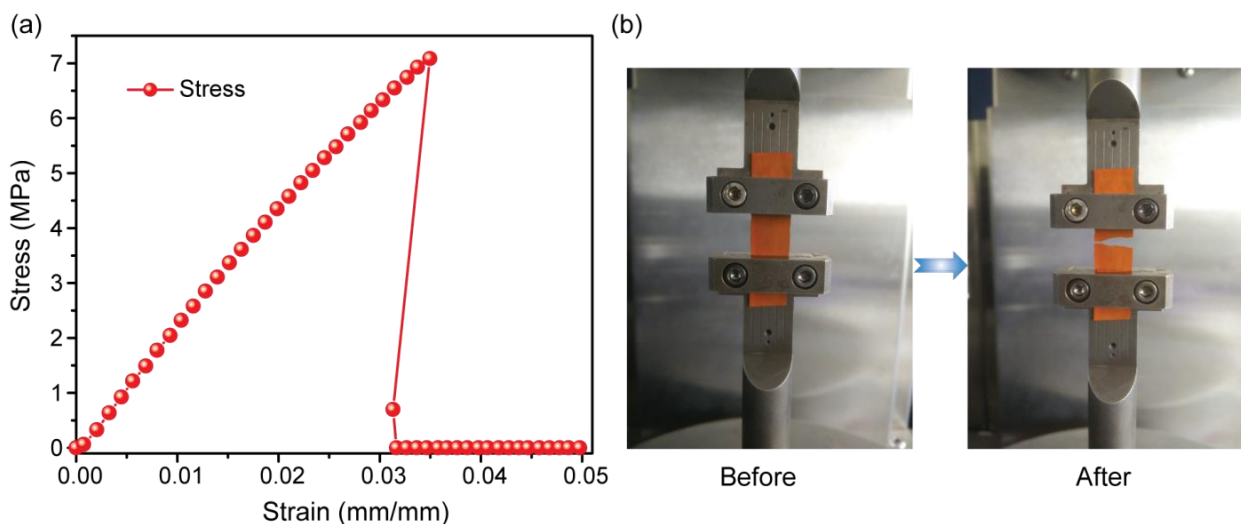


Figure 4.12: Mechanical strength performance of the **TpOMe-DAQ** thin sheet. (a) Stress (MPa) vs strain (mm/mm) measurement and (b) Digital photograph of the sheet before after the experiment.

revealed $\sim 3.5\%$ of the breaking strain (**Figure 4.12**).

4.3 Electrochemical study

This excellent chemical stability along with long-range ordered pore channels (as evidenced from its high crystalline and porous nature), judiciously functionalized with redox-active groups enabled us to employ **TpOMe-DAQ** as a free-standing electrode for SCs. The free-standing thin sheets were fabricated using simple hand-casting of resulted slurry (a mixture of precursors) on a suitable glass slide (ca. area $\sim 5 \times 2 \text{ cm}^2$) with subsequent heating at 90°C for 24 h (**Figure 4.1a-d** & **Figure 4.2**). SEM revealed that the thin sheet (thickness $\sim 200\text{-}220 \text{ }\mu\text{m}$) is composed of small crystallites (length ca. $1\text{-}3 \text{ }\mu\text{m}$) that are perfectly packed to produce the self-standing and crack-free nature (**Figure 4.7**). The efficient crystallite-crystallite packing could significantly reduce the number of grain boundaries and thus internal defects within the crystallites and could enhance the electrical conductivity during electrochemical studies. This observation has empowered to realize COF in thin sheet form, would have enhanced electrical conductivity compared to its powdered form, and thus could showcase higher capacitive performance.

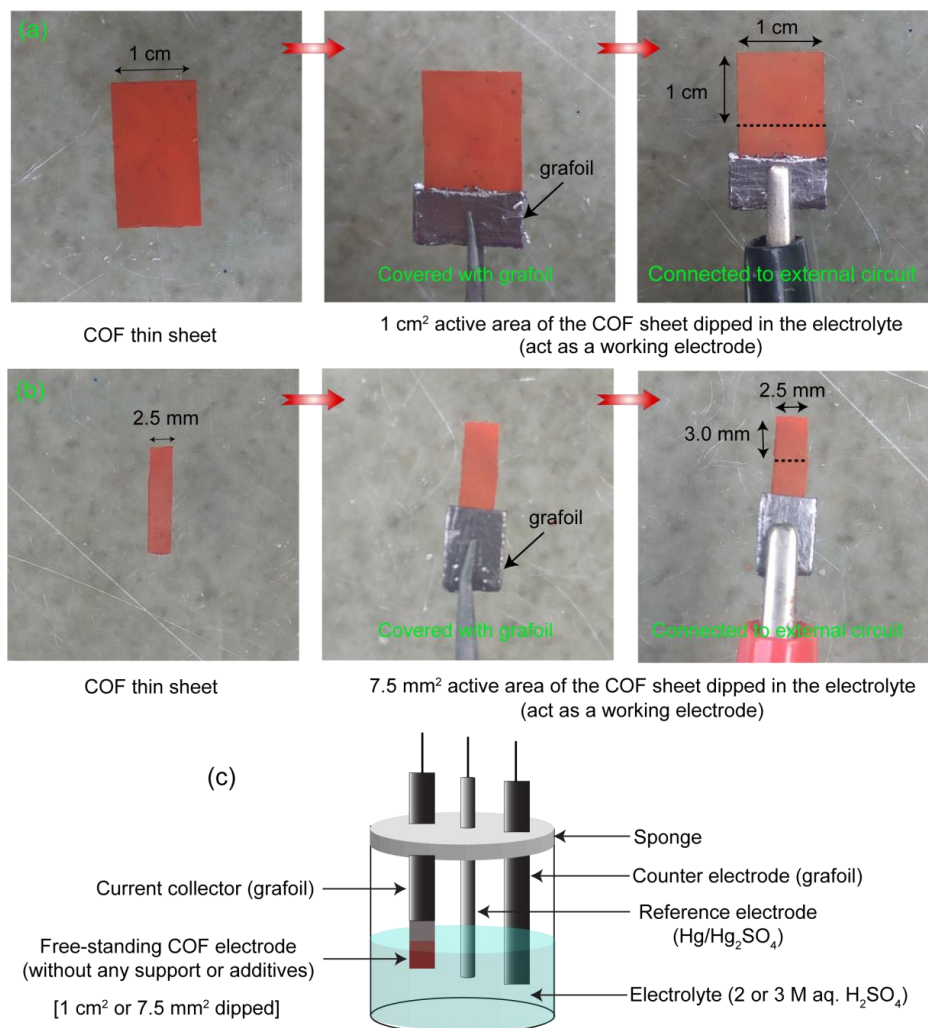


Figure 4.13: (a, b) Working electrode fabrication for three electrode system using 1 cm² or 7.5 mm² active area COF thin sheets. (c) Complete set up of a three-electrode cell.

4.3.1 Three electrode supercapacitor

To accomplish the advantage of the high acid stability of the COF sheet (as discussed in the previous section) we have studied the electrochemical performance of the TpOMe-DAQ at higher conc. aq. H₂SO₄ strength such as 2.0 and 3.0 M. Initially, the self-standing COF thin sheet electrode with the calculated thickness ~200 μm (thickness is measured by the electronic screw gauge) is prepared based on the procedure as reported. Before electrochemical characterization of the sheet in three-electrode assembly, the COF thin sheet is completely dipped in (2 and 3) M aq. H₂SO₄ for 12 hours for the activation of pores and to improve the electrode-electrolyte interaction. Later on, the **TpOMe-DAQ** thin sheet was

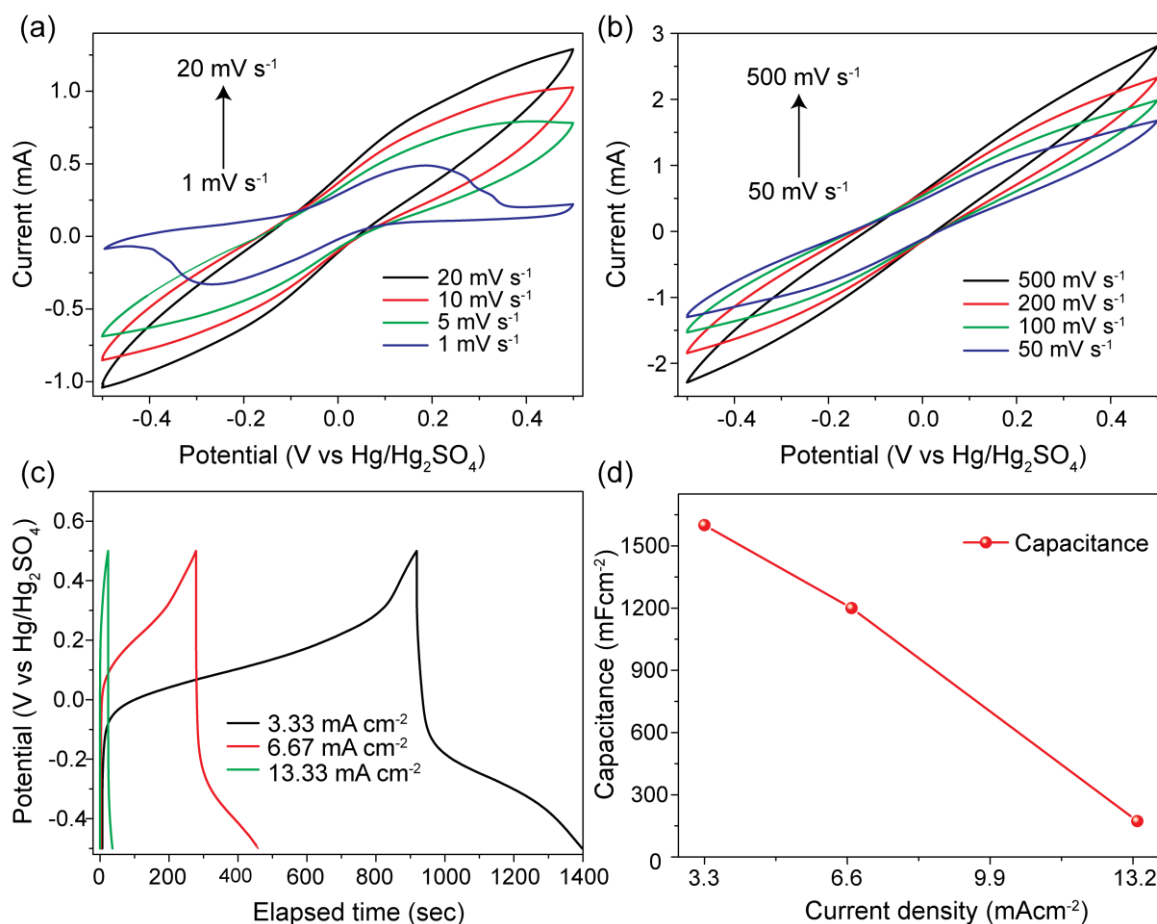


Figure 4.14: (a, b) Cyclic voltammetry (CV); (c) Galvanostatic charge-discharge (GCD) and (d) Current density vs areal capacitance plot of **TpOMe-DAQ** COF thin sheet (active area $2.5 \times 3.0 \text{ mm}^2$) using $3 \text{ M H}_2\text{SO}_4$ as an electrolyte in three electrode assemblies.

directly used as the working electrode by covering with a grafoil and connected to an external circuit (**Figure 4.13a-b**). The free-hanging COF electrode is dipped in (2 and 3 M) H_2SO_4 electrolyte by keeping grafoil current collector 2.5 mm above from the electrolyte solution (**Figure 4.13c**). During the electrochemical study, $\text{Hg}/\text{Hg}_2\text{SO}_4$ and grafoil are used as reference and counter electrodes, respectively. In the present study, a COF thin sheet with two different active areas such as 1 cm^2 and 7.5 mm^2 have been selected for the electrochemical study. Moreover, to understand the redox behavior of the TpOMe-DAQ COF sheet at different electrolyte concentration the cyclic voltammetry (CV) and galvanostatic charge-discharge study were executed using a constant potential window of 1 V (-0.5 to + 0.5 V). During cyclic voltammetry (CV) analysis, the scan rate was set from 1 mVs^{-1} to a maximum of 500 mVs^{-1} .

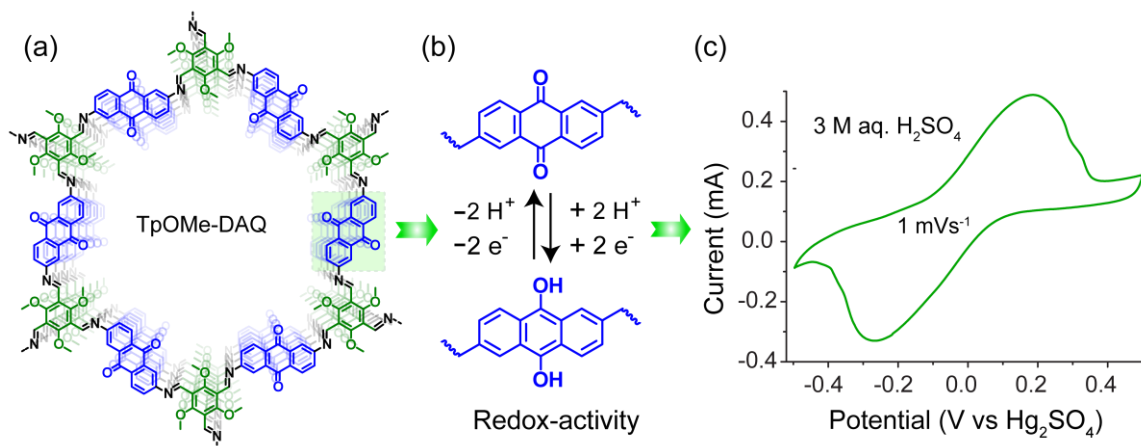


Figure 4.15: (a) Basic structure of TpOMe-DAQ COF. (b) Redox behavior of COF sheet via $2H^+/2e^-$ reversible quinone to hydroquinone transformation. (c) Cyclic voltammetry (CV) plot of TpOMe-DAQ COF thin sheet (active area $2.5 \times 3.0 \text{ mm}^2$) during 1 mVs^{-1} scanning using $3 \text{ M H}_2\text{SO}_4$ as an electrolyte in three electrode system.

The experiment was initially conducted considering $3 \text{ M aq. H}_2\text{SO}_4$ to understand the redox behavior of the as-synthesized COF thin sheet in mordant electrolyte condition considering 7.5 mm^2 as active area exposed within the electrolyte. During cyclic voltammetry (CV) analysis a pair of quasi-reversible redox peaks were observed at a lower scan rate of 1 mVs^{-1} signifying the pseudo-capacitive behavior of the COF however, the distinct appearance of the redox peaks were inconspicuous at higher scan rate (**4.14a-b** & **Figure 4.15c**). Moreover, this is a common observation for most of the pseudo-capacitive materials. During electrochemical analysis, the occurrence of reversible faradic reaction can be ascribed to the reversible switching between quinone (C=O) to hydroquinone (C-OH) via $2H^+/2e^-$ transformation (associated to DAQ amine) (**Figure 4.15b**). The GCD analysis was performed at various current densities such as 3.3 , 6.7 and 13.3 mAcm^{-2} whereas the maximum capacitance value was estimated from the overall discharge time during 3.3 mAcm^{-2} current density (**Figure 4.14c**). Notably, the discharge time calculated from 3.3 mAcm^{-2} current density was 480 sec which provides outstandingly high areal capacitance value of 1600 mFcm^{-2} . However, under the similar condition, the areal capacitance reduces to 1280 mFcm^{-2} (discharge time 384 sec) when the strength of the electrolyte goes down to $2 \text{ M aq. H}_2\text{SO}_4$ (calculations are provided later). Hence, we assume, during 3.3 mAcm^{-2} scanning the areal capacitance, moved from 2 to 3 M electrolyte concentration, enhances from 1280 (135 Fg^{-1}) to 1600 mFcm^{-2} (169 Fg^{-1})

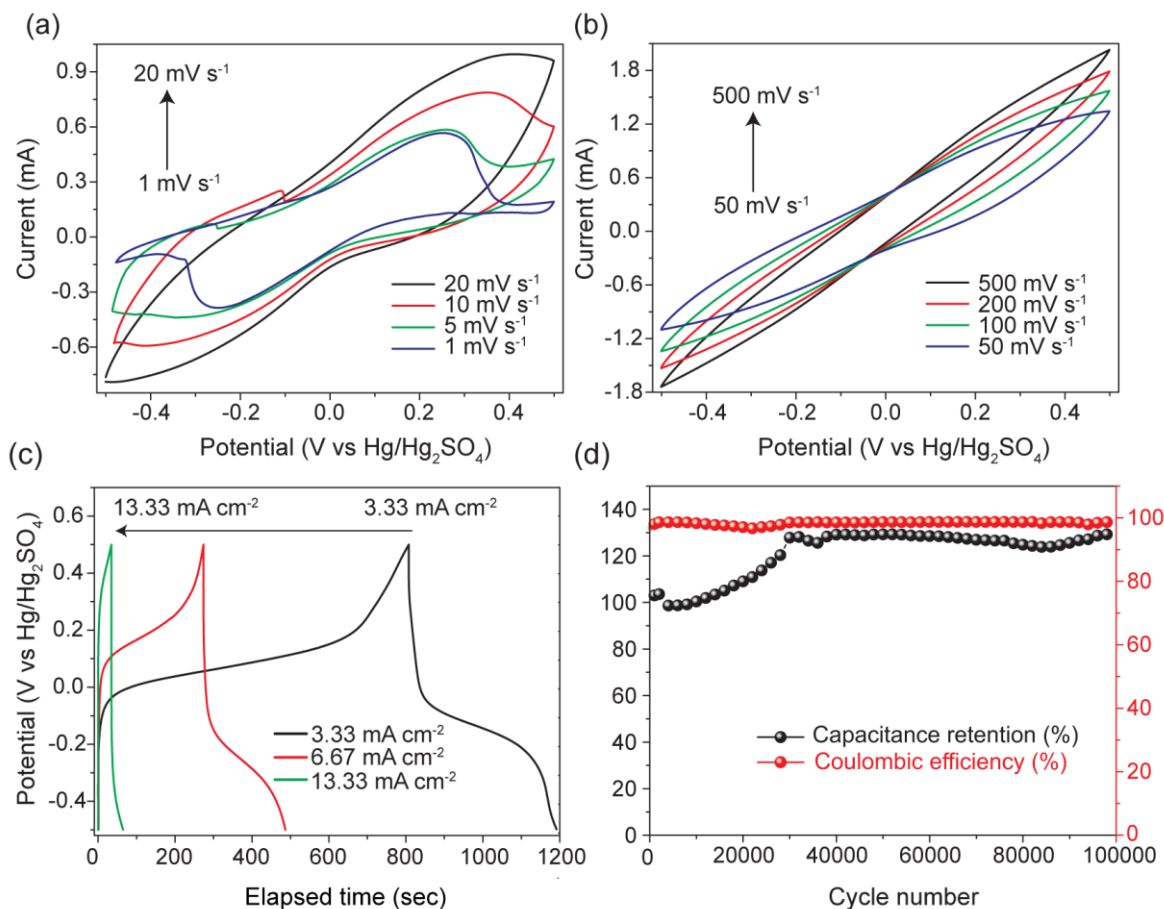


Figure 4.16: (a, b) Cyclic voltammetry (CV); (c) Galvanostatic charge-discharge (GCD) of 7.5 mm^2 ($2.5 \times 3.0 \text{ mm}^2$) active area of the thin sheet using $2 \text{ M aq. H}_2\text{SO}_4$ as an electrolyte. (d) Cyclic stability of *TpOMe-DAQ* COF thin sheet exposing 1 cm^2 active area in $2 \text{ M aq. H}_2\text{SO}_4$ as an electrolyte in three electrode assemblies.

which could be due to the availability of more H^+ ions (comes from electrolyte) around the redox-active quinone ($\text{C}=\text{O}$) centers or *vice-versa*. Notably, for applications in flexible or wearable electronics, measurement of areal capacitance is significant to unveil effective specific capacitance of the electrode [4.27]. Moreover, considering its moderate acid strength and promising capacitance value (1280 mFcm^{-2}) with a significant current response, 2 M electrolyte concentration was used for the remaining studies. Similar to 3 M electrolyte strength, similar CV and GCD curve was also observed when the electrochemical study was performed considering 2 M electrolyte concentration using both 7.5 mm^2 (Figure 4.16a-c) and 1 cm^2 active area of the COF thin sheet (Figure 4.17a-b).

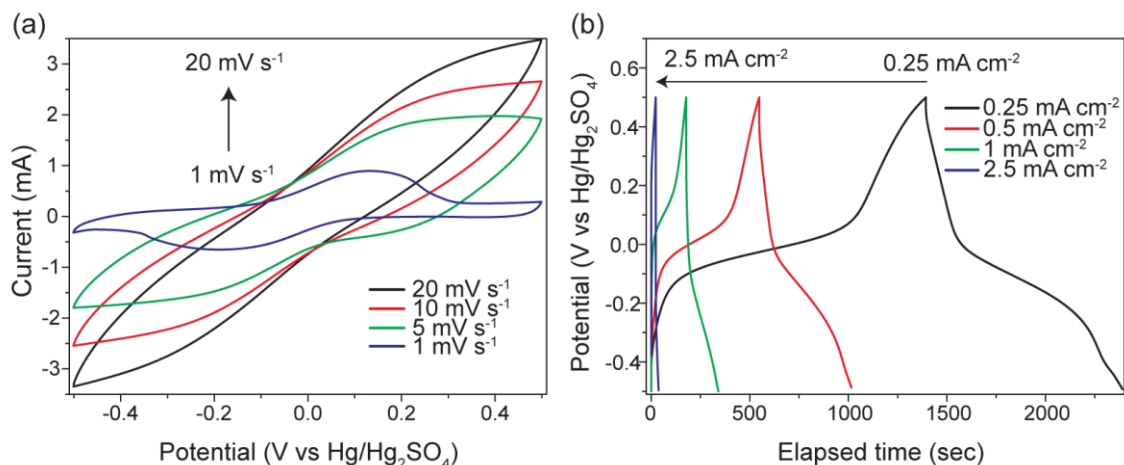


Figure 4.17: (a) Cyclic voltammetry (CV); (b) Galvanostatic charge-discharge (GCD) of 1 cm² active area of the thin sheet using 2 M aq. H₂SO₄ as an electrolyte.

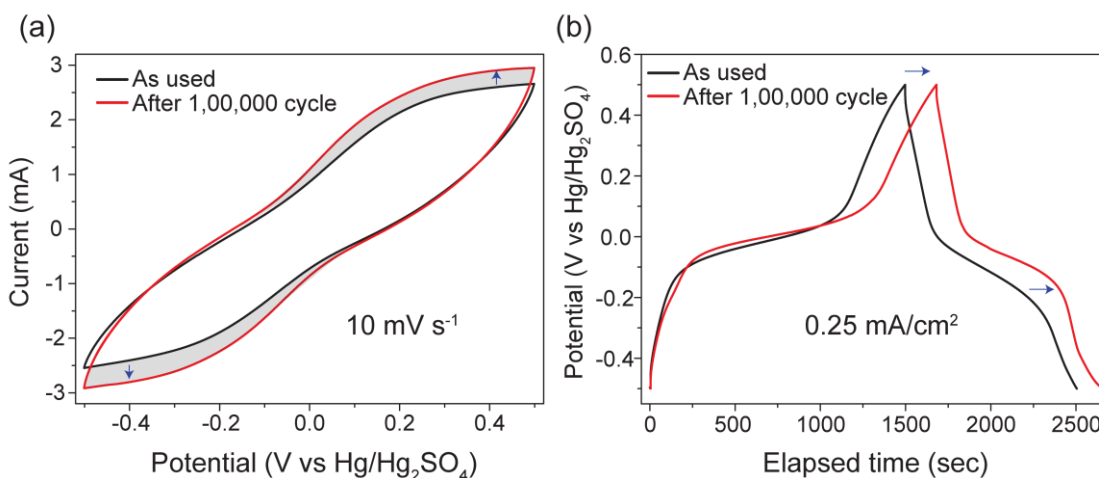


Figure 4.18: (a) Cyclic voltammetry (CV); (b) Galvanostatic charge-discharge (GCD) comparison before and after the cyclic stability of 1 cm² active area of the thin sheet using 2 M aq. H₂SO₄ as an electrolyte.

As the as-synthesized sheet exhibit exceptionally high chemical stability in vigorous conditions, we performed the electrochemical cyclic stability of the material considering 1 cm² active area exposed in 2 M H₂SO₄ solution. Notably, the estimation of cyclic stability is highly important for an electrode material to estimate its long-lived performing ability. From GCD experiments (10 mAcm⁻²; 1 cm² area exposed), we could observe an increment of initial capacitance running up to 30,000 cycles, which we believe could be due to the accessibility of a greater number of redox-active centers by the electrolytes, hence its

activation as the cycling progressed. However, saturation occurred after that and showcased high cycle life even exceeding 1,00,000 continuous charge-discharge cycles without compromising its capacitance or coulombic efficiency (**Figures 4.16d**). Furthermore, the CV and GCD comparison of the thin sheet before and after cyclic stability revealed only slight alteration in their overall curving features without leading to any alternative redox peaks (**Figure 4.18**). Alternatively, we have performed other characterizations such as PXRD, IR, N₂ adsorption, SEM analysis of the thin sheet after cyclic stability performance to observe any of its internal structural change. Moreover, the PXRD and IR data comparison between as-synthesized and treated sample reflect no significant change in the spectrum pattern, revealing the structural rigidity of the TpOMe-DAQ COF sheet in such mordant electrolyte

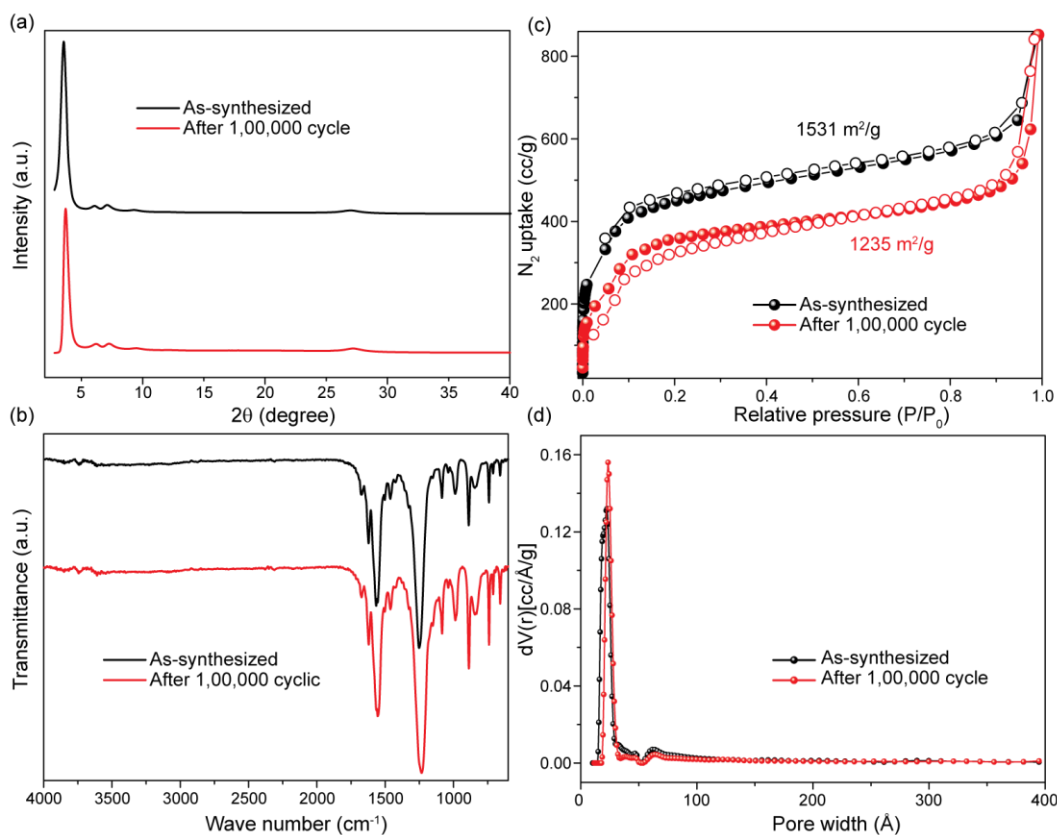


Figure 4.19: Comparison of (a) PXRD, (b) FTIR, (c) N₂ adsorption and (d) Pore size distribution (cylindr./sphere pores, QSDFT adsorption branch model) of as-synthesized and after 1,00,000 cyclic stability study of TpOMe-DAQ COF electrode.

condition. Again, TpOMe-DAQ could retain decent porosity such as $S_{\text{BET}}=1235 \text{ m}^2\text{g}^{-1}$ compared to as-synthesized COF $S_{\text{BET}}=1531 \text{ m}^2\text{g}^{-1}$. Again, no significant alteration was

observed in its pore size distribution after long cyclic treatment of the sheet compared to its as-synthesized form.

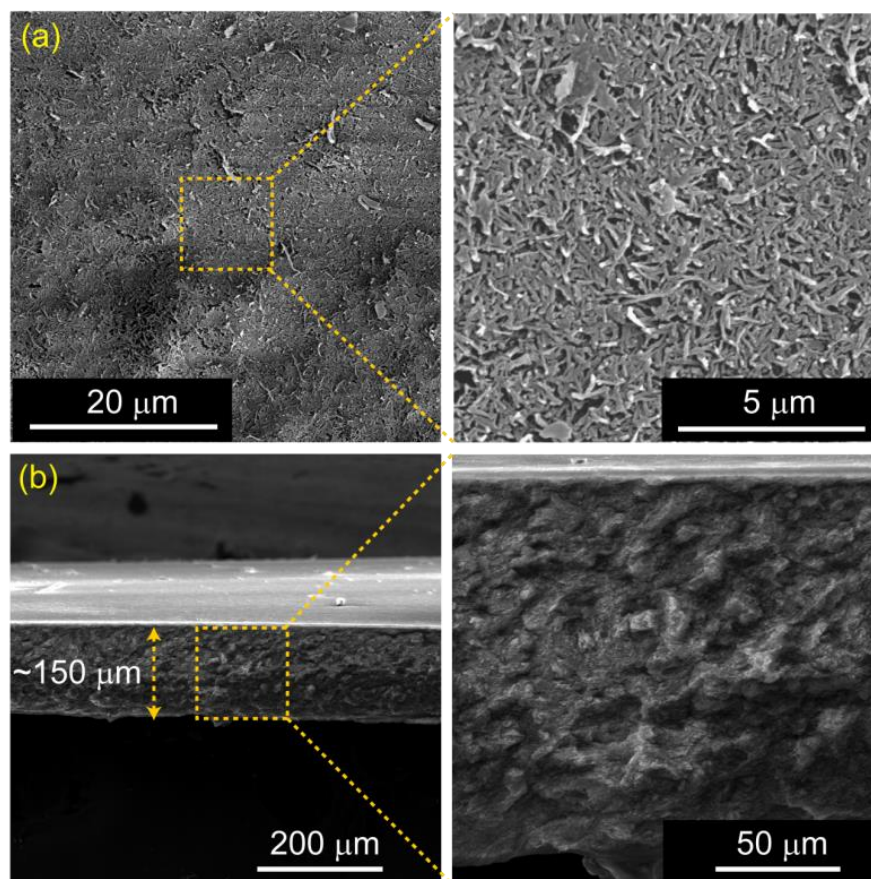


Figure 4.20: (a) Top and (b) cross-section view of the *TpOMe-DAQ* thin sheet after 1,00,000 cyclic performance.

The scanning electron microscopic (SEM) images revealed the thickness of the membrane were still maintained $\sim 150 \mu\text{m}$ even after $> 1,00,000$ cyclic performance signifying its everlasting longevity during the electrochemical performance. The COF sheet although could well maintain its crystallites shape/sizes however a tiny disturbance or defects were observed in crystallites' close-packing after completion of the cyclic stability experiment.

The overall capacitance has been evaluated using the following procedures.

The equation (1) is used for the calculation of areal capacitance from the charge-discharge method in three electrode assemblies.

$$C_a = \frac{(I \times \Delta t)}{\Delta V * a}$$

Equation (1)

Whereas equation (2) is used for the calculation of gravimetric capacitance from the charge-discharge method.

$$C_s = \frac{(I \times \Delta t)}{\Delta V * m}$$

Equation (2)

where,

Δt = Discharge time (Sec) from GCD study

ΔV = Potential window (V)

I = Constant current used for charging and discharging (mA)

a = Geometrical area of COF thin sheet in one electrode (cm^2)

m = Active mass of the COF sheet exposed in the electrolyte (mg)

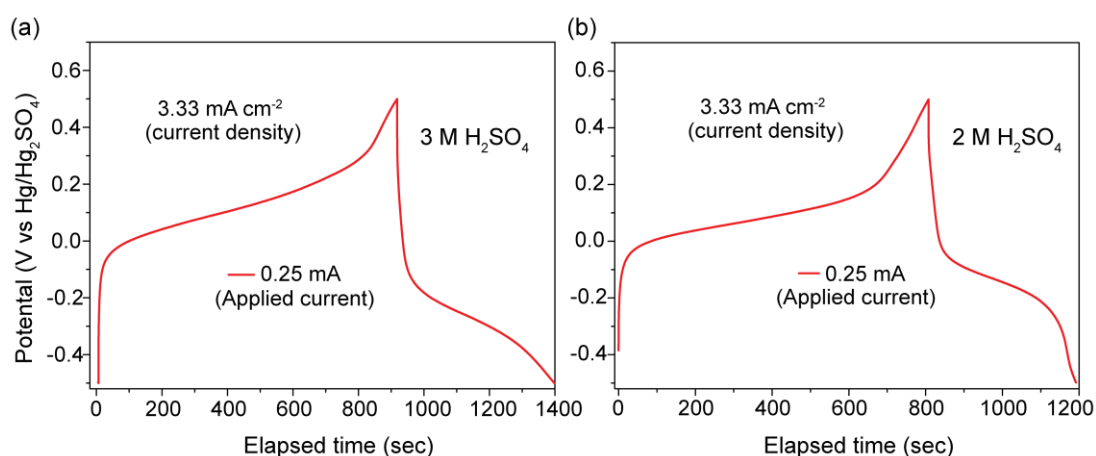


Figure 4.21: Galvanostatic charge-discharge (GCD) plots for **TpOMe-DAQ** thin sheet ($2.5 \times 3.0 \text{ mm}^2$ active area) using 3 M (left) and 2 M (right) aq. H_2SO_4 as an electrolyte in a three-electrode cell.

(a) Areal capacitance calculation in three electrode system using $2.5 \times 3.0 \text{ mm}^2$ active area of the COF sheet exposed in **3 M aq. H_2SO_4** electrolyte (**Figure 4.21a**):

➤ Calculation using 0.25 mA current:

- (1) The elapsed time from the GCD experiment (oxidation of anthraquinones) $\Delta t = 480 \text{ s}$
- (2) It was Multiplied by applied current to get charge: $480 \text{ s} \times 0.25 \text{ mA} = 120 \text{ mA.s}$
- (3) Divide this value with potential window under consideration: $120 \text{ mA.s} / 1\text{V} = 120 \text{ mF}$
- (4) Normalized by the overall geometric area for a given sheet (0.075 cm^2 area) = $120 \text{ mF} / 0.075 \text{ cm}^2 = 1600 \text{ mFcm}^{-2}$ (using equation 1)
- (5) Normalized by overall weight for a given sheet (0.71 mg) = $120 \text{ mF} / 0.71 \text{ mg} = 169 \text{ Fg}^{-1}$ (using equation 2)

(b) Areal capacitance calculation in three electrode system using $2.5 \times 3.0 \text{ mm}^2$ active area of the COF sheet exposed in **2 M aq. H_2SO_4** electrolyte (**Figure 4.21b**):

➤ Calculation using 0.25 mA current:

- (1) The elapsed time from the GCD experiment (oxidation of anthraquinones) $\Delta t = 384 \text{ s}$
- (2) It was Multiplied by applied current to get charge: $384 \text{ s} \times 0.25 \text{ mA} = 96 \text{ mA.s}$
- (3) Divide this value with potential window under consideration: $96 \text{ mA.s} / 1\text{V} = 96 \text{ mF}$
- (4) Normalized by the overall geometric area for a given sheet (0.075 cm^2 area) = $96 \text{ mF} / 0.075 \text{ cm}^2 = 1280 \text{ mFcm}^{-2}$ (using equation 1)
- (5) Normalized by overall weight for a given sheet (0.71 mg) = $96 \text{ mF} / 0.71 \text{ mg} = 135 \text{ Fg}^{-1}$ (using equation 2)

4.3.2 Two electrode supercapacitor (solid state device)

Subsequently, for real life device application, we could fabricate a symmetric solid-state device using two 1 cm^2 pristine COF thin sheets to get an overview about its real-life applicability. Herein, a grafoil with adhesive carbon tape was utilized as the current collector. A $2 \text{ M H}_2\text{SO}_4$ activated (1 hr) and subsequently partially dried COF thin sheet (area- 1 cm^2) is pressed on adhesive portion of the carbon tape. A thin layer of H_2SO_4 -PVA electrolyte gel (polyvinyl alcohol), acting as an electrolyte, is uniformly coated on COF thin sheet and allowed to wet the electrode completely. Two electrodes are made by aforementioned procedure and these two electrodes are sandwiched by keeping a celgard separator in between so that electrodes could not touch each other and any self-discharging could be avoided (**Figure 4.23**).

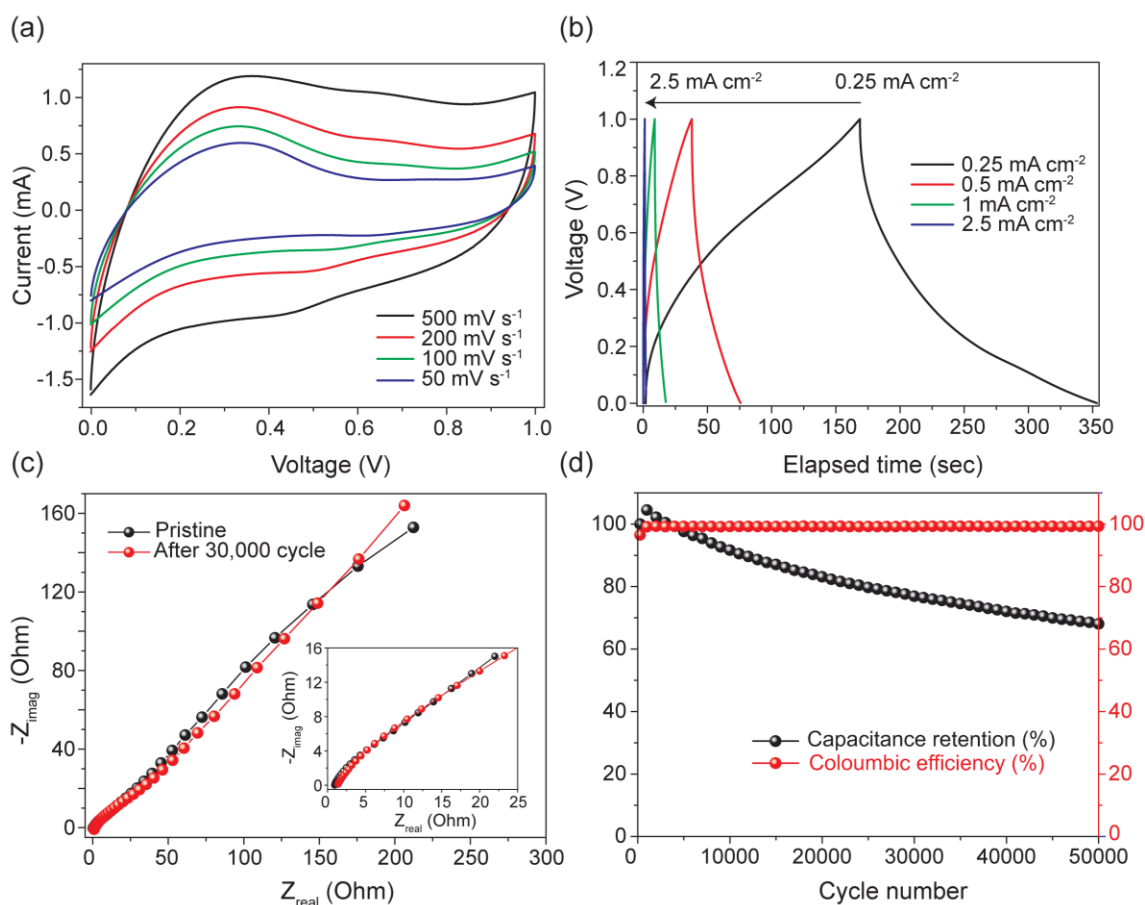


Figure 4.22: (a) CV, (b) GCD, (c) Impedance plot and (d) cyclic stability (from GCD using 5 mA cm^{-2}) of TpOMe-DAQ COF thin sheet (active area 1 cm^2) in two electrode solid-state device using $2 \text{ M H}_2\text{SO}_4$ /PVA as an electrolyte.

Similar to three electrode system, we initially collected CV and GCD of the device as well (**Figure 4.22a-b**). The maximum areal capacitance of the device was calculated from overall discharge time from GCD curve operating in 0.25 mA cm^{-2} current density. Moreover, in the device also we could achieve a promising areal capacitance value of 84 mF cm^{-2} (8.8 F g^{-1}) with significantly high energy and power density of $\sim 2.9 \text{ Wh cm}^{-2}$ and $\sim 61.8 \text{ W cm}^{-2}$ respectively. Electrochemical impedance spectroscopy (EIS) was used to calculate the electrochemical series resistance of the **TpOMe-DAQ** thin sheet (**Figure 4.22c**). For the electrochemical impedance spectroscopy analysis, the frequency was varied from a higher frequency of 1 MHz to a lower frequency of 100 mHz at open circuit potential with an amplitude of 10 mV. A low equivalent series resistance (ESR) of 0.5 ohms is obtained from the Nyquist plot. Nevertheless, no obvious change in the ESR value is observed even after continuous 30000 cycles of charge/discharge. Notably, **TpOMe-DAQ** exhibits good cyclic stability in the device, with $\sim 65\%$ retention of its initial capacitance even operating over 50,000 continuous charge-discharge cycles at a current density of 5 mA cm^{-2} (**Figure 4.22d**). In either case, this is the highest cyclic stability (both in two- and three-electrode assemblies) ever achieved in COF based free-standing supercapacitor studies, even when employing 2 M aq. H_2SO_4 as an electrolyte.

The equation (3) is used for the calculation of areal capacitance from the charge-discharge method.

$$C_a = \frac{2 \times (I \times \Delta t)}{\Delta V * a}$$

Equation (3)

The equation (4) is used for the calculation of gravimetric (specific) capacitance from the charge-discharge method.

$$C_s = \frac{2 \times (I \times \Delta t)}{\Delta V * m}$$

Equation (4)

where,

Δt = Discharge time (Sec) from GCD study

ΔV = Potential window (V)

I = Constant current used for charging and discharging (mA)

a = Geometrical area of COF thin sheet in one electrode (cm^2)

m = Weight of the COF thin sheet in one electrode (mg)

(a) Areal capacitance calculation in solid state device using 1 cm^2 active area of the two COF thin sheets and $2 \text{ M aq. H}_2\text{SO}_4/\text{PVA gel}$ electrolyte (Figure 4.22b):

(1) The average elapsed time from the GCD experiment (oxidation of anthraquinones) $\Delta t = 169 \text{ s}$

(2) It was Multiplied by applied current to get charge: $169 \text{ s} \times 0.25 \text{ mA} = 42.25 \text{ mA.s}$

(3) Divide this value with potential window under consideration: $42.25 \text{ mA.s} / 1\text{V} = 42.25 \text{ mF}$

(4) Normalized by the overall geometric area for a given sheet (1 cm^2 area) = $42.25 \text{ mF} / 1 \text{ cm}^2 = 42.25 \text{ mFcm}^{-2}$ (using equation 3)

(5) Multiplied by two as two equivalent sheets are used in a device = $42.25 \times 2 = 84.5 \text{ mFcm}^{-2}$ (using equation 3)

(6) Normalized by overall weight for a given sheet (9.5 mg) = $42.25 \text{ mF} / 9.5 \text{ mg} = 4.4 \text{ Fg}^{-1}$ (using equation 4)

(7) Multiplied by two as two equivalent sheets are used in a device = $4.4 \times 2 = 8.8 \text{ Fg}^{-1}$ (using equation 4)

The energy density and power density of the electrode were calculated by the equations

$$\text{Energy density (E}_d\text{) (mWhcm}^{-2}\text{)} = \frac{C_a}{8 \times 3600} V^2 \dots\dots\dots \text{Equation (5)}$$

where 'Ca' is the areal capacitance calculated by the charge-discharge (mFcm^{-2}) method and 'V' is the voltage window.

$$\text{Power density (P}_d\text{) (mWcm}^{-2}\text{)} = \frac{E_d}{t} \dots\dots\dots \text{Equation (6)}$$

where 'E_d' is the energy density from Equation (5) and 't' is the discharge time in hour calculated from the discharge curve.

Table 4.3: Comparison of areal (mF cm^{-2}) and gravimetric (F g^{-1}) capacitances with state-of-art promising electrode materials made up off COF and MOF

Electrode type	Specific capacitance (mF cm^{-2})	Gravimetric capacitance (F g^{-1})	Electrolyte used	Scan rate/current density	Cell Configuration	References
DAAQ-TFP/carbon black	0.4	48±10	1 M H_2SO_4	10 mV/s	three electrode	<i>J. Am. Chem. Soc.</i> 2013 , 135, 16821
DAAQ-TFP COF thin film	3.0	—	1 M H_2SO_4	0.4 mA cm^{-2}	three electrode	<i>ACS Nano</i> 2015 , 9, 3178
DAAQ-TFP/PEDOT	350 F cm^{-3} 34 mF cm^{-2}	—	0.5 M H_2SO_4	20 mV s^{-1}	three electrode	<i>ACS Cent. Sci.</i> 2016 , 2, 667
[TEMPO]100% NiP-COF	—	167	0.1 M (C_4H_9) ₄ NClO ₄	0.1 Ag^{-1}	three electrode	<i>Angew. Chem., Int. Ed.</i> 2015 , 54, 6814
Ni ₃ (HITP) ₂	118 F cm^{-3}	111	TEABF ₄ /ACN	0.05 Ag^{-1}	three electrode	<i>Nat. Mater.</i> 2017 , 16, 220
TpOMe-DAQ	1600	169	3 M H_2SO_4	3.3 mA cm^{-2} (0.35 Ag^{-1})	three electrode	this work
	1280	135	2 M H_2SO_4	3.3 mA cm^{-2} (0.35 Ag^{-1})		

Table 4.4: Comparison of areal capacitance (mF cm^{-2}) with state-of-art electrode materials

Electrode type	Specific capacitance (mF cm^{-2})	Electrolyte used	Scan rate/current density	Cell Configuration	References
Carbon nanoparticle/MnO ₂	109	0.1 M Na_2SO_4	5 mV S^{-1}	three electrode	<i>ACS Nano</i> 2012 , 6, 656
VN/CNTs	178	0.5 M Na_2SO_4	1.1 mA cm^{-2}	three electrode	<i>Adv. Mater.</i> 2013 , 25, 5091
Co-Al LDH-NS/GO	7	1 M KOH	5 mV S^{-1}	three electrode	<i>Langmuir.</i> 2012 , 28, 293
ZnO@C@MnO ₂	138.7	0.5 M Na_2SO_4	1 mA cm^{-2}	three electrode	<i>ACS Nano</i> 2013 , 7, 2617
PANI-NWs/CC	1800	1 M H_2SO_4	1.73 Ag^{-1}	three electrode	<i>Power Sources</i> 2010 , 195, 4418
PANI/Au/paper	800	1 M H_2SO_4	1 mA cm^{-2}	three electrode	<i>Angew. Chem. Int. Ed.</i> 2012 , 51, 4934
Activated carbon cloth	88	1 M H_2SO_4	10 mV S^{-1}	three electrode	<i>Adv. Mater.</i> 2014 , 26, 2676
PANI-ZIF-67-CC	2140	3 M KCl	10 mV S^{-1}	three electrode	<i>J. Am. Chem. Soc.</i> 2015 , 137, 4920
ZIF-67-CC	1.47				
PANI-CC	727				
TpOMe-DAQ	1600	3 M H_2SO_4	3.3 mA cm^{-2} (0.35 Ag^{-1})	three electrode	this work
	1280	2 M H_2SO_4	3.3 mA cm^{-2} (0.35 Ag^{-1})		
CNTs/bacterial nano	18.8	[EMIN][NTf ₂]	100 mV S^{-1}	two electrode	<i>ACS Nano</i> 2012 , 6, 6400
Graphene	372	1 M H_2SO_4	1 Ag^{-1}	two electrode	<i>Adv. Energy Mater.</i> 2011 , 1, 917
graphene-cellulose paper	81	1 M H_2SO_4	1 mV S^{-1}	two electrode	<i>Adv. Energy Mater.</i> 2011 , 1, 917
PPy/nanoporous gold	1.8	HClO ₄	100 mV S^{-1}	two electrode	<i>Adv. Mater.</i> 2011 , 23, 4098
TpOMe-DAQ	84	2 M H_2SO_4 /PVA	0.25 mA cm^{-2}	two electrode	this work

The high areal capacitance value with decent energy and power density in the device has led us to fabricate real-time energy storage devices and its fruitful delivery application. Herein, we have prepared three solid-state devices in a similar way and were connected in a series. The CV and GCD were collected using the high potential window of 3 V (0 to 3 V) (**Figure 4.24**). Moreover, as-a-proof of concept study, a 1.8 V LED was taken into consideration and was used for its successful kindling. Initially, the devices as a whole were charged from 0 to 3 V potential and the whole system was immediately removed from the external electric circuit. Then, immediately a 1.8 V LED was connected with the device and it was successfully kindled for 30-40 sec (**Figure 4.23**). During discharging at very starting, the LED glows with high brightness, however, the brightness was decreased as the discharge process goes on.

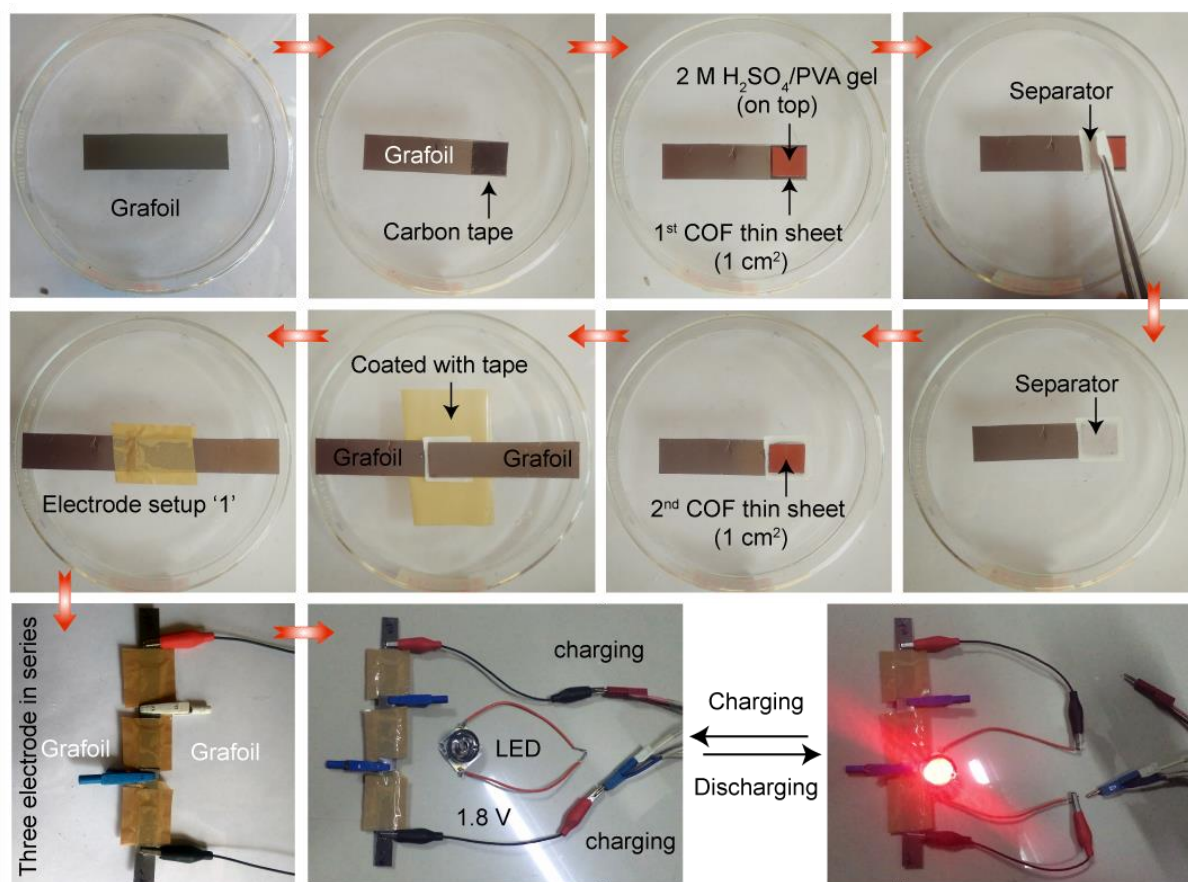


Figure 4.23: Stepwise fabrication of two electrode device using pristine COF thin sheet. Three solid state device connected in a series to enkindle a 1.8 V LED.

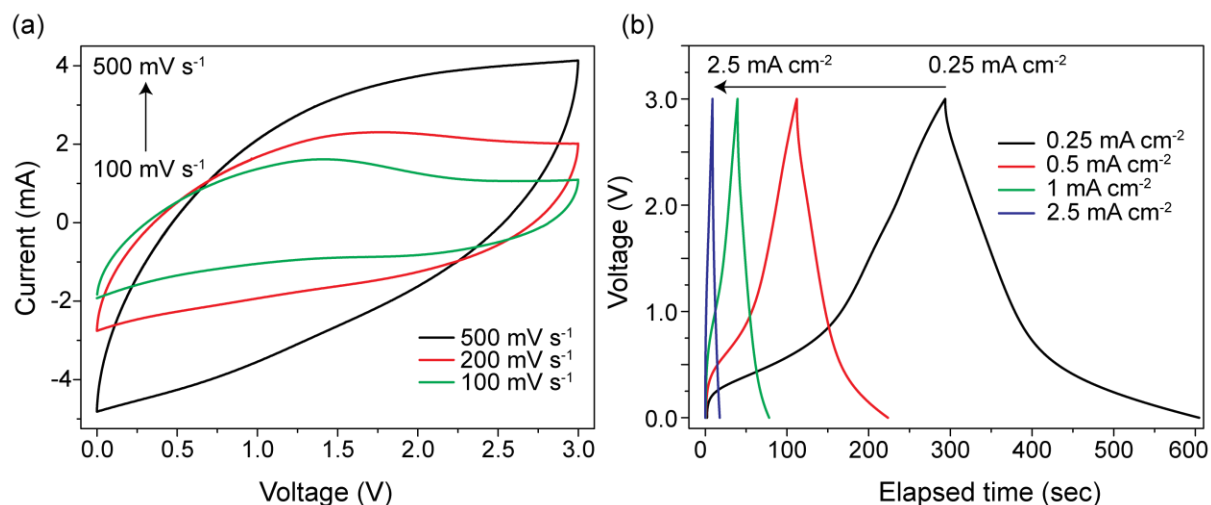


Figure 4.24: (a) CV and (b) GCD plot of three solid state devices connected in series operating in a 3 V potential window.

4.4 Conclusion

In summary, a redox-active chemically stable COF was employed as a self-standing supercapacitor electrode material where the energy was believed to be stored in the form of EDLC as well as pseudo-capacitive owing to its high porosity and redox transformation between quinone to hydroquinone respectively. The as-synthesized thin sheet showcased exceptionally high areal capacitance of 1600 mFcm⁻² (gravimetric 169 Fg⁻¹) when operating in a three-electrode assembly which is the highest ever achieved in a pristine COF based supercapacitor electrode. The thin sheet exhibit exceptionally high cycle life (> 1,00,000) in a three-electrode assembly which originates from its robust framework structure. Again, the chemical robustness of the COF empowered us to execute the electrochemical study using extreme electrolyte concentration (2 M aq. H₂SO₄/PVA gel) where it showcased long cycle life (> 50,000) with 65% capacitance retention when operating in a two-electrode solid-state device. We believe that the overall strategic design, as well as fabrication of the COF thin sheets with long-standing and high performing supercapacitor electrodes, could pave its future application in electrochemical devices.

4.5 Experimental procedures

4.5.1 Materials

2,4,6-Trimethoxy-benzene-1,3,5-tricarbaldehyde (TpOMe) was prepared from 1,3,5-trimethoxybenzene using the reported literature procedure [2.11] and discussed in detail in chapter 2 of the thesis. 2,6-diaminoanthraquinone were purchased from Sigma Aldrich as was used as received. All other reagents and solvents were commercially available and used as received.

4.5.2 General methods for characterization

(a) Powder X-Ray Diffraction (PXRD): The PXRD data were recorded on a Phillips PANalytical diffractometer using a Cu K α radiation ($\lambda = 1.5406 \text{ \AA}$), with a scan rate of 2° min^{-1} . The tube current and voltage were fixed at 30 mA and 40 kV respectively. The sample holder containing the COF powders was scanned between 2 and $50^\circ 2\theta$ (step size of 0.02°).

(b) Thermogravimetric Analysis (TGA): TGA was recorded on an SDT Q 600 TG-DTA analyzer instrument. Approximately 5-7 mg of the COF sample was added to an aluminum crucible and heated from 25 to 900°C under N_2 atmosphere (heating rate of $10^\circ \text{C min}^{-1}$).

(c) IR Spectroscopy: The Fourier transform infrared spectra (FTIR) of the COFs were collected on a PERKIN ELMER FT-IR SPECTRUM (Nicolet) spectrometer in ATR mode.

The FTIR data were collected over the range of 4000 - 600 cm^{-1} .

(d) Gas Adsorption: The gas adsorption experiments were performed specifically for the activated COF powders using Autosorb automatic volumetric instrument (*Quantachrome*).

COF powder activation procedure: Approximately 40 mg of the as-synthesized COF powders were evacuated under vacuum at 120°C for 12 h. Finally, the activated samples were used for gas adsorption (N_2).

(e) Electrochemical analysis: All electrochemical analysis including cyclic voltammetry (CV), impedance measurements (Electrochemical Impedance Spectroscopic [EIS]) investigation was performed from 1 MHz to a lower frequency of 100 MHz frequency against the open circuit potential with a sinus amplitude of 10 mV [$V_{\text{rms}} = 7.07\text{mV}$] and galvanostatic charge/discharge measurements (GCDC) were carried out using a Bio-Logic SP-300 PG Stat instrument. Electrochemical data were analyzed in EC-Lab software **V10.19**.

(f) Mechanical strength measurement: Tensile testing was performed on a TA Instruments dynamic mechanical analyzer (DMA, RSA- III). We performed stretching experiments using the rectangular tension geometry for the COF thin sheets. Sheets were cut into rectangular shapes and then clamped vertically in the rectangular geometry and stretched at a constant rate of 0.1 mm/s. All the experiments were done at room temperature. Stress-strain Calculation: We have calculated the engineering stress (σ_E) by dividing the stretching force (F) with the initial cross-sectional area (A) ($\sigma_E = F/A$). The engineering strain is calculated using the equation: $\epsilon_E = (l-l_0)/l_0$, where, l is the final length and l_0 is the initial length.

4.5.3 Structure Modeling of COFs

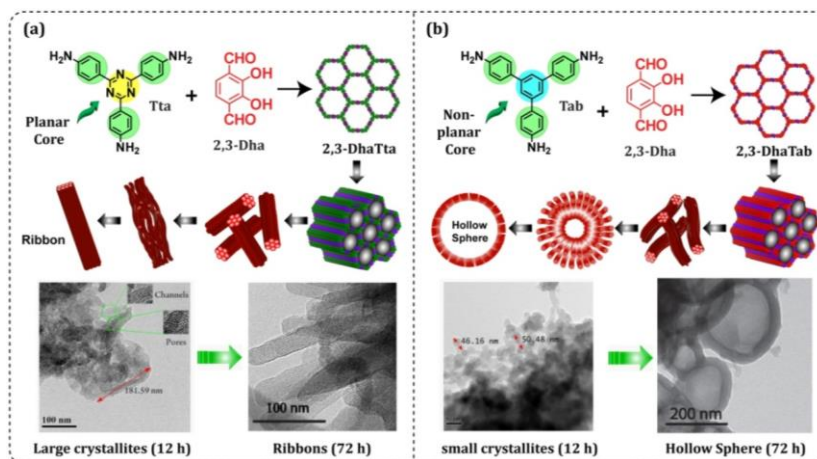
Atomic positions and cell sizes of modeled COF layers were optimized using the Self-Consistent-Charge Density-Functional Tight-Binding (SCC-DFTB) method. All atoms were described using the mio-0-1 parameter set [DOI: 10.1103/PhysRevB.58.7260] and Lennard-Jones dispersion. The layer stacking is affected by the Coulomb repulsion between the partial atomic charges in adjacent layers.^[2] Hence, several slipped AA stacking possibilities were considered for each COF by shifting adjacent layers with respect to each other in different directions up to 6Å. In addition, different orientations of the methoxy groups (in plane, above plane, below plane) were considered. The predicted slipped structure has the lowest energy while maintaining an agreement with the experimental PXRD pattern. The fractional coordinates of all the COFs have been provided in **Table 4.1**. The COF has been modeled in the triclinic space group ($P1$) by comparing the experimental and simulated PXRD patterns. Refinements of PXRD pattern were done using Reflex module of the Material studio.^[3]

The lowest energy slipped-AA structure of TpOMe-DAQ was noted to be locked in place by several interlayer C-H...N hydrogen bonds (**Figure 4.11 & Table 4.1**). In order to confirm the stability conferred by the hydrogen bonds, Molecular Dynamics (MD) simulations were run from the lowest energy slipped-AA structure. Simulations were run in the NVT ensemble, at the optimized volume. The temperature of 300K was maintained by a Nose-Hoover thermostat. 50ps of simulation was run with a time step of 1fs. Throughout the simulation, the layers slipped over each other within bounds defined by allowing each methoxy group of one layer forming a hydrogen bond with the imine nitrogen of the adjacent layer. Transient C-H...O (methoxy – methoxy) bonds were occasionally seen as intermediates.

NOTE: The results of this chapter have already been submitted in *J. Am. Chem. Soc.*, as a communication format entitled “*Interlayer Hydrogen-Bonded Covalent Organic Frameworks as High-Performance Supercapacitors*”. The manuscript was prepared based on the results obtained from the group of Dr. Rahul Banerjee and his students Mr. Arjun Halder and Mr. Abdul Khayum M., from CSIR-National Chemical Laboratory, Pune, India. Dr. Sreekumar Kurungot and his student Ms. Meena Ghosh for their contribution in electrochemical studies from CSIR-National Chemical Laboratory, Pune, India and Dr. Matthew Addicoat from School of Science and Technology, Nottingham Trent University, Nottingham, United Kingdom for computation study. Apart from electrochemical and computational study major works were contributed by Mr. Arjun Halder.

Morphological Diversity in 2D Porous Covalent Organic Frameworks: An Effect of Core Planarity modulation

Abstract: Covalent Organic Frameworks (COFs) are pristine sets of porous organic nano-materials, which earned immense attention in recent years due to their structural tunability and diverse applicability.



COFs are usually synthesized as micro or nanocrystalline powders and its growth are mostly limited to nano domain with various interesting morphology/shape. The morphologies of nano-porous crystallites are considered as one of the very important properties for applications such as in molecular adsorption or charge carrier mobility etc. However, practical understanding of the mechanism behind the formation of COF crystallites and subsequent framework crystallization with certain morphologies were poorly explored. Herein, in this chapter we examine in detail about the mechanism of formation for two diverse morphologies in COFs such as ribbons (**2,3-DhaTta**) and hollow sphere (**2,3-DhaTab**) whereas the formation of the hollow sphere was believed due to an inside-out Ostwald ripening process. Moreover, herein for the first time, we have attempted to understand in deep, the relationship of dihedral angles of the linkers at the molecular level with the final morphology of the COF crystallites. Besides, we have also shown how crystallinity and surface area of COFs gets tuned based on overall core planarity of the linkers.

5.1 Introduction

The design and development of nanomaterials with well-defined superstructures is considered to be one of the major breakthroughs in the field of supramolecular chemistry in current decades [5.1]. However, to attain definite control over its function and material properties the nanoscale organization of the molecular building blocks must be precisely overlooked. As for example, various biological functions in natural systems are most often governed based on its defined nano or microarchitectures [5.2]. To this end, the precise construction of an artificial superstructure with well-defined molecular nano or micro-domains using bottom-up approach is not straightforward and is profoundly challenging. Hence, if such issues are overcome there would be a significant improvement on a structure-property relationship which is important for a material for its real-time applications.

Among all other chemical reactions reported in the literature, the reactions controlled over dynamic covalent chemistry (DCC) are found to be promising towards the formation of well-defined ordered superstructures [5.3]. The DCC favours simultaneous error checking and its correction during framework formation, hence, based on which, the compositional exchange and morphological transformation among the crystallites can be precisely realized. In this context, morphological evaluation in 2 D nano-framework material build up entirely under controlled of DCC chemistry, such as covalent organic frameworks (COFs), are highly important owing to their various potential applications [5.4]. For example, Yaghi et al. could synthesize crystalline COFs using dynamic borate ester bonding [5.5]. Recently, Kubo et al. documented a very interesting morphology transformation of microspheres to microribbons in dynamic polymers containing reversible borate ester linkages [5.6]. Additionally, the scientists have realized the DCC could also control the morphology evolution in aromatic polymers even at micrometre scale where it is barely observed in other polymers formed without the aid of dynamic covalent bonds [5.7]. However, the mechanism of DCC controlled morphology and their behaviour is still under scrutiny and many other interesting aspects till date are largely unexplored. Moreover, despite significant progress in COFs in recent years, reports based on its template-free nano- or microstructures construction have been rarely reported. Notably, the successful applications of such network materials not only depend on its special chemical structures but also on its nano-scale sizes, morphologies and

architectures. Therefore, an explicit understanding of the morphology-modulation with respect to their constituents is highly required.

5.2 Detailed investigation of nano-ribbon and hollow spherical morphological evolution in 2D COFs

The previous chapters revealed about the synthesis of ultra-stable, crystalline and permanently porous covalent organic frameworks (COFs) and discussed their potential usage in water purification (membrane form) or in energy storage (as a thin sheet). Apart from solving the chemical stability issues, the other prevailing problem in COFs is the detailed understanding of the mechanism behind the COF crystallite formation and its subsequent crystallization to form certain important morphologies [5.8]. COFs are usually synthesized as insoluble micro-crystalline powders and the crystallite's growth is limited only in nanodomains owing to several internal defects during its crystallization [5.8b]. As a result, in micro or nano domain COFs are found to adopt diverse morphologies such as sheets [5.9], belts [5.10], cubes [5.11], rectangular prismatic [5.12], nano-fibres [5.13], nano-flowers [5.14a], hollow spheres [5.14b-c] etc. As discussed, the overall properties and real-time employment of those materials not only rely on the compositions but also on their nano-scale morphology which plays an incredible role in diverse applications such as in charge carrier mobility, energy storage, drug delivery, and molecular adsorption [5.15].

In 2015, Kandambeth *et al.* reported the hollow spherical morphology in a COF (DhaTab), but it was exempted from the detailed molecular level investigation [5.16a]. Xin Zhao and co-workers could prepare boronate ester linked two-dimensional polymer hollow spheres [5.17]. However, the hollow spheres were difficult to isolate as they were synthesized in a mixture with other nano-sheet morphologies and its limited chemical stability restricts their real-life applications [5.17]. This realization prompted us to prosecute further investigation and herein we report two new chemically stable imine-based COFs, which self-assemble to ribbons (**2,5-DhaTta**) and hollow spheres (**2,5-DhaTab**) upon crystallization in a single step without any templating agents. Among them, hollow spherical structure is considered as a highly important morphology owing to its promising applications towards catalysis and molecular sensors [5.18], energy storage [5.19] and drug delivery [5.20]. Notably, achieving hollow spherical morphology of any polymeric or related materials are extremely difficult as well as their existence is very rare and does often require

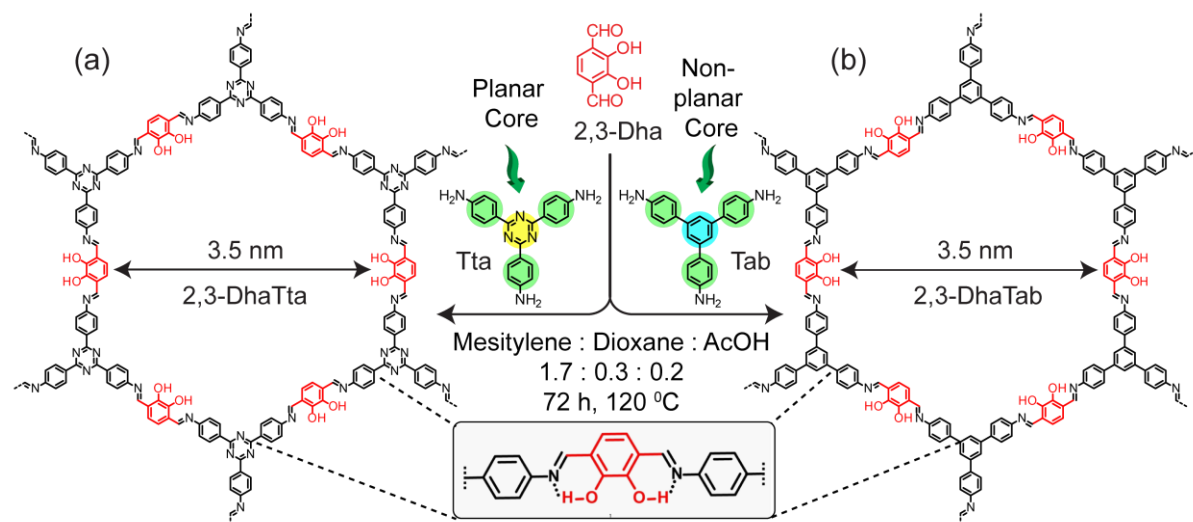


Figure 5.1. Schematic representation of the synthesis of (a) **2,3-DhaTta** COF and (b) **2,3-DhaTab** COF separately reacting **2,3-Dha** aldehyde with **Tta** and **Tab** amines respectively. The existence of $O-H\cdots N$ intralayer H-bonding has been shown in the inset.

usage of templating agents [5.21]. Whereas, the self-template strategy during COF hollow sphere formation is considered to be cost-effective as it is devoid from additional templates usage and required no further removal of other contaminants from the pores [5.22]. In the present study, the self-templated intermediates, accountable for the formation of the final morphology of the COFs (ribbon and hollow sphere), were isolated and their mechanisms of formation have been thoroughly and systematically investigated using SEM, TEM and AFM microscopic study. Moreover, after careful evaluation of intermediates morphology, herein the formation of hollow spheres was believed to originate *via* an inside-out Ostwald ripening phenomenon. Besides, we have separately attempted to understand in deep the relationship of dihedral angles of the linkers at the molecular level with the final morphology of the COF crystallites. The as-synthesised COFs (**2,3-DhaTta** and **2,3-DhaTab**) were found to be highly crystalline, permanently porous (S_{BET} as high as $1700 \text{ m}^2/\text{g}$) with remarkable stability towards water and 3(N) HCl beyond 3 days treatment, which was believed due to the presence of intramolecular $O-H\cdots N$ hydrogen bonding [5.23]. Moreover, for the first time, we have shown how the crystallinity and surface area of COFs gets tuned based on core planarity at the molecular level of the used linkers. Additionally, based on DFT (Density Functional Theory) study a significant correlation between stacking energy of two adjacent COF layers with their backbone planarity was established, which was believed to be the

predominant guiding factor for governing their crystallinity, porosity and morphological diversity evaluation.

5.2.1 Synthesis of COFs

2,3-DhaTta: A pyrex tube (o.d. \times i.d. = 18×16 mm² and length 18 cm) was charged with 4,4',4''-(1,3,5-triazine-2,4,6-triyl)trianiline (**Tta**) (92 mg, 0.26 mmol), 2,5-dihydroxyterethaldehyde (**2,3-Dha**) (65 mg, 0.39 mmol), 5.1 mL of mesitylene, 0.9 mL of dioxane, 0.6 mL of 6 M aqueous acetic acid. This mixture was sonicated for 15 minutes in order to get a homogenous dispersion. The tube was then flash frozen at 77 K (liquid N₂ bath) and degassed by three freeze-pump-thaw cycles. The tube was sealed off and then heated at 120 °C for 3 days. A red coloured precipitate formed was collected by centrifugation or filtration and washed with first dioxane (2-3 times) and then with N,N-dimethylacetamide until a clear solution comes from the precipitate. The powder collected was then solvent exchanged with anhydrous ethanol 5-6 times and then dried at 120 °C under vacuum for 24 hours to give a deep red coloured powder in 80% (89 mg) isolated yield (**Figure 5.1a**). **IR (powder, cm⁻¹):** 1585(m), 1509(s), 1416 (m), 1366(s), 1302(m), 1200(w), 1173(m), 1146(w).

2,3-DhaTab: The COF **2,3-DhaTab** was synthesised following same technique from the mixture of 1,3,5-tris(4-aminophenyl)benzene (**Tab**) (91 mg, 0.26 mmol), 2,3-dihydroxyterethaldehyde (65 mg, 0.39 mmol) (**2,3-Dha**), 5.1 mL of mesitylene, 0.9 mL of dioxane, 0.6 mL of 6 M aqueous acetic acid. The whole reaction mixture was kept at 120 °C for 3 days and after the reaction, a deep brown coloured solid was found to appear at the bottom of the pyrex tube was isolated by filtration and washed with dioxane (2-3 times) and then with N,N-dimethylacetamide to have almost pure precipitate. The powder collected was then solvent exchanged with anhydrous ethanol for 5-6 times and then dried at 120 °C under vacuum for 24 hours to give a deep brown coloured powder in 82% (isolated yield) (**Figure 5.1b**). **IR (powder, cm⁻¹):** 2980 (m), 2885(w), 1617(m), 1593(m), 1545(m), 1494(m), 1440(m), 1392(m), 1358(w), 1298(s).

5.2.2 Structural simulation and characterization

Both the COFs reported here show high crystallinity as revealed by their PXRD patterns (**Figure 5.2**). High intense peaks at 2.8 ($2\theta \pm 0.1$) for **2,3-DhaTta** and **2,3-DhaTab** appear due to the strong reflections from the 100 planes. The **2,3-DhaTta** show other minor

peaks at ~ 4.9 , ~ 5.7 , ~ 7.5 , $\sim 9.9^\circ$ (2θ) due to the reflections from 110, 200, 120, and 220 planes respectively. Similarly, **2,3-DhaTab**, minor peaks at ~ 4.9 , 5.6 , ~ 7.4 , $\sim 9.8^\circ$ (2θ) appear

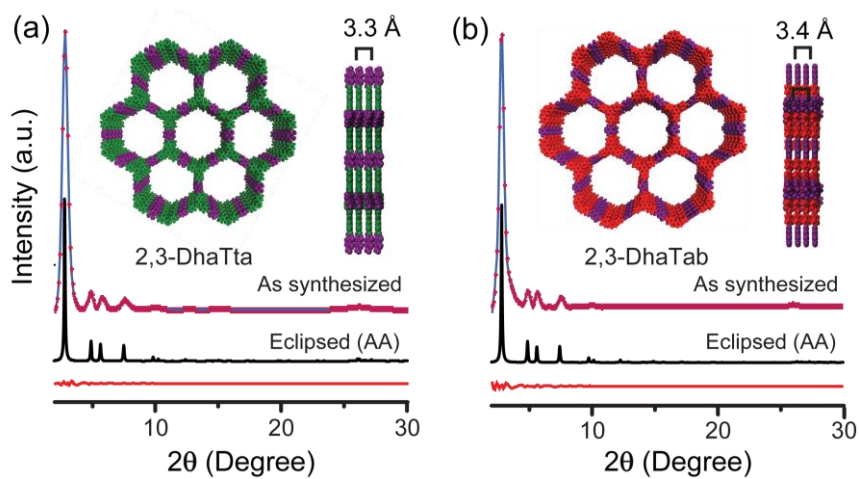


Figure 5.2. Crystal structures of the reference compounds (a) *SaTta*, (b) *2,3-Dha-ani* and (c) *SaTab*. The torsion angles have been shown with double-headed arrows.

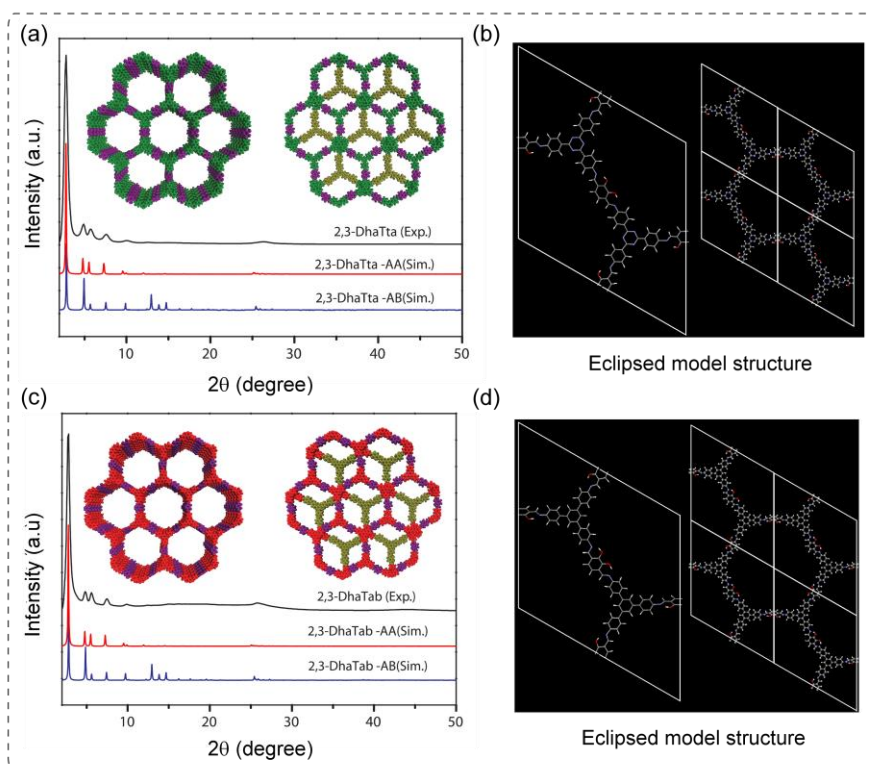


Figure 5.3. (a, c) PXR D comparison of as-synthesized COFs with its simulated eclipsed (AA) and staggered (AB) stacking models. (b,d) Eclipsed model structures of respective COFs.

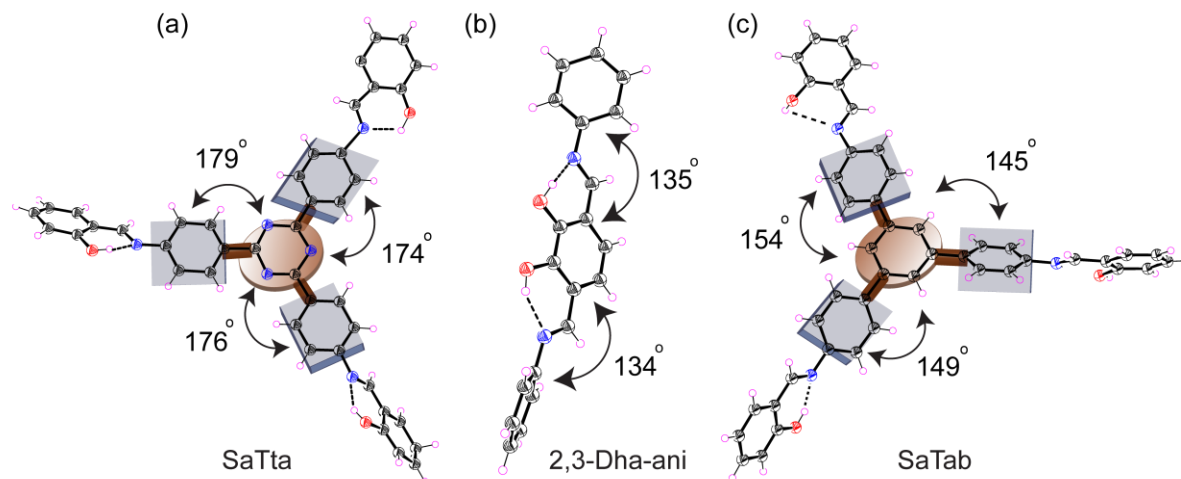


Figure 5.4. Crystal structures of the reference compounds (a) **SaTta**, (b) **2,3-Dha-ani** and (c) **SaTab**. The torsion angles have been shown with double-headed arrows.

due to the reflections from the 110, 200, 120, 220 planes. Peaks at $\sim 26.1^\circ$ ($2\theta \pm 0.2$) present in both COFs correspond for their 001 plane reflections. The d-spacing value between the corresponding 001 planes was used to calculate the π - π stacking distances between vertically stacked COF layers. The high crystallinity of these COFs was attributed due to the presence of strong intramolecular O-H \cdots N hydrogen bonding between imine nitrogen and hydroxyl functionality of the aldehyde core, which attempts to keep the phenyl rings in one plane and increases stacking interactions within adjacent COF layers (**Figure 5.1** & **Figure 5.4b**). To get an overview of the hydrogen bonding effect on the COF backbone we have crystallized three reference compounds such as **SaTta**, **SaTab** and **2,3-Dha-ani** (**Figure 5.4**). X-Ray single crystal structure analysis shows three phenyl rings connected to the central triazine core in **SaTta** are almost in the same plane (torsion angles are 174.7, 176.3 and 179.9 $^\circ$), whereas for **SaTab**, the central triphenyl cores are not in the same plane (torsion angles are 149.6, 154.5 and 145.5 $^\circ$) as to avoid steric interactions among the orthohydrogen atoms. On the other hand, the crystal structure of **2,3-Dha-ani** reflects the central benzene ring of the aldehyde counterpart is slightly out of plane (torsion angles are 135.9 and 134.5 $^\circ$). Interestingly, the structural features of these reference compounds largely depend upon the intramolecular O-H \cdots N hydrogen bonding [**SaTta**- $D=2.63\text{\AA}$, $d=1.98\text{\AA}$, $\theta=141.6^\circ$; for **SaTab**- $D=2.61$, $d=1.88$, $\theta=146.6$; and **2,3-Dha-ani**- $D=2.59$, $d=1.86$, $\theta=146.6$ respectively] phenomenon associated in their backbone structure. All these observations clearly indicate

that **2,3-DhaTta** should exhibit most planer structure compared **2,3-DhaTab**. Moreover, to find out the probable structure, a possible 2D structure was proposed with eclipsed and staggered stacking models with the help of SCC-DFTB method. The experimental PXRD patterns match well with the simulated slipped-AA stacking model for these two COFs (**Figure 5.3**). The model structure matches well with the space group triclinic 'P1' in both the COFs. To elucidate the unit cell parameters Pawley refinement is performed which indicates good agreement between the simulated and experimental PXRD patterns. The unit cell parameters for the COFs **2,3-DhaTta** and **2,3-DhaTab** appear as $a = 37.1$, $b = 37.1$, $c = 3.5$ and $a = 37.3$, $b = 37.3$, $c = 3.5$ respectively.

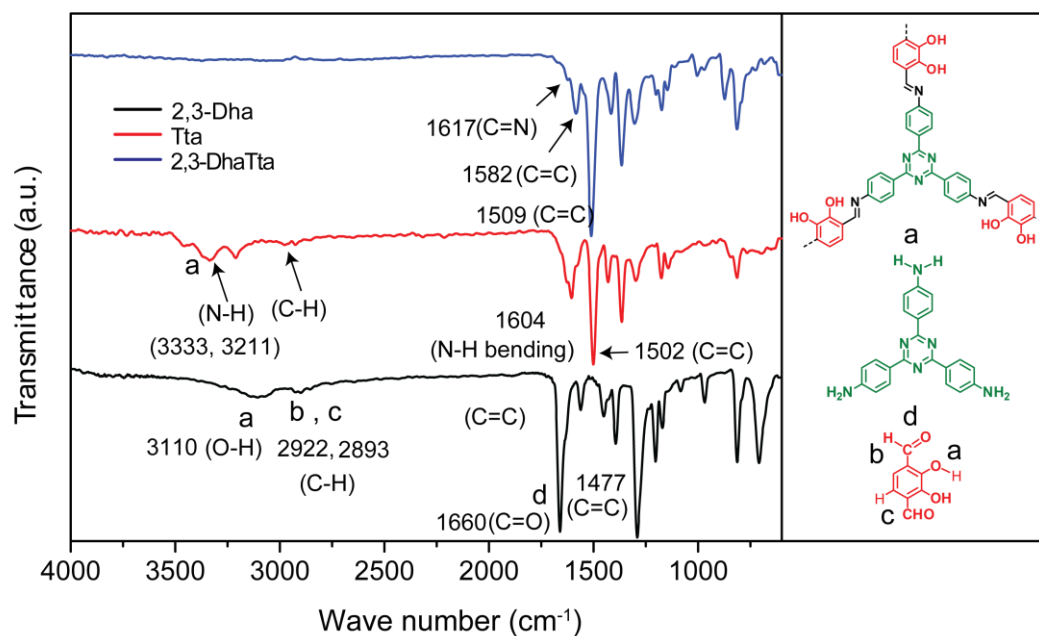


Figure 5.5. FT-IR spectra comparison among **2,3-DhaTta**, 4,4',4''-(1,3,5-triazine-2,4,6-triyl)trianiline (**Tta**) and 2,3-dihydroxyterethaldehyde (**2,3-Dha**).

5.2.3 Chemical characterization

FT-IR analysis for the COFs reported here show the complete disappearance of primary –N–H stretching band ($3200\text{--}3460\text{ cm}^{-1}$) of parent amines as well as the –C=O stretching frequency around 1660 cm^{-1} for aldehydes used in the synthesis (**Figure 5.5** & **Figure 5.6**). Moderate and strong bands, respectively for triazine and phenyl core based COFs, appear around 1616 cm^{-1} reflect the formation of –C=N linkages as found in the reference compounds (**SaTta** and **SaTab**). Solid state ^{13}C NMR spectra of **2,3-DhaTta** indicate a

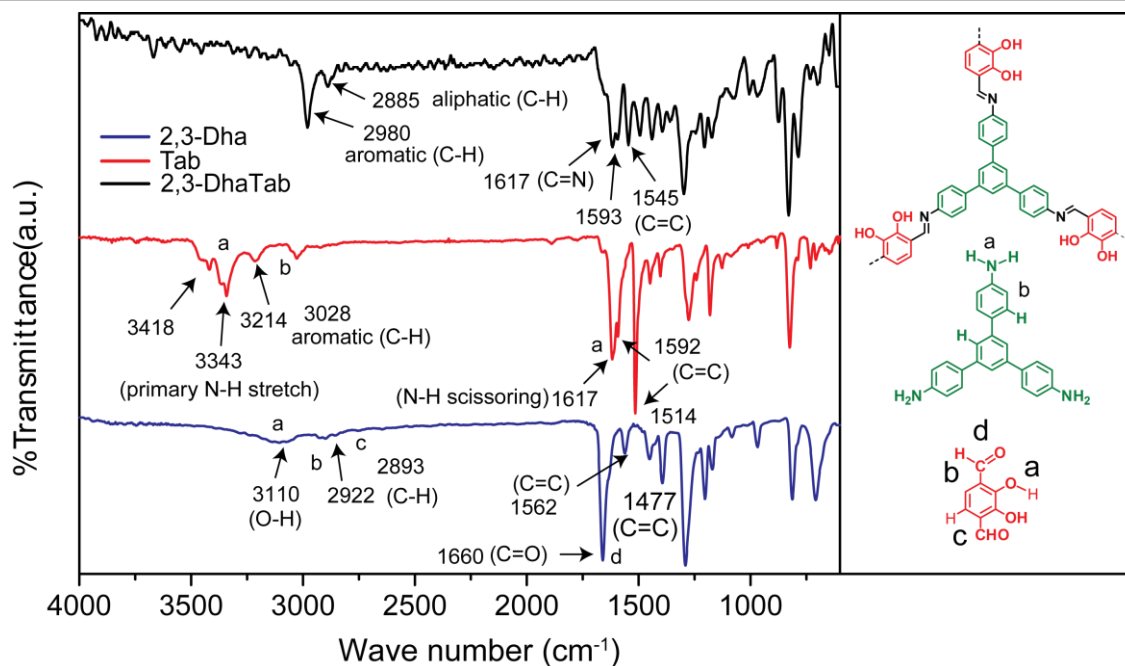


Figure 5.6. FT-IR spectra comparison among **2,3-DhaTab**, **4,4',4''-(1,3,5-triazine-2,4,6-triyl)trianiline (Tab)** and **2,3-dihydroxyterethaldehyde (2,3-Dha)**.

strong signal at ~ 166.5 ppm which originates from triazine core carbon atoms only as this peak was completely absent in **2,3-DhaTab** (Figure 5.7a-b). The signal at around ~ 157.6 ppm can be assigned for the imine linkage carbon atoms present in both the COFs. The aromatic carbon signals appeared in the range 150-110 ppm in the spectrum. TGA profile shows the COFs are thermally stable up to 350 °C. Above this temperature, gradual weight loss signifies the gradual framework degradation (Figure 5.7c).

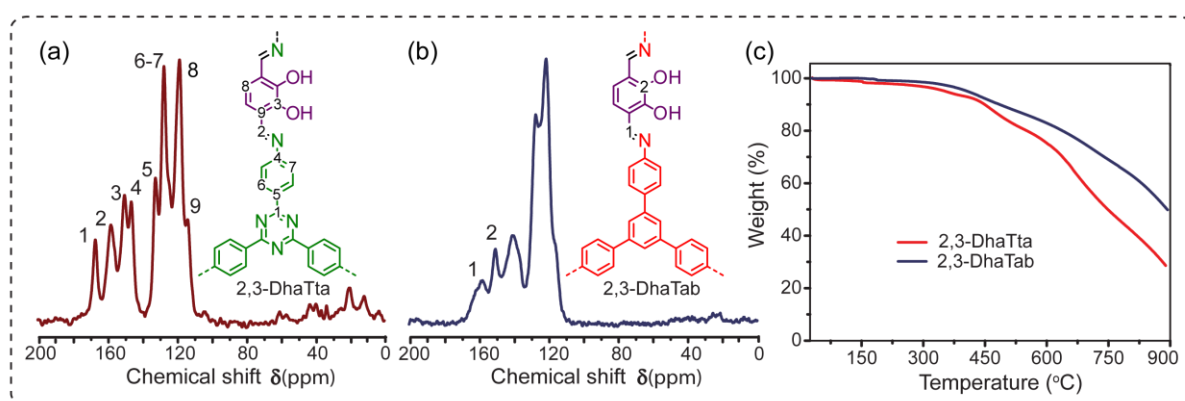


Figure 5.7. (a, b) Solid state ^{13}C spectra of COFs **2,3-DhaTa** and **2,3-DhaTab** respectively with partial chem. draw structure on inset. (c) TGA profile of the respective COFs.

5.2.4 Gas adsorption studies

N_2 adsorption was carried out for the COFs in their fully activated state after exposing the samples under vacuum and subsequent heating at around 120 °C. Both the COFs follows type IV reversible isotherm, which reflects their mesoporous nature (**Figure 5.8a**). The Brunauer–Emmett–Teller (BET) surface areas, calculated in the pressure range $P/P_0 = 0.1$ to 0.2, of **2,3-DhaTta** and **2,3-DhaTab** were evaluated as 1700 and 413 m^2g^{-1} respectively. The extremely high surface area of **2,3-DhaTta** compared to **2,3-DhaTab** COF could be due to its high crystallinity and long-range exposed pore structure, which basically originates from strong π - π stacking interaction between the layers (higher flattened structure). Flatness and hence stacking interaction between the vertically stacked layers decreases moving from **2,3-DhaTta** to **2,3-DhaTab** which reflects higher surface area to the former one compared to the later COF.

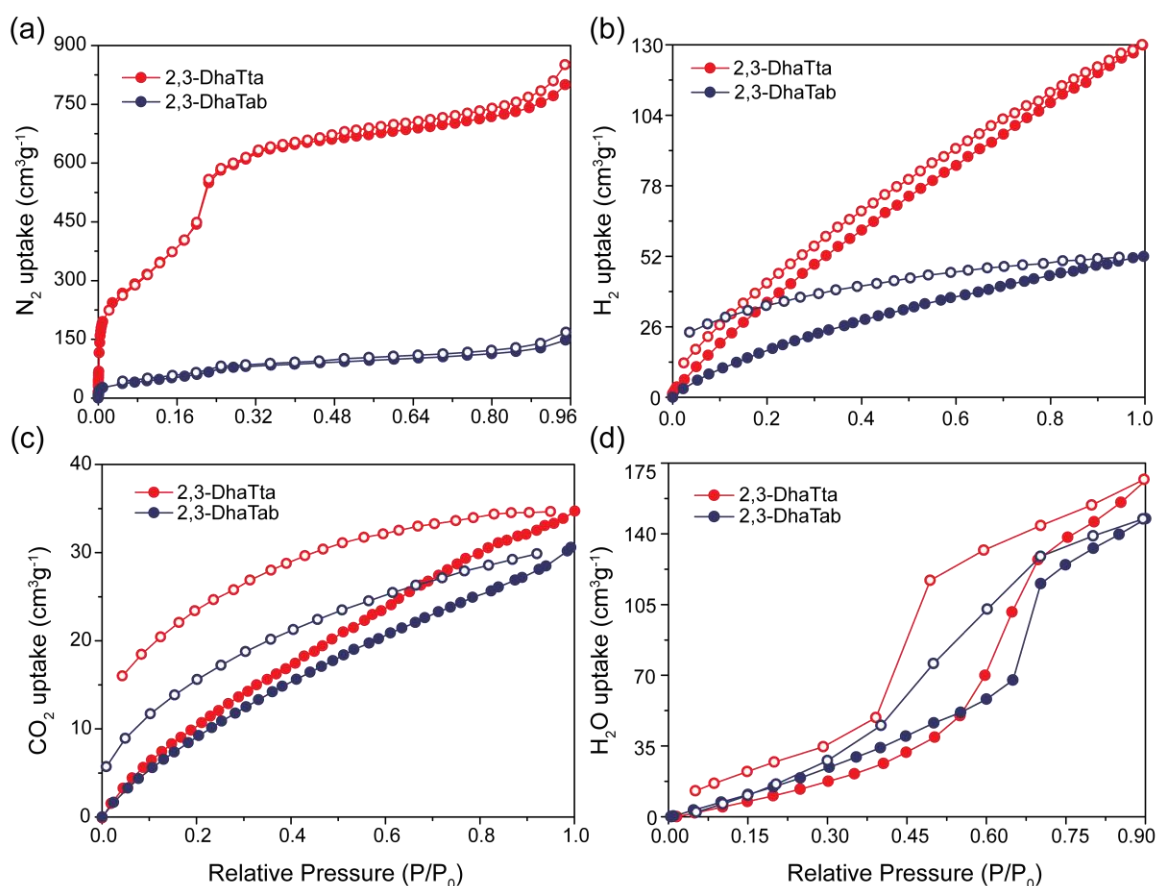


Figure 5.8: Comparison of (a) N_2 adsorption (at 77 K), (b) H_2 adsorption (at 77 K), (c) CO_2 adsorption (at 273 K), (d) water vapor adsorption (at 298 K) isotherms of **2,3-DhaTta** and **2,3-DhaTab** COFs.

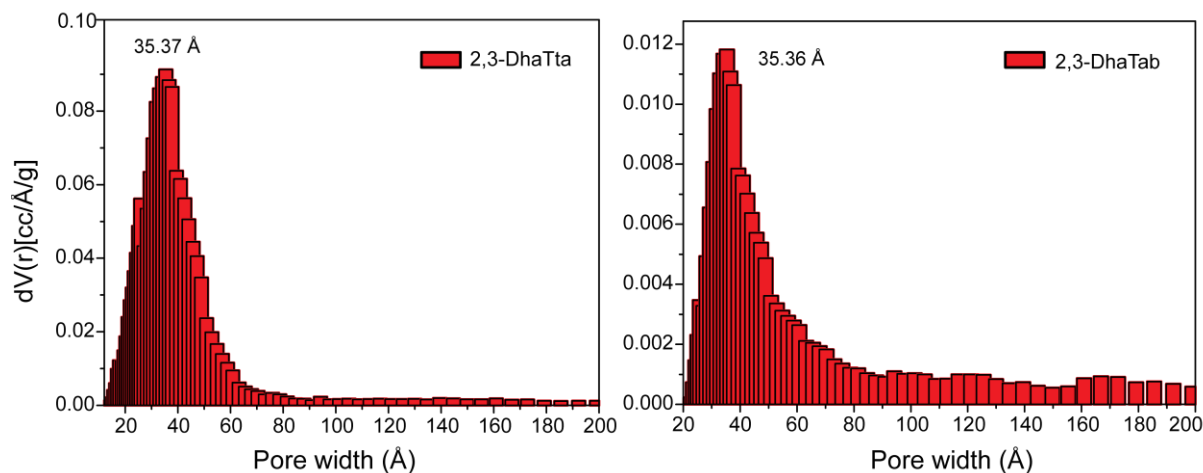


Figure 5.9: Experimental pore size distribution of **2,3-DhaTta** (left) and **2,3-DhaTab** (right) COFs.

The pore Size distribution was calculated using **DFT** model from N_2 adsorption isotherm (cylindrical pore, NLDFT adsorption branch model) for **2,3-DhaTta** and **2,3-DhaTab** COFs (**Figure 5.9**). The experimental pore width in both COFs **2,3-DhaTta** and **2,3-DhaTab** were calculated as 3.5 nm which nicely more or less matches with the theoretically predicted values 3.1 and 3.2 nm respectively.

Hydrogen adsorption/desorption was performed at 77 K (liquid N_2), which shows reversible hydrogen uptake in both COFs (**Figure 5.8b**). At 1 atm vapour pressure **2,3-DhaTta** and **2,3-DhaTab** show hydrogen uptake up to 130 and 51 $cm^3 g^{-1}$ respectively. Curiously, we have also carried out CO_2 adsorption at 273 K, which show moderate CO_2 uptakes of 34 and 30 $cm^3 gm^{-1}$ for **2,3-DhaTta** and **2,3-DhaTab** respectively (**Figure 5.8c**). Both the COFs were found to be hydrophobic in nature, as revealed by their water adsorption isotherms (**Figure 5.8d**). No significant water vapour uptake up to 0.4 bar vapour pressure and the reversible water vapour uptake capability indicates their hydrolytic stability.

5.2.5 Chemical stability investigation

The hydrolytic stability test of the COFs was performed by submerging about 40 mg of the COF samples in 50 ml of water for 3 days. Exact matching of the PXRD pattern (**Figure 5.10c-d**) along with identical FTIR spectra (**Figure 5.11c-d**) reveals structural rigidity of COFs in water. N_2 adsorption isotherm shows the COFs were still porous with lower surface areas after prolonged water treatment (**Figure 5.12c-d**).

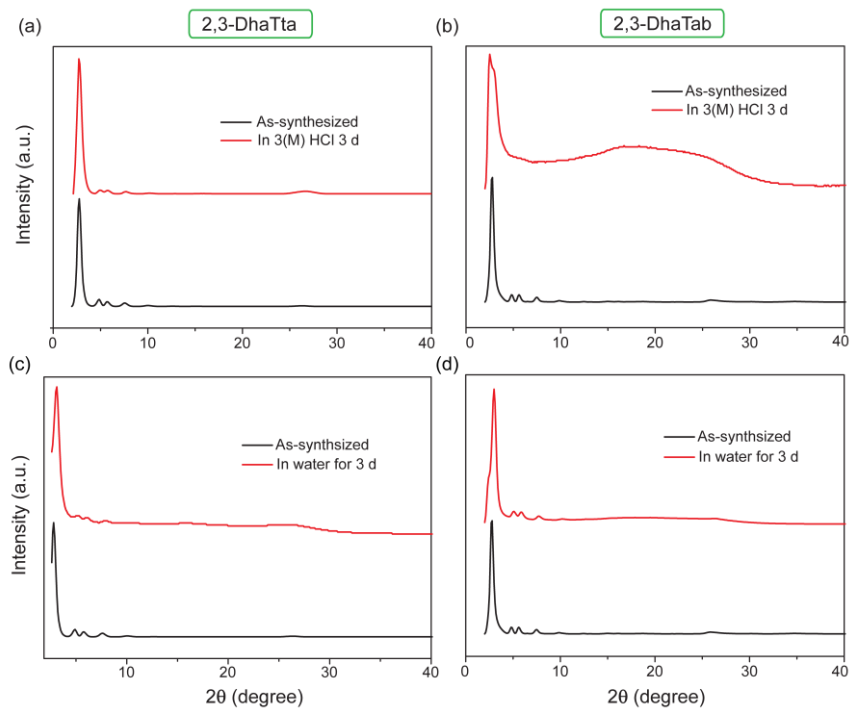


Figure 5.10: Comparison of PXRD patterns of 2,3-DhaTta (a & b) and 2,3-DhaTab (c & d) of as-synthesized with after 3 days treatment in water and 3 (M) HCl respectively.

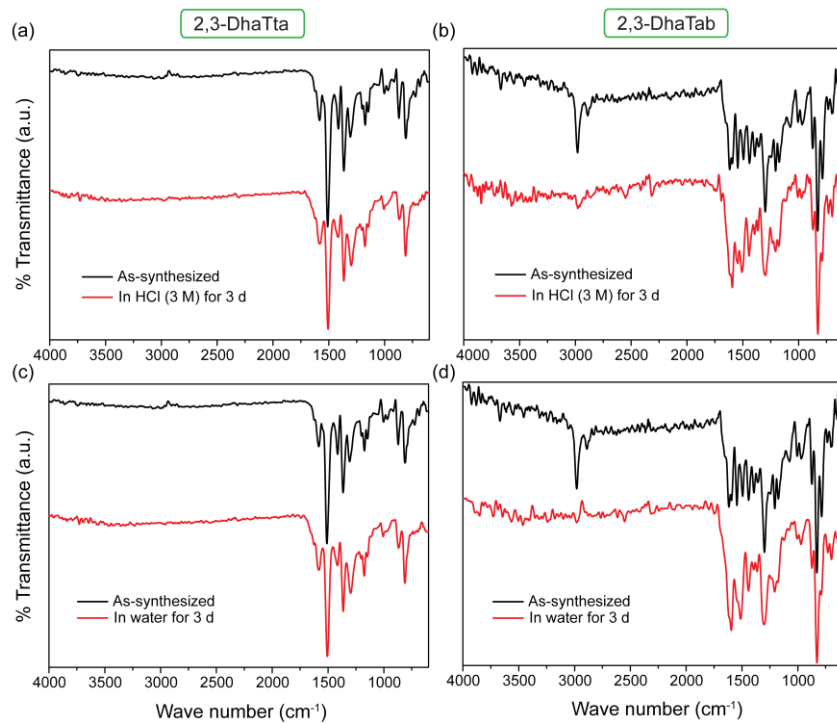


Figure 5.11: Comparison of IR spectrums of 2,3-DhaTta (a & b) and 2,3-DhaTab (c & d) of as-synthesized with after 3 days treatment in water and 3 (M) HCl respectively.

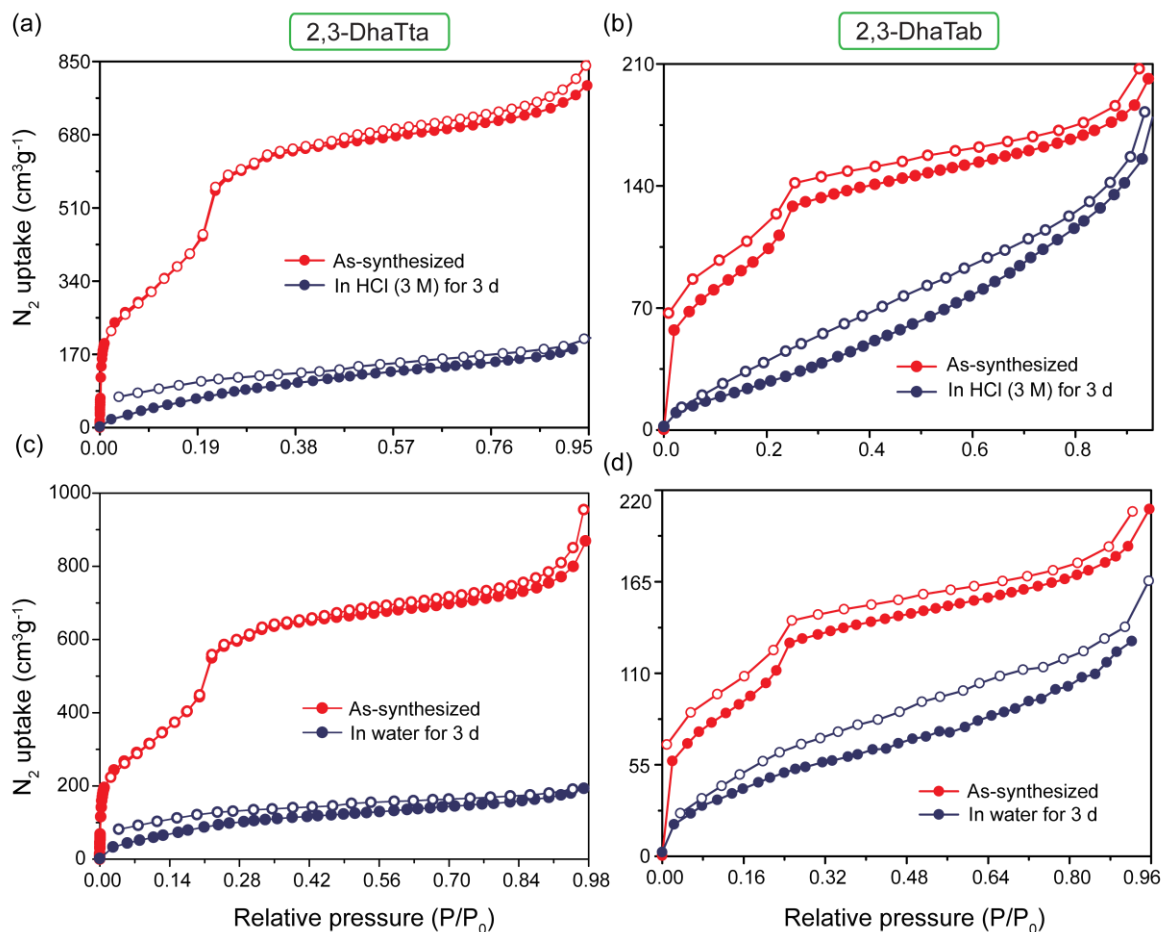


Figure 5.12: Comparison of N_2 adsorption isotherms of **2,3-DhaTta** (a & b) and **2,3-DhaTab** (c & d) of as-synthesized with after 3 days treatment in water and 3 (M) HCl respectively.

Following a similar way, the COF samples were treated with 3 (N) HCl and 3 (N) NaOH to find out their acid and basic stability respectively. After 3 days treatment in acid, retention in PXRD (**Figure 5.10a-b**) pattern along with no alteration in FTIR (**Figure 5.11a-b**) spectra indicates its stability in 3(N) HCl. Though surface areas of all these COFs decrease dramatically (**Figure 5.12a-b**). We can assume, in acid media the imine nitrogen gets protonated, O–H•••N hydrogen bonding gets disrupted, which allows a nucleophilic attack from water molecule at imine carbon centre leading partial framework collapse. In contrast, the COFs were found to be completely unstable in 3(N) NaOH. Here we believe, the strong nucleophile OH^- not only pluck the phenolic O–H proton from aldehyde counterpart by destructing hydrogen bonding phenomenon, but it also has the ability for faster attack (compared to water) to the imine carbon centre resulting rapid framework degradation.

5.2.6 Morphological study of COFs and explanation behind their formation

Scanning electron microscopy (SEM) and transmittance electron microscopy (TEM) techniques were utilized to reveal the underlying morphology of the COF crystallites and the way of their formation after 72 h. In **2,3-DhaTta**, ribbon-shaped crystallites are found after 72 h as revealed from SEM and TEM analysis (**Figure 5.13b-c**). On the other hand, 72 h SEM and TEM imaging show **2,3-DhaTab** forms hollow spheres which are interconnected through their mesoporous walls (**Figure 5.13e-f**). The spherical nature of **2,3-DhaTab** (diameter; ca. 400 nm) is confirmed by AFM analysis (**Figure 5.14**). We were very much curious to find out the mechanism behind the final morphological evolution. Hence, to investigate the mechanism behind the ribbon (**2,3-DhaTta**) and hollow sphere (**2,3-DhaTab**) formation, COF reactions were quenched at different time intervals (12, 24, 36, 48 and 72 h). For that, in five different set of tubes, one particular COF was synthesized at a different time interval such as 12, 24, 36, 48 and 72 h maintaining starting materials concentration, solvent ratio, reaction time as mentioned above.

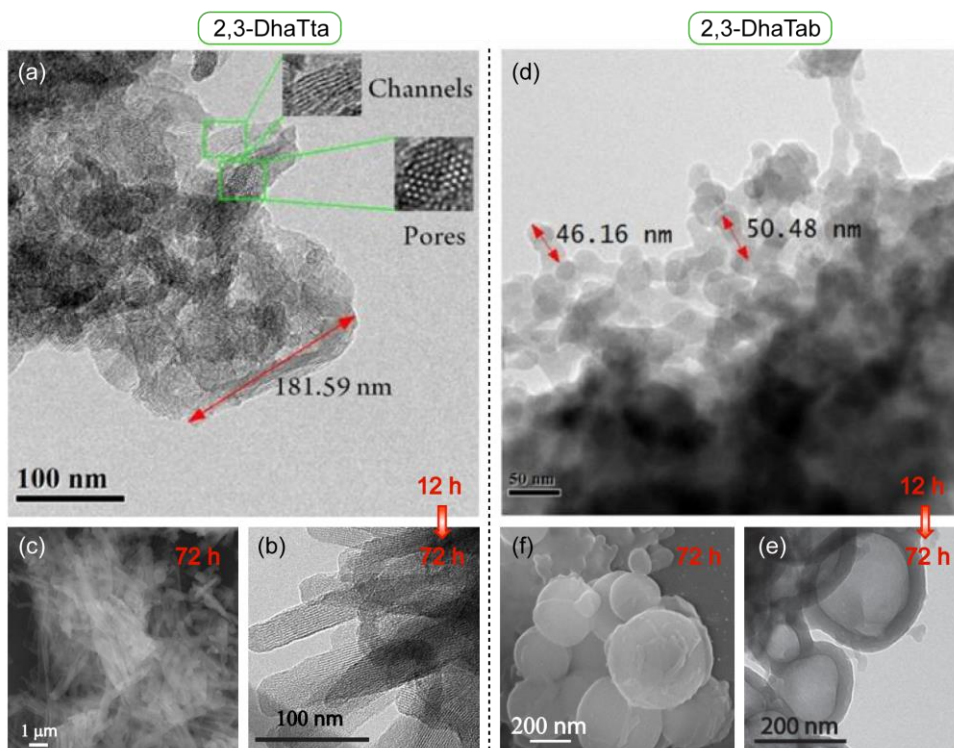


Figure 5.13: From SEM (c, f) & TEM imaging (rest), from 12 to 72 h (a-b) The way of formation of ribbon-shaped morphology in case of **2,3-DhaTta** COF and (d-e) Hollow spherical morphology formation in case of **2,3-DhaTab**.

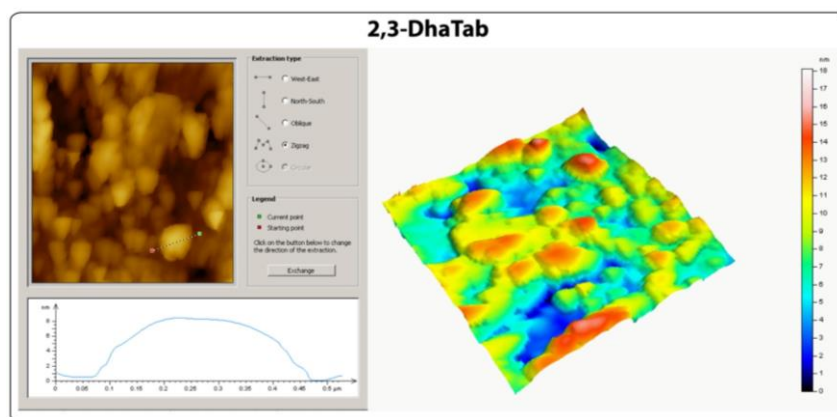


Figure 5.14: AFM image of the **2,3-DhaTab** hollow sphere. Height profile reflects spherical nature.

After the isolation and purification steps as mentioned for 72 h sample, COF powders were collected and its crystallinity, porosity and internal morphology were analyzed. Interestingly the PXRD of 12 h COF samples displayed all the characteristic peaks, which indicate COF framework formation is even possible at a short reaction time of 12 hours (**Figure 5.15**). Further, the PXRD pattern of the other COF samples synthesized at the intermediate steps (24, 36, 48 hours) also displayed similar crystallinity (**Figure 5.15**). The characteristic FT-IR 12, 24, 36, 48 hours samples match completely with the final 72 hours COF samples (**Figure 5.16**). This result also confirms the successful COF framework formation at different time intervals. We have also checked the porosity of respective COF samples isolated at the shortest reaction time (12 h). As expected the 12 h COF sample also showed a decent surface area compared to the 72 h COF samples (**Figure 5.17**). The porosity of the material was found to increase as we move from 12 to 72 h. The surface area calculation indicates the COF samples become more crystalline as the time progresses. The reason could be, due to extending reaction condition the crystallites have enough time to self-correct its structural errors and leads thermodynamically more stable crystalline product. It also helps to stack a higher number of COF layers one top to other hence to grow the COF along stacking direction, hence provides larger and ordered crystallites which in turn reflect to result in higher surface area as the time progresses from 12 to 72 h.

Apart from that, the detail exploration of the mechanism of formation of **2,3-DhaTta** (ribbon) and **2,3-DhaTab** (hollow sphere), we have characterized the internal morphology of the intermediate samples using various microscopic techniques such as TEM and SEM. **2,3-DhaTta** at smaller reaction time forms ribbon-shaped crystallites (length ca. $\sim 200 \mu\text{m}$ from

TEM) as revealed by its SEM and TEM imaging (**Figure 5.13a, 5.19 & 5.20; 12 h**). No more change in the morphology was observed moving from 12 h to 72 h as the small ribbon-shaped crystallites self-assemble to form larger ribbon-shaped crystallites.

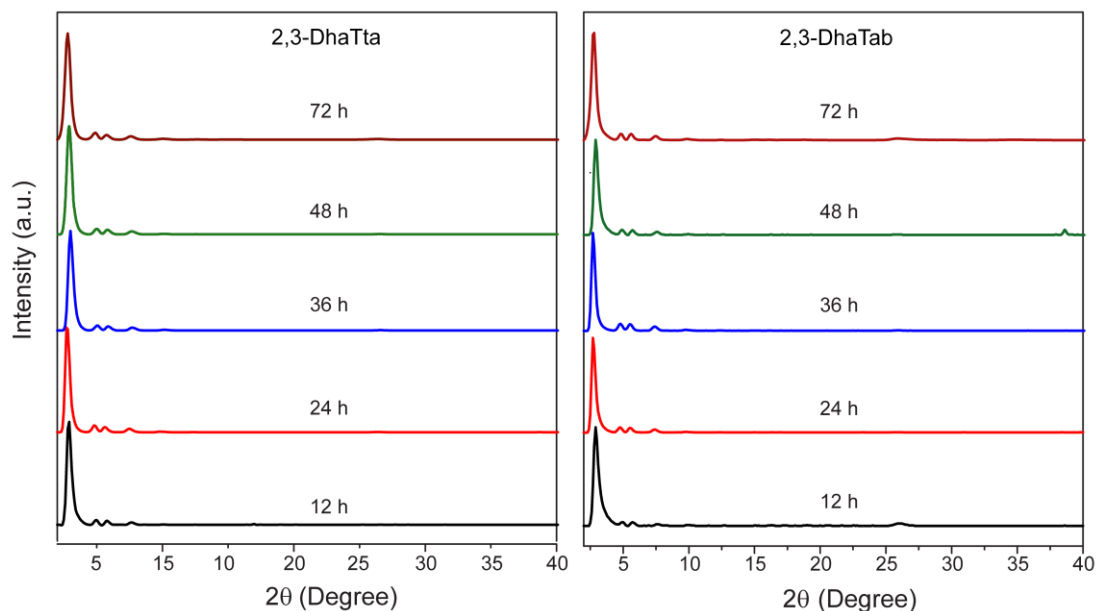


Figure 5.15: PXRD of **2,3-DhaTta** and **2,3-DhaTab** at different time intervals (12 h, 24 h, 36 h, 48 h and 72 h).

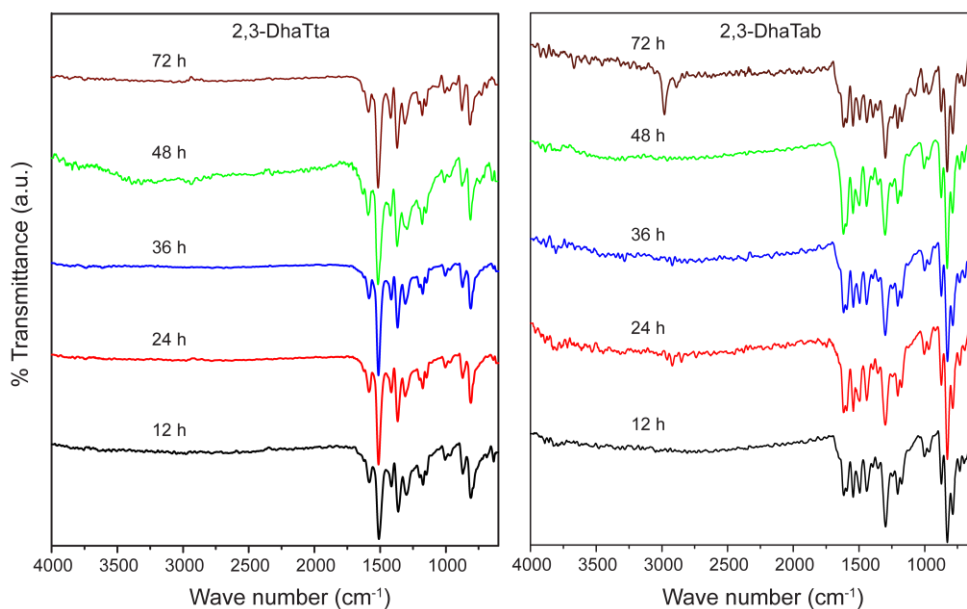


Figure 5.16: FT-IR spectra of **2,3-DhaTta** and **2,3-DhaTab** at different time intervals (12 h, 24 h, 36 h, 48 h and 72 h).

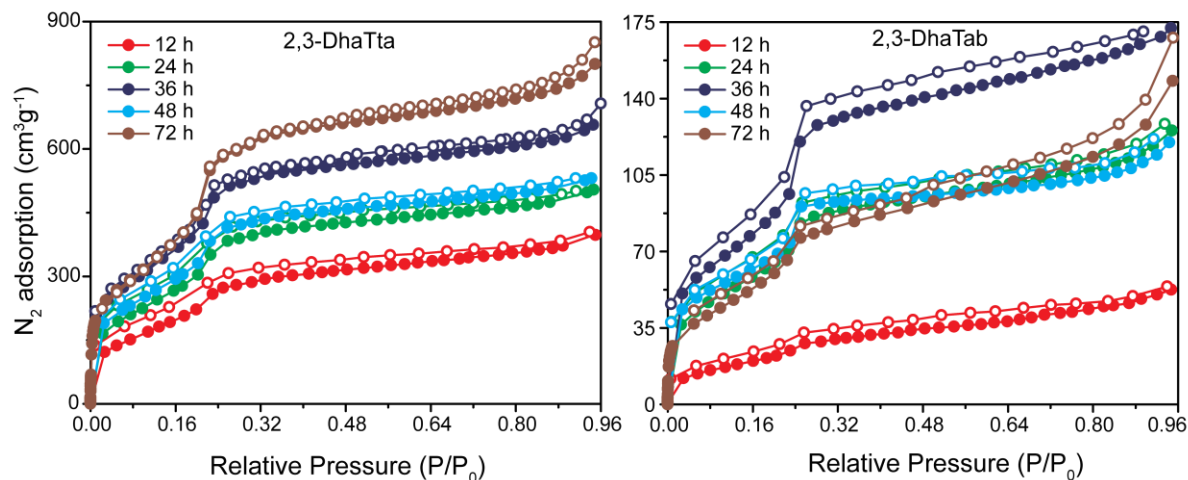


Figure 5.17: N_2 adsorption isotherm of **2,3-DhaTta** and **2,3-DhaTab** at different time intervals (12 h, 24 h, 36 h, 48 h and 72 h).

However, **2,3-DhaTab** sample synthesized at 12 hours showed small (length 20-40 μm) and bent morphology (**Figure 5.13d**, **5.23** & **5.24**; **12 h**). The bent morphology of the COF crystallites was believed to form due to the imperfect self-assembly (π - π stacking) of COF layers along the c axis. The COF crystallites are randomly aggregated in different directions/shape at 12 hours reaction time. The morphology of the crystallite aggregation includes dense spheres, coiled and aggregated structure. As the time progress, at 24 hours in **2,3-DhaTab** samples TEM, image mainly shows dense spheres, which was formed by the aggregation of COF crystallites (**Figure 5.23** & **5.24**; **24 h**). However, after 36 hours **2,3-DhaTab** from TEM, revealed an important morphological transformation. Herein, a hollow interior was developed inside of **2,3-DhaTab** dense spheres, as seen from TEM imaging the crystallites were moving from the centre of the sphere to its surface wall (**Figure 5.24**; **36 h**). Hence, the number of dense sphere morphology was drastically reduced and formation of hollow spherical morphology starts originating. But the basic bent crystallites of COF were still visible at the hollow sphere walls in higher magnification TEM images (**Figure 5.24**; **36 h**). Moreover, the transformation of the **2,3-DhaTab** dense sphere to corresponding **2,3-DhaTab** hollow spheres was resulted due to a phenomenon so-called inside-out Ostwald ripening mechanism (**Figure 5.25**) [5.9]. This phenomenon mostly happens due to the difference in free energy of the crystallites which are very inside of the sphere. The detailed Ostwald ripening phenomenon has been discussed in the latter section.

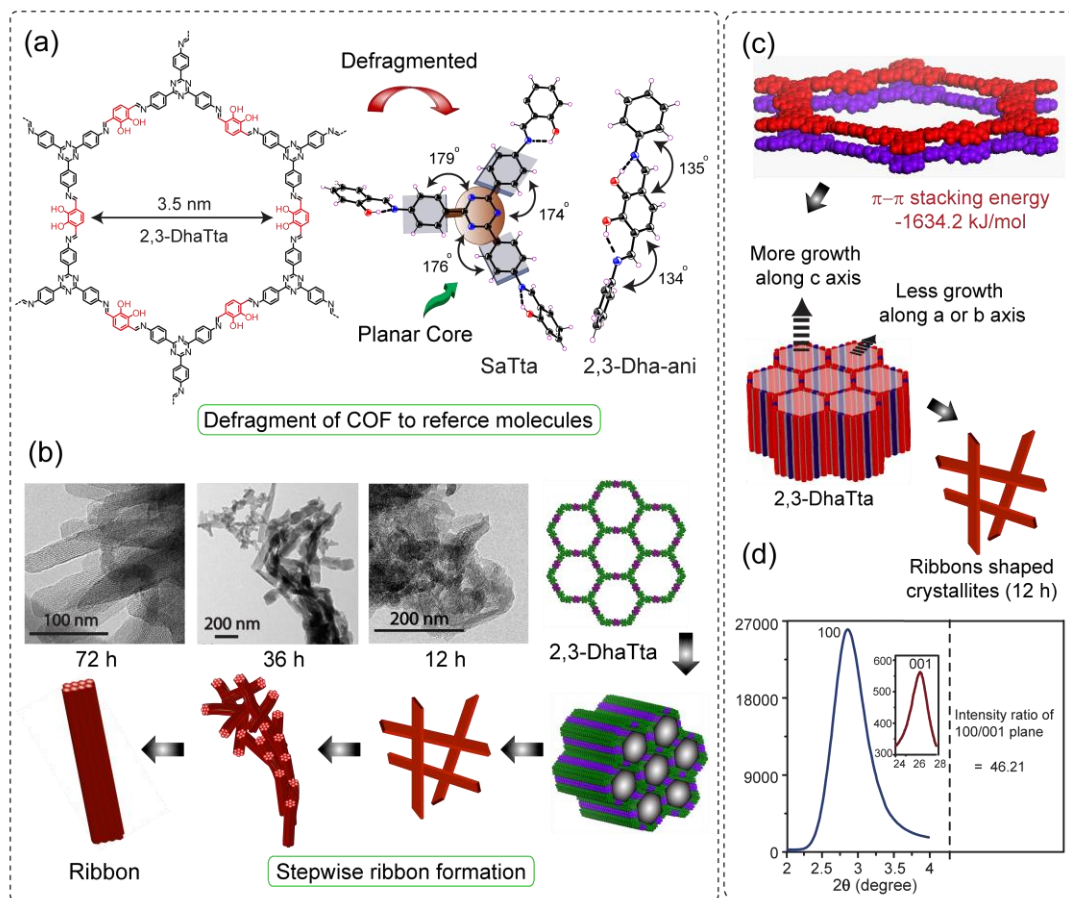


Figure 5.18: (a) Defragmented of **2,3-DhaTta** COF into reference compounds **SaTta** (planar core) and **2,3-Dha-ani**. (b) TEM imaging (12-72 h) and cartoon representation for ribbon-shaped crystallite formation in **2,3-DhaTta** COF. (c) The expected growth mechanism of the COF crystallites at 12h, stacking model along with stacking energy value (from DFT) mentioned for the adjacent hexagonal COF layers. (d) PXRD pattern (of 12 h sample) along with intensity ratio of 100 to 001 planes for **2,3-DhaTta** COF.

We have tried to establish a correlation between the crystallite morphology and its molecular level structure based on microscopy images. The structure of **2,3-DhaTta** can be defragmented into two reference compounds **SaTta** and **2,3-Dha-ani** (Figure 5.18a). The reference compound **SaTta** shows three nearly planar phenyl rings with respect to the triazine core (torsion angles are 174.7, 176.3 and 179.9°), whereas the phenyl rings from the aldehyde part (between two cis imine linkages) in **2,3-Dha-ani** are slightly out of plane (torsion angles 135.9 and 134.5°). Moreover, the π - π stacking energy per hexagon is calculated in order to find out the stacking efficiency among the vertically stacked COF

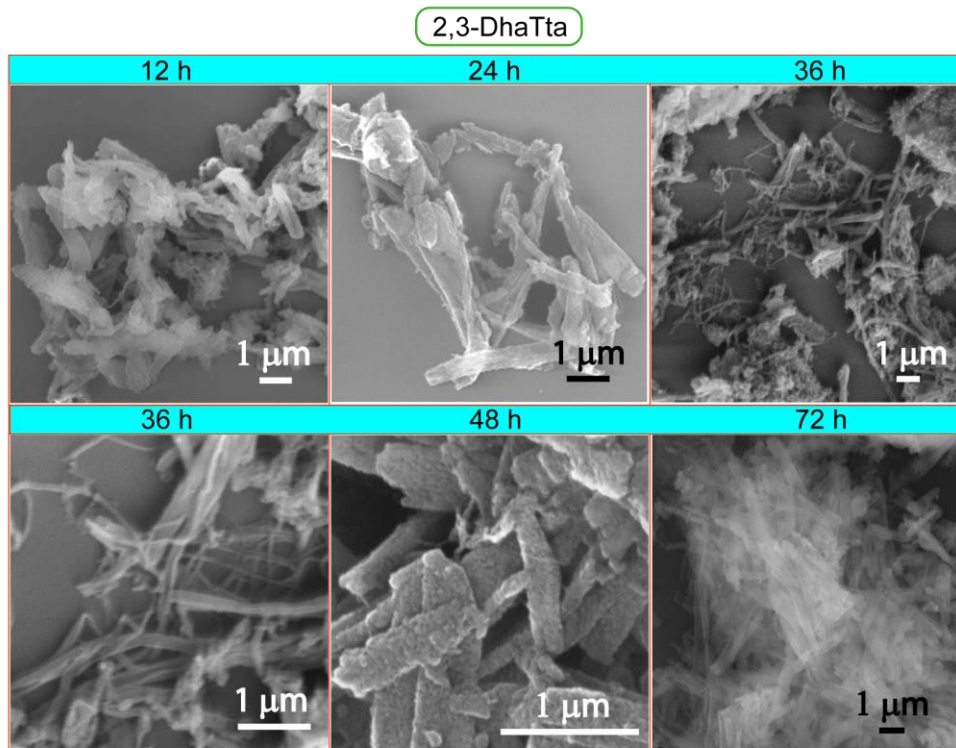


Figure 5.19: SEM images of 2,3-DhaTta at different time intervals.

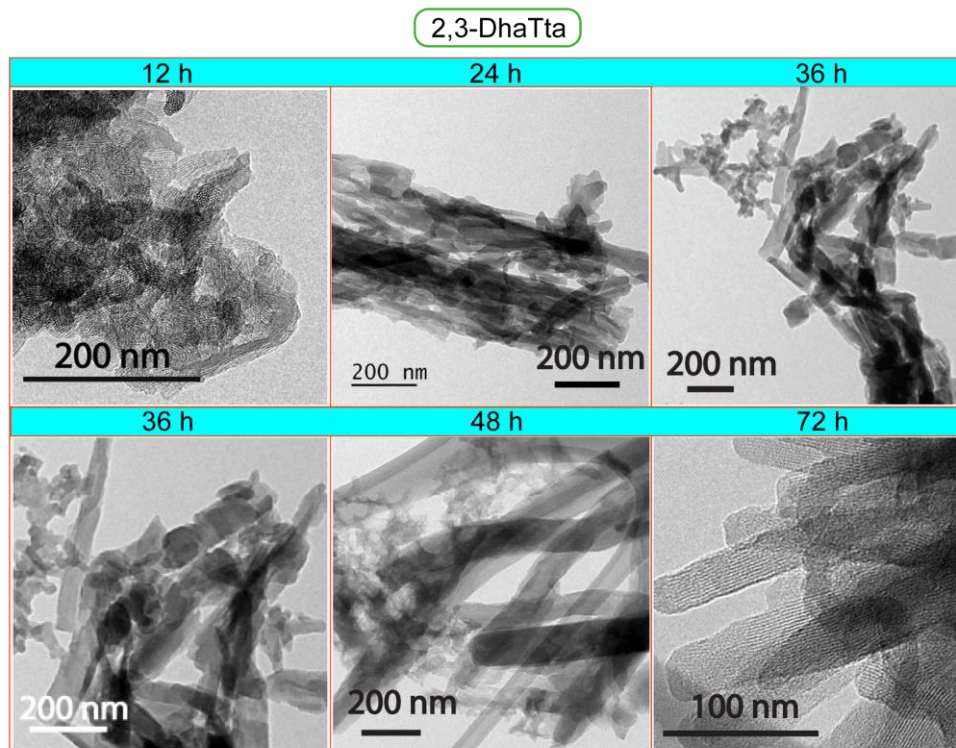


Figure 5.20: TEM images of 2,3-DhaTta at different time intervals.

layers and it is -1634.2 kJ/mole in **2,3-DhaTta** (*Figure 5.18c*). Again calculated PXRD intensity ratio between 100 to 001 plane of the sample retrieved after 12 h of reaction is 46.2 (*Figure 5.18d*). This high value directly indicates that each individual layer utilizes the strong π - π stacking interaction to interact with other layers to extend along the Z direction compared to X and Y direction (*Figure 5.21*). Hence, the growth continues to form ribbons (*Figure 5.13a, 5.18b-c*; 12 h). These crystallites self-aggregate to larger ribbon-shaped crystallites after 36 h (length ca. 515 nm, width ca. 90 nm) (*Figure 5.18b*; 36 h). Finally, this ribbon-like morphology is prominently visible at 72 h SEM and TEM (*Figure 5.19 & 5.20*).

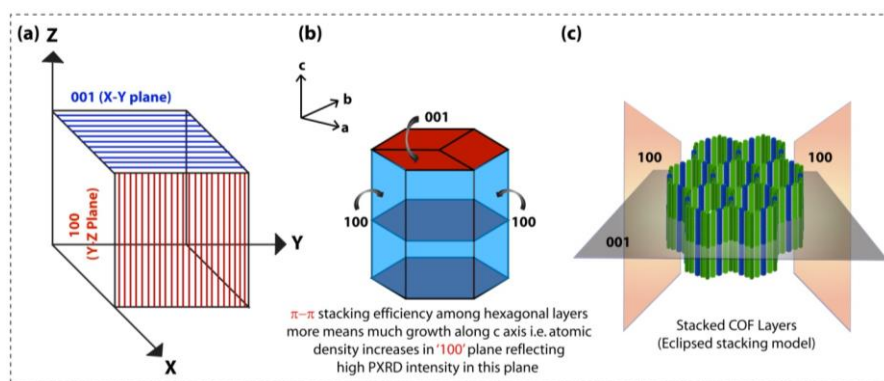


Figure 5.21: (a) General definition of '100' and '001' planes in a cubic system. (b) Expansion of the defined planes in a hexagonal system and (c) Finally expanded the concept of planes in stacked hexagonal 2D COF layers.

As observed from SEM and TEM, **2,3-DhaTab** has a hollow spherical morphology after 72 h (*Figure 5.23 & Figure 5.24*). TEM images clearly show that at the beginning of the reaction mostly small bent fibres (length ca. 25-55 nm) are formed (*Figure 5.13 & Figure 5.24*). We try to understand again from their molecular level structure and PXRD and subsequently defragmented the COF structure to **SaTab** and **2,3-Dha-ani** reference compound (*Figure 5.22a*). The central four phenyl rings (one core phenyl and three outer phenyls from amine counterpart) are completely out of plane with respect to each other in **SaTab** (torsion angles 149.6, 154.5 and 145.5°) and the benzene core, connected between two cis imine bonds, are not in the same plane in **2,3-Dha-ani** (torsion angles 134.5 and 135.9°), which means that the π - π stacking interaction, in this case, is completely imperfect as the layers are extremely non planner (ca. π - π stacking energy -1578.7 kJ/mole from DFT) (*Figure 5.22c*). This imperfect stacking hinders the growth of COF fibres along the Z axis. The PXRD intensity ratio between 100 to 001 planes is 5 (*Figure 5.22d*) which is 9 times smaller compared to the

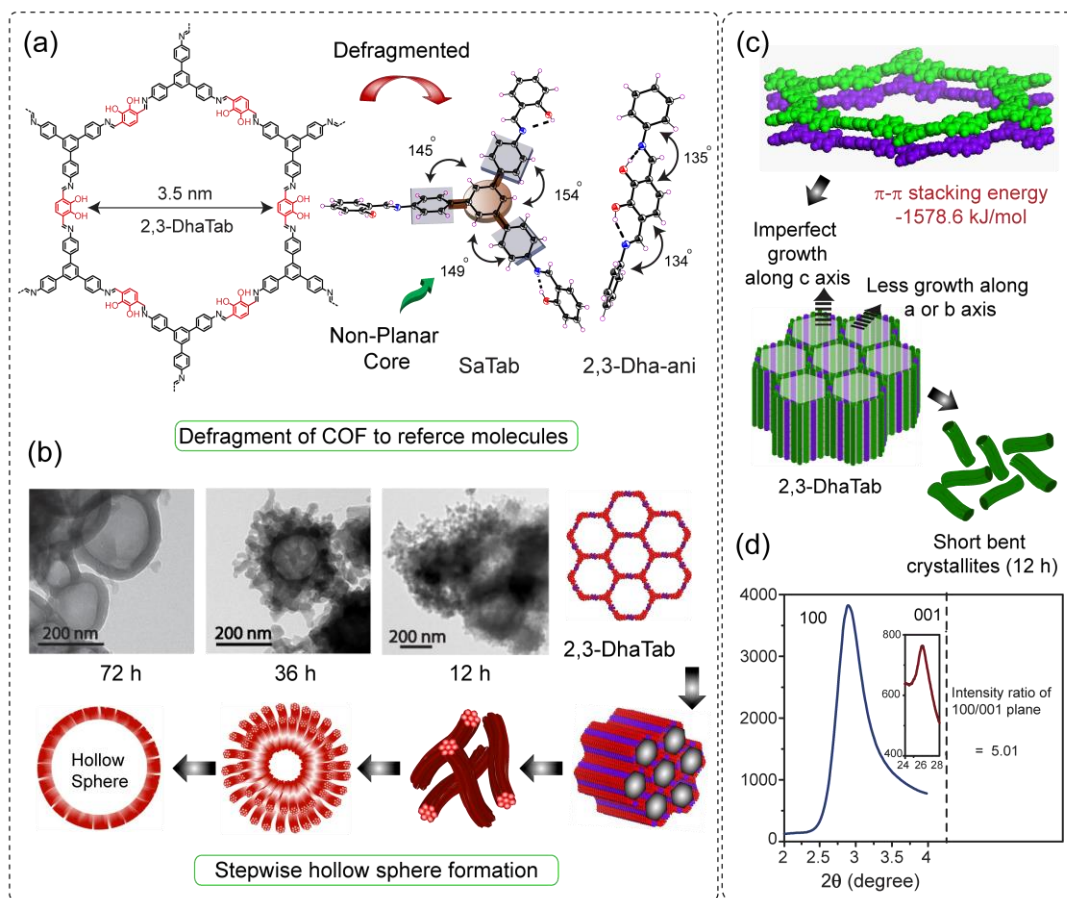


Figure 5.22: (a) Defragmented of 2,3-DhaTab COF into reference compounds SaTab (non-planar core) and 2,3-Dha-ani. (b) TEM imaging (12-72 h) and cartoon representation for hollow sphere crystallite formation in 2,3-DhaTab COF. (c) The expected growth mechanism of the COF crystallites at 12h, stacking model along with stacking energy value (from DFT) mentioned for the adjacent hexagonal COF layers. (d) PXRD pattern (of 12 h sample) along with intensity ratio of 100 to 001 planes for 2,3-DhaTab COF.

PXRD the intensity ratio between 100 to 001 planes in 2,3-DhaTta (Figure 5.18d). This reflects that the growth along Z direction is absolutely minimal. From TEM, it is clear that the fibres are bent, which perhaps originates from improper stacking between the layers (Figure 5.22b, 5.23 & 5.24; 12 h). At the time the crystallites also self-aggregate to give dense spherical shapes (Figure 5.23 & 5.24; 24 h). However, as time progresses the crystallites gradually diffuse from the centre of the dense sphere to its wall making hollow interior inside after 36 h (Figure 5.22b, 5.23 & 5.24; 36 h). Finally, at 72 h hollow spheres with wall thickness ca. 25-50 nm and diameter ca. 200 nm-1.5 μm were observed

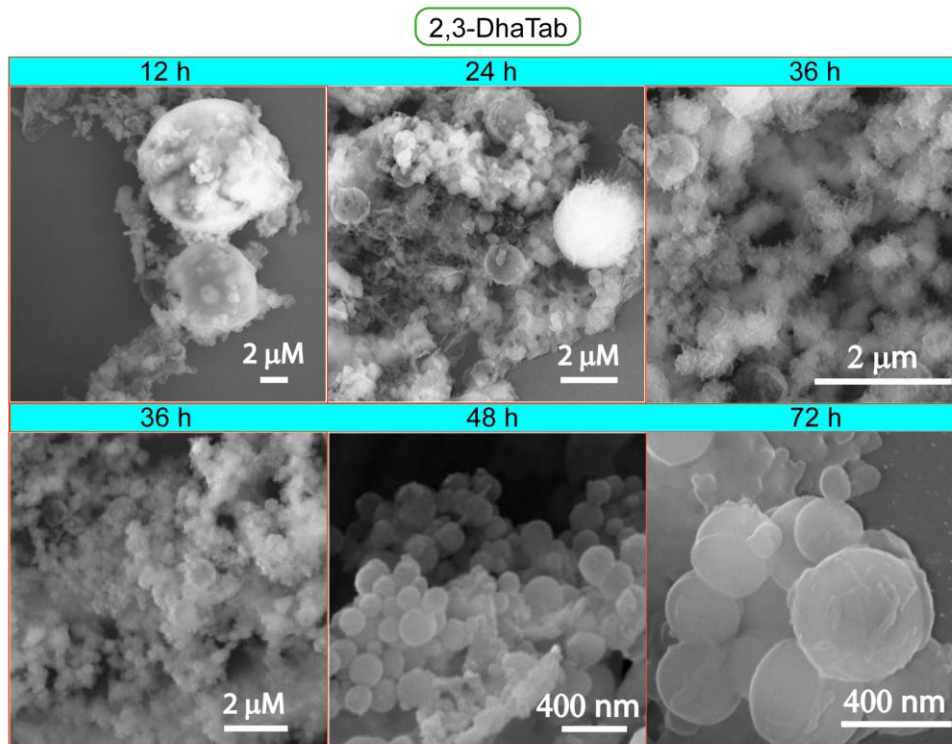


Figure 5.23: SEM images of 2,3-DhaTta at different time intervals.

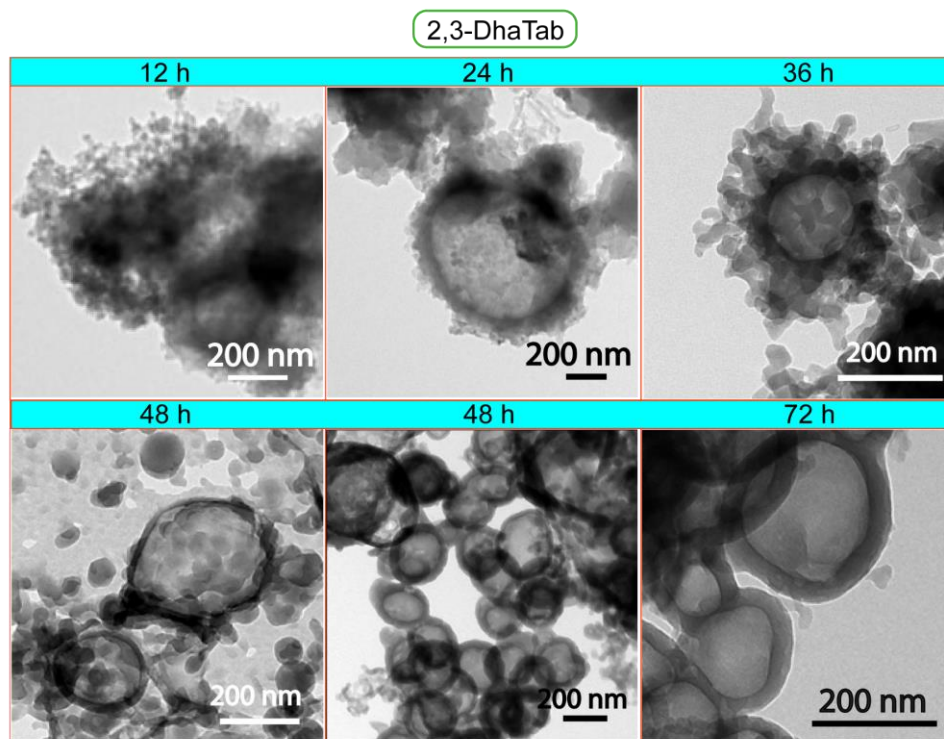


Figure 5.24: TEM images of 2,3-DhaTta at different time intervals.

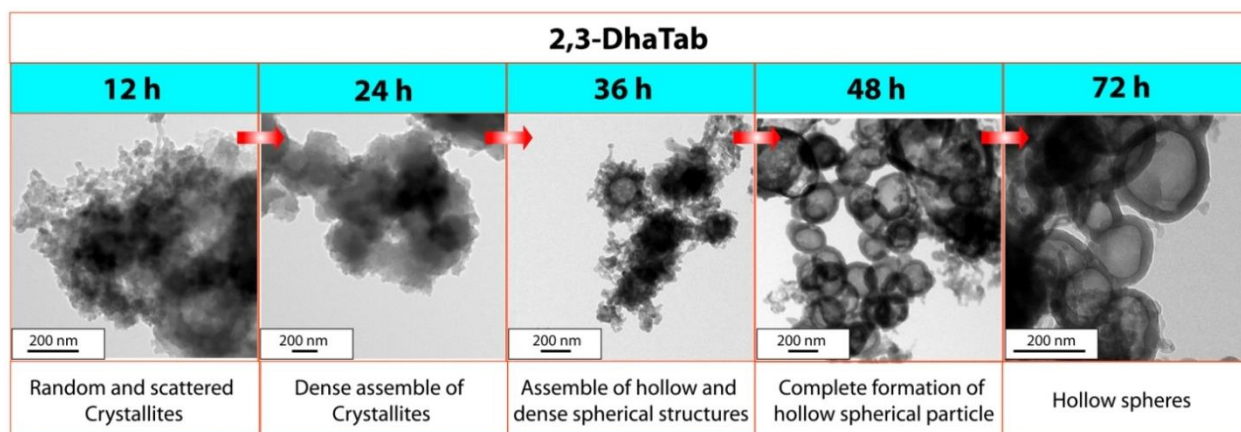


Figure 5.25: Understanding of Ostwald ripening process in 2,3-DhaTab.

(**Figure 5.22b, 5.23 & 5.24; 72 h**). However, we believe that Ostwald Ripening is perhaps responsible for the formation of a hollow sphere. It is noteworthy that higher curvature associates with higher surface energy [5.22]. Hence, the crystallites those are very close to the centre of the dense sphere (with higher curvature) experience more surface energy than the crystallites close to the wall (with lower curvature). Ostwald ripening occurs to those crystallites which are near to the centre to reduce their surface energy. The crystallites gradually move from the centre and assemble to the surface leading hollow interior inside. After 72 h, an entirely dark wall with bright contrast inside of the sphere is found to form, as revealed by TEM, which reflects hollow spherical nature (**Figure 5.25**).

5.3 Conclusion

In summary, we have designed and have successfully synthesized two new imine bonded, chemically stable covalent organic frameworks, which exhibit good crystallinity and porosity along with some interesting morphological features. The presence of strong intramolecular H-bonding and molecular level core planarity force a stiff and planner COF structure, which is the basis of high surface area and crystallinity. After 72 h the COFs display different morphologies, as found from both SEM and TEM images cling to their building units. In the case of triazine-based COF, the crystallite self-assembles to ribbons. In contrast, in phenyl core based COF the morphology dramatically reshapes to hollow spheres where the crystallites assemble through inside-out Ostwald- Ripening mechanism. DFT study is carried out in order to validate the experimental result. It is established that extent of π - π stacking efficiency among the 2D COF layers is accountable for their morphological diversity along

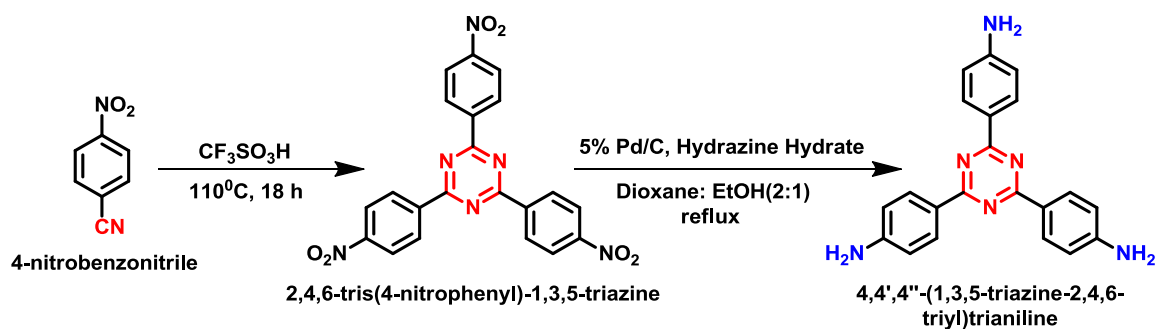
with dramatic change on surface area or crystallinity. We believe that a detailed investigation of diversity in self-assembly process along with valuable morphologies will open up a new domain of exciting research area in COFs.

5.4 Experimental procedures

5.4.1 Materials

2,3-dihydroxyterethaldehyde was prepared from 1,2-dimethoxybenzene using the reported literature procedure [5.24]. 1,3,5-tris(4-aminophenyl)benzene was directly purchased from TCI fine chemicals and was used without further purification. All other reagents and solvents were commercially available and used as received.

5.4.2 Synthesis of 4,4',4''-(1,3,5-triazine-2,4,6-triyl)trianiline (Tta)



Scheme 5.1: General synthetic scheme for the preparation of 4,4',4''-(1,3,5-triazine-2,4,6-triyl)trianiline (Tta).

4,4',4''-(1,3,5-triazine-2,4,6-triyl)trianiline: 12 gm of 4-nitrobenzonitrile was heated with 10-15 mL of trifluoromethane sulfonic acid at 110 °C for around 18 hrs. The reaction was monitored by TLC. After completion of the reaction, the whole reaction mixture was poured into distilled water. After complete precipitation, it was filtered off and washed with distilled water for several times in order to remove excess acid. The residue was vacuum dried at 100 °C, which gives 10.2 gm of grey coloured **2,4,6-tris(4-nitrophenyl)-1,3,5-triazine** (85% isolated yield) as an intermediate product. It was then directly used for the next step without any further purification.

In a 1000 mL three-neck flask a suspension of **2,4,6-tris(4-nitrophenyl)-1,3,5-triazine** (9.67 g, 0.021 mmol) and 2.054 g of Pd/C (5 wt %) in 410 mL of dioxane/ethanol (v/v, 2/1) was heated to reflux under nitrogen atmosphere. Then 46 mL of hydrazine monohydrate was

added dropwise over a period of 60 min, and the reaction mixture was further refluxed for 24 h and was monitored by TLC. After cooling to room temperature, the mixture was filtered and the filtrate was poured into 1.5 L of water. The precipitate was collected by filtration after several times washing with distilled water and dried in vacuo to give 5.5 g (56.8% isolated yield) of **4,4',4''-(1,3,5-triazine-2,4,6-triyl)trianiline (Tta)**. $^1\text{H NMR}$ (200 MHz, DMSO-d_6): 7.75-7.7(d, 6H), 6.68-6.64 (d, 6H), 5.97 (s, 6H). IR (powder, cm^{-1}): 3462 (w), 3333 (m), 3211(m), 2977(w), 1604(s), 1501(s), 1430(m), 1365 (s).

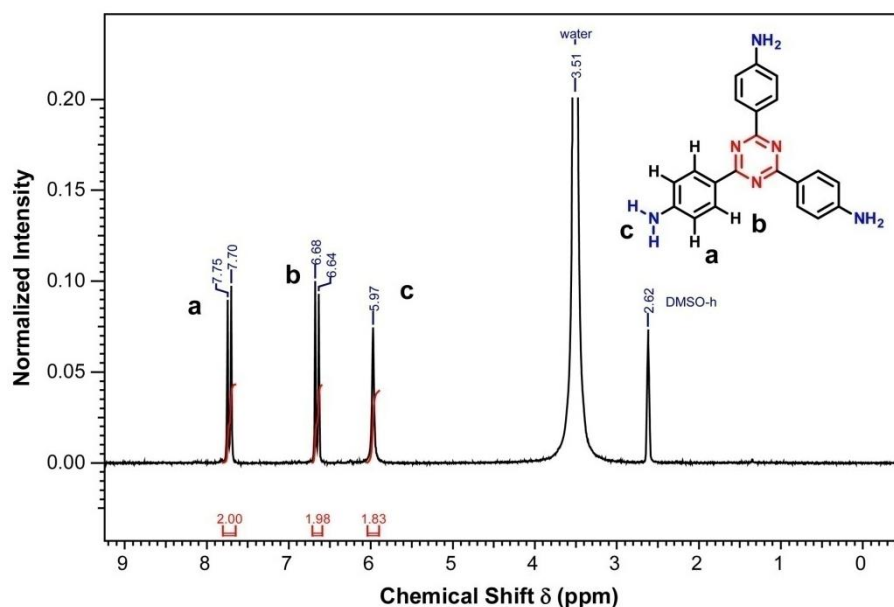
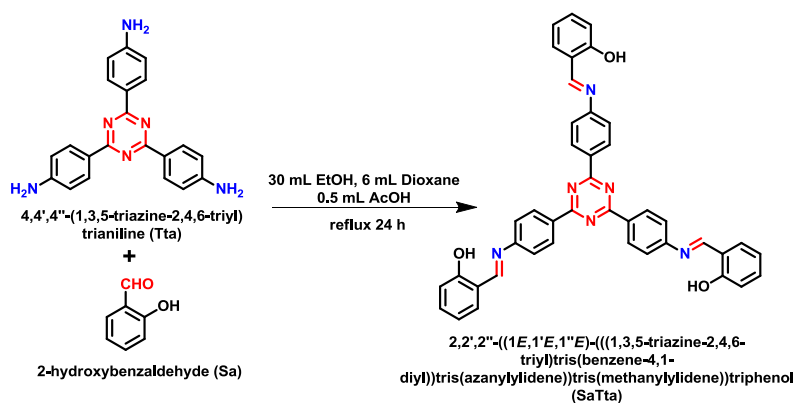


Figure 5.26: $^1\text{H NMR}$ spectrum (in DMSO-d_6) of **4,4',4''-(1,3,5-triazine-2,4,6-triyl)trianiline (Tta)**.

The reference compound was synthesized by the reaction between 1,3,5-Tris(4-aminophenyl)benzene (**Tab**) (0.175 g, 0.5 mmol) and salicylaldehyde (0.366 g, 3.0 mmol) in 20 mL ethanol under refluxing condition for 24 h. After this time the solution was allowed to reach room temperature. The precipitate formed was then collected by filtration. After washing with ethanol and drying under vacuum the final product was isolated as yellow solid 0.265 g (80%). The single crystals of the reference compound were grown in DMF, chloroform solvent combination. IR (powder, ATR): 1617, 1595, 1568, 1448, 1391, 1363, 1280, 1193, 1152, 910, 829, 749, 654; $^1\text{H NMR}$ (300 MHz, CDCl_3): δ 13.28 (s, 3H), 8.71 (s, 3H), 7.83 (s, 3H), 7.78 (d, $J = 8.24$ Hz, 6H), 7.48-7.39 (m, 12H), 7.07 (d, $J = 8.24$ Hz, 3H) and 6.98 (t, $J = 7.32$ Hz, 3H); $^{13}\text{C NMR}$ (75 MHz, CDCl_3): δ 166.55, 169.19, 147.19, 141.68, 139.53, 133.28, 133.23, 128.30, 124.88, 121.75, 119.22, 119.13 and 117.29.

5.4.3 Synthesis of reference compound 2,2',2''-((1E,1'E,1''E)-(((1,3,5-triazine-2,4,6-triyl)tris(benzene-4,1-diyl)tris(azanylylidene))tris(methanylylidene))triphenol (SaTta)



Scheme 5.2: General synthetic scheme for the preparation of **SaTta**.

This reference compound was synthesized by the reaction between 4,4',4''-(1,3,5-triazine-2,4,6-triyl)trianiline (**Tta**) (354 mg, 1 mmol) and salicylaldehyde (**Sa**) (610 mg, 5 mmol) in 30 mL ethanol, 6 mL dioxane and 0.5 mL of aqueous acetic acid mixture under refluxing condition for one day. After that, the solution was cooled to room temperature and the precipitate was collected by filtration, washed with ethanol to remove excess salicylaldehyde, and dried under vacuum to give 0.533 g (0.8 mmol, 80%) of **SaTta** as a yellow solid compound. $^1\text{H NMR}$ (200 MHz, CDCl_3): 13.15 (s, 3H), 8.89-8.85 (d, 6H), 8.76 (s, 3H), 7.52-7.43 (m, 12H), 7.13-6.99 (m, 6H). **IR** (powder, cm^{-1}): 2975(w), 1619 (m), 1596 (m), 1569 (m), 1511 (s), 1413 (m), 1361 (s), 1280 (m).

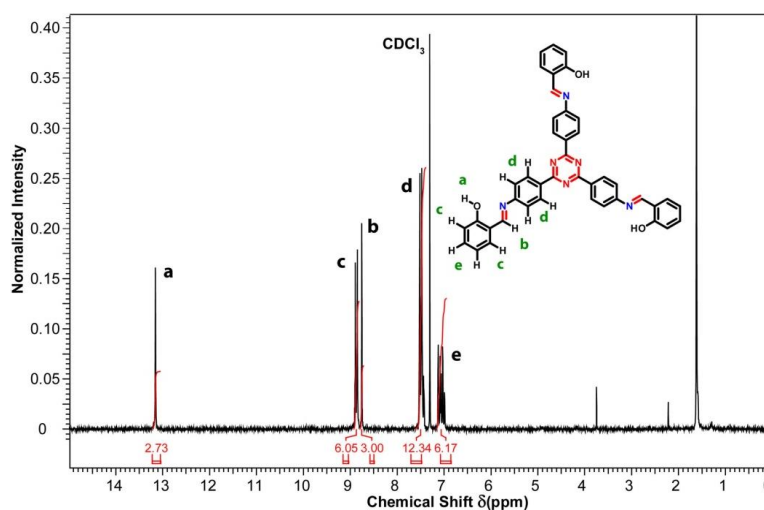


Figure 5.27: $^1\text{H NMR}$ spectrum (in CDCl_3) of the reference compound **SaTta**.

5.4.4 X-Ray investigation of single crystals of reference compounds

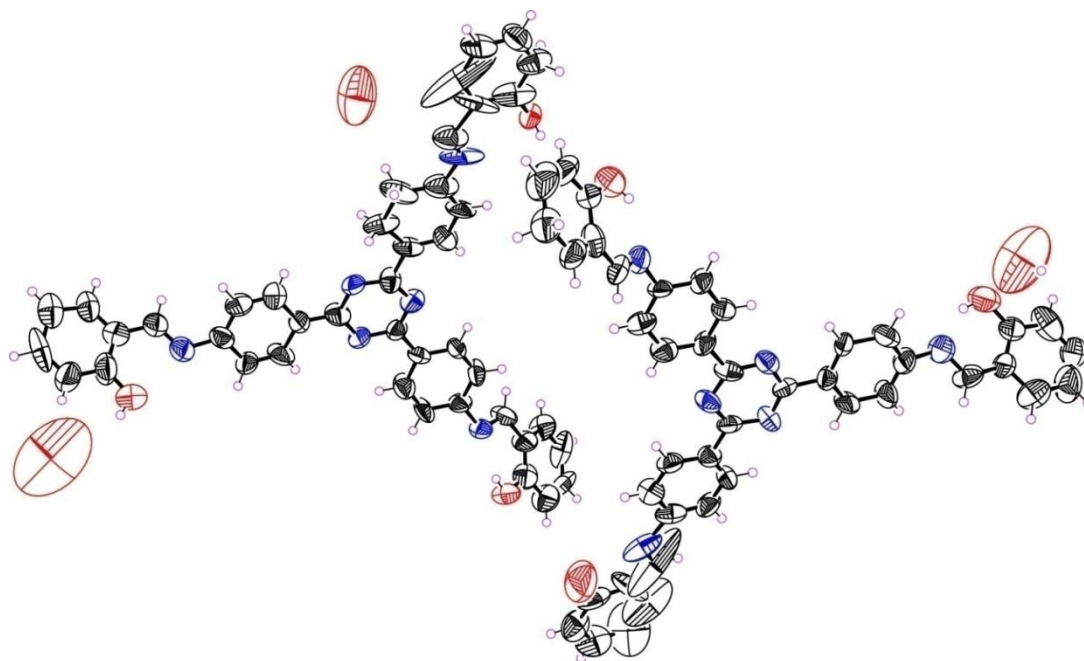


Figure 5.28: Single Crystal X-ray diffraction structure of the reference compound **SaTta**. In the ORTEP (with 40% probability level); Carbon (black), Nitrogen (blue), Oxygen (red) and Hydrogen (pink) have been shown [CCDC No: 1451702].

Table 5.1. Structural information of the reference monomer **SaTta**.

Structural information	
Empirical formula	C ₃₉ H ₃₁ N ₄ O ₇
Formula weight	667.68
Temperature/K	298
Crystal system	triclinic
Space group	<i>P</i> 1
<i>a</i> /Å	6.1550(5)
<i>b</i> /Å	12.6175(10)
<i>c</i> /Å	26.054(2)
α /°	102.990(7)
β /°	91.911(7)
γ /°	102.838(7)

Volume/Å ³	1914.9(3)
Z	2
ρ_{calc} mg/mm ³	1.158
m/mm ⁻¹	0.081
F(000)	698.0
Crystal size/mm ³	0.5 × 0.2 × 0.2
2 Θ range for data collection	6.44 to 58.38°
Index ranges	-7 ≤ h ≤ 8, -16 ≤ k ≤ 16, -35 ≤ l ≤ 32
Reflections collected	18165
Independent reflections	13454[R(int) = 0.0583]
Data/restraints/parameters	13454/3/927
Goodness-of-fit on F ²	1.215
Final R indexes [I ≥ 2 σ (I)]	R ₁ = 0.1253, wR ₂ = 0.3018
Final R indexes [all data]	R ₁ = 0.3131, wR ₂ = 0.4086
Largest diff. peak/hole / e Å ⁻³	0.58/-0.28
Flack parameter	-8(4)

5.4.5 Structure Modelling of COFs

Atomic positions and cell sizes of modelled COF layers were optimized using the Self-Consistent-Charge Density-Functional Tight-Binding (SCC-DFTB) Method. Stacking of layers is affected by the Coulomb repulsion between the partial atomic charges in adjacent layers. Hence, we performed a Mulliken population analysis for the charges. The adjacent layers were shifted with respect to each other in different directions in order to avoid Coulomb repulsion from charges alike. Several possibilities were considered, however, the best was taken from a comparison of simulated PXRD pattern with the experimental. Interlayer separation was also determined from the comparison of PXRD patterns.

In order to elucidate the structure of these COFs and to calculate the unit cell parameters (*Table 5.1 & 5.2*), possible 2-D models were optimized using the Density-Functional Tight-Binding method. Several stacking possibilities were considered for reasons reported in the literature.^[2] The experimental PXRD patterns are agreeable with the simulated patterns of some slipped-AA stacking models. COFs **2,3-DhaTta** and **2,3-DhaTab** have been

modelled in the triclinic space group (*P1*) by comparing the experimental and simulated PXRD patterns. Refinements of PXRD pattern were done using Reflex module of the Material studio.

Table 5.2. Fractional atomic coordinates for the unit cell of 2,3-DhaTta

2,3-DhaTta (Space group- <i>P1</i>)											
a =37.1407Å, b= 37.1469Å, c=3.54025Å; α =90.1853, β =89.4554, γ =120.5590											
Atom	x	y	z	Atom	x	y	z	Atom	x	y	z
C1	0.04946	0.01983	0.97127	C21	0.17366	0.28974	0.99129	C112	0.88384	0.57538	0.4856
C2	0.02783	0.97525	0.97255	C22	0.17378	0.3517	0.99309	C113	0.94904	0.63981	0.5463
C3	0.98539	0.95167	0.03082	C23	0.23593	0.35226	0.00147	C119	0.0265	0.53975	0.47147
C4	0.96522	0.9741	0.08586	C24	0.88401	0.70455	0.99783	C120	0.00683	0.49739	0.52987
C5	0.98618	0.0173	0.08473	C25	0.88313	0.64227	0.0101	C121	0.06929	0.5595	0.41402
C6	0.029	0.04159	0.02838	C26	0.82131	0.64235	0.99914	C122	0.02909	0.47541	0.52785
O1	0.05075	0.95785	0.91465	C27	0.28208	0.37571	0.00387	C123	0.09088	0.53823	0.4123
C7	0.04922	0.08712	0.03758	C28	0.30447	0.35503	0.03626	C124	0.07145	0.49543	0.46759
C8	0.9612	0.90606	0.04136	C29	0.30451	0.41927	0.97256	O8	0.48913	0.5203	0.55908
N1	0.97549	0.88273	0.98126	C30	0.34803	0.37699	0.03577	O9	0.96631	0.47501	0.59112
N2	0.0869	0.11167	0.97595	C31	0.34804	0.44152	0.97188	N15	0.96781	0.55021	0.52044
C9	0.10661	0.15536	0.98173	C32	0.37036	0.42054	0.00045	N16	0.41414	0.4446	0.5023
C10	0.08493	0.17726	0.96083	C33	0.15069	0.37436	0.99412	C131	0.09626	0.47504	0.45457
C11	0.15059	0.17814	0.99986	C16	0.90783	0.81629	0.96306	N19	0.21588	0.374	0.49918
C12	0.10683	0.2208	0.96404	C17	0.9732	0.81694	0.0088	N20	0.15174	0.30958	0.48664
C13	0.17214	0.22163	0.00377	C18	0.88618	0.77276	0.9667	N21	0.21575	0.31014	0.50013
C14	0.1506	0.24362	0.98671	C19	0.95124	0.77342	0.01284	N22	0.84191	0.68446	0.49211
C15	0.9517	0.83895	0.98724	C20	0.9074	0.75068	0.99279	N23	0.90558	0.68441	0.50812
C34	0.17159	0.41776	0.02817	C43	0.70838	0.55442	0.03333	N24	0.84098	0.6203	0.50693
C35	0.10714	0.35278	0.96432	C44	0.68684	0.57596	0.99722	C102	0.14987	0.43924	0.53165
C36	0.14987	0.43924	0.03165	C45	0.90561	0.619	0.01438	C103	0.08513	0.37392	0.46806
C37	0.08513	0.37392	0.96806	C46	0.88384	0.57538	0.9856	C114	0.90482	0.55322	0.48734
C38	0.10626	0.41753	0.99944	C47	0.94904	0.63981	0.0463	C115	0.97036	0.61793	0.54795
C39	0.77516	0.61948	0.9984	C48	0.90482	0.55322	0.98734	C116	0.94848	0.57429	0.51565
C40	0.75352	0.64093	0.96578	C49	0.97036	0.61793	0.04795	C117	0.43754	0.43011	0.44564
C41	0.75195	0.57607	0.03292	C50	0.94848	0.57429	0.01565	C118	0.00582	0.56429	0.46258
C42	0.71	0.61962	0.96633	C51	0.43754	0.43011	0.94564	C130	0.57308	0.49821	0.45458
C52	0.00582	0.56429	0.96258	C57	0.09088	0.53823	0.9123	C125	0.48316	0.45451	0.45341
C53	0.0265	0.53975	0.97147	C58	0.07145	0.49543	0.96759	C126	0.50568	0.4342	0.40264
C54	0.00683	0.49739	0.02987	C59	0.48316	0.45451	0.95341	C127	0.50664	0.49719	0.50604
C55	0.06929	0.5595	0.91402	C60	0.50568	0.4342	0.90264	C128	0.54889	0.45519	0.40345
C56	0.02909	0.47541	0.02785	C63	0.55123	0.51889	0.00637	C129	0.55123	0.51889	0.50637
C61	0.50664	0.49719	0.00604	C64	0.57308	0.49821	0.95458	C132	0.61864	0.51829	0.44693
C62	0.54889	0.45519	0.90345	N3	0.96781	0.55021	0.02044	N17	0.0822	0.43685	0.50785
O2	0.48913	0.5203	0.05908	N4	0.41414	0.4446	0.0023	N18	0.64313	0.55648	0.50047
O3	0.96631	0.47501	0.09112	C65	0.09626	0.47504	0.95457	O10	0.09015	0.03897	0.41218
C66	0.61864	0.51829	0.94693	C79	0.17214	0.22163	0.50377	O11	0.57027	0.55984	0.55947
N5	0.0822	0.43685	0.00785	C80	0.1506	0.24362	0.48671	O12	0.00696	0.43485	0.58747
N6	0.64313	0.55648	0.00047	C81	0.9517	0.83895	0.48724	C106	0.75352	0.64093	0.46578
O4	0.09015	0.03897	0.91218	C82	0.90783	0.81629	0.46306	C107	0.75195	0.57607	0.53292
O5	0.57027	0.55984	0.05947	C83	0.9732	0.81694	0.5088	C108	0.71	0.61962	0.46633

O6	0.00696	0.43485	0.08747	C84	0.88618	0.77276	0.4667	C109	0.70838	0.55442	0.53333
N7	0.21588	0.374	0.99918	C85	0.95124	0.77342	0.51284	C110	0.68684	0.57596	0.49722
N8	0.15174	0.30958	0.98664	C86	0.9074	0.75068	0.49279	C111	0.90561	0.619	0.51438
N9	0.21575	0.31014	0.00013	C87	0.17366	0.28974	0.49129	C96	0.34803	0.37699	0.53577
N10	0.84191	0.68446	0.99211	C88	0.17378	0.3517	0.49309	C97	0.34804	0.44152	0.47188
N11	0.90558	0.68441	0.00812	C89	0.23593	0.35226	0.50147	C98	0.37036	0.42054	0.50045
N12	0.84098	0.6203	0.00693	C90	0.88401	0.70455	0.49783	C99	0.15069	0.37436	0.49412
C67	0.04946	0.01983	0.47127	C91	0.88313	0.64227	0.5101	C100	0.17159	0.41776	0.52817
C68	0.02783	0.97525	0.47255	C92	0.82131	0.64235	0.49914	C101	0.10714	0.35278	0.46432
C69	0.98539	0.95167	0.53082	C93	0.28208	0.37571	0.50387	C77	0.15059	0.17814	0.49986
C70	0.96522	0.9741	0.58586	C74	0.9612	0.90606	0.54136	C104	0.10626	0.41753	0.49944
C71	0.98618	0.0173	0.58473	N13	0.97549	0.88273	0.48126	C105	0.77516	0.61948	0.4984
C72	0.029	0.04159	0.52838	N14	0.0869	0.11167	0.47595	C78	0.10683	0.2208	0.46404
O7	0.05075	0.95785	0.41465	C75	0.10661	0.15536	0.48173	C94	0.30447	0.35503	0.53626
C73	0.04922	0.08712	0.53758	C76	0.08493	0.17726	0.46083	C95	0.30451	0.41927	0.47256

Table 5.3. Fractional atomic coordinates for the unit cell of 2,3-DhaTab

2,3-DhaTab (Space group- P1)											
a =37.3226Å, b= 37.3414Å, c=3.56415 Å; α =87.4249, β =95.5139, γ =119.89											
atoms	x	y	Z	atoms	x	y	Z	atoms	x	y	Z
C1	0.05679	0.02077	0.02731	C5	0.99511	0.021	0.10776	C39	0.78414	0.61784	0.0166
C2	0.03485	0.97674	0.0341	C6	0.03717	0.04366	0.06263	C40	0.75949	0.63586	0.95664
C3	0.99282	0.95471	0.07629	O1	0.05719	0.95848	0.99585	C41	0.76354	0.5759	0.07116
C4	0.97382	0.9783	0.11425	C7	0.05742	0.08878	0.05748	C42	0.71641	0.61323	0.95253
C9	0.1146	0.15463	0.995	C8	0.96796	0.90963	0.08287	C43	0.72038	0.55266	0.06322
C10	0.09444	0.17714	0.93359	N1	0.98197	0.88602	0.0376	C44	0.69611	0.57103	0.00208
C11	0.15788	0.17634	0.04167	N2	0.09432	0.1114	0.00358	C45	0.92058	0.62382	0.96917
C12	0.117	0.22019	0.92655	C37	0.10106	0.38271	0.96321	C46	0.90176	0.58252	0.90565
C13	0.17991	0.21931	0.03813	C38	0.12288	0.4249	0.01394	C47	0.96341	0.64396	0.02817
C14	0.15994	0.24225	0.98199	C48	0.92439	0.56207	0.90564	C67	0.2295	0.37496	0.98142
C15	0.95874	0.84278	0.03401	C49	0.98653	0.62405	0.02556	C72	0.85311	0.62236	0.99638
C16	0.91609	0.82043	0.97246	C50	0.96718	0.58256	0.96447	O4	0.09693	0.03816	0.98385
C17	0.97997	0.82076	0.08248	C51	0.4496	0.42095	0.91507	O5	0.57949	0.55106	0.04152
C18	0.89543	0.77737	0.9642	H29	0.43635	0.38783	0.87185	O6	0.02667	0.44513	0.06963
C19	0.95884	0.77777	0.07768	C52	0.02625	0.57498	0.94369	C73	0.07279	0.01765	0.51502
C20	0.91609	0.75501	0.01846	C33	0.16488	0.3789	0.01295	C80	0.98433	0.90672	0.57905
C21	0.18369	0.28805	0.98175	C34	0.18609	0.42077	0.07002	N7	0.99906	0.88289	0.54736
C22	0.18663	0.35496	0.00304	C35	0.12188	0.36052	0.9596	N8	0.11195	0.10875	0.5141
C23	0.2499	0.35243	0.95919	C36	0.16578	0.4436	0.06958	C81	0.13207	0.15203	0.51183
C24	0.89407	0.70922	0.01188	C63	0.56163	0.51051	0.99169	C82	0.11186	0.17458	0.45205
C25	0.89627	0.64501	0.98288	C64	0.58418	0.49077	0.95271	C104	0.39993	0.41575	0.4424
C26	0.82995	0.64217	0.01626	O2	0.49958	0.51085	0.02257	C105	0.17977	0.3746	0.51269
C27	0.2953	0.37341	0.94447	O3	0.98704	0.4856	0.05641	C106	0.20022	0.41623	0.57259
C28	0.31771	0.35277	0.99949	N3	0.9876	0.55958	0.97223	C107	0.13664	0.35521	0.46156
C29	0.31796	0.41476	0.88345	N4	0.42635	0.43643	0.94377	C108	0.17893	0.43802	0.57637
C30	0.36062	0.37222	0.99538	C65	0.11498	0.48399	0.9712	C109	0.11492	0.37642	0.46811
C31	0.36095	0.43474	0.88186	C66	0.62936	0.51166	0.95406	C110	0.13599	0.41845	0.521
C32	0.383	0.41377	0.9366	N5	0.10014	0.4455	0.01574	C111	0.80077	0.61704	0.52313
C53	0.04673	0.55015	0.95908	N6	0.65275	0.55026	0.99815	C112	0.77717	0.63617	0.46324
C54	0.0271	0.50787	0.01024	C94	0.20237	0.35166	0.49957	C113	0.7795	0.57558	0.58363

C55	0.08908	0.56942	0.9188	C95	0.26642	0.35053	0.45796	C114	0.73414	0.61473	0.46149
C56	0.04897	0.48551	0.01791	C96	0.91135	0.7063	0.51767	O8	0.51649	0.51426	0.51799
C57	0.11025	0.54769	0.92558	C97	0.91179	0.6414	0.48031	O9	0.99859	0.47763	0.55413
C58	0.09086	0.50502	0.97425	C98	0.84641	0.64009	0.51746	N9	0.99945	0.55204	0.47396
C59	0.49488	0.44577	0.93161	C99	0.31203	0.37283	0.44743	N10	0.44324	0.43919	0.44766
C60	0.51814	0.42635	0.89512	C100	0.33554	0.35342	0.50417	C137	0.12711	0.47668	0.47602
C61	0.51742	0.48823	0.98104	C101	0.33381	0.41448	0.38914	C138	0.64628	0.51435	0.46084
C62	0.561	0.44798	0.90483	C102	0.37854	0.37407	0.5004	N11	0.11265	0.4384	0.52324
C74	0.0508	0.97362	0.52191	C103	0.37687	0.43577	0.38966	C144	0.86854	0.6195	0.49181
C68	0.16449	0.31144	0.00962	C125	0.05837	0.54228	0.45869	O10	0.11291	0.03507	0.47133
C69	0.22622	0.30901	0.95389	C126	0.03875	0.5	0.51025	O11	0.59657	0.55426	0.54267
C70	0.85114	0.68561	0.0303	C127	0.10079	0.56169	0.41952	O12	0.03867	0.43741	0.57227
C71	0.916	0.68844	0.98546	C128	0.06083	0.47783	0.52001	C129	0.12212	0.54013	0.42824
C79	0.07386	0.08569	0.55317	C115	0.73635	0.55356	0.57916	C130	0.10279	0.4975	0.4776
C75	0.00885	0.95168	0.56526	C116	0.71309	0.57279	0.51471	C131	0.51187	0.44913	0.4292
C76	0.98961	0.97528	0.59915	C117	0.93509	0.61907	0.46879	C132	0.53507	0.42961	0.39353
C77	0.01094	0.01796	0.59258	C118	0.91535	0.57761	0.40627	C133	0.53439	0.49158	0.47904
C78	0.05328	0.04059	0.55139	C119	0.97775	0.63813	0.53004	N12	0.66973	0.55271	0.50846
O7	0.07302	0.95522	0.48364	C120	0.93693	0.55605	0.40843	C139	0.24511	0.37235	0.47545
C83	0.17529	0.17386	0.56067	C121	0.99995	0.61726	0.52746	C140	0.18112	0.30825	0.51007
C84	0.13443	0.21755	0.44338	C122	0.97971	0.57568	0.46678	C141	0.24358	0.307	0.45686
C85	0.19741	0.21687	0.55507	C123	0.46662	0.42427	0.41259	C142	0.86842	0.68337	0.53567
C86	0.17755	0.2397	0.49511	C124	0.03788	0.56708	0.44203	C143	0.93249	0.68492	0.48696
C87	0.97578	0.83967	0.55028	C134	0.57793	0.45107	0.40593	C90	0.91251	0.77423	0.48194
C88	0.93299	0.8172	0.49124	C135	0.5786	0.51369	0.49219	C91	0.97606	0.77467	0.59379
C89	0.99701	0.81769	0.60022	C136	0.60109	0.49377	0.45529	C92	0.93346	0.75197	0.53208
C93	0.20108	0.28544	0.48614								

NOTE: The results of this chapter have already been published in *Angew. Chem. Int. Ed.* **2016**, *55*, 7806, with the title: “*Decoding the Morphological Diversity in Two Dimensional Crystalline Porous Polymers by Core Planarity Modulation*”. These publications were the results from the group of Dr. Rahul Banerjee and his students Mr. Arjun Halder, Sharath Kandambeth, Bishnu P. Biswal from CSIR-National Chemical Laboratory, Pune, India. Theoretical collaboration from Dr. Kumar Vanka and his student Mr. Subhrashis Banerjee working at CSIR- National Chemical Laboratory and Dr. Thomas Heine and his student Dr. Matthew Addicoat from Jacobs University, Germany. Dr. Sandeep Verma and his student Ms. Gagandeep Kaur (from Indian Institute of Technology, Kanpur) have performed the AFM analysis of the COF samples. Major work was contributed by Mr. Arjun Halder with the help of the instrumental facilities of CSIR-National Chemical Laboratory. The manuscript was primarily written by Mr. Arjun Halder under the guidance of Dr. Rahul Banerjee.

CHAPTER 6

Conclusions of all Chapters and Future Directive

6.1 *Conclusions*

The first chapter of the thesis briefly introduces advanced porous crystalline framework materials specifically of covalent organic frameworks (COFs), their gradual synthetic development and various important applications. It describes the reticular synthetic approaches, different reversible reactions responsible, basic symmetry rules of linker combination and mechanism for their formation. Furthermore, it also discussed the synthetic methods used in its preparation and potential applications such as in gas uptake, separation, catalysis, energy storage, photoelectric and drug delivery. Finally, it has specifically focused on a careful emphasis on the chemical stability issues of COFs. COFs are generally prepared by reversible chemical reactions and hence, the possibility of reversible back reaction after the COF crystallite formation is primarily responsible for the chemical stability issues of COFs. The various reported methods, to enhance the chemical stability of COFs, are thoroughly and systematically discussed in the initial introduction section. Apart from chemical stability, we have outlined other important criteria such as the processability and scalability of imine-based ($-C=N-$) COFs owing to their more versatile nature. In the last part, we have discussed about morphological diversity in COFs.

In the second chapter, we examined chemical stability enhancement in imine-based ($-C=N-$) COFs and their bulk scale production using 2,4,6-trimethoxy-1,3,5-benzenetricarbaldehyde (TpOMe) as a prime aldehyde building unit. Herein, for the first time, we have introduced a new methodology of interlayer hydrogen bonding (H-bonding) for the construction of a series of porous, crystalline imine-based COFs with ultrahigh chemical stability in strong acids (H_2SO_4 , 18 M; HCl; 12 M) and base (NaOH, 9 M). The density functional theory (DFT) calculations revealed the presence of a significant number of interlayer C-H \cdots N H-bonding between the methoxy ($-OCH_3$) C-H of a particular layer with the imine ($-C=N-$) nitrogen atoms present in the adjacent layers. Such interlayer C-H \cdots N H-

bonding provides enough steric hindrance and the hydrophobic environment around the imine bonds and protects them from being hydrolyzed in such mordant conditions. The present synthetic strategy also provides the opportunity for the rapid production of imine-based COFs in industrial scale for the first time. Therefore, we believe, the high chemical robustness of these imine-based ($-C=N-$) COFs associated with its rapid and scalable production could make them suitable for real-life applications.

In the third chapter, we discussed about the fabrication of an imine-based ($-C=N-$) self-standing **TpOMe-Azo** covalent organic framework membrane (COFMs) exhibiting high crystallinity and porosity with extraordinary chemical stability in conc. H_2SO_4 (18 M) due to the presence of strong interlayer H-bonding throughout the framework. The high surface area ($S_{BET} = 2154 \text{ m}^2\text{g}^{-1}$) and uniform pore size distribution (pore diameter 2.8 nm) of the COFM signifies the existence of long-range ordered pore-channels with unique pore aperture present in its backbone structure. The advantage of ordered nano-channels made the COFMs excellent candidate for their successful utilization to separate various environmentally toxic materials from drinking water with high water flux. In addition, owing to their highly robust backbone, the COFMs were also employed for unprecedented sulfuric acid (6 M) permeance and their potential applications for sulfuric acid purification from nitro-aromatic impurities as well. Also, the as-synthesized COFMs exhibit exceptionally high permeance of acetonitrile ($280 \text{ Lm}^{-2}\text{h}^{-1}\text{bar}^{-1}$) and acetone ($260 \text{ Lm}^{-2}\text{h}^{-1}\text{bar}^{-1}$) reflecting its applicability for waste solvent treatment.

In the fourth chapter, we reported an imine-based, redox active COF **TpOMe-DAQ** that was constructed from 2,4,6-trimethoxy-1,3,5-benzenetricarbaldehyde (TpOMe) and 2,6-diaminoanthraquinone (DAQ) as building units. The judicious choice of such linker units could combine both electrochemical stability (due to the explicit incorporation of the methoxy functionality) and reversible redox response due to the quinone/hydroquinone transformation (DAQ amine) for energy storage. **TpOMe-DAQ** COF exhibit with ultrahigh chemical stability in conc. H_2SO_4 (18 M), conc. HCl (12 M) and NaOH (9 M) due to the presence of strong interlayer H-bonding. The as-synthesized COF fabricated as thin sheets were efficiently employed as a free-standing supercapacitor electrode material using 3 M aq. H_2SO_4 as an electrolyte. Moreover, the pristine COF sheet showcased outstanding areal capacitance 1600 mFcm^{-2} (gravimetric 169 Fg^{-1}) and excellent cyclic stability ($> 1,00,000$)

without compromising its capacitive performance or coulombic efficiency which is the highest ever achieved in a pristine COF based electrode material. The superior capacitive performance was believed owing to excellent pseudo-capacitance behavior by virtue of precise molecular level control over redox functionalities present in the COF backbone. Moreover, as a proof-of-concept, a solid-state supercapacitor device was also assembled and a 1.8 V red LED was successfully kindled for 30 sec *via* connecting three similar devices in series and charging in a 3 V potential window.

In the fifth chapter, we for the first time reported molecular level morphological control in two dimensional crystalline and porous (S_{BET} as high as $1700 \text{ m}^2 \text{ g}^{-1}$) COFs. Herein, we examine in detail about the mechanism of formation for two diverse morphologies in COFs such as nano-ribbons (**2,3-DhaTta**) and hollow sphere (**2,3-DhaTab**) whereas the formation of the hollow sphere was believed due to an inside-out Ostwald ripening process. Moreover, herein for the first time, we have attempted to understand in deep, the relationship of dihedral angles of the linkers at the molecular level with the final morphology of the COF crystallites. Besides, we have also shown how crystallinity and surface area of COFs gets tuned based on overall core planarity of the linkers. Moreover, density functional theory (DFT) study was carried out in order to validate the experimental result. It was established that extent of π - π stacking efficiency among the 2D COF layers is accountable for their morphological diversity along with dramatic effect on surface area or crystallinity. We believe that a detailed investigation of diversity in self-assembly process along with valuable morphologies will open up a new domain of exciting research area in COFs.

6.2 Future directive

Developing self-standing and functionalized covalent organic framework membranes for arsenic-contaminated water purification

6.2.1 Introduction

Arsenic is in one of the most toxic heavy metals although in low concentration present in the groundwater causes severe effects to the human health and ecosystem. Millions of people throughout the world are mostly depending on groundwater are in the risk of arsenic contamination to their lives. A severe disease like arsenicosis, characterized as disabling and deteriorating disease could lead various symptoms like patches on palms, pigmentation of the skin etc., caused due to prolonged and excessive exposure of arsenic to drinking water (**Figure 6.1**). Arsenic poisoning could lead potentially fatal disease like cancer too and is one of the most severe effects to the human health worldwide. It is known as the ‘kings of poison’ and was first discovered by scientist Albertus Magnus (1250 AD). Arsenic in drinking water mainly exists in two major forms such as arsenite (As^{III} ; H_3AsO_3 or NaH_2AsO_3) and arsenate (As^{V} ; H_2AsO_4^- or HAsO_4^{2-}). Arsenite is about 40-50 times more toxic than arsenate and is more labile and soluble and can easily immobilize with water. Although various techniques for the detection and removal of arsenic from drinking water have been developed to date, still a significant number of research are going on for its permanent solution. [6.1]

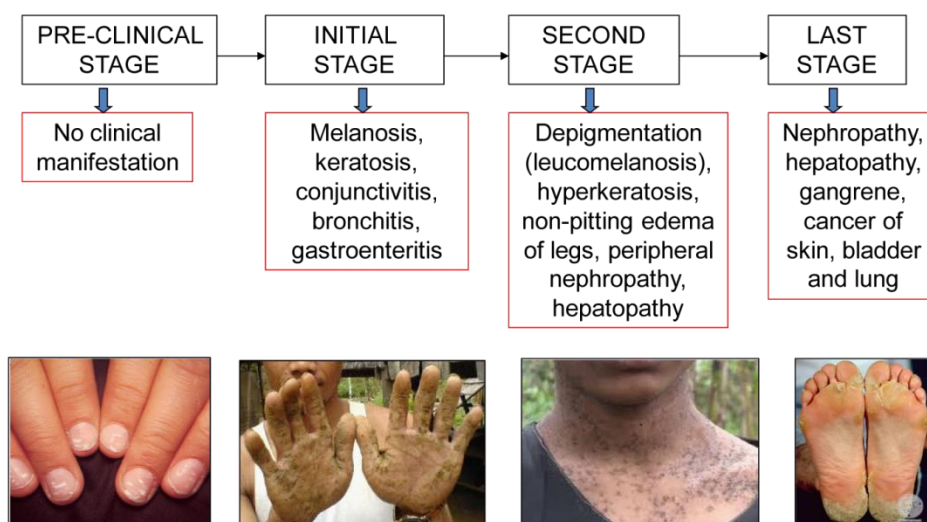


Figure 6.1: Various symptoms of arsenic poisoning to human health and its different affected stages.

6.2.2. The commercial technique used for arsenic removal

It is very important to remove arsenic from water before it is used for drinking by the humans. There are various techniques available for arsenic removal from water and these are based on four major categories such as membrane technologies (mostly used), Oxidation, Ion exchange and adsorption basis. Although all these procedures are potential in terms of arsenic removal still they have some drawbacks (**Figure 6.2**). Here the most used and latest technologies such as membrane separation have been discussed-

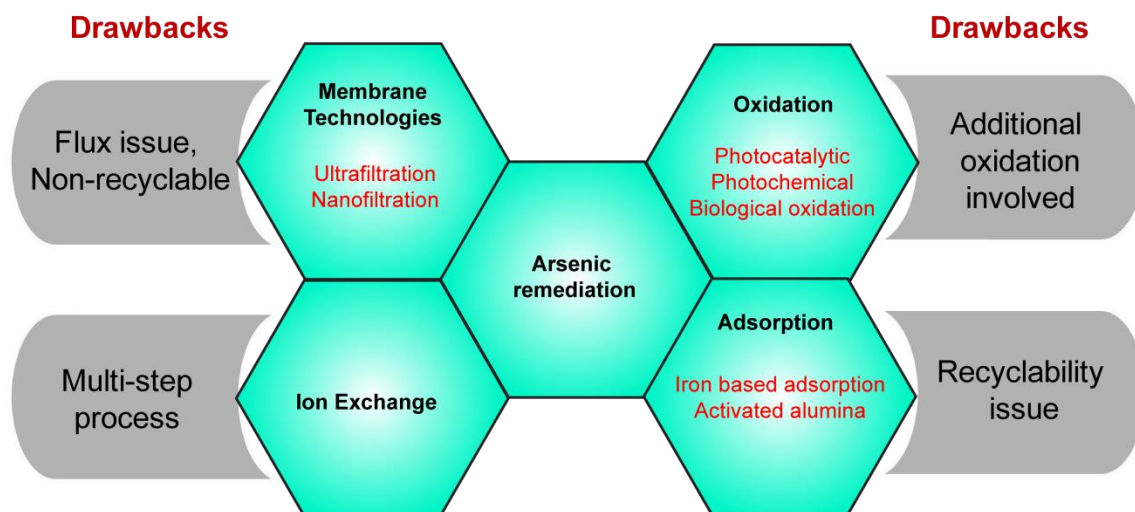


Figure 6.2: Commercial technique used for arsenic removal from drinking water and their drawbacks.

Membrane technologies:

Ultrafiltration membrane: Nowadays this is the most used technique in the industry for the wastewater treatment process. The purification by using this membrane work on the basis of molecular weight cut off. The pressure or concentration gradient dictates the separation through a semi-permeable membrane. Suspended solids or the suspension gets rejected through this membrane during passing and thus low molecular weight materials can easily pass out. The basic drawback of this membrane is the recyclability technique which requires multiple steps (**Figure 6.2**).

Nanofiltration membrane: Nanofiltration (NF) is a recent membrane filtration process mostly used for water such as surface water and fresh groundwater treatment. The purpose of

this membrane filtration is to soften (polyvalent cation removal) and to remove natural organic matter as well as synthetic organic matter. The pore sizes of Nanofiltration membranes varies in the range of 1-10 nanometers which is smaller than that used ultrafiltration, but larger than that of in reverse osmosis. Membranes used are vastly created from available polymer thin films and are commonly used include polyethylene terephthalate or metals like aluminum. The major drawbacks of this method are the flux issue due to the small pore aperture of the membrane (**Figure 6.2**) [6.2].

6.2.3. The proposed approach for arsenic removal from drinking water through self-standing COF membrane

Covalent organic frameworks (COFs), in recent years, have delighted significant potential importance to the scientific community in accounts of their widespread applications. COFs are associated with long-range ordered pore-channels with unique pore aperture (1-3 nm) present in its backbone structure. The advantage of ordered nano-channels could make the COFs excellent candidate for their successful utilization as a nanofiltration membrane to separate various environmentally toxic materials from drinking water with high water flux.

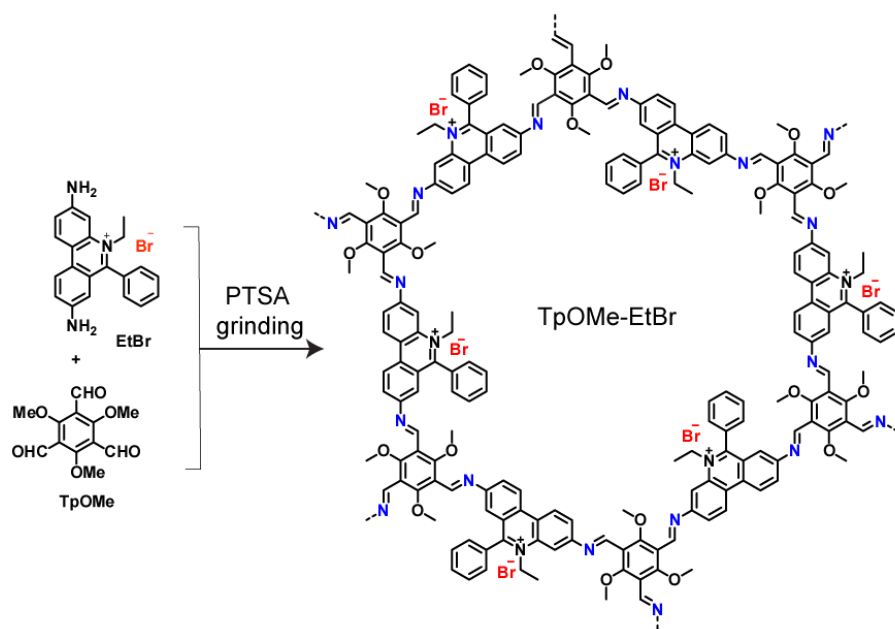


Figure 6.3: Proposed synthetic scheme for *TpOMe-EtBr* Covalent Organic Framework Membrane (COFM) synthesis.

Recent theoretical proceedings esteemed covalent organic framework membranes (COFMs) as a true potential entrant in terms of molecular separation. For this purpose, COFs can be

transformed to the corresponding COFMs form for selective arsenic separation based on ion exchange method [6.3]. Using the same procedure depicted in chapter 3, we could design an ionic COFM for arsenic removal from drinking water.

Herein, the proposed approach is based on anion exchange to remove arsenic from drinking water. For this purpose, an ionic Covalent Organic Framework Membrane (COFM) **TpOMe-EtBr** have been designed considering PTSA mediated solid-state synthesis approach (**Figure 6.3**).

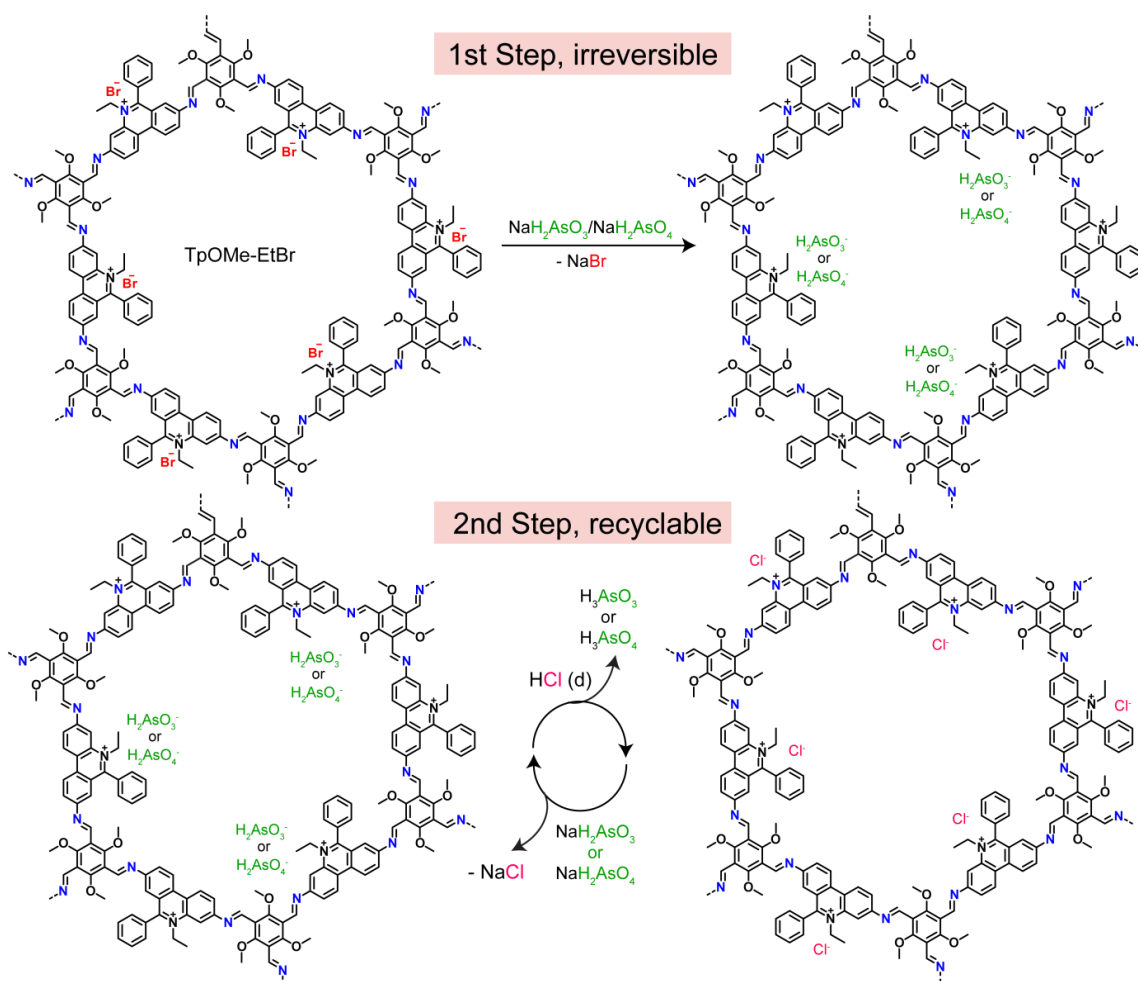


Figure 6.4: Trapping of arsenite/arsenate in COFM **TpOMe-EtBr** through irreversible ligand exchange (step 1). Dilute hydrochloric acid treatment for recycling use of the membrane (step 2).

The synthesized COFM will have bromide anions (Br^-) within the pore [6.3]. Once the arsenic contaminated water will be passed through the membrane, larger anions such as arsenite and arsenate will replace smaller bromide anion (**Figure 6.4, step 1**). Hence in the

first shot, it will generate arsenate trapped membrane and bromide will come out with water solution. Hence the water gets purified from arsenic. In the second step, dilute hydrochloric acid (aq. HCl) is passed which will remove both arsenate and arsenite through protonation and will come out as arsenic and arsenous acids which are highly water soluble (*Figure 6.4, step 2*). Now there will be chloride in the framework structure. Now like the first step again arsenic contaminated water will replace chloride in the membrane in the 2nd cycle and arsenic ions will get trapped accordingly and can be removed via diluted HCl pass. So 1st step is irreversible and 2nd step is recyclable and will keep on going on through several cycles of arsenic removal from drinking water.

6.2.4 COFM based device fabrication for arsenic removal from groundwater

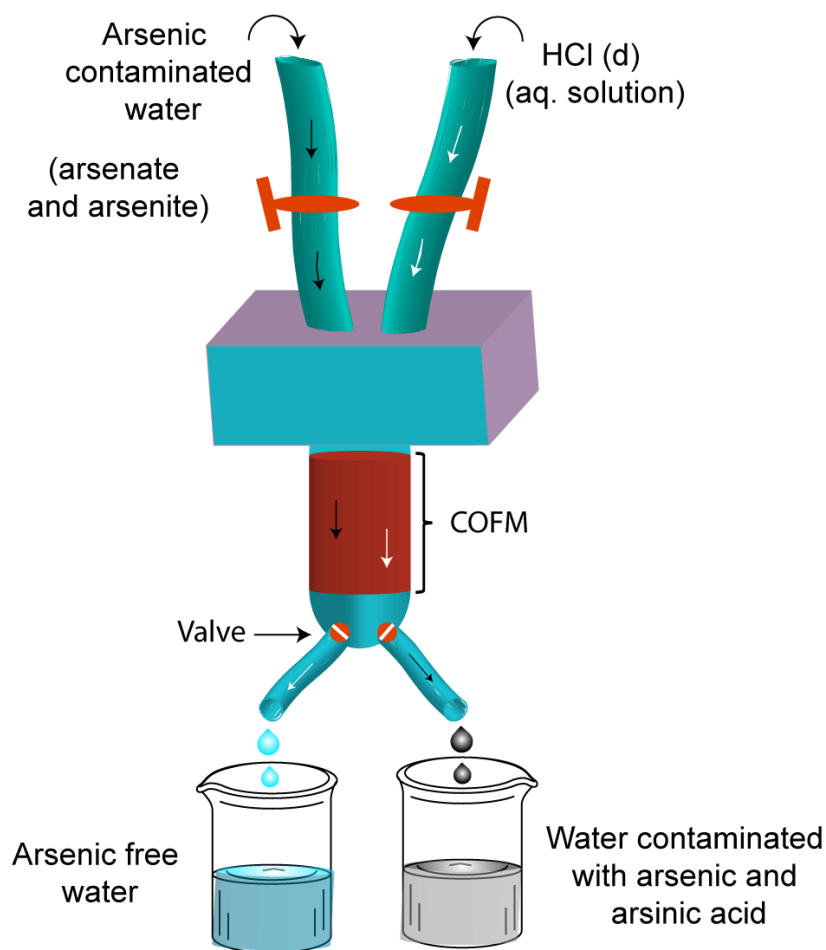


Figure 6.5: Proposed design of arsenic contaminated water purification instrument using COFM.

The design principle of the device: As discussed above, the COF can be readily transformed to the corresponding COFM with any shape or sizes. Now, one can easily fabricate membrane with variable thickness as well. In the above device, there are two different pipelines (green colored) through which separately arsenic contaminated water (denoted as a black arrow) and diluted hydrochloric acid solution (denoted as a white arrow) can be passed. Both of them have separate open-close valves (shown in red). These two pipes have been joined in one semi-cubic container which further connected with one narrow-headed hollow cylinder within which COFM have been tightly packed. The end part of the cylinder connected with other two separated pipelines containing auto open-close valves in their joints (**Figure 6.5**).

The working principle of the device: If arsenic contaminated water gets passed (as shown with black arrow) both the valves in the same side will be opened (left side valves of pipe and left side joint valve). Now when arsenic contaminated water (shown with black arrow) will pass through the membrane it will be trapped either through hydrogen bonding through anion exchange. Finally, arsenic purified water will pass out through left side joint pipe (shown with white arrow). On the other hand, when diluted HCl (as shown with white arrow) will pass right side both valves will be opened. Now diluted HCl solution will wash out both the toxic anions such as arsenate and arsenite during passing through COFM and will eject as arsenic and arsenous acids through a right side joint pipe (as shown with black arrow). Thus the membrane can be utilized cyclically using this preferred device. The above technique may lead to the simplest way of arsenic purification from drinking water (**Figure 6.5**).

REFERENCES

CHAPTER 1

- [1.1] D. Wu, F. Xu, B. Sun, R. Fu, H. He, K. Matyjaszewski, *Chem. Rev.* **2012**, *112*, 3959. (b) G. M. Whitesides, E. E. Simanek, J. P. Mathias, C. T. Seto, D. Chin, M. Mammen, D. M. Gordon, *Acc. Chem. Res.*, **1995**, *28*, 37. (c) J. D. Wuest, *Chem. Commun.*, **2005**, *47*, 5830. (d) J. M. Zayed, N. Nouvel, U. Rauwald and O. A. Scherman, *Chem. Soc. Rev.*, **2010**, *39*, 2806. (e) S. J. Rowan, S. J. Cantrill, G. R. L. Cousins, J. K. M. Sanders, J. F. Stoddart, *Angew. Chem., Int. Ed.*, **2002**, *41*, 898.
- [1.2] K. Ishizaki, S. Komarneni, M. Nanko. *Porous Materials: Process, technology and applications*. Kluwer Academic, **1998**.
- [1.3] (a) M. Eddaoudi, D. B. Moler, H. Li, B. Chen, T. M. Reinecke, M. O’Keeffe, O. M. Yaghi, *Acc. Chem. Res.* **2001**, *34*, 319. (b) C. Janiak, *Angew. Chem., Int. Ed.*, **1997**, *36*, 1431. (c) A. J. Blake, N. R. Champness, P. Hubberstey, W.-S. Li, M. A. Withersby, M. Schroder, *Coord. Chem. Rev.*, **1999**, *183*, 117. (d) B. Kesanli, Y. Cui, M. Smith, E. Bittner, B. Bockrath, W. Lin, *Angew. Chem., Int. Ed.*, **2005**, *44*, 72. (e) S. Kitagawa, R. Kitaura, S. -I. Noro, *Angew. Chem., Int. Ed.*, **2004**, *43*, 2334. (f) G. Ferey, *Chem. Soc. Rev.* **2008**, *37*, 191. (g) B. Chen, S. Xiang, G. Qian, *Acc. Chem. Res.*, **2010**, *43*, 1115.
- [1.4] (a) Y. Ma, W. Tong, H. Zhou, S. L. Suib, *Microporous Mesoporous Mater.*, **2000**, *37*, 243. (b) S. Cavenati, C. A. Grande, A. E. Rodrigues, *J. Chem. Eng. Data*, **2004**, *49*, 1095. (c) J. Rouquerol, D. Avnir, C. W. Fairbridge, D. H. Everett, J. H. Haynes, N. Pernicone, J. D. F. Ramsay, K. S. W. Sing, K. K. Unger, *Pure and Applied Chemistry*, **1994**, *66*, 1739. (d) T. Sawaki, T. Dewa, Y. Aoyama, *J. Am. Chem. Soc.*, **1998**, *120*, 8539. (e) R. E. Morris, P. S. Wheatley. *Angew. Chem., Int. Ed.* **2008**, *47*, 4966.
- [1.5] (a) J. Lee, J. Kim, T. Hyeon. *Adv. Mater.* **2006**, *18*, 2073. (b) M. C. Orilall, U. Wiesner. *Chem. Soc. Rev.* **2011**, *40*, 520. (c) Y. Zhou, Y. Kim, C. Jo, J. Lee, C. W. Lee, S. Yoon. *Chem. Commun.* **2011**, *47*, 4944. (d) Y. Ishii, Y.

-
- Kanamori, T. Kawashita, I. Mukhopadhyay, S. Kawasaki. *J. Phys. Chem. Solids*, **2010**, *71*, 511. (e) L. Fu, H. Liu, H. Zhang, C. Li, T. Zhang, Y. Wu, H. Wu. *J. Power Sources*, **2006**, *159*, 219. (f) D.-H. Lee, J. -G. Park, K. Jin Choi, H. -J. Choi, D.-W. Kim, *Eur. J. Inorg. Chem.* **2008**, *2008*, 878.
- [1.6] (a) J. Lee, J. Kim, T. Hyeon. *Adv. Mater.* **2006**, *18*, 2073. (b) M. C. Orilall, U. Wiesner. *Chem. Soc. Rev.* **2011**, *40*, 520. (c) Y. Zhou, Y. Kim, C. Jo, J. Lee, C. W. Lee, S. Yoon. *Chem. Commun.* **2011**, *47*, 4944. (d) Y. Ishii, Y. Kanamori, T. Kawashita, I. Mukhopadhyay, S. Kawasaki. *J. Phys. Chem. Solids*, **2010**, *71*, 511. (e) L. Fu, H. Liu, H. Zhang, C. Li, T. Zhang, Y. Wu, H. Wu. *J. Power Sources*, **2006**, *159*, 219. (f) D.-H. Lee, J. -G. Park, K. Jin Choi, H. -J. Choi, D.-W. Kim, *Eur. J. Inorg. Chem.* **2008**, *2008*, 878.
- [1.7] (a) D. W. Breck, *Zeolite molecular sieves: structure, chemistry, and use*. Wiley: New York, **1974**. (b) C. S. Cundy, P. A. Cox, *Chem. Rev.* **2003**, *103* (3), 663. (c) Z. Wang, J. Yu, R. Xu, *Chem. Soc. Rev.*, **2012**, *41*, 1729. (d) J. Yu and R. Xu, *Acc. Chem. Res.*, **2010**, *43*, 1195. (e) J. J. Pluth, J. V. Smith, *Am. Mineral.*, **1990**, *75*, 501. (f) R. M. Barrer, P. J. Denny, *J. Chem. Soc.*, **1961**, *0*, 971. (g) A. F. Cronsted, *Akad. Handl.*, **1756**, *17*, 20.
- [1.8] F. Schuth, K. S. W. Sing, J. Weitkamp, editors. *Handbook of Porous Solids*. Wiley-VCH Verlag GmbH, **2002**.
- [1.9] (a) M. Eddaoudi, D. B. Moler, H. Li, B. Chen, T. M. Reinecke, M. O’Keeffe, O. M. Yaghi, *Acc. Chem. Res.* **2001**, *34*, 319. (b) C. Janiak, *Angew. Chem., Int. Ed. Engl.*, **1997**, *36*, 1431. (c) A. J. Blake, N. R. Champness, P. Hubberstey, W.-S. Li, M. A. Withersby, M. Schroder, *Coord. Chem. Rev.*, **1999**, *183*, 117. (d) O. M. Yaghi, G. Li, H. Li, *Nature*, **1995**, *378*, 703. (e) S. Kitagawa, R. Kitaura, S. -I. Noro, *Angew. Chem., Int. Ed.*, **2004**, *43*, 2334. (f) G. Ferey, *Chem. Soc. Rev.* **2008**, *37*, 191. (g) B. Chen, S. Xiang, G. Qian, *Acc. Chem. Res.*, **2010**, *43*, 1115. (h) L. Ma, C. Abney, W. Lin, *Chem. Soc. Rev.*, **2009**, *38*, 124. (i) Z. G. Gu, Y. P. Cai, H. C. Fang, Z. Y. Zhou, P. K. Thallapally, J. A. Tian, J. Liu, G. J. Exarhos, *Chem. Commun.*, **2010**, *46*, 5373. (j) B. Chen, M. Eddaoudi, S. T. Hyde, M. O’Keeffe, O. M. Yaghi, *Science*, **2001**, *291*, 1021. (k) P. Pachfule, Y. Chen, J. Jiang, R. Banerjee *J.*

- Mater. Chem.*, **2011**, *21*, 17737. (l) J. W. Yoon, S. H. Jhung, Y. K. Hwang, S. M. Humphrey, P. T. Wood, J. -S. Chang, *Adv. Mater.* **2007**, *19*, 1830. (m) K. L. Mulfort, O. K. Farha, C. D. Malliakas, M. G. Kanatzidis, J. T. Hupp, *Chem. Eur. J.*, **2010**, *16*, 276. (n) H. -S. Choi, M. P. Suh, *Angew. Chem.* **2009**, *121*, 6997. (o) X. Gu, Z.-H. Lu, Q. Xu, *Chem. Commun* **2010**, *46*, 7400. (p) S. -T. Zheng, J. T. Bu, Y. Li, T. Wu, F. Zuo, P. Feng, X. Bu. *J. Am. Chem. Soc.* **2010**, *132*, 17062. (q) J. An, N. L. Rosi, *J. Am. Chem. Soc.* **2010**, *132*, 5578. (r) A. G. Wong-Foy, O. Lebel, A. J. Matzger, *J. Am. Chem. Soc.* **2007**, *129*, 15740. (s) H. Chun, D. N. Dybtsev, H. Kim, K. Kim, *Chem. Eur. J.* **2005**, *11*, 3521. (t) J. Rowsell, A. Millward, K. Park, O. Yaghi *J. Am. Chem. Soc.* **2004**, *126*, 5666.
- [1.10] (a) Y. Li, R. T. Yang, *AIChE J.* **2008**, *54*, 269. (b) Z. Liang, M. Marshall, A. L. Chaffee, *Energy Fuels* **2009**, *23*, 2785. (c) F. Gul-E-Noor, B. Jee, A. Poppl, M. Hartmann, D. Himsl, M. Bertmer, *Phys. Chem. Chem. Phys.* **2011**, *13*, 7783. (d) N. C. Burtch, H. Jasuja, K. S. Walton, *Chem. Rev.*, **2014**, *114*, 10575.
- [1.11] (a) Y. Luo, B. Li, W. Wang, K. Wu and B. Tan, *Advanced Materials*, **2012**, *24*, 5703. (b) D. C. Wu, F. Xu, B. Sun, R. W. Fu, H. K. He, K. Matyjaszewski, *Chem. Rev.*, **2012**, *112*, 3959. (c) P. kaur, J. T. Hupp and S. T. Nguyen, *ACS Catal.*, **2011**, *1*, 819. (d) Z. H. Xiang and D. P. Cao, *J. Mater. Chem. A*, **2013**, *1*, 2691.
- [1.12] A. P. Cote, A. I. Benin, N. W. Ockwig, M. O’Keeffe, A. J. Matzger, O. M. Yaghi, *Science*, **2005**, *310*, 1166.
- [1.13] P. A. Wright, *Microporous Framework Solids*, RSC Publishing, Cambridge, **2008**.
- [1.14] S. T. Wilson, B. M. Lok, C. A. Messina, T. R. Cannan, E. M. Flanigen, *J. Am. Chem. Soc.* **1982**, *104*, 1146.
- [1.15] (a) Q. Huang, M. Ulutagay, P. A. Michener, S.-J. Hwu, *J. Am. Chem. Soc.* **1999**, *121*, 10323. (b) J. B. Parise, *Inorg. Chem.* **1985**, *24* (25), 4312. (c) T. E. Gier, G. D. Stucky, *Nature*, **1991**, *349*, 508.

- [1.16] (a) U. Wingenfelder, C. Hansen, G. Furrer, R. Schulin, *Environ. Sci. Technol.* **2005**, *39* (12), 4606. (b) N. Moreno, X. Querol, C. Ayora, C. F. Pereira, M. Janssen-Jurkovicová, *Environ. Sci. Technol.* **2001**, *35*, 3526. (c) A. Clearfield, *Chem. Rev.* **1988**, *88* (1), 125.
- [1.17] (a) Y. Cui, H. Xu, Y. Yue, Z. Guo, J. Yu, Z. Chen, J. Gao, Y. Yang, G. Qian, B. Chen, *J. Am. Chem. Soc.* **2012**, *134*, 3979. (b) A. M. Shultz, O. K. Farha, J. T. Hupp, S. T. Nguyen, *J. Am. Chem. Soc.* **2009**, *131*, 4204. (c) V. Stavila, R. K. Bhakta, T. M. Alam, E. H. Majzoub, M. D. Allendorf, *ACS Nano* **2012**, *6*, 9807.
- [1.18] (a) Y. Lee, J. Kim, W. Ahn, *Korean J. Chem. Eng.* **2013**, *30*, 1667. (b) A. Schneemann, V. Bon, I. Schwedler, I. Senkowska, S. Kaskel, R. A. Fischer *Chem. Soc. Rev.*, **2014**, *43*, 6062. (c) F. X. Coudert, *Chem. Mater.*, **2015**, *27* (6), 1905.
- [1.19] (a) H. Furukawa, K. E. Cordova, M. O’Keeffe, O. M. Yaghi, *Science*, **2013**, *341*, 6149. (b) R. J. Kupplera, D. J. Timmons, Q. -R. Fanga, J. -R. Lia, T. A. Makala, M. D. Younga, D. Yuana, D. Zhaoa, W. Zhuanga, H. -C. Zhou. *Coord. Chem. Rev.*, **2009**, *253*, 3042. (c) A. Morozan, F. Jaouen, *Energy Environ. Sci.*, **2012**, *5*, 9269, (d) A. U. Czaja, N. Trukhan, U. Müller, *Chem. Soc. Rev.*, **2009**, *38*, 1284. (e) U. Mueller, M. Schubert, F. Teich, H. Puetter, K. Schierle-Arndt, J. Pastré *J. Mater. Chem.*, **2006**, *16*, 626.
- [1.20] (a) Y. Luo, B. Li, W. Wang, K. Wu, B. Tan, *Advanced Materials*, **2012**, *24*, 5703. (b) T. Ben, S. L. Qiu, *Cryst Eng Comm*, **2013**, *15*, 17. (c) T. Ben, H. Ren, S. Q. Ma, D. P. Cao, J. H. Lan, X. F. Jing, W. C. Wang, J. Xu, F. Deng, J. M. Simmons, S. L. Qiu, G. S. Zhu, *Angew. Chem., Int. Ed.*, **2009**, *48*, 9457. (d) S. Y. Ding, W. Wang, *Chem. Soc. Rev.*, **2013**, *42*, 548. (e) P. M. Budd, B. S. Ghanem, S. Makhseed, N. B. McKeown, K. J. Msayib, C. E. Tattershall, *Chem. Commun.*, **2004**, 230. (f) X. Feng, X. Ding, D. Jiang, *Chem. Soc. Rev.*, **2012**, *41*, 6010.
- [1.21] (a) G. Cheng, T. Hasell, A. Trewin, D. J. Adams, A. I. Cooper, *Angew. Chem., Int. Ed.*, **2012**, *51*, 12727. (b) L. Chen, Y. Honsho, S. Seki, D. Jiang, *J. Am. Chem. Soc.*, **2010**, *132*, 6742. (c) J. X. Jiang, F. B. Su, A. Trewin, C. D.

- Wood, N. L. Campbell, H. J. Niu, C. Dickinson, A. Y. Ganin, M. J. Rosseinsky, Y. Z. Khimyak, A. I. Cooper, *Angew. Chem., Int. Ed.*, **2007**, *46*, 8574. (d) J. X. Jiang, A. Trewin, D. J. Adams, A. I. Cooper, *Chem. Sci.*, **2011**, *2*, 1777. (e) Y. H. Xu, L. Chen, Z. Q. Guo, A. Nagai, D. Jiang, *J. Am. Chem. Soc.*, **2011**, *133*, 17622. (f) S. W. Yuan, B. Dorney, D. White, S. Kirklin, P. Zapol, L. P. Yu, D. J. Liu, *Chem. Commun.*, **2010**, *46*, 4547. (g) A. Li, R. F. Lu, Y. Wang, X. Wang, K. L. Han, W. Q. Deng, *Angew. Chem., Int. Ed.*, **2010**, *49*, 3330. (h) A. Li, H. X. Sun, D. Z. Tan, W. J. Fan, S. H. Wen, X. J. Qing, G. X. Li, S. Y. Li, W. Q. Deng, *Energy Environ. Sci.*, **2011**, *4*, 2062. (i) Q. Chen, J. X. Wang, F. Yang, D. Zhou, N. Bian, X. J. Zhang, C. G. Yan, B. H. Han, *J. Mater. Chem.*, **2011**, *21*, 13554. (j) Y. Kou, Y. Xu, Z. Guo, D. Jiang, *Angew. Chem., Int. Ed.*, **2011**, *50*, 8753. (k) A. I. Cooper, *Advanced Materials*, **2009**, *21*, 1291. (l) J.-X. Jiang, F. Su, A. Trewin, C. D. Wood, H. Niu, J. T. Jones, Y. Z. Khimyak, A. I. Cooper, *J. Am. Chem. Soc.*, **2008**, *130*, 7710.
- [1.22] (a) E. L. Spitler, W. R. Dichtel, *Nat. Chem.*, **2010**, *2*, 672. (b) J. X. Jiang, A. I. Cooper, *Top. Curr. Chem.*, **2010**, *293*, 1. (c) P. J. Waller, F. Gandara, O. M. Yaghi, *Acc. Chem. Res.*, **2015**, *48*, 3053.
- [1.23] H. M. El-Kaderi, J. R. Hunt, J. L. Mendoza-Cortes, A. P. Cote, R. E. Taylor, M. O’Keeffe, O. M. Yaghi, *Science*, **2007**, *316*, 268.
- [1.24] E. L. Spitler, B. T. Koo, J. L. Novotney, J. W. Colson, F. J. Uribe-Romo, G. D. Gutierrez, P. Clancy, W. R. Dichtel, *J. Am. Chem. Soc.*, **2011**, *133*, 19416.
- [1.25] (a) Côté, A. P., El- Kaderi, H. M., Furukawa, H., Hunt, J. R. Yaghi, O. M. *J. Am. Chem. Soc.* **2007**, *129*, 12914. (b) A. Nagai, Z. Guo, X. Feng, S. Jin, X. Chen, X. Ding, D. Jiang, *Nat. Commun.*, **2011**, *2*, 536.
- [1.26] (a) P. Kuhn, M. Antonietti, A. Thomas, *Angew. Chem., Int. Ed.*, **2008**, *47*, 3450. (b) M. J. Bojdys, J. Jeromenok, A. Thomas, M. Antonietti, *Adv. Mater.*, **2010**, *22*, 2202. (c) R. Palkovits, M. Antonietti, P. Kuhn, A. Thomas, F. Schuth, *Angew. Chem., Int. Ed.*, **2009**, *48*, 6909. (d) C. E. Chan-Thaw, A. Villa, L. Prati, A. Thomas, *Chem.–Eur. J.*, **2011**, *17*, 1052.

- [1.27] (a) F. J. Uribe-Romo, J. R. Hunt, H. Furukawa, C. Klock, M. O’Keeffe, O. M. Yaghi, *J. Am. Chem. Soc.*, **2009**, *131*, 4570. (b) F. J. Uribe-Romo, C. J. Doonan, H. Furukawa, K. Oisaki, O. M. Yaghi, *J. Am. Chem. Soc.*, **2011**, *133*, 11478. (c) S.-Y. Ding, J. Gao, Q. Wang, Y. Zhang, W.-G. Song, C.-Y. Su, W. Wang, *J. Am. Chem. Soc.*, **2011**, *133*, 19816. (d) S. Wan, F. Gandara, A. Asano, H. Furukawa, A. Saeki, S. K. Dey, L. Liao, M. W. Ambrogio, Y. Y. Botros, X. Duan, S. Seki, J. F. Stoddart, O. M. Yaghi, *Chem. Mater.*, **2011**, *23*, 4094.
- [1.28] (a) L. M. Lanni, R. W. Tilford, M. Bharathy, J. J. Lavigne, *J. Am. Chem. Soc.*, **2011**, *133*, 13975. (b) R. W. Tilford, W. R. Gemmill, H.-C. Z. Loye, J. J. Lavigne, *Chem. Mater.*, **2006**, *18*, 5296. (c) B. M. Rambo, J. J. Lavigne, *Chem. Mater.*, **2007**, *19*, 3732. (d) Y. Du, K. Mao, P. Kamakoti, P. Ravikovitch, C. Paur, S. Cundy, Q. Li, D. Calabro, *Chem. Commun.* **2012**, *48*, 4606. (e) R. W. Tilford, S. J. Mugavero III, P. J. Pellechia, J. J. Lavigne, *Adv. Mater.*, **2008**, *20*, 2741.
- [1.29] L. Chen, K. Furukawa, J. Gao, A. Nagai, T. Nakamura, Y. Dong, D. Jiang, *J. Am. Chem. Soc.*, **2014**, *136*, 9806.
- [1.30] S. Dalapati, M. Addicoat, S. Jin, T. Sakurai, J. Gao, H. Xu, S. Irle, S. Seki, D. Jiang, *Nat. Commun.*, **2015**, *6*, 7786.
- [1.31] T. Y. Zhou, S. Q. Xu, Q. Wen, Z. F. Pang, X. Zhao, *J. Am. Chem. Soc.*, **2014**, *136*, 15885.
- [1.32] (a) N. L. Campbell, R. Clowes, L. K. Ritchie, A. I. Cooper, *Chem. Mater.*, **2009**, *21*, 204. (b) M. Dogru, A. Sonnauer, A. Gavryushin, P. Knochel, T. Bein, *Chem. Commun.*, **2011**, *47*, 1707.
- [1.33] (a) N. A. A. Zwaneveld, R. Pawlak, M. Abel, D. Catalin, D. Gimes, D. Bertin, L. Porte, *J. Am. Chem. Soc.*, **2008**, *130*, 6678. (b) J. W. Colson, A. R. Woll, A. Mukherjee, M. P. Levendorf, E. L. Spitler, V. B. Shields, M. G. Spencer, J. Park, W. R. Dichtel, *Science*, **2011**, *332*, 228. (c) X. H. Liu, C. Z. Guan, S. Y. Ding, W. Wang, H. J. Yan, D. Wang, L. J. Wan, *J. Am. Chem. Soc.*, **2013**, *135*, 10470.

- [1.34] (a) D. D. Medina, J. M. Rotter, Y. H. Hu, M. Dogru, V. Werner, F. Auras, J. T. Markiewicz, P. Knochel, T. Bein, *J. Am. Chem. Soc.*, **2015**, *137*, 1016. (b) D. R. S. Miguel, A. Abrishamkar, J. A. R. Navarro, R. R. Trujillo, D. B. Amabilino, R M. Ballesté, F. Zamora, J. P. Luis, *Chem. Commun.*, **2016**, *52*, 9212.
- [1.35] (a) B. P. Biswal, S. Chandra, S. Kandambeth, B. Lukose, T. Heine, R. Banerjee, *J. Am. Chem. Soc.*, **2013**, *135*, 5328. (b) S. Kandambeth, B. P. Biswal, H. D. Chaudhari, K. C. Rout, H. S. Kunjattu, S. Mitra, S. Karak, A. Das, R. Mukherjee, U. K. Kharul, R. Banerjee, *Adv. Mater.* **2017**, *29*, 1603945. (c) S. Karak, S. Kandambeth, B. P. Biswal, H. S. Sasmal, S. Kumar, P. Pachfule, R. Banerjee, *J. Am. Chem. Soc.* **2017**, *139*, 1856. (d) S. Kandambeth, V. Venkatesh, D. B. Shinde, S. Kumari, A. Halder, S. Verma, R. Banerjee, *Nat. Commun.* **2015**, *6*, Article No. 6786. (e) S. Kandambeth, A. Mallick, B. Lukose, M. V. Mane, T. Heine, R. Banerjee, *J. Am. Chem. Soc.* **2012**, *134*, 19524. (f) J. H. Chong, M. Sauer, B. O. Patrick, M. J. MacLachlan, *Org. Lett.* **2003**, *5*, 3823 (g) S. Kandambeth, D. B. Shinde, M. K. Panda, B. Lukose, T. Heine, R. Banerjee, *Angew. Chem. Int. Ed.* **2013**, *52*, 13052. (h) H. Xu, J. Gao, D. Jiang, *Nat. Chem.* **2015**, *7*, 905. (i) P. F. Wei, M. Z. Qi, Z. P. Wang, S. Y. Ding, W. Yu, Q. Liu, L. Wang, H. Z. Wang, W. K. An, W. Wang *J. Am. Chem. Soc.* **2018**, *140*, 4623.
- [1.36] (a) M. P. Suh, H. J. Park, T. K. Prasad, D.-W. Lim, *Chem. Rev.*, **2012**, *112*, 782. (b) W. Huang, Y. Jiang, X. Li, X. Li, J. Wang, Q. Wu, X. Liu, *ACS Appl. Mater. Interfaces*, **2013**, *5*, 8845. (c) X. W. Lou, L. A. Archer, Z. C. Yang, *Adv. Mater.* **2008**, *20*, 3987.
- [1.37] H. Furukawa, O. M. Yaghi, *J. Am. Chem. Soc.*, **2009**, *131*, 8875.
- [1.38] J.-T. Yu, Z. Chen, J. Sun, Z.-T. Huang, Q.-Y. Zheng, *J. Mater. Chem.*, **2012**, *22*, 5369.
- [1.39] (a) E. Klontzas, E. Tylianakis, G. E. Froudakis, *J. Phys. Chem. C*, **2009**, *113*, 21253. (b) F. Li, J. Zhao, B. Johansson, L. Sun, *Int. J. Hydrogen Energy*, **2010**, *35*, 266.

- [1.40] H. Furukawa, N. Ko, Y. B. Go, N. Aratani, S. B. Choi, E. Choi, A. O. Yazaydin, R. Q. Snurr, M. O’Keeffe, J. Kim, O. M. Yaghi, *Science*, **2010**, 329, 424.
- [1.41] K. Sumida, D. L. Rogow, J. A. Mason, T. M. McDonald, E. D. Bloch, Z. R. Herm, T.-H. Bae, J. R. Long, *Chem. Rev.*, **2012**, 112, 724.
- [1.42] Y. J. Choi, J. H. Choi, K. M. Choi, J. K. Kang, *J. Mater. Chem.*, **2011**, 21, 1073.
- [1.43] C. J. Doonan, D. J. Tranchemontagne, T. G. Glover, J. R. Hunt, O. M. Yaghi, *Nat. Chem.*, **2010**, 2, 235.
- [1.44] (a) S. Y. Ding, J. Gao, Q. Wang, Y. Zhang, W. G. Song, C. Y. Su, W. Wang, *J. Am. Chem. Soc.*, **2011**, 133, 19816. (b) D. B. Shinde, S. Kandambeth, P. Pachfule, R. R. Kumar R. Banerjee, *Chem. Commun.*, **2015**, 51, 310. (c) P. Pachfule, S. Kandmabeth, A. Mallick, R. Banerjee, *Chem. Commun.*, **2015**, 51, 11717. (d) P. Pachfule, S. Kandambeth, D. Diaz Diaz, R. Banerjee, *Chem. Commun.*, **2014**, 50, 3169.
- [1.45] (a) S. Wan, J. Guo, J. Kim, H. Ihee, D. Jiang, *Angew. Chem., Int. Ed.*, **2009**, 48, 5439. (b) S. Wan, J. Guo, J. Kim, H. Ihee, D. Jiang, *Angew. Chem., Int. Ed.*, **2008**, 47, 8826. (c) X. Feng, L. Liu, Y. Honsho, A. Saeki, S. Seki, S. Irle, Y. Dong, A. Nagai, D. Jiang, *Angew. Chem., Int. Ed.*, **2012**, 51, 2618. (d) X. S. Ding, J. Guo, X. Feng, Y. Honsho, J. D. Guo, S. Seki, P. Maitarad, A. Saeki, S. Nagase, D. Jiang, *Angew. Chem., Int. Ed.*, **2011**, 50, 1289. (e) X. Feng, L. Chen, Y. Honsho, O. Saengsawang, L. Liu, L. Wang, A. Saeki, S. Irle, S. Seki, Y. Dong, D. Jiang, *Adv.Mater.*, **2012**, 24, 3026.
- [1.46] (a) C. R. DeBlase, K. E. Silberstein, T. T. Truong, H. D. Abruna, W. R. Dichtel, *J. Am. Chem. Soc.*, **2013**, 135, 16821. (b) C. R. DeBlase, K. Hernandez-Burgos, K. E. Silberstein, G. G. Rodriguez-Calero, R. P. Bisbey, H. D. Abruna, W. R. Dichtel, *ACS Nano*, **2015**, 9, 3178. (c) F. Xu, H. Xu, D. Wu, Y. Wu, H. Liu, C. Gu, R. Fu, D. Jiang Chen, *Angew. Chem Int. Ed.* **2015**, 54, 6814.

- [1.47] (a) H. Lu, C. Wang, J. Chen, R. Ge, W. Leng, B. Dong, J. Huang, Y. Gao, *Chem. Commun.* **2015**, 51, 15562. (b) B. P. Biswal, H. D. Chaudhari, R. Banerjee, U. K. Kharul, *Chem. Eur. J.*, **2016**, 22, 4695. (c) L. C. Lin, J. Choi, J. C. Grossman, *Chem. Commun.*, **2015**, 51, 14921.
- [1.48] Q. Fang, J. Wang, S. Gu, R. B. Kaspar, Z. Zhuang, J. Zheng, H. Guo, S. Qiu, Y. Yan, *J. Am. Chem. Soc.*, **2015**, 137, 8352.

CHAPTER 2

- [2.1] F. J. Uribe-Romo, J. R. Hunt, H. Furukawa, C. Klöck, M. O’Keeffe, O. M. Yaghi, *J. Am. Chem. Soc.* **2009**, 131, 4570. (b) X. Han, Q. Xia, J. Huang, Y. Liu, C. Tan, Y. Cui, *J. Am. Chem. Soc.* **2017**, 139, 8693. (c) X-H. Liu, C-Z. Guan, S-Y. Ding, W. Wang, H-J. Yan, D. Wang, L-J. Wan, *J. Am. Chem. Soc.* **2013**, 135, 10470. (d) S. F. Pang, S. Q. Xu, T. Y. Zhou, R. R. Liang, T. G. Zhan, X. Zhao, *J. Am. Chem. Soc.* **2016**, 138, 4710. (e) P. Kuhn, M. Antonietti, A. Thomas, *Angew. Chem., Int. Ed.* **2008**, 47, 3450. (f) Y. Zhang, J. Duan, D. Ma, P. Li, S. Li, H. Li, J. Zhou, X. Ma, X. Feng, B. Wang, *Angew. Chem. Int. Ed.* **2017**, 56, 16313.
- [2.2] (a) L. Stegbauer, K. Schwinghammer, B. V. Lotsch, *Chem. Sci.* **2014**, 5, 2789. (b) L. Ascherl, T. Sick, J. T. Margraf, S. H. Lapidus, M. Calik, C. Hettstedt, K. Karaghiosoff, M. Döblinger, T. Clark, K. W. Chapman, F. Auras, T. Bein, *Nat. Chem.* **2016**, 8, 310. (c) S. Y. Ding, J. Gao, Q. Wang, Y. Zhang, W. G. Song, C. Y. Su, W. Wang, *J. Am. Chem. Soc.* **2011**, 133, 19816. (d) C. J. Doonan, D. J. Tranchemontagne, T. G. Glover, J. R. Hunt, O. M. Yaghi, *Nat. Chem.* **2010**, 2, 235. (e) L. Jiao, Y. Hu, H. Ju, C. Wang, M. R. Gao, Q. Yang, J. Zhu, S. H. Yu, H. L. Jiang, *J. Mater. Chem. A*, **2017**, 5, 23170. (f) W. Yang, J. Wang, H. Wang, Z. Bao, J. Zhao, B. Chen, *Cryst. Growth Des.*, **2017**, 17, 6132.
- [2.3] (a) V. S. Vyas, F. Haase, L. Stegbauer, G. Savasci, F. Podjaski, C. Ochsenfeld, B. V. Lotsch, *Nat. Commun.* **2015**, 6, 8508. (b) C. R. Deblase, K. E. Silberstein, T. Truong, H. D. Abruña, W. R. Dichtel, *J. Am. Chem. Soc.* **2013**, 135, 16821.

- (c) W. Yan, X. Yu, T. Yan, D. Wu, E. Ning, Y. Qi, Y.-F. Han, Q. Li, *Chem. Commun.*, **2017**, 53, 3677.
- [2.4] (a) S. Kandambeth, A. Mallick, B. Lukose, M. V. Mane, T. Heine, R. Banerjee, *J. Am. Chem. Soc.* **2012**, 134, 19524. (b) Y. Du, K. Mao, P. Kamakoti, P. Ravikovitch, C. Paur, S. Cundy, Q. Li, D. Calabro, *Chem. Commun.* **2012**, 48, 4606. (c) L. M. Lanni, R. W. Tilford, M. Bharathy, J. J. Lavigne, *J. Am. Chem. Soc.* **2011**, 133, 13975. (d) S. Kandambeth, D. B. Shinde, M. K. Panda, B. Lukose, T. Heine, R. Banerjee, *Angew. Chem. Int. Ed.* **2013**, 52, 13052. (e) Xu, H., Gao, J., Jiang, D. *Nat. Chem.* **2015**, 7, 905. (f) P. F. Wei, M. Z. Qi, Z. P. Wang, S. Y. Ding, W. Yu, Q. Liu, L. Wang, H. Z. Wang, W. K. An, W. Wang *J. Am. Chem. Soc.* **2018**, 140, 4623.
- [2.5] S. Kandambeth, B. P. Biswal, H. D. Chaudhari, K. C. Rout, H. S. Kunjattu, S. Mitra, S. Karak, A. Das, R. Mukherjee, U. K. Kharul, R. Banerjee, *Adv. Mater.* **2017**, 29, 1603945.
- [2.6] (a) J. L. Segura, M. J. Mancheño, F. Zamora, *Chem. Soc. Rev.* **2016**, 45, 5635. (b) B. J. Smith, A. C. Overholts, N. Hwang, W. R. Dichtel, *Chem. Commun.* **2016**, 52, 3690. (c) M. G. Schwab, M. Hamburger, X. Feng, J. Shu, H. W. Spiess, X. Wang, M. Antonietti, K. Müllen, *Chem. Commun.* **2010**, 46, 8932. (d) A. Halder, S. Kandambeth, B. P. Biswal, G. Kaur, N. C. Roy, M. Addicoat, J. K. Salunke, S. Banerjee, K. Vanka, T. Heine, S. Verma, R. Banerjee, *Angew. Chem. Int. Ed.* **2016**, 55, 7806.
- [2.7] M. Matsumoto, R. R. Dasari, W. Ji, C. H. Feriante, T. C. Parker, S. R. Marder, W. R. Dichtel, *J. Am. Chem. Soc.* **2017**, 139, 4999.
- [2.8] (a) G. R. Desiraju, *Acc. Chem. Res.*, **2002**, 35, 565. (b) G. R. Desiraju, *J. Am. Chem. Soc.* **2013**, 135, 9952. (c) A. Halder, S. Karak, M. Addicoat, S. Bera, A. Chakraborty, S. H. Kunjattu, P. Pachfule, T. Heine, R. Banerjee *Angew. Chem. Int. Ed.*, **2018**, 57, 5797. (d) G. R. Desiraju, T. Steiner, *The weak hydrogen bond in structural chemistry and biology*. Oxford University Press: Oxford, 1999. (e) M. Köse, G. Ceyha, M. Tümer, I. Demirtas, I. Gönül, V. McKee, *Spectrochimica Acta Part A: Molecular and Biomolecular Spectroscopy*, **2015**, 137, 477. (f) A. D. Khalajia, J. Simpson, *Acta Cryst.*

- 2009**, *E65*, o553. (f) W. H. Ojala, T. M. Arola, N. Herrera, B. Balidemaja, C. R. Ojala, *ActaCryst.* **2007**, *C63*, o207.
- [2.9] Accelrys, Material Studio Release Notes, Release 4.2, Accelrys Software, San Diego 2006.
- [2.10] (a) M. Köse, G. Ceyha, M. Tümer, I. Demirtas, I.Gönül, V.McKee, *SpectrochimicaActa Part A: Molecular and Biomolecular Spectroscopy*, **2015**, *137*, 477. (b) A. D. Khalajia, J. Simpson, *ActaCryst.* **2009**, *E65*, o553. (c) W. H. Ojala, T. M. Arola, N. Herrera, B. Balidemaja, C. R. Ojala, *ActaCryst.* **2007**, *C63*, o207.
- [2.11] K. Shivakumar, A. Vidyasagar, A. Naidu, R. G. Gonnade, K. M. Sureshan *CrystEngComm*, **2012**, *14*, 519.
- [2.12] B. W. Domagalska, L. Syper, K. A. Wilk, *Tetrahedron* **2004**, *60*, 1931.
- [2.13] M. Albrecht, I. Janser, A. Lützen, M. Hapke, R. Fröhlich, P. Weis, *Chem. Eur. J.*, **2005**, *11*, 5742.
- [2.14] H. F. Li, E. A. Homan, A. J. Lampkins, I. Ghiviriga, R. K. Castellano, *Org. Lett.* **2005**, *7*, 443.
- [2.15] B. Lukose, A. Kuc, T. Heine, *Chem. Eur. J.*, **2011**, *17*, 2388.

CHAPTER 3

- [3.1] J. A. Camargo, A. Alonso, *Environ. Int.* **2006**, *32*, 831–849
- [3.2] Schaidler, L.A. Rudel, R.A. Ackerman, J.M.. Dunagan, S.C. Brody, J. G. *Sci. Total Environ.* **2014**, *468*, 384.
- [3.3] (a) <http://www.un.org/waterforlifedecade/background.shtml> (b) M. A. Shannon, P. W. Bohn, M. Elimelech, J. G. Georgiadis, B. J. Marinas and A. M. Mayes, *Nature*, **2008**, *452*, 301. (c) J. Eliasson, *Nature*, **2015**, *517*, 6.
- [3.4] (a) B. Bethi, S. H. Sonawane, B. A. Bhanvase and S. P. Gumfekar, *Chem. Eng. Process.*, **2016**, *109*, 178. (b) K. Goh, H. E. Karahan, L. Wei, T.-H. Bae, A. G. Fane, R. Wang and Y. Chen, *Carbon*, **2016**, *109*, 694. (c) H. Lu, J. Wang, M. Stoller, T. Wang, Y. Bao and H. Hao, *Adv. Mater. Sci. Eng.*, **2016**, *496*. (d) S. Daer, J. Kharraz, A. Giwa and S. W. Hasan, *Desalination*, **2015**, *367*, 37. (e) A. Cincinelli, T. Martellini, E. Coppini, D. Fibbi and A.

- Katsoyiannis, J. *Nanosci. Nanotechnol.*, **2015**, *15*, 3333. (f) G. Ghasemzadeh, M. Momenpour, F. Omid, M. R. Hosseini, M. Ahani and A. Barzegari, *Front. Environ. Sci. Eng.*, **2014**, *8*, 471. (g) S. Kumar, W. Ahlawat, G. Bhanjana, S. Heydarifard, M. M. Nazhad and N. Dilbaghi, *J. Nanosci. Nanotechnol.*, **2014**, *14*, 1838. (h) C. Santhosh, V. Velmurugan, G. Jacob, S. K. Jeong, A. N. Grace and A. Bhatnagar, *Chem. Eng. J.*, **2016**, *306*, 1116. (i) M. M. Khin, A. S. Nair, V. J. Babu, R. Murugan and S. Ramakrishna, *Energy Environ. Sci.*, **2012**, *5*, 8075.
- [3.5] (a) S. Fendorf, H. A. Michael, and A. van Geen, *Science*, **2010**, *vol. 328*, 1123. (b) N. Mirlean, P. Baisch, and D. Diniz, *Science of the Total Environment*, **2014**, *vol. 482*, 148. (c) A. Mukherjee, M. K. Sengupta, M. A. Hossain *et al. Journal of Health, Population and Nutrition*, 2006, *vol. 24*, 142. (d) D. Chakraborti, M. M. Rahman, B. Das *et al.*, *Water Research*, **2010**, *vol. 44*, 5789
- [3.6] P. Marchetti, M. F. Jimenez Solomon, G. Szekely, A. G. Livingston, *Chem. Rev.* **2014**, *114*, 10735
- [3.7] P. Vandezande, L. E. M. Geversb, I. F. J. Vankelecom, *Chem. Soc. Rev.* **2008**, *37*, 365.
- [3.8] a) S. Karan, Z. Jiang, A. G. Livingston, *Science* **2015**, *348*, 1347. b) S. Karan, S. Samitsu, X. Peng, K. Kurashima, I. Ichinose, *Science* **2012**, *335*, 444. c) Q. Fu, E. H. H. Wong, J. Kim, J. M. P. Scofield, P. A. Gurr, S. E. Kentish, G. G. Qiao, *J. Mater. Chem. A* **2014**, *2*, 17751. d) N. Y. Yip, W. A. Phillip, J. D. Schiffman, M. Elimelech, *Environ. Sci. Technol.* **2010**, *44*, 3812.
- [3.9] J. T. Chen, C. C. Shih, Y. J. Fu, S. H. Huang, C. C. Hu, K. R. Lee, J. Y. Lai, *Ind. Eng. Chem. Res.* **2014**, *53*, 2781
- [3.10] (a) S. Sorribas, P. Gorgojo, C. Téllez, J. Coronas, A. G. Livingston, *J. Am. Chem. Soc.* **2013**, *135*, 15201. (b) T. Rodenas, I. Luz, G. Prieto, B. Seoane, H. Miro, A. Corma, F. Kapteijn, F. X. Llabrés i. Xamena, J. Gascon, *Nat. Mater.* **2015**, *14*, 48. (c) X. Cui, K. Chen, H. Xing, Q. Yang, R. Krishna, Z. Bao, H. Wu, W. Zhou, X. Dong, Y. Han, B. Li, Q. Ren, M. J. Zaworotko, B. Chen, *Science* **2016**, *353*, 141. (d) R. K. Motkuri, H. V. R. Annapureddy, M.

- Vijaykumar, H. T. Schaef, P. F. Martin, B. P. McGrail, L. X. Dang, R. Krishna, P. K. Thallapally, *Nat. Commun.* **2014**, *5*, 4368. (e) Z. R. Jiang, J. Ge, Y. X. Zhou, Z. U. Wang, D. Chen, S. H. Yu, H. L. Jiang, *NPG Asia Mater.* **2016**, *8*, e253. (f) A. Cadiou, K. Adil, P. M. Bhatt, Y. Belmabkhout, M. Eddaoudi, *Science* **2016**, *353*, 137. (g) Y. Zhang, X. Feng, H. Li, Y. Chen, J. Zhao, S. Wang, L. Wang, B. Wang, *Angew. Chem., Int. Ed.* **2015**, *54*, 4259.
- [3.11] (a) K.Song, Q. Q.Meng, F.Shu, Z. F.Ye, *Chemosphere* **2013**, *90*, 1558. (b) G. Li, E. Asselin, Z. Li, *Ind. Eng. Chem. Res.* **2014**, *53*, 11794. (c) S. Chairapat, S. Wongchan, S. Loykulnant, C. Kongkaew, B. Charnnok *Process Saf. Environ.* **2015**, *94*, 420.
- [3.12] (a) F. J. Uribe-Romo, J. R. Hunt, H. Furukawa, C. Klöck, M. O’Keeffe, O. M. Yaghi, *J. Am. Chem. Soc.* **2009**, *131*, 4570. (b) X. Han, Q. Xia, J. Huang, Y. Liu, C. Tan, Y. Cui, *J. Am. Chem. Soc.* **2017**, *139*, 8693. Guan, S-Y. Ding, W. Wang, H-J. Yan, D. Wang, L-J. Wan, *J. Am. Chem. Soc.* **2013**, *135*, 10470.
- [3.13] (a) L. M. Lanni, R. W. Tilford, M. Bharathy, J. J. Lavigne, *J. Am. Chem. Soc.* **2011**, *133*, 13975. (b) Y. Du, K. Mao, P. Kamakoti, P. Ravikovitch, C. Paur, S. Cundy, Q. Li, D. Calabro, *Chem. Commun.* **2012**, *48*, 4606. (c) S. Kandambeth, A. Mallick, B. Lukose, M. V. Mane, T. Heine, R. Banerjee, *J. Am. Chem. Soc.* **2012**, *134*, 19524. (d) P. J. Waller, F. Gándara, O. M. Yaghi, *Acc. Chem. Res.* **2015**, *48*, 3053. (e) D. D. Medina, J. M. Rotter, Y. Hu, M. Dogru, V. Werner, F. Auras, J. T. Markiewicz, P. Knochel, T. Bein, *J. Am. Chem. Soc.* **2015**, *137*, 1016.
- [3.14] (a) L. C. Lin, J. Choib, J. C. Grossman, *Chem. Commun.* **2015**, *51*, 14921. (b) M. Elimelech, W. A. Phillip, *Science* **2011**, *33*, 712.
- [3.15] S. Kandambeth, B. P. Biswal, H. D. Chaudhari, K. C. Rout, H. S. Kunjattu, S. Mitra, S. Karak, A. Das, R. Mukherjee, U. K. Kharul, R. Banerjee, *Adv. Mater.* **2017**, *29*, 1603945.
- [3.16] B. W. Domagalska, L. Syper, K. A. Wilk, *Tetrahedron* **2004**, *60*, 1931
- [3.17] B. Lukose, A. Kuc, T. Heine, *Chem. Eur. J.*, **2011**, *17*, 2388

CHAPTER 4

- [4.1] S. Chu, A. Majumdar, *Nature*, **2012**, 488, 294.
- [4.2] A. S. Arico, P. Bruce, B. Scrosati, J. M. Tarascon, W. Van Schalkwijk, *Nat. Mater.* **2005**, 4, 366.
- [4.3] G. Wang, L. Zhang, J. Zhang, *Chem. Soc. Rev.*, **2012**, 41, 797.
- [4.4] D. G. Nocera, *Chem. Soc. Rev.*, **2009**, 38, 13.
- [4.5] P. Simon, Y. Gogotsi, *Nat. Mater.*, **2008**, 7, 845.
- [4.6] B. Luo, B. Wang, X. L. Li, Y. Y. Jia, M. H. Liang, L. J. Zhi, *Adv. Mater.*, **2012**, 24, 3538.
- [4.7] X. Xiao, X. Liu, H. Zhao, D. Chen, F. Liu, J. Xiang, Z. Hu, Y. Li, *Adv. Mater.*, **2012**, 24, 5762.
- [4.8] H.-C. Chien, W.-Y. Cheng, Y.-H. Wang, S.-Y. Lu, *Adv. Funct. Mater.*, **2012**, 22, 5038.
- [4.9] Y. Zhai, Y. Dou, D. Zhao, P. F. Fulvio, R. T. Mayes, S. Dai, *Adv. Mater.*, **2011**, 23, 4828.
- [4.10] J. R. Miller, P. Simon, *Science*, **2008**, 321, 651.
- [4.11] L. L. Zhang, X. S. Zhao, *Chem. Soc. Rev.*, **2009**, 28, 2520.
- [4.12] B. E. Conway, *Electrochemical supercapacitors: Scientific fundamentals and technological applications*, *Kluwer Academic/Plenum, New York* **1999**.
- [4.13] Y. Wang, Y. Song, Y. Xia, *Chem. Soc. Rev.*, **2016**, 45, 5925.
- [4.14] A. M. Österholm, J. F. Ponder, J. A. Kerszulis, J. R. Reynolds, *ACS Appl. Mater. Interfaces*, **2016**, 8, 13492–13498.
- [4.15] H. Ma, J. He, D.-B. Xiong, J. Wu, Q. Li, V. Dravid, Y. Zhao, *ACS Appl. Mater. Interfaces*, **2016**, 8, 1992.
- [4.16] P. Du, H. C. Liu, C. Yi, K. Wang, X. Gong, *ACS Appl. Mater. Inter.* **2015**, 7, 3263.
- [4.17] M. F. El-Kady, V. Strong, S. Dubin, R. B. Kaner, *Science*, **2012**, 335, 1326.
- [4.18] (a) C. J. Doonan, D. J. Tranchemontagne, T. G. Glover, J. R. Hunt, O. M. Yaghi, *Nat. Chem.* **2010**, 2, 235. (b) P. Kuhn, M. Antonietti, A. Thomas, *Angew. Chem., Int. Ed.* **2008**, 47, 3450. (c) F. J. Uribe-Romo, J. R. Hunt, H. Furukawa, C. Klöck, M. O’Keeffe, O. M. Yaghi, *J. Am. Chem. Soc.* **2009**,

- 131, 4570. (d) L. Ascherl, T. Sick, J. T. Margraf, S. H. Lapidus, M. Calik, C. Hettstedt, K. Karaghiosoff, M. Döblinger, T. Clark, K. W. Chapman, F. Auras, T. Bein, *Nat. Chem.* **2016**, *8*, 310. (e) A. Sun, B. Aguila, J. Perman, N. Nguyen, S. Ma, *J. Am. Chem. Soc.* **2016**, *138*, 15790. (f) X. Han, Q. Xia, J. Huang, Y. Liu, C. Tan, Y. Cui, *J. Am. Chem. Soc.* **2017**, *139*, 8693. (g) X-H. Liu, C-Z. Guan, S-Y. Ding, W. Wang, H-J. Yan, D. Wang, L-J. Wan, *J. Am. Chem. Soc.* **2013**, *135*, 10470.
- [4.19] (a) L. M. Lanni, R. W. Tilford, M. Bharathy, J. J. Lavigne, *J. Am. Chem. Soc.*, **2011**, *133*, 13975. (b) Y.-X. Ma, Z.-J. Li, L. Wei, S.-Y. Ding, Y.-B. Zhang, W. Wang, *J. Am. Chem. Soc.* **2017**, *139*, 4995. (c) M. Elsabahy, K. L. Wooley, *Chem. Soc. Rev.* **2012**, *41*, 2545. (d) V.S. Vyas, M. Vishwakarma, I. Moudrakovski, F. Haase, G. Savasci, C. Ochsenfeld, J. P. Spatz, B. V. Lotsch, *Adv. Mater.* **2016**, *28*, 8749. (e) S. Wang, Q. Wang, P. Shao, Y. Han, X. Gao, L. Ma, S. Yuan, X. Ma, J. Zhou, X. Feng, B. Wang, *J. Am. Chem. Soc.* **2017**, *139*, 4258.
- [4.20] (a) S. Chandra, D. Roy Chowdhury, M. Addicoat, T. Heine, A. Paul, R. Banerjee, *Chem. Mater.* **2017**, *29*, 2074.
- [4.21] (a) S. Kandambeth, A. Mallick, B. Lukose, M. V. Mane, T. Heine, R. Banerjee, *J. Am. Chem. Soc.* **2012**, *134*, 19524. (b) C. R. DeBlase, K. E. Silberstein, T.-T. Truong, H. D. Abruña, W. R. Dichtel, *J. Am. Chem. Soc.* **2013**, *135*, 16821. (b) C. R. DeBlase, K. Hernandez-Burgos, K. E. Silberstein, G. G. Rodriguez-Calero, R. P. Bisbey, H. D. Abruna, Dichtel, W. R. *ACS Nano* **2015**, *9*, 3178.
- [4.22] (a) M. Winter R. J. Brodd, *Chem. Rev.*, **2004**, *104*, 4245. (b) P. Simon, Y. Gogotsi, *Nat. Mater.* **2008**, *7*, 845. (c) G. Wang, L. Zhang, J. Zhang, *Chem. Soc. Rev.* **2012**, *41*, 797. (d) S. Das, P. Chakraborty, S. Mondal, A. Shit, A. K. Nandi, *ACS Appl. Mater. Interfaces* **2016**, *8*, 28055.
- [4.23] (a) C. R. Mulzer, L. Shen, R. P. Bisbey, J. R. McKone, N. Zhang, H. D. Abruña, W. R. Dichtel, *ACS Cent. Sci.* **2016**, *2*, 667. (b) Xu, F.. H. Xu, X. Chen, D. Wu, Y. Wu, H. Liu, C. Gu, R. Fu, D. Jiang, *Angew. Chem., Int. Ed.* **2015**, *54*, 6814.

- [4.24] (a) A. Halder, S. Karak, M. Addicoat, S. Bera, A. Chakraborty, S. H. Kunjattu, P. Pachfule, T. Heine, R. Banerjee *Angew. Chem. Int. Ed.*, **2018**, *57*, 5797. (b) G. R. Desiraju, *Acc. Chem. Res.*, **2002**, *35*, 565.. (b) G. R. Desiraju, T. Steiner, *The weak hydrogen bond in structural chemistry and biology*. Oxford University Press: Oxford, **1999**.
- [4.25] A. Halder, S. Karak, M. Addicoat, S. Bera, A. Chakraborty, H. K. Shebeeb, P. Pachfule, T. Heine, R. Banerjee, *Angew. Chem. Int. Ed.* **2018**, *57*, 5797.
- [4.26] Z. Chen, H. I. Wang, J. Teyssandier, K. S. Mali, T. Dumschlaff, I. Ivanov, W. Zhang, P. Ruffieux, R. Fasel, H. J. Räder, D. Turchinovich, S. De Feyter, X. Feng, M. Kläui, A. Narita, M. Bonn, K. Müllen, *J. Am. Chem. Soc.* **2017**, *139*, 3635.
- [4.27] (a) L. Wang, X. Feng, L. Ren, Q. Piao, J. Zhong, Y. Wang, H. Li, Y. Chen, B. Wang, *J. Am. Chem. Soc.* **2015**, *137*, 4920. (b) D. Sheberla, J. C. Bachman, J. S. Elias, C.-J. Sun, Y. Shao-Horn, M. Dincă, *Nat. Mater.* **2017**, *16*, 220.

CHAPTER 5

- [5.1] (a) T. Aida, E. W. Meijer, S. I. Stupp, *Science* **2012**, *335*, 813. (b) G. Zhang, O. Presly, F. White, I. M. Oppel, M. Mastalerz, *Angew. Chem. Int. Ed.* **2014**, *53*, 1516. (c) S. Klotzbach, F. Beuerle, *Angew. Chem. Int. Ed.* **2015**, *54*, 10356. (d) F. Wgrthner, C. R. Saha-Mçller, B. Fimmel, S. Ogi, P. Leowanawat, D. Schmidt, *Chem. Rev.* **2016**, *116*, 962.
- [5.2] (a) L. B. Gower, *Chem. Rev.* **2008**, *108*, 4551. (b) H. Cçlfen, *Nat. Mater.* **2010**, *9*, 960. (c) G. M. Whitesides, B. Grzybowski, *Science* **2002**, *295*, 2418. (d) J.-F. Lutz, J.-M. Lehn, E. W. Meijer, K. Matyjaszewski, *Nat. Rev. Mater.* **2016**, *1*, 16024. (e) X. Zhou, Q. Jin, L. Zhang, Z. Shen, L. Jiang, M. Liu, *Small* **2016**, *12*, 4743.
- [5.3] (a) H. M. El-Kaderi, J. R. Hunt, J. L. Mendoza-Cortes, A. P. Cote, R. E. Taylor, M. O’Keeffe, O. M. Yaghi, *Science*, **2007**, *316*, 268. (b) A. Nagai, Z. Guo, X. Feng, S. Jin, X. Chen, X. Ding, D. Jiang, *Nat. Commun.*, **2011**, *2*, 536. (c) P. Kuhn, M. Antonietti, A. Thomas, *Angew. Chem., Int. Ed.*, **2008**, *47*, 3450. (b) M. J. Bojdys, J. Jeromenok, A. Thomas, M. Antonietti, *Adv.*

-
- Mater.*, **2010**, 22, 2202. (d) F. J. Uribe-Romo, J. R. Hunt, H. Furukawa, C. Klock, M. O’Keeffe, O. M. Yaghi, *J. Am. Chem. Soc.*, **2009**, 131, 4570.
- [5.4] (a) C. J. Doonan, D. J. Tranchemontagne, T. G. Glover, J. R. Hunt, O. M. Yaghi, *Nat. Chem.* **2010**, 2, 235. (b) P. Kuhn, M. Antonietti, A. Thomas, *Angew. Chem., Int. Ed.* **2008**, 47, 3450. (c) F. J. Uribe-Romo, J. R. Hunt, H. Furukawa, C. Klöck, M. O’Keeffe, O. M. Yaghi, *J. Am. Chem. Soc.* **2009**, 131, 4570. (d) L. Ascherl, T. Sick, J. T. Margraf, S. H. Lapidus, M. Calik, C. Hettstedt, K. Karaghiosoff, M. Döblinger, T. Clark, K. W. Chapman, F. Auras, T. Bein, *Nat. Chem.* **2016**, 8, 310. (e) A. Sun, B. Aguila, J. Perman, N. Nguyen, S. Ma, *J. Am. Chem. Soc.* **2016**, 138, 15790. (f) X. Han, Q. Xia, J. Huang, Y. Liu, C. Tan, Y. Cui, *J. Am. Chem. Soc.* **2017**, 139, 8693. (g) X-H. Liu, C-Z. Guan, S-Y. Ding, W. Wang, H-J. Yan, D. Wang, L-J. Wan, *J. Am. Chem. Soc.* **2013**, 135, 10470.
- [5.5] (a) A. P. Cote, A. I. Benin, N. W. Ockwig, M. O’Keeffe, A. J. Matzger, O. M. Yaghi, *Science*, **2005**, 310, 1166.
- [5.6] Nishiyabu, R.. Teraoka, S.. Matsushima, Y.. Kubo, Y. *ChemPlusChem.* **2012**, 77, 201.
- [5.7] (a) Yan, Y. Z.. Chen, L.. Dai, H. J.. Chen, Z. H.. Li, X.. Liu, X. K. *Polymer* **2012**, 53, 1611. (b) Chen, Z. H.. Jiang, Y.. Chen, L.. Huang, W.. Li, X.. Li, X. J.. Liu, X. K. *Polym. J.* DOI: 10.1038/pj.2013.23.
- [5.8] (a) E. L. Spitler, W. R. Dichtel, *Nat. Chem.*, **2010**, 2, 672. (b) X. H. Liu, C. Z. Guan, S. Y. Ding, W. Wang, H. J. Yan, D. Wang, L. J. Wan, *J. Am. Chem. Soc.*, **2013**, 135, 10470.
- [5.9] (a) B. P. Biswal, S. Chandra, S. Kandambeth, B. Lukose, T. Heine, R. Banerjee, *J. Am. Chem. Soc.*, **2013**, 135, 5328.
- [5.10] S. Wan, J. Guo, J. Kim, H. Ihee, D. Jiang, *Angew. Chem.,Int. Ed.*, **2008**, 47, 8826.
- [5.11] S. Wan, J. Guo, J. Kim, H. Ihee, D. Jiang, *Angew. Chem.,Int. Ed.*, **2009**, 48, 5439.
- [5.12] E. L. Spitler, W. R. Dichtel, *Nat. Chem.*, **2010**, 2, 672.

- [5.13] W. Huang, Y. Jiang, X. Li, X. Li, J. Wang, Q. Wu, X. Liu, *ACS Appl. Mater. Interfaces*, **2013**, *5*, 8845.
- [5.14] (a) S. Kandambeth, A. Mallick, B. Lukose, M. V. Mane, T. Heine, R. Banerjee, *J. Am. Chem. Soc.*, **2012**, *134*, 19524. (b) A. Halder, S. Kandambeth, B. P. Biswal, G. Kaur, N. C. Roy, M. Addicoat, J. K. Salunke, S. Banerjee, K. Vanka, T. Heine, S. Verma, R. Banerjee, *Angew. Chem. Int. Ed.*, **2016**, *55*, 7806. (c) S. Kandambeth, V. Venkatesh, D. B. S., S. Kumari, **A. Halder**, S. Verma, R. Banerjee, *Nat. Commun.*, **2015**, *6*, 6786.
- [5.15] (a) S. Wan, J. Guo, J. Kim, H. Ihee, D. Jiang, *Angew. Chem., Int. Ed.*, **2009**, *48*, 5439. (b) S. Wan, J. Guo, J. Kim, H. Ihee, D. Jiang, *Angew. Chem., Int. Ed.*, **2008**, *47*, 8826. (c) X. Feng, L. Liu, Y. Honsho, A. Saeki, S. Seki, S. Irle, Y. Dong, A. Nagai, D. Jiang, *Angew. Chem., Int. Ed.*, **2012**, *51*, 2618. (d) X. S. Ding, J. Guo, X. Feng, Y. Honsho, J. D. Guo, S. Seki, P. Maitarad, A. Saeki, S. Nagase, D. Jiang, *Angew. Chem., Int. Ed.*, **2011**, *50*, 1289. (e) X. Feng, L. Chen, Y. Honsho, O. Saengsawang, L. Liu, L. Wang, A. Saeki, S. Irle, S. Seki, Y. Dong, D. Jiang, *Adv. Mater.*, **2012**, *24*, 3026. (f) Lou, X. W., Archer, L. A. & Yang, Z. C. *Adv. Mater.* **2008**, *20*, 3987.
- [5.16] S. Kandambeth, V. Venkatesh, D. B. S., S. Kumari, **A. Halder**, S. Verma, R. Banerjee, *Nat. Commun.*, **2015**, *6*, 6786.
- [5.17] T. Y. Zhou, F. Lin, Z.-T. Li, X. Zhao, *Macromolecules*, **2013**, *46*, 7745.
- [5.18] (a) S. Y. Ding, J. Gao, Q. Wang, Y. Zhang, W. G. Song, C. Y. Su, W. Wang, *J. Am. Chem. Soc.*, **2011**, *133*, 19816. (b) D. B. Shinde, S. Kandambeth, P. Pachfule, R. R. Kumar R. Banerjee, *Chem. Commun.*, **2015**, *51*, 310.
- [5.19] (a) C. R. DeBlase, K. E. Silberstein, T. T. Truong, H. D. Abruna, W. R. Dichtel, *J. Am. Chem. Soc.*, **2013**, *135*, 16821. (b) C. R. DeBlase, K. Hernandez-Burgos, K. E. Silberstein, G. G. Rodriguez-Calero, R. P. Bisbey, H. D. Abruna, W. R. Dichtel, *ACS Nano*, **2015**, *9*, 3178.
- [5.20] Q. Fang, J. Wang, S. Gu, R. B. Kaspar, Z. Zhuang, J. Zheng, H. Guo, S. Qiu, Y. Yan, *J. Am. Chem. Soc.*, **2015**, *137*, 8352.
- [5.21] (a) B. Wang, J. S. Chen, H. B. Wu, Z. Wang, X. W. Lou, *J. Am. Chem. Soc.* **2011**, *133*, 17146. (b) C. A. Wang, S. Li, L. An, *Chem. Commun* **2013**, *49*,

7427. (c) L. Hua, Q. Chen, *Nanoscale* **2014**, *6*, 1236. (d) Y. Zhu, J. Shi, W. Shen, X. Dong, J. Feng, M. Ruan, Y. Li, *Angew. Chem., Int. Ed.*, **2005**, *44*, 5083.
- [5.22] Lou, X. W., Archer, L. A. & Yang, Z. C. *Adv. Mater.* **2008**, *20*, 3987.
- [5.23] a) G. R. Desiraju, T. Steiner, *The Weak Hydrogen Bond in Structural Chemistry and Biology*, Oxford University Press, Oxford, 1999. b) G. R. Desiraju, *Acc. Chem. Res.* **2002**, *35*, 565.
- [5.24] K. Grudzie, M. Malinska, M. Barbasiewicz, *Organometallics* **2012**, *31*, 3636.

CHAPTER 6

- [6.1] (a) P. Bhowmick, D. Banerjee, S. Santra, D. Sen, B. Das, K. K. Chattopadhyay, *RSC Adv.*, **2016**, *6*, 8913. (b) Ali A. Ensafi, N.Kazemifard, B. Rezaei, *Biosensors and Bioelectronics* **2016**, *Vol 77*, 499. (c) A. Dhillon, M. Nair, D. Kumar *Anal. Methods*, **2015**, *7*, 10088. (d) N. Yogarajaha, Scott S. H. Tsai *Environ. Sci.: Water Res.Technol.*, **2015**, *1*, 426. (e) R. Touilloux, M. L. T. Waeber, E. Bakker, *Analyst*, **2015**, *140*, 3526
- [6.2] S. Fendorf, H. A. Michael, and A. van Geen, *Science*, **2010**, *vol. 328*, 1123. (b) N. Mirlean, P. Baisch, and D. Diniz, *Science of the Total Environment*, **2014**, *vol. 482*, 148. (c) A. Mukherjee, M. K. Sengupta, M. A. Hossain *et al. Journal of Health, Population and Nutrition*, 2006, *vol. 24*, 142. (d) D. Chakraborti, M. M. Rahman, B. Das *et al.*, *Water Research*, **2010**, *vol. 44*, 5789.
- [6.3] H. Ma, B. Liu, B. Li, L. Zhang, Y. G. Li, H. Tan, H. Zang and G. Zhu, *J. Am. Chem. Soc.*, **2016**, *138*, 5897

ABOUT THE AUTHOR



Mr. Arjun Halder, son of Sahadeb Halder and Chanchala Halder, was born in Narayanpur village of East Burdwan district, West Bengal, India, in 1991. He did his schooling (2007) from Srirampur Bharati Bhaban High School. He has completed his higher secondary (2009) in science stream and B.Sc. in Chemistry (2012) from Visva Bharati University, Santiniketan, Birbhum. After qualifying all India Joint Admission Test to M.Sc. (JAM) he moved to Department of Chemistry, Indian Institute of Technology Kanpur to pursue his M.Sc. in Chemistry (2012-2014). Again, after qualifying all India joint CSIR-UGC National Eligibility Test (NET-JRF) examination, he moved to Physical and Materials Chemistry Division, CSIR-National Chemical Laboratory, Pune, India to pursue his Ph.D. degree in July 2014 under the guidance of Prof. Dr. Rahul Banerjee. He has received the research fellowship (JRF and SRF) from Council of Scientific & Industrial Research (CSIR), New Delhi, India for the period of October 2014 - September 2019 to carry out the Ph.D. thesis work.

LIST OF PUBLICATIONS

1. **Arjun Halder**, Suvendu Karak, Matthew Addicoat, Saibal Bera, Amit Chakraborty, Shebeeb H. Kunjattu, Pradip Pachfule, Thomas Heine and Rahul Banerjee*. “Ultra-stable Imine-based Covalent Organic Frameworks for Sulfuric acid Recovery: An Effect of Interlayer Hydrogen Bonding”.
Angew. Chem. Int. Ed., 2018, 57, 5797. (DOI: 10.1002/anie.201802220)
‘Selected as Very Important Paper (VIP)’ & ‘Highlighted in Chem views magazine’
2. Himadri Sekhar Sasmal, Harshitha Barike Aiyappa, Siddheshwar N. Bhange, Suvendu Karak, **Arjun Halder**, Sreekumar Kurungot,* and Rahul Banerjee*. “Superprotonic Conductivity in Flexible Porous Covalent Organic Framework Membranes”.
Angew. Chem. Int. Ed., 2018, 57, 1. (DOI: 10.1002/anie.201804753)
3. Saibal Bera, Amit Chakraborty, Suvendu Karak, **Arjun Halder**, Soumyajyoti Chatterjee, Subhadeep Saha* and Rahul Banerjee*. “Multistimuli-Responsive Interconvertible Low-molecular Weight Metallo-hydrogels and the In-situ Entrapment of CdS Quantum Dots Therein”.
Chem. Mater., 2018, 30, 4755. (DOI: 10.1021/acs.chemmater.8b01698)
4. **Arjun Halder**, Sharath Kandambeth, Bishnu P. Biswal, Gagandeep Kaur, Neha Chaki Roy, Matthew Addicoat, Jagadish K. Salunke, Subhrashis Banerjee, Kumar Vanka, Thomas Heine, Sandeep Verma and Rahul Banerjee*. “Decoding the Morphological Diversity in Two Dimensional Crystalline Porous Polymers by Core Planarity Modulation”.
Angew. Chem. Int. Ed., 2016, 55, 7806. (DOI: 10.1002/anie.201600087)
5. Sharath Kandambeth, V. Venkatesh, Digambar B. Shinde, Sushma Kumari, **Arjun Halder**, Sandeep Verma and Rahul Banerjee*. “Self-templated chemically stable hollow spherical covalent organic framework”.
Nat. Commun., 2015, 6, 6786. (DOI: 10.1038/ncomms7786)

CONFERENCES AND PRESENTATIONS

1. Presented poster in “*44th National Seminar on Crystallography*”, **2016**, Pune.
2. Presented oral in “*24th Congress and General Assembly of the International Union of Crystallography (IUCr) conference*”, **2017**, Hyderabad, India